University of London
Imperial College of Science, Technology and Medicine
Department of Materials

Modelling of Nuclear Structural Materials

Than Yan Ren

Submitted in part fulfilment of the requirements for the degree of
Doctor of Philosophy and
the Diploma of Imperial College, Jan 2021

Declaration

I declare that the work presented in this thesis is my own and other published works have been referenced appropriately.

The copyright of this thesis rests with the author and is made available under a Creative Commons Attribution Non-Commercial No Derivatives licence. Researchers are free to copy, distribute or transmit the thesis on the condition that they attribute it, that they do not use it for commercial purposes and that they do not alter, transform or build upon it. For any reuse or redistribution, researchers must make clear to others the licence terms of this work.

Abstract

Two material systems, both significant as structural materials in nuclear reactors are modelled using atomic-scale simulations. The first is beryllium metal, which in fusion and fission reactors, is used as a neutron reflector, but in fusion applications is also being considered as a neutron multiplier and a plasma facing material. The low neutron absorption cross-section and high neutron scattering cross-section of beryllium makes it suitable in these roles. The second system is ZrO_2, which forms on the surface of zirconium-based fuel cladding during operation in fission reactors. ZrO_2 acts as a barrier layer between the cladding metal and the coolant water. Dopants in the cladding metal inevitably end up in the ZrO_2 as a consequence of its formation due to oxidation of the cladding metal and can impact its performance as the barrier layer and in turn the expected cladding lifetime. Zirconium is also a low absorption cross-section element.

For the beryllium system, molecular dynamics (MD) damage cascade simulations were performed. Displacement damage in beryllium was predicted as a function of temperature and energy. For each temperature and energy pair, 10 simulations were performed with a predetermined set of PKA directions. Branch-like damage cascades were observed, with defects being formed primarily on the cascade backbone. The number of residual defects remaining after 1 ps increased linearly with primary knock-on atom (PKA) energy from 0.5 keV to 2.5 keV, while the extent of residual damage was largely temperature independent from 300 K to 1100 K. This was attributed to the mechanism by which displaced atoms within the disordered damage region recombine and are thus are unlikely to survive as residual damage. The same simulation model was used to predict the directionally averaged probability of displacement as a function of displacement energy, $P(E_{PKA})$, and thereby the threshold displacement energy at which the probability for displacement is 100%, $E_d^{1.0} = 105$ eV. There is an excellent correspondence between the Kinchin-Pease (K-P) prediction using $E_d = E_d^{1.0}$ and the number of residual defects remaining after the initial recovery phase. Also, by utilising $P(E_{PKA})$, a modification to the K-P model that utilises the probabilistic nature of threshold displacement is proposed.

The behaviour of dopant ions was investigated in monoclinic and tetragonal ZrO_2. Formation energies of dopant-containing as well as intrinsic defects were calculated via density functional theory (DFT). The formation energies were then used to construct defect concentration diagrams (i.e. Brouwer diagrams), which are a function of oxygen partial pressure P_{O_2}. All the

dopant elements considered (Fe, Ni, Cr, Cu and Sb), were found to bind strongly to oxygen vacancies in tetragonal ZrO_2. At low P_{O_2}, expected in the vicinity of the oxide metal interface, a cluster consisting of an oxygen vacancy adjacent to a charge neutral Ni^0 atom was identified as the most populous cluster. Further simulations show that a hydrogen molecule will dissociate in the vicinity of this cluster. No other cluster containing any of the five dopants is both sufficiently populous and acts in this manner. This is proposed to be the mechanism by which Ni is detrimental to hydrogen pickup in Zr alloys. Consequently, neither Cu nor Sb are expected to increase hydrogen pickup in the same way. Sb was identified as a particularly suitable alloy addition compared to Cu as potential alloying element in Zr-based cladding because Cu in ZrO_2 leads to an increase in oxygen vacancy concentration whereas Sb does not.

Acknowledgements

Firstly I would like to thank my supervisors Professor Robin Grimes and Dr Mark Wenman for the opportunity to pursue this PhD, as well as the supervision and guidance throughout the four years. I would also like to thank my fellow PhD students, postdocs and colleagues in the CNE for all the help they have rendered.

I would like to thank my family, as well as my then fiancé and now wife, Iris, for supporting me on every step of my PhD journey away from home.

Finally I would like to express my gratitude to the Singapore Nuclear Research and Safety Initiative for the financial support.

Contents

Declaration **i**

Abstract **ii**

Acknowledgements **iv**

1 Introduction **1**

1.1 Nuclear power 1

1.1.1 BWR and PWR reactors 2

1.1.2 Fusion reactors 4

1.2 Zirconium based fuel cladding 5

1.2.1 Waterside corrosion 6

1.2.2 Oxide transition 8

1.2.3 Hydrogen pick up 9

1.2.4 Oxide structure 10

1.2.5 Alloying elements in Zr cladding 12

1.3 Beryllium in fusion reactors 16

1.3.1 Crystallography 18

1.4 Radiation damage 21

1.4.1 Threshold displacement 21

1.4.2 Damage generation 22

1.4.3 Analytical damage models 25

1.4.4 Computational simulations of radiation damage 26

1.5 Aims and objectives 28

2 Theory **30**

2.1 Molecular dynamics 30

2.1.1 Macroscopic constraints 32

2.1.2 Interatomic potentials 33

2.2 Density functional theory 34

2.2.1 Schrödinger equation 34

2.2.2 Born-Oppenheimer approximation 35

2.2.3 Hohenberg-Kohn theorems 35

2.2.4 Kohn-Sham DFT 38

2.2.5 Exchange-correlation functionals 41

2.2.6 Periodic Systems 44

2.2.7 Plane wave basis 45

2.2.8 Pseudopotentials 46

3 Methodology **49**

3.1 Be-Be interatomic potentials 49

3.1.1 Tersoff potential 51

3.1.2 Potential fitting 52

3.1.3 New Be-Be potential 60

3.2 MD simulations 62

3.2.1 Melting point calculations 62

3.2.2 Radiation damage cascades 62

3.2.3 Defect detection 64

3.2.4 Threshold displacement 65

3.3 Defects in doped ZrO_2 67

3.3.1 Convergence testing 68

3.3.2 Brouwer Diagrams 69

3.3.3 Defect properties 72

4 Radiation damage in beryllium **76**

4.1 Damage cascade simulations 77

4.1.1 Threshold displacement 84

4.2 Temperature dependence of residual defects 88

4.3 Further comparison with original potential 92

4.4 Revisiting the Kinchin-Pease model 94

4.5 Summary 100

5 Prediction of defect concentrations in ZrO_2 102

5.1 Undoped ZrO_2 . . . 103

5.1.1 Monoclinic ZrO_2 . . . 104

5.1.2 Tetragonal ZrO_2 . . . 104

5.2 Iron . . . 106

5.2.1 Brouwer diagrams . . . 106

5.2.2 Binding Energies and Relaxation Volumes . . . 111

5.3 Nickel . . . 114

5.4 Chromium . . . 117

5.5 Fe, Cr and Ni interaction with hydrogen . . . 119

5.6 Copper and Antimony . . . 123

5.6.1 Brouwer diagrams . . . 124

5.6.2 Cu and Sb interaction with hydrogen . . . 130

5.6.3 Space charge considerations . . . 132

5.7 Lithium . . . 134

5.8 Summary . . . 138

6 Future Work 141

6.1 Electronic effects in MD damage cascade simulations . . . 141

6.2 Brouwer diagrams with multiple dopant elements . . . 143

6.3 MD radiation damage simulations in ZrO_2 . . . 143

7 Summary **145**

Bibliography **148**

List of Tables

1.1 Alloying and impurity content of Zr based alloys used in nuclear applications, reported as percentage weight or parts per million. 12

3.1 Predicted properties of HCP beryllium for various Be-Be potentials with comparison to experiment and DFT values. 50

3.2 Fitting table for HCP beryllium values. 54

3.3 Values for the properties of HCP beryllium that were used in the fitting process. Comparisons are made to experiment, DFT, the values predicted using the potential from Björkas *et al.* [150], and the new potential. 60

3.4 Values of the properties of theoretical beryllium structures that were used in the fitting process. Comparisons are made to experiment, DFT, the values predicted using the potential from Björkas *et al.* [150], and the new potential. 61

3.5 Parameters for the Tersoff potential used in this work. 62

3.6 Vacancy and intersititial defect energies predicted with the new Be-Be potential, compared with DFT values [101]. 62

3.7 List of directions in cartesian coordinates for displacement simulations. 63

4.1 Proportion of defects in respective cluster sizes identified for varying PKA energy at 300 K. nV and nI indicate clusters of n vacancies and n interstitials respectively. 84

4.2 Proportion of defects in respective cluster sizes identified for varying simulation temperature with 1 keV PKA energy. nV and nI indicate clusters of n vacancies and n interstitials respectively. 84

4.3 Proportion of residual defects in respective cluster sizes identified at 800 K temperature 1 keV PKA energy for the original Björkas potential [150] and the new potential. nV and nI indicate clusters of n vacancies and n interstitials respectively. 94

5.1 All input parameters for Brouwer diagrams except for the DFT defect energies. . 103

5.2 Comparison between relaxation volumes obtained using constant volume calculations versus constant pressure calculations for relevant charged defects. 112

5.3 Binding energies, relaxation volumes and clustering volumes of defects in monoclinic ZrO_2 at 635 K. Binding energies for clustered defects are calculated from the $V_O^{\bullet\bullet}$ ground state. ^3V_O and ^4V_O refer to vacancies in the 3-coordinated and 4-coordinated oxygen sites respectively. 114

5.4 Binding energies, relaxation volumes and clustering volumes of defects in tetragonal ZrO_2 at 1500 K. Binding energies for clustered defects are calculated assuming the oxygen vacancies have a 2^+ charge. 114

5.5 Mulliken bond populations and bond length (or atomic separation) between the two H^+ ions associated with oxygen vacancy-dopant cluster defects. Defects marked with a $(*)$ are not present in the Brouwer diagram figures. 121

5.6 Relaxation volumes and clustering volumes of selected Cu and Sb defects in tetragonal ZrO_2. 130

5.7 Energy difference between split H^+ and molecular H_2^+ configurations when two H^+ ions are placed into the oxygen vacancy sites of the specified defects. A positive value indicates the H_2^+ configuration is lower in energy but an energy barrier between the configurations exists. (* For $\{Ni_{Zr}'''' : V_O^{\bullet\bullet}\}''$ no barrier exists with the split configuration exhibiting the minimum energy.) 132

5.8 Relaxation volumes and clustering volumes of selected Li defects in tetragonal ZrO_2. 138

5.9 Relaxation volumes and clustering volumes of selected Li defects in monoclinic ZrO_2. 138

List of Figures

1.1 Average binding energies of atomic nuclei, reproduced from Wikimedia Commons. 2

1.2 Schematic of a typical PWR reactor, adapted from [3]. 3

1.3 Schematic of a Tokamak fusion reactor, reproduced from [4]. 4

1.4 Schematic of a PWR fuel assembly and fuel rod, reproduced from world-nuclear.org. 5

1.5 Schematic diagram outlining the corrosion process of zirconium cladding. . . . 6

1.6 Oxide growth curves of various Zr-based alloys with different oxide transition behaviour. Reproduced from [8]. 8

1.7 Unit cell and parameters for the three ZrO_2 phases, with zirconium atoms in green and oxygen atoms in red. Monoclinic ZrO_2 data obtained from [31], tetragonal and cubic ZrO_2 data from [32]. 10

1.8 Phase diagram of ZrO_2 reproduced from [33]. 11

1.9 Five interstitial sites identified in HCP beryllium, reproduced from [101]. The indicated sites are Oc: non-basal octagonal, Te: non-basal tetrahedral, NBt: non-basal trigonal, Hx: basal hexagonal and Tr: basal trigonal. 19

1.10 Unit cell of $Be_{12}V$ viewed from (0 0 1) direction, illustrating the typical unit cell of $Be_{12}M$ intermetallics. Different shades of green indicate symmetrically distinct Be sites while red indicates the V site. 19

1.11 Phase diagrams of Be-Ti system reproduced from [117] and Be-V system reproduced from [118]. 20

1.12 Directionally averaged displacement probability as a function of PKA energy in molecular dynamics simulations of HCP beryllium reproduced from [119]. Error bars indicate 1 standard deviation. 22

1.13 Distinct phases of radiation damage cascades identified in metals and their respective timescales. Figure reproduced from [121]. 23

1.14 Nuclear and electronic stopping power for an α-particle into beryllium. Reproduced from [128]. 24

1.15 Length and time scales typically accessible, with today's computing power, to the common branches of simulation in materials. Figure reproduced from [136]. 27

2.1 Band structure plot of tetragonal ZrO_2 used in this work along indicated high symmetry points in the Brillouin zone. Band energies are taken relative to the Fermi energy. 46

2.2 In the pesudopotential method, dashed lines representing the pseudopotential and the corresponding pseudowavefunction which replaces the all-electron wavefunction and Kohn-Sham potential at $r < r_c$. Adapted from [54]. 48

3.1 Comparison of experimental thermal expansion [161] with those predicted using the current modified and original Björkas *et al.* [150] potential. 53

3.2 Illustration of how thermal expansion arises from the form of the interatomic potential. The dots show the average interatomic spacing at each temperature. . 55

3.3 Plot of $V(r_{ij})$ against lattice parameter a in a HCP structure. The potential shows a small 'kink' where the cut-off function abruptly begins. 55

3.4 Plot of the average atomic separation in HCP beryllium against the atomic energy, which is directly related to temperature, for the potential from Björkas *et al.* [150]. The onset of negative thermal expansion is indicated. 56

3.5 Plot of $V(r_{ij})$ against lattice parameter a in HCP beryllium using the same parameter set from Björkas *et al.* [150] with the exception that the cut-off function was modified by changing the parameters R from 2.685 Å to 6 Å and D from 0.223 Å to 1 Å. 56

3.6 Correspondence of static material properties to interatomic potential. 58

3.7 Inverse relationship of the γ parameter in Tersoff potentials with melting point, shown here for Be-Be I and Be-Be II from Björkas *et al* [150] as well as the potential fitted in this work. 59

3.8 Possible results from the moving-interface method. 63

3.9 Construction of a Wigner-Seitz cell for the central atom in a group of seven atoms (black dots). The dotted lines are the path to the nearest neighbour atoms, for which the solid lines are the perpendicular bisectors that enclose the Wigner-Seitz cell. 65

3.10 Directional points considered for threshold displacement, the arrow indicates the $[10\bar{1}0]$ direction. 66

3.11 Convergence parameters plotted against error for: a) maximum ion displacement, b) energy change per ion, c) maximum force on each ion and d) plane wave cutoff energy. The errors are defined against the strictest value considered, shown here as points with zero error. 69

3.12 Brouwer diagram for intrinsic m-ZrO_2 (based on preliminary results) where the correspondence to oxide depth is indicated. 73

4.1 Examples of cascade trajectories from simulations at 300 K with 2 keV PKA energy after 0.12 ps. Atoms with displacements >2.4 Å are shown as blue circles, with the PKA in red. The atoms displaced >6 Å have trajectories indicated as grey lines and are highlighted green. The initial PKA direction is indicated by a red arrow and Miller index. 78

4.2 PKA displacement as a function of time first 0.2 ps, averaged over the 10 simulations carried out at 1 keV PKA energy and 300 K temperature. Error bars indicated one standard deviation. 79

4.3 PKA displacement as a function of time first 1.2 ps, averaged over the 10 simulations carried out at a given PKA energy and temperature. 80

4.4 Frenkel pairs detected as a function of time first 0.2 ps and 1.2 ps, averaged over the 10 simulations carried out at 1 keV PKA energy and 300 K temperature. Error bars indicate one standard deviation. 81

4.5 The damage identified as the simulations progress over the first 1.2 ps, averaged over the 10 simulations carried out at a given PKA energy and temperature. . . 82

4.6 Some key parameters of the damage cascade (namely maximum PKA displacement, peak damage and residual damage) as a function of PKA energy and temperature. Values are averaged over 10 simulations. The inner markings on the error bars indicate the standard error while the outer markings indicate one standard deviation. The R^2 value for a linear least squares fit (not weighted to errors) is also indicated. 83

4.7 $E_d^{0.0}$ and $E_d^{0.5}$ as a function of PKA direction at 300 K plot using stereographic projection on the [0 0 0 1] and [$\bar{1}$ 0 $\bar{1}$ 0] direction. The '+' symbols indicate nearest neighbour positions. 85

4.8 The probability for displacement $P(E_{PKA})$ as a function of PKA energy at 300 K. Points marked E_d^P are the minimum energies at which the directionally averaged probability of displacement is P, except for $E_d^{0.0}$, which is the maximum energy with no probability of displacement. 86

4.9 The probability for displacement $P(E_{PKA})$ as a function of PKA energy at 300 K, with a theoretical fit using Equation (4.3) with values $\alpha = 0.073$ fs^{-1} and $x_0 = -1.97$ Å. 87

4.10 Timelapse series showing the progression of a 1.5 keV PKA fired in the c-direction in a 5-atom thick slice of the simulation box in the (1 0 0) orientation at 300 K. The PKA is coloured red while secondary atoms displaced > 6 Å are indicated in green. The red cross marks a reference position where the PKA first entered the slice, with the black line indicating its trajectory. The red circle in the final snapshot highlights a residual defect associated with a secondary atom displaced > 6 Å. 88

4.11 a) - d), Graphs detailing the number of atoms (not including the PKA) that have ever been displaced (taken as > 1.2 Å) and atoms that have ever been highly displaced (defined here as > 6 Å) throughout the 11.2 ps simulation time. The error bars indicate one standard deviation, calculated by averaging the 10 simulation conducted for each PKA energy at the specified temperature. e) and f), the percentage of atoms that ever displaced > 6 Å. 90

4.12 Mechanism for defects surviving the thermal spike recovery phase. Reproduced from [134]. In this diagram the PKA moves directly into (or out of) the plane. A hot cascade region with radius R is produced along the PKA trajectory which recrystallises after the thermal spike phase. Atoms that are pushed beyond the cascade core avoid the recrystallisation process and result in the formation of interstitials. 91

4.13 Comparison of PKA displacement and Frenkel pairs detected over the first 1.2 ps of simulation time (averaged over 10 simulations) between the original Björkas potential [150] and this work at 1 keV PKA energy and 800 K temperature. . . 93

4.14 Comparison of PKA displacement over the first 0.2 ps and 1.2 ps of simulation time (averaged over 10 simulations) between the original Björkas potential [150] and this work at 1 keV PKA energy and 800 K temperature. Error bars indicate one standard deviation. 97

4.15 Comparison of Frenkel pairs detected over the first 1.2 ps of simulation time (averaged over 10 simulations) between the original Björkas potential [150] and this work at 1 keV PKA energy and 800 K temperature. Error bars indicate one standard deviation. 98

4.16 MD predicted maximum and residual damage as a function of PKA energy at 300 K. Also shown are predictions using the K-P model assuming a threshold displacement energy of 25 eV [140] as well as 15 eV and 105 eV corresponding to $E_d^{0.0}$ and $E_d^{1.0}$ values calculated using the current potential model. 99

4.17 Predicted Frenkel pairs, N_{FP}, as a function of E_{PKA} based on equation 4.9 in comparison with the original K-P model using $E_d = E_d^{1.0}$. 99

5.1 Brouwer diagram showing the predicted defect concentration as a function of oxygen partial pressure in monoclinic ZrO_2 at 635 K. 104

5.2 Brouwer diagram showing the predicted defect concentration as a function of oxygen partial pressure in tetragonal ZrO_2 at 1500 K. Defects with concentrations below 10^{-6} at all P_{O_2} are not shown. 105

5.3 Brouwer diagram showing the predicted defect concentration as a function of oxygen partial pressure in tetragonal ZrO_2 at 635 K. 106

5.4 Brouwer diagrams showing defect concentrations in monoclinic ZrO_2 at 635 K as a function of oxygen partial pressure with 0.0001 units of iron per ZrO_2. ^3V_O and ^3V_O refer to vacancies in the 3-coordinated and 4-coordinated oxygen sites respectively. The double colon indicates the oxygen vacancy at a 2nd nearest neighbour site with respect to the iron atom Defects with concentrations below 10^{-7} at all P_{O_2} are not shown. 107

5.5 Brouwer diagrams showing defect concentrations in tetragonal ZrO_2 as a function of oxygen partial pressure for a) ZrO_2 with no iron at 1500 K, b) 0.0001 units of iron per ZrO_2 at 1500 K, c) 0.0001 units of iron per ZrO_2 at 900 K and d) 0.01 units of iron per ZrO_2 at 1500 K showing only the oxygen vacancies and paired iron defects. The double colon indicates the oxygen vacancy at a 2nd nearest neighbour site with respect to the iron atom. In all diagrams, defects with concentrations below 10^{-6} at all P_{O_2} are not shown. 109

5.6 Brouwer diagram showing the predicted defect concentration as a function of oxygen partial pressure in tetragonal ZrO_2 at 1500 K at a total Ni dopant concentration of 10^{-4} atoms per formula unit ZrO_2. Defects with concentrations below 10^{-6} at all P_{O_2} are not shown. 115

5.7 Brouwer diagram showing the predicted defect concentration as a function of oxygen partial pressure in monoclinic ZrO_2 at 635 K at a total Ni dopant concentration of 10^{-4} atoms per formula unit ZrO_2. Defects with concentrations below 10^{-7} at all P_{O_2} are not shown. ^3V_O refers to vacancies at the 3-coordinated oxygen site (as opposed to the 4-coordinated site) in m-ZrO_2. 116

5.8 Brouwer diagram showing the predicted defect concentration as a function of oxygen partial pressure in tetragonal ZrO_2 at 1500 K at a total Cr defect concentration of 10^{-4} atoms per formula unit ZrO_2. Defects with concentrations below 10^{-6} at all P_{O_2} are not shown. 118

5.9 The dominant dopant containing defect for each of Fe, Cr and Ni, are identified as a function of P_{O_2}. Numbers beside the indicated defects are the binding energies per bond of each cluster. The charge state of the dopant cations are indicated in parenthesis. 119

5.10 Diagram illustrating ion positions during the geometry optimisation calculation of two H^+ ions in the oxygen vacancy site of a $\{Ni''''_{Zr} : V^{\bullet\bullet}_O\}''$ defect. The two H^+ explore the energy space that would consider H_2 formation before finding the lowest energy configuration split apart. 120

5.11 Predicted bonding interactions resulting from placing two H^+ ions into the oxygen vacancy site of the $\{M^Z_{Zr} : V^{\bullet\bullet}_O\}$ cluster with M = Ni, Cr or Fe. The numbers indicate the Mulliken bond populations. 122

5.12 Brouwer diagram showing the predicted defect concentrations as a function of oxygen partial pressure in tetragonal ZrO_2 at 1500 K at a total Sb defect concentration of 10^{-4} atoms per formula unit ZrO_2. Substitutional dopants, dimer and trimer clusters are in orange, dark blue and light blue lines respectively. Defects with concentrations below 10^{-6} at all P_{O_2} are not shown. 124

5.13 Brouwer diagram showing defect concentrations as a function of oxygen partial pressure in tetragonal ZrO_2 at 1500 K, at a total Sb defect concentration of 10^{-3} atoms per formula unit ZrO_2. a) highlights the intrinsic defects while b) highlights the dopant containing defects. Substitutional dopants, dimer and trimer clusters are shown as orange, dark blue and light blue lines respectively. Defects with concentrations below 10^{-5} at all P_{O_2} are not shown. 125

5.14 Brouwer diagram showing defect concentrations as a function of oxygen partial pressure in tetragonal ZrO_2 at 1500 K, at a total Cu defect concentration of 10^{-4} atoms per formula unit ZrO_2. Substitutional dopants, dimer and trimer clusters are shown as orange, dark blue and light blue lines respectively. Defects with concentrations below 10^{-6} at all P_{O_2} are not shown. 126

5.15 Brouwer diagram showing defect concentrations as a function of oxygen partial pressure in tetragonal ZrO_2 at 1500 K, at a total Cu defect concentration of 10^{-3} atoms per formula unit ZrO_2. a) highlights the intrinsic and dopant substitution defects while b) highlights the cluster defects. Substitutional dopants, dimer and trimer clusters are shown as orange, dark blue and light blue lines respectively. Defects with concentrations below 10^{-5} at all P_{O_2} are not shown. 127

5.16 The dominant dopant containing defect for Cu and Sb, at a concentration of 10^{-4} units per ZrO_2, as a function of P_{O_2}. Energies beside the indicated defects are the binding energies per bond of each cluster. The charge state of the dopant cations are indicated in parenthesis. 128

5.17 Change in free $V_O^{\bullet\bullet}$ concentration as a function of dopant concentration at $P_{O_2} = 10^{-12}$ atm and 1500 K temperature. The grey dashed line indicates the case of undoped ZrO_2. 129

5.18 Final atomic configurations resulting from placing two H^+ ions into the oxygen vacancy site of $\{Ni_{Zr}'''' : V_O^{\bullet\bullet}\}''$ and $\{Cu_{Zr}''' : V_O^{\bullet\bullet}\}'$ clusters. 131

5.19 Boundaries signifying changes to the dominant Sb defect (when included at 10^{-3} units per ZrO_2) as a function of applied space charge and P_{O_2}. 133

5.20 Boundaries signifying changes to: a) the dominant Cu defect and b) the dominant Cu charge state (when included at 10^{-4} units per ZrO_2) as a function of applied space charge and P_{O_2}. 134

5.21 Brouwer diagram showing the predicted defect concentration as a function of oxygen partial pressure in tetragonal ZrO_2 at 1500 K at a total Li defect concentration of 10^{-4} atoms per formula unit ZrO_2. Transition points for the prefered sites for Li and oxygen vacancies are also shown. Defects with concentrations below 10^{-6} at all P_{O_2} are not shown. 135

5.22 Brouwer diagrams showing defect concentrations in tetragonal ZrO_2 at 1500 K as a function of oxygen partial pressure at Li concentration of a) 10^{-5} atoms per formula unit ZrO_2 and b) 10^{-3} atoms per formula unit ZrO_2. Defects with concentrations below 10^{-6} at all P_{O_2} are not shown. 135

5.23 Plot showing transition points for Li favouring $Li_i^{\bullet}$, to clustering with $V_O^{\bullet\bullet}$, and then to Li_{Zr}''' as a function of Li concentration. Also shown are the transition points for single $V_O^{\bullet\bullet}$ being favoured to clustering with Li being favoured as a function of Li concentration. Below a Li concentration of 3×10^{-5}, $V_O^{\bullet\bullet}$ is the dominant oxygen vacancy defect at all P_{O_2}. 136

5.24 Brouwer diagram showing the predicted defect concentration as a function of oxygen partial pressure in monoclinic ZrO_2 at 635 K at a total Li defect concentration of a) 10^{-5} atoms per formula unit ZrO_2 and b) 10^{-3} atoms per formula unit ZrO_2. Defects with concentrations below 10^{-7} at all P_{O_2} are not shown. ^3V_O refers to vacancies at the 3-coordinated oxygen site (as opposed to the 4-coordinated site) in m-ZrO_2. 137

Chapter 1

Introduction

1.1 Nuclear power

Nuclear power plants generate energy through nuclear processes; the fission of heavy radioactive nuclei or the fusion of light nuclei. The energy liberated is the consequence of the difference between the per nucleon binding energies of atomic nuclei as shown in Figure 1.1. This means that for nuclei less than half the size of ^{56}Fe, fusion would yield energy, while fission would yield energy for nuclei at least twice the size of ^{56}Fe. Fusion reactors are still in the developmental phase, whereas fission reactors continue to be in widespread commercial use. Currently, there are over 400 operational fission reactors generating more than 2000 TWh of power per year [1], which constitutes about 10% of the world's electricity production [2].

The safety of nuclear power plants has been a huge concern due to the volatility of the chain fission process. As such reactors are subject to strong scrutiny and safety regulations that demand an understanding of the processes by which radiation affects structural materials within a reactor. Therefore, it is necessary to ensure the integrity of these materials during both normal operation and under accident conditions. The regulatory licensing of nuclear power plants thus includes ensuring that structural materials should be able to contain the radioactive materials within the plant during the occurrence of accidents classified as design basis accidents. Design

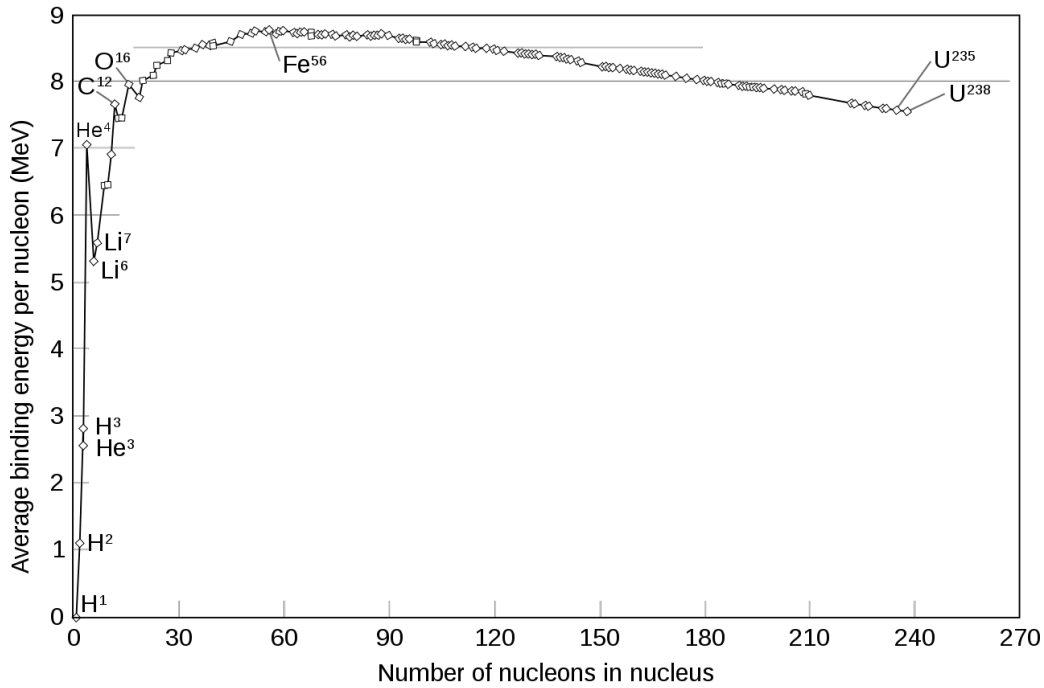


Figure 1.1: Average binding energies of atomic nuclei, reproduced from Wikimedia Commons.

basis accidents include internal factors such as loss of coolant and burst fuel cladding and external factors such as earthquakes or hurricanes that the local region is known to experience. The inherent risk of internal factors are also minimised by ensuring the probability of failure is kept within regulatory limits in regular operation. There are also beyond design basis accidents, such as direct impact from heavy aircraft, that are not covered in the licensing process as their occurrence is deemed unlikely, but the risk of such events should nevertheless be minimised.

1.1.1 BWR and PWR reactors

Boiling water reactors (BWR) and pressurised water reactors (PWR) are the most common types of fission reactors in operation today. For these reactors, nuclear fuel is fabricated in the form of solid pellets encased in rods as described in Section 1.2. The nuclear fission reaction is self-sustained by neutrons via reactions such as:

$$^{235}\mathrm{U} + \mathrm{n} \rightarrow {}^{141}\mathrm{Ba} + {}^{92}\mathrm{Kr} + 3\mathrm{n} \tag{1.1}$$

This reaction, which is controlled by neutron absorbers such as the control rods, heats up the coolant water that fills the vessel which in turn powers a traditional turbine generator. A schematic of a PWR design is shown in Figure 1.2. The main difference between BWR and PWR reactors is that the coolant water turns into steam in a BWR and directly drives the turbine, while in a PWR the coolant water is pressurised to prevent boiling and instead exchanges heat with a secondary lower pressure water system in which the steam is generated to drive the turbine.

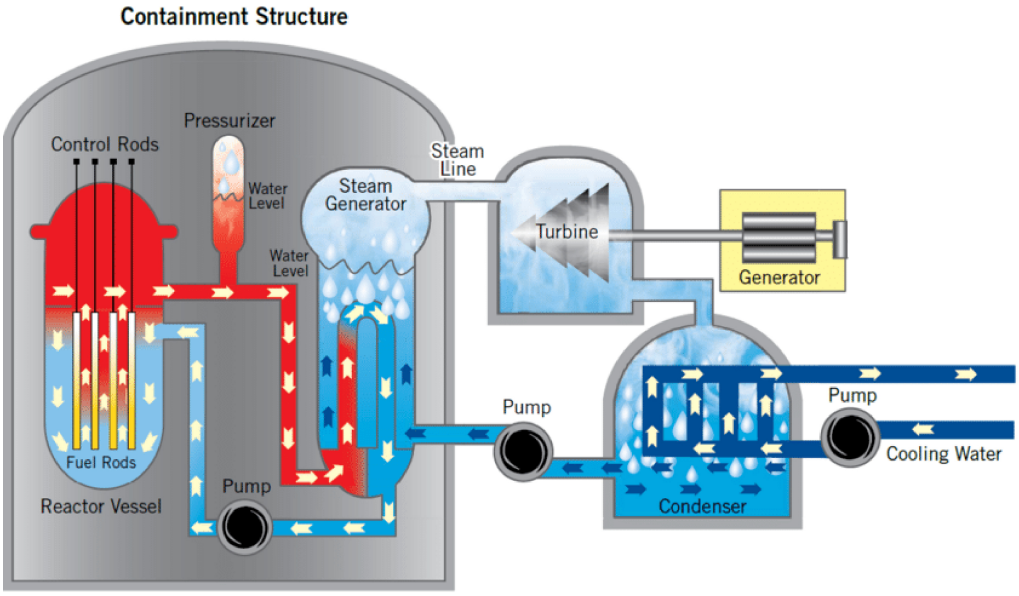


Figure 1.2: Schematic of a typical PWR reactor, adapted from [3].

In fission reactors, the fuel used is highly radioactive for a significantly long time (on human time scales) due to the formation of hazardous fission products such as ^{137}Cs and ^{90}Sr (which have half-lives of around 30 years) and for much longer times scales due to the formation of minor actinides (which have half-lives of thousands of years). Further, the high temperatures sustained during reactor operation means that loss of coolant in the system can lead reactor meltdown, even when the fission reaction is stopped. Therefore the containment of radioactive material, especially in event of emergency is a focus for research. Lastly, throughout the lifetime of the reactor and its fuel, components are subjected to radiation damage. The effect of this on component integrity must also be considered in any safety assessment.

1.1.2 Fusion reactors

Fusion reactors are currently in the developmental phase, but are considered safer than fission reactors as they do not generate heat once the nuclear reaction ceases (i.e. no decay heat), there is no equivalent to prompt criticality and also do not produce radioactive waste that is also long lived (as no minor actinides are produced). Proposed fusion reactor designs most commonly rely on the reaction:

$$^{2}\mathrm{H} + {}^{3}\mathrm{H} \rightarrow {}^{4}\mathrm{He} + \mathrm{n} \tag{1.2}$$

While ^{2}H (deuterium), is stable and commonly available (e.g. in water), ^{3}H (tritium) is scarce as it undergoes β-decay and it is usually anticipated to be produced in-reactor via neutron capture in lithium blankets. As the optimum cross section for the deuterium-tritium reaction is achieved only when the components have about 60 keV kinetic energy, the fuel has to be accelerated to such high energies that it forms a plasma. Sustaining and containing this high energy plasma in an economical way is an ongoing topic of research. A design that has seen alot of focus is the Tokamak reactor (see Figure 1.3), which aims to contain the charged plasma in a solenoid trajectory around a toroidal chamber via magnetic fields.

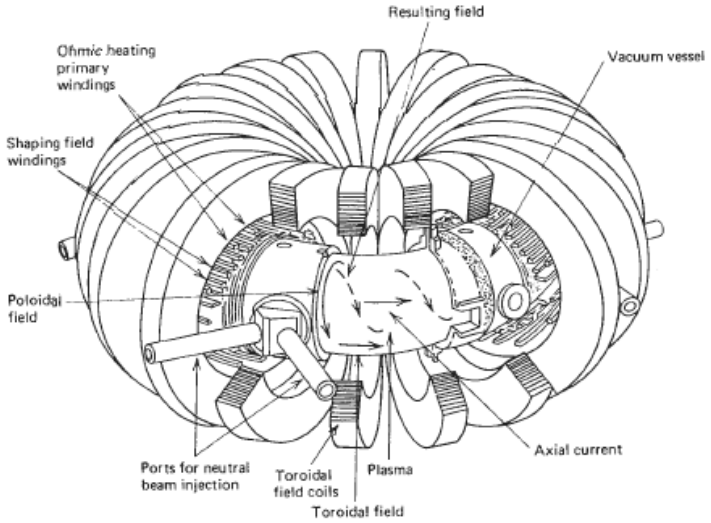


Figure 1.3: Schematic of a Tokamak fusion reactor, reproduced from [4].

1.2 Zirconium based fuel cladding

In a typical PWR reactor, fuel rods are fabricated from solid UO_2 fuel pellets stacked and sealed within long metal rods, which is the fuel cladding (see). The fuel rods are bundled into fuel assemblies of around 200 individual rods, while a typical reactor vessel is then able to accommodate about 150 fuel assemblies.

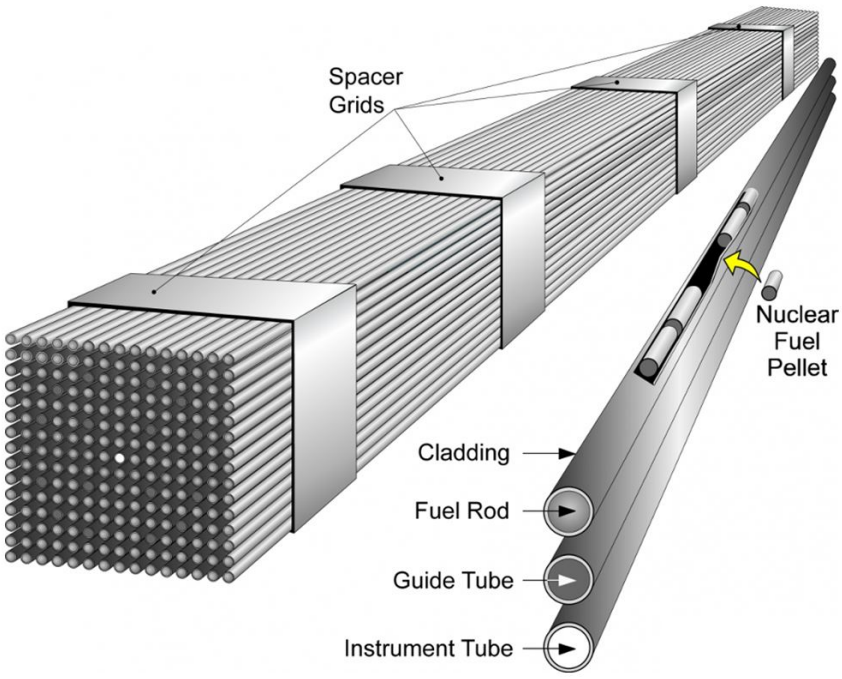


Figure 1.4: Schematic of a PWR fuel assembly and fuel rod, reproduced from world-nuclear.org.

Fuel cladding in fission reactors should ideally have high resistance to irradiation, be relatively transparent to neutrons in order to maintain neutron economy in the reactor core, as well as have high thermal conductivity to allow for efficient transport of heat away from the fuel. As the fuel cladding provide an important first layer of containment for the radioactive fuel from the environment, they should also have good mechanical properties such as high ductility and hardness, as well as corrosion resistance, to minimise the risk of cladding rupture. For water cooled reactors, zirconium alloys are among the most commonly used materials for fuel cladding as they are able satisfy the above requirements [5]. Further, given the interest of increasing fuel burnup, or uprating the output of existing LWRs and PWRs, there has been an interest in improving the performance of these zirconium alloys to satisfy the increased

regulatory requirements as a short to medium term solution.

1.2.1 Waterside corrosion

Given the constant contact between the fuel cladding and the coolant water in the reactor, a main determining factor of cladding service lifetime is water corrosion [6]. This is an electrochemical process between the metal, the oxide layer that forms during reactor operation and the coolant. The outline of this process is shown in Figure 1.5. The process begins by the

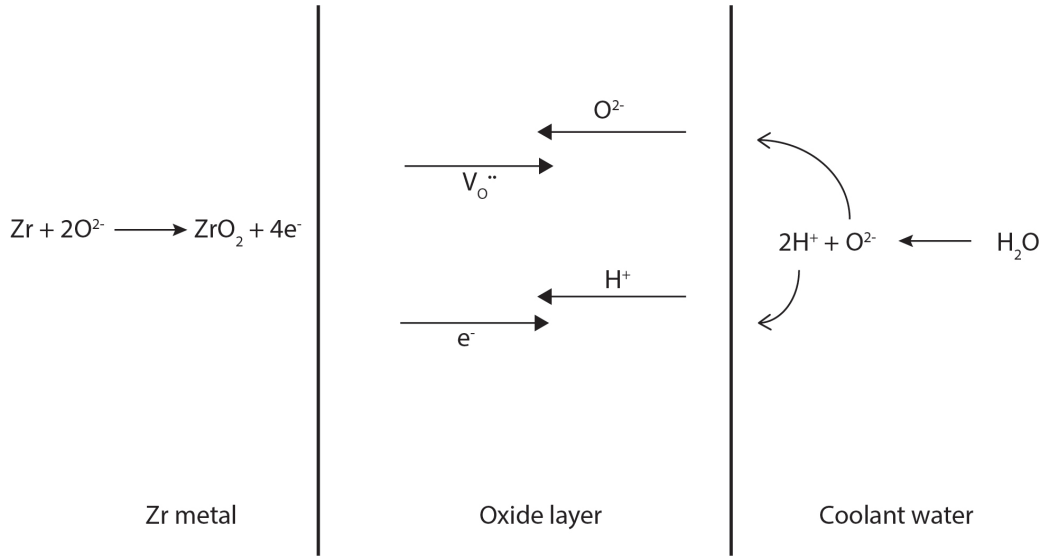


Figure 1.5: Schematic diagram outlining the corrosion process of zirconium cladding.

water molecules in the coolant dissociating into oxygen and hydrogen ions. The oxygen ion is then incorporated onto an available oxygen vacancy at the oxide surface, which then diffuses inwards due to the stoichiometric gradient of the oxide [7,8]. The oxygen ions eventually reach the metal and oxidise it, forming ZrO_2 and releasing electrons, which migrate back out through the oxide to reduce H^+ ions [7,8].

In bulk ZrO_2, the diffusion rate of oxygen is determined by the concentration of oxygen vacancies and interstitials by the equation:

$$D_{oxygen} = \sum_q [\mathrm{V}_\mathrm{O}^q] D_{\mathrm{V}_\mathrm{O}^q} + \sum_q [\mathrm{O}_\mathrm{i}^q] D_{\mathrm{O}_\mathrm{i}^q} \tag{1.3}$$

where D_{X^q} is the diffusivity of defect X with charge q and the square brackets indicate the defect concentration. Theoretical calculations in monoclinic ZrO_2 show that oxygen interstitials have higher diffusivities (but within an order of magnitude) compared to vacancies [9], thus it is still expected that the rate limiting diffusing species will primarily be determined by their concentrations.

As the oxide layer thickens, the oxygen ions take longer to migrate into the metal layer, thereby slowing the rate of corrosion [10, 11]. This typically results in a parabolic to cubic rate law of oxide weight gain w, which is described by the equation:

$$w(t) = At^n \tag{1.4}$$

for some constant A, with the value of n being dependent on the type of alloy used [12, 13]. The Zircaloy series of alloys as well as ZIRLO that are used commonly today exhibit n values of around $n = 0.3$ to $n = 0.4$, while experiments have shown that n can be as low as 0.17 in Zr-0.5Cu and be as high as almost 0.5 in Zr-Nb alloys [13, 14].

Coolant water chemistry

The chemistry of the primary coolant water in direct contact with ZrO_2 also plays a significant role. For instance, boric acid is added into the coolant water as a neutron absorber to control reactivity in pressurised water reactors. To maintain the pH level in the coolant in response to boric acid, the alkaline LiOH is also added. However, it has also been known for some time that LiOH increases the corrosion rate of the fuel cladding [15]. The dissolution of ZrO_2 by LiOH has been suggested as a possible cause for this increase [16]. Secondary ion mass spectrometry analysis have found that Li^+ ions are incorporated evenly into the oxide, with irradiated samples showing higher concentrations of Li^+ [17]. Simulation work has investigated the changes in chemistry due to Li incorporation and found elevated oxygen interstitial concentrations in ZrO_2, suggesting enhanced oxygen diffusion rates leading to increased corrosion rate [18]. LiOH exposure has also been found to decrease the presence tetragonal ZrO_2, presumably due to

destabilisation of the tetragonal phase [18, 19].

1.2.2 Oxide transition

As the oxide continues to grow, it reaches a threshold point where the protective oxide breaks down in an event known as transition, possibly due to compressive stresses that build up as the oxide grows due to its Pilling-Bedworth ratio of around 1.56 [20]. This process then resets as a new protective oxide layer is grown [21]. This results in the segmented weight gain curve seen in experiments (see Figure 1.6). The post-transition oxide would therefore consist of cracked

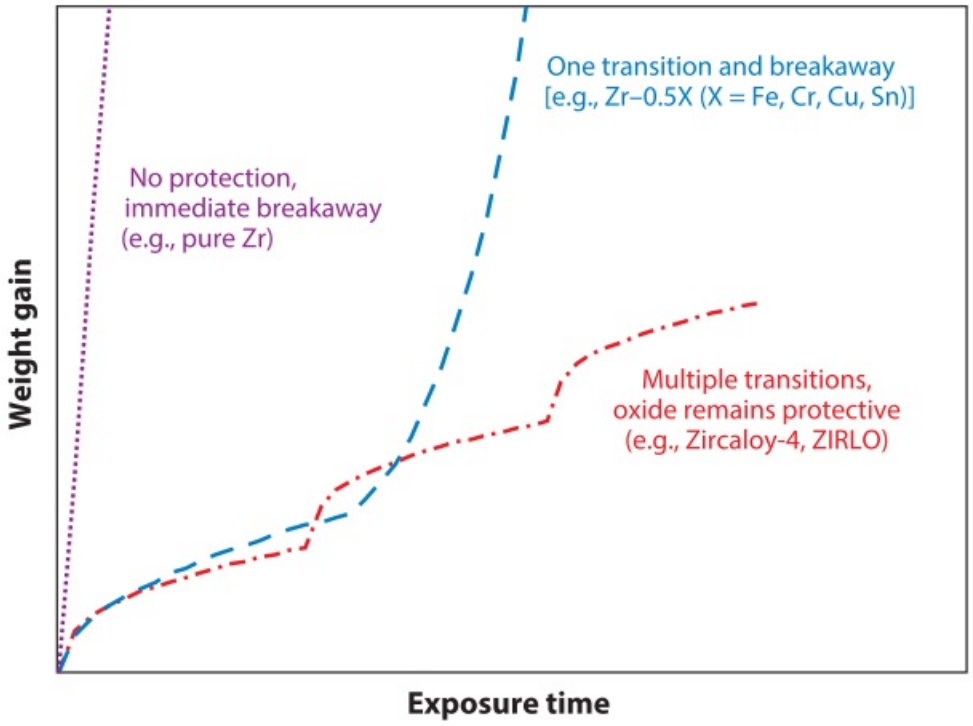


Figure 1.6: Oxide growth curves of various Zr-based alloys with different oxide transition behaviour. Reproduced from [8].

non-protective oxide on the outer layer, while the intact inner new oxide is protecting the cladding metal. Not all Zr-based cladding have oxides that undergo transition; some alloys like Zr-0.5Cu only go through one transition before breaking away. Having an oxide layer that is able to go through multiple transitions without breaking away is crucial in fuel cladding and is a property seen in commonly used alloys such as Zircaloy-4 and ZIRLO (see Figure 1.6).

1.2.3 Hydrogen pick up

Another important factor is H^+ ions migrating into the metal. When the hydrogen content increases beyond its solubility limit in zirconium, hydrides will precipitate. This creates weaknesses and embrittles the Zr: this is termed delayed hydride cracking (DHC) [22, 23].

The fraction of available H^+ picked up by the cladding is called hydrogen pick-up fraction (HPUF), its value depends on alloying elements [7]. The importance of this process is well recognised and there are even safety case regulations that limit the amount of hydrogen that a serviceable material or alloy is allowed to pick up [24].

The experimental H^+ diffusion rate in the oxide is reported to be around 10^{-18} m^2/s [25]. Several possible diffusion pathways have been suggested, such as grain boundary diffusion [26] and interstitial diffusion [27]. The propensity for the coolant water itself to enter the oxide through cracks before dissociating into H^+ and O^{2-} is also crucial [28]. Moreover, the size of inter-metallic precipitates has also been linked to the HPUF, with larger precipitates suggested to better function as bridges for hydrogen transport [29]. It is unclear however, the exact contributions of each of the pathways and other factors have on the overall diffusion rate of H^+ in ZrO_2 and which is the limiting factor under reactor conditions. Finally, it is also important to consider the effect of electrons migrating out of the oxide as shown in Figure 1.5, where an increase in electron concentration or oxide conductivity may better facilitate the reduction of H^+ into harmless H_2 molecules [30].

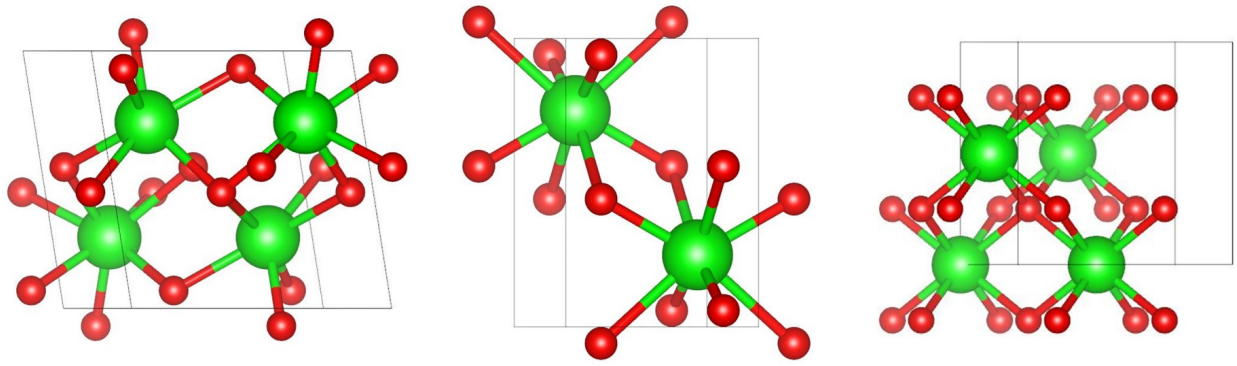
Relation to corrosion rate

The processes of oxidation and hydrogen pick-up are strongly correlated. It has been shown in several different alloys that the instantaneous HPUF follows the same periodicity as oxidation kinetics, in that the HPUF increases with corrosion initally but then decreases to oxide transition. Furthermore, it has been reported that alloys with slower oxidation rates can show higher overall HPUF [7, 14].

It is suggested that the HPUF is related to the electronic conductivity of the oxide, where a higher conductivity means that more electrons will flow freely out through the oxide to recombine with any H^+ ions migrating in through the oxide [14]. This could imply that it is the change in oxide conductivity during the corrosion process , and/or change in alloying content, that affects the HPUF.

1.2.4 Oxide structure

ZrO_2 exists in three different phases: monoclinic (α-ZrO_2), tetragonal (β-ZrO_2) and cubic (γ-ZrO_2). The unit cells and cell parameters of the three phases are shown in Figure 1.7. The phase diagram in Figure 1.8 shows that below approximately 1478 K, ZrO_2 is stable in the monoclinic phase. From approximately 1478 K to 2338 K the tetragonal phase is stable and above that, until the melting point is reached, the cubic phase becomes stable.



Monoclinic	Tetragonal	Cubic
Space group: $P2_1/c$	Space group: $P4_2/nmc$	Space group: $Fm\bar{3}m$
a: 5.169 Å ; b: 5.232 Å ; c: 5.341 Å	a: 3.5948 Å ; b: 3.5948 Å ; c: 5.1824 Å	a: 4.925 Å ; b: 4.925 Å ; c: 4.925 Å
α: 90°; β: 99.25°; γ: 90°	α: 90°; β: 90°; γ: 90°	α: 90°; β: 90°; γ: 90°

Figure 1.7: Unit cell and parameters for the three ZrO_2 phases, with zirconium atoms in green and oxygen atoms in red. Monoclinic ZrO_2 data obtained from [31], tetragonal and cubic ZrO_2 data from [32].

In autoclave samples of Zircaloy cladding, the ZrO_2 oxide layer only consists of two phases:

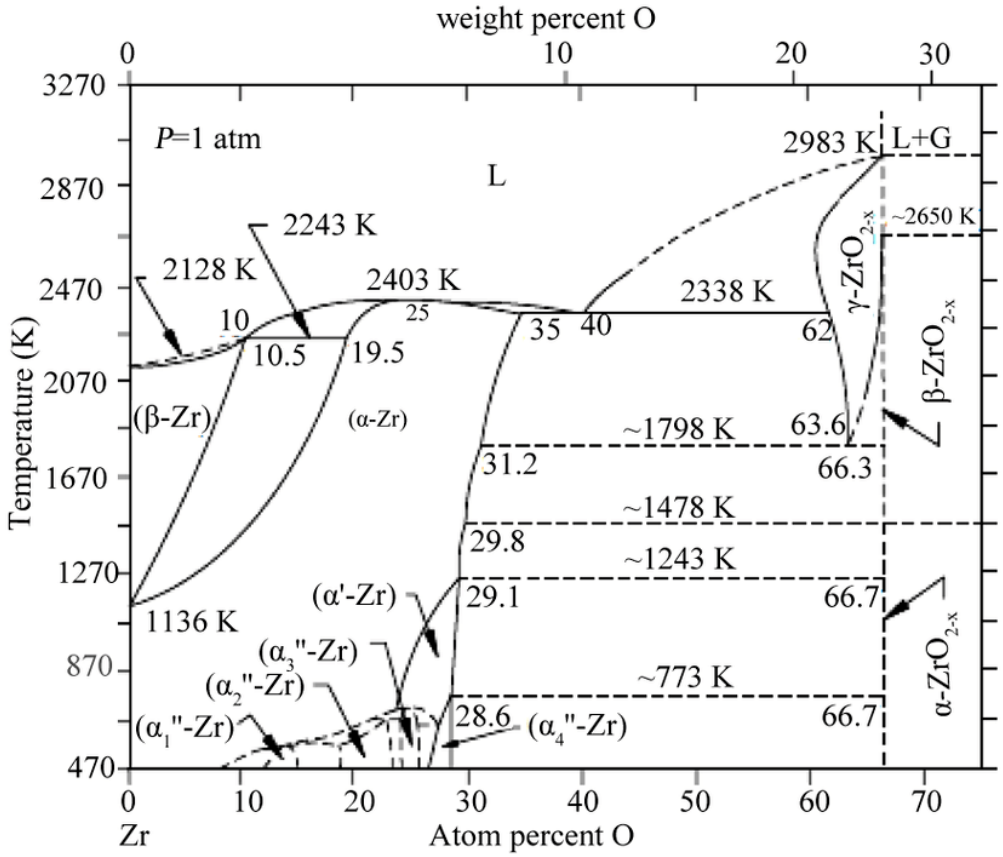


Figure 1.8: Phase diagram of ZrO_2 reproduced from [33].

monoclinic (α) and tetragonal (β) ZrO_2. Monoclinic ZrO_2 is predominantly made up of columnar grains of about 200 nm in length, while tetragonal ZrO_2 is seen in transmission electron microscope (TEM) images as small equiaxed grains of about 10 nm in diameter. Tetragonal ZrO_2 is found in small amounts throughout the oxide, but in general occurs in larger proportion nearer the metal-oxide interface [8, 13, 19, 34]. At reactor operating temperatures of around 635 K, the tetragonal phase is stabilised by compressive stresses in the oxide, which various experiments estimate to be around 1 GPa [20, 35]. At the metal-oxide interface, an uneven layer of intermediate oxide up to several tens of nanometres have been observed. While its composition is not entirely clear, observations of phases such as ZrO and Zr_3O have been reported [34,36–38], which are suggested to eventually transform into the monoclinic phase and start growing into the columnar grains [39].

The inner protective layer of the oxide therefore has a higher proportion of tetragonal ZrO_2 and the formation of the protective oxide itself has been linked to the occurrence of tetragonal ZrO_2

in the metal-oxide interface [13]. Furthermore, monoclinic ZrO_2 has been seen to transform into tetragonal ZrO_2 under irradiation, suggesting a link between tetragonal phase stability and time between transitions. [40, 41].

Pores running along the columnar grains and even towards the metal/oxide interface have been found [42, 43]. It is believed that the processes of transition is linked to these pores: cracks form within the oxide due to stresses which link-up these pores, giving a free path for oxygen ions to migrate directly into the metal/oxide surface, thereby causing the oxide to lose its protective function [43, 44].

1.2.5 Alloying elements in Zr cladding

In general, the understanding of the mechanisms by which alloying elements modify the behaviour of Zr-based cladding is lacking [7]. It is clear, however, that at least some of the variation in behaviour is associated with the effect of alloying elements on the properties of the oxide layer that forms on the surface of the cladding alloys during corrosion. The alloying content of some commonly used Zr-based claddings are shown in Table 1.1.

Table 1.1: Alloying and impurity content of Zr based alloys used in nuclear applications, reported as percentage weight or parts per million.

	Zircaloy-2[a]	Zircaloy-4[a]	Zr-1Nb[a]	Zr-2.5Nb[a]	ZIRLO[b]	M5[c]
Sn (%)	1.2-1.7	1.2-1.7	–	–	0-0.99	–
Nb (%)	–	–	1	2.4-2.8	0.98	1
Fe (%)	0.07-0.20	0.18-0.24	–	–	0.11	0.038
Cr (%)	0.05-0.15	0.07-0.13	–	–	–	–
Ni (%)	0.03-0.08	–	–	–	–	–
O (%)	0.021-0.025	0.021-0.025	0.021-0.025	0.021-0.025	0.11	0.11
Co (ppm)	20	20	20	20	–	–
Hf (ppm)	100	100	100	100	40	–
U (ppm)	3.5	3.5	3.5	3.5	–	–

[a]Ref: [45], [b]Ref: [46], [c]Ref: [47]

Theoretical and experimental studies have been carried out to investigate the underlying mech-

anisms. For experimental work, techniques such as experimental X-ray absorption near edge structure measurements (XANES) are often used to probe the structure as well as the distribution and charge states of dopant elements in the oxide [48–51]. There has also been significant theoretical work utilising Density functional theory (DFT) simulations focusing on ZrO_2 [52–57], which are often used to guide the construction of defect concentration diagrams via the method first introduced by Zhang and Northup [58].

The current understanding of the role and behaviour of alloying elements in Zr-based cladding relevant to this work is described below.

Tin

During the development of Zircaloy-2 cladding, the addition of Sn was shown to reduce the corrosion rate of the cladding [59,60]. It was, however, later found that this primarily stemmed from the suppression of the deleterious effects of nitrogen [60, 61]. In fact, lowering of Sn content in modern Zr cladding has been shown to delay the oxide transition as well as decrease HPUF [62–64]. Nevertheless, Sn is still included in Zr alloys today to improve strength and creep resistance [65, 66].

Experimental studies report that Sn adopts a 2+ and 4+ charge state when dissolved in ZrO_2 [67, 68] though it resists oxidation for longer and can form metallic precipitates in the oxide [69]. A computational study by Bell *et al.* has suggested that Sn interaction with Nb in Zr-Sn-Nb alloys leads to a preference for Sn^{2+} over Sn^{4+}, inhibiting oxygen vacancy suppression and thus leading to increased corrosion rates and an earlier oxide transition [52].

Iron

The behaviour of Fe in ZrO_2 has been studied from both theoretical and experimental standpoints. XANES have shown that in the oxide layer of corroded zirconium alloys, Fe mainly assumes a 3+ charge state, while the 2+ charge state has also been observed in significant

proportions [48, 70–72].

Atom probe tomography experiments showed that Fe tends to precipitate and segregate to grain boundaries, leaving only between 0.003 at% and 0.018 at% iron in the metal [73]. The elevated conentrations of Fe at grain boundaries have also been reported to continue into the oxide for at least 70 nm [74], therefore a similar distribution may be expected throughout the protective layer of the oxide. α-Fe has been observed in corroded Zr intermetallic samples and shown to stabilise tetragonal ZrO_2 [75].

While Fe has already been incorporated into most cladding alloys used today, recent developments in zirconium alloys have been looking towards higher iron content, such as the HiFi (High corrosion resistance and high iron zirconium) alloy developed by Nuclear Fuel Industries Ltd., which demonstrate superior corrosion resistance (mainly in terms of nodular corrosion) [76]. Other reports suggest that iron can also be beneficial to the general corrosion in zirconium alloys [77]. The addition of iron has been reported to reduce the HPUF in zirconium alloys [78], although other authors suggest the opposite effect through a different mechanism [29, 79]. The corrosion resistant properties of Fe has been demonstrated in the intermetallic $Zr(Fe,Nb)_2$ which exhibits the C14 Laves phase. It is suggested that the ability of Fe to exhibit multiple charge states promotes the formation of a layered oxide structure, within which the Fe-deficient layers provide a barrier for oxygen transport [80].

Chromium

Addition of Cr as an alloying element, as well as via ion implantation has been shown to slow the corrosion rate of Zr-based cladding [59, 60, 81] and has been a component in the Zircaloy series of alloys. Cr is not observed to segregate to grain boundaries, but nevertheless tends to form nano-sized clusters, so that the concentration profile of Cr varies greatly from grain to grain; from entirely depleted regions to up to 25 at.% concentration [74]. While chromium has common charge states 3+ and 4+, there are no prior studies known describing the oxidation states of Cr in ZrO_2 distribute on corroded Zr alloys.

Nickel

While Ni was included in early versions of Zr-based cladding, around the same time as Zircaloy-3 began to be developed, the effects of hydrogen embrittlement on the cladding became better realised [60]. Through subsequent in-reactor and out-of-pile experiments on zirconium alloys, Ni was found to be responsible for enhanced hydrogen pick-up fraction (HPUF) [59, 60, 82, 83]. Thus, Ni was largely removed, first resulting in Ni-free Zircaloy-2, while the Fe content was then increased to compensate for the lower Ni content in Zircaloy-4, which is still in use today [59, 60]. It has long been suspected that the increased HPUF may be due to the catalytic properties of Ni [84]. Ni does however, reduce the corrosion rate, which is why it was included in early alloy designs.

Solute Ni in ZrO_2 has mostly been seen in the 2+ charge state [51]. Similar to Fe, enriched concentrations of Ni are also observed along grain boundaries in Zr metal, which extend into the oxide [85]. Recent XANES work by Shivprasad *et al.* [50] showed the presence of metallic Ni in the non-protective oxide layer of Zircaloy-2 samples exhibiting high HPUF, hinting at a possible role of Ni^0.

Copper

Copper is not incorporated in current Zr alloys for fuel cladding, but studies have been performed to assess its possible benefit. Autoclave tests showed the optimal Cu content for corrosion resistance in Zircaloy-4 to be 0.1 wt.% [86]. Such Cu addition was also shown to be a suitable replacement for Sn as it too enhances the tensile strength of the cladding [87]. While Cu commonly adopts the 1+ and 2+ charge state, there are no known studies for prefered Cu charge states in ZrO_2.

Antimony

Sb was previously proposed as a potential alloying element because it has a similar electronic structure to Nb, which is a key component in some of the current Zr based cladding [53]. Sb has common charge states 3+ and 5+ in comparison to 2+ and 4+ for Nb. Initial experiments indicated both reduced corrosion rate and hydrogen pickup with respect to the 1% Nb alloy ZIRLO, especially when Sb was included in conjunction with Nb [53, 88]. Sb is also reported to have up to 1.9 at.% solubility at 1136 K in α-Zr [89].

Secondary phase particles

Fe, Cr and Ni, alloying elements that have been used in past and current fuel cladding, have very low solid solubility in α-Zr, thus they tend to form second phase precipitates (SPPs) in the alloy. Consequently, they have previously been assumed to influence corrosion and HPUF by methods other than oxide layer doping. However, as corrosion progresses, SPPs are shown to oxidise within the oxide layer (after Zr) and atom probe studies have observed these insoluble alloying elements within the bulk oxide [74, 85, 90]. Dissolution of Fe, Cr and Ni from the SPPs into the Zr matrix have been seen as they oxidise, with increased concentrations in solid solution observed around such features [91]. Furthermore, it has been suggested that the sudden increase in HPUF of Zircaloy-2 that accompanies neutron irradiation may be a result of the dissolution of alloying elements from the SPPs.

1.3 Beryllium in fusion reactors

Due to its low absorption cross-section and high scattering cross-section, beryllium is used as a neutron reflector and in moderators in the nuclear industry, [92, 93]. It is also one of the primary choices as the plasma facing material in tokamak fusion reactors such as ITER [94].

Tritium breeder blankets in fusion reactors are primarily based on the reaction:

$$^{2}\mathrm{Li} + \mathrm{n} \rightarrow {}^{3}\mathrm{H} + \alpha \tag{1.5}$$

which will require a substantial neutron flux. Beryllium is therefore added into breeder blankets to yield neutron multiplication [95], which is achieved via:

$$^{9}\mathrm{Be} + \mathrm{n} \rightarrow 2\alpha + 2\mathrm{n} \tag{1.6}$$

In these applications beryllium is subject to high flux neutron irradiation. For instance, in the proposed 2000 MW DEMO design, the plasma facing wall can expect radiation damage of around 120 displacements per atom (dpa) [96], while breeder blankets can expect about 17 dpa over 2-5 years of operation [97].

Radiation damage can lead to effects such as cascades of displacement and transmutation of beryllium atoms [98]. Several studies have been carried out on the effects of neutron irradiation, which report swelling [99] and embrittlement [100]. This may be a consequence of the mobility of atomic scale defects, leading to cluster formation. Efforts to understand these processes using computational models have ranged in scale from atomic quantum DFT analysis [101] to macroscopic finite-element methods [102]. Such studies are restricted to modelling the direct consequence of displacements at much smaller energies than those of energetic neutrons but nonetheless may provide insight into defect evolution at low displacement energies.

Computational studies suggest that atoms displaced in the beryllium lattice readily recombine with vacancies, leading to efficient damage recovery [101,103]. This implies that beryllium could be a suitable material for use within the high neutron flux environment of fusion reactors. Besides neutrons, beryllium as a plasma-facing materials is also subject to bombardment from hydrogen and helium ions escaping from the plasma, their retention and diffusion behaviour has also been studied using computational models [101, 104].

Beryllium intermetallics have been considered for nuclear applications due to their similar neutronic properties and possible advantage in radiation tolerance [105]. In particular, the beryllium-rich $Be_{12}M$ (M = transition metal) intermetallics have been proposed as replacements for pure beryllium in fusion reactors [106]. $Be_{12}Ti$ has been identified as a promising candidate in breeder blankets due to fast tritium release, low chemical reactivity and good mechanical properties at reactor temperatures in comparison to other beryllium intermetallics [97,107,108]. Similarly, $Be_{12}V$ has been identified as a potential candidate as neutron multiplier [97, 107], while $Be_{12}W$ exhibits lower neutron multiplicity and thus may not be as desirable [107, 109], though this does not preclude $Be_{12}W$ as a plasma facing material candidate [106].

1.3.1 Crystallography

Elemental beryllium has a hexagonal-closed pack structure (space group $P6_3/mmc$) with a c/a ratio of 1.5677 [110]. A c/a ratio below that of the ideal hexagonal (1.633) indicates directional deviations in bonding which have an impact on thermal and mechanical properties [111]. More so than the other group IIA elements, beryllium is able to participate in covalent bonding via *s-p* orbital hybridisation despite being a metal [112], which provides additional factors to consider when modelling the material.

Five interstitial sites were identified for HCP beryllium: non-basal octagonal, non-basal tetrahedral, non-basal trigonal, basal hexagonal and basal trigonal (as illustrated in Figure 1.9), in which the basal trigonal site has been identified as the most energetically favourable for self-interstitials from computational studies [101, 111].

$Be_{12}M$ intermetallics share a tetragonal crystal structure (space group I_4/mmm) [113, 114], with unit cell shown in Figure 1.10. This structure has three symmetrically distinct Be sites and one transition metal site. $Be_{12}Ti$ has $a = 7.39$ Å and $c = 4.19$ Å [115] while $Be_{12}V$ has $a = 7.35$ Å and $c = 4.24$ Å [116]. The Be-Ti and Be-V phase diagrams are shown in Figure 1.11.

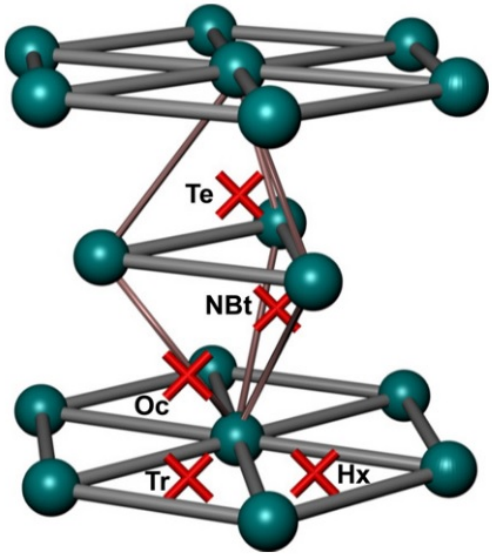


Figure 1.9: Five interstitial sites identified in HCP beryllium, reproduced from [101]. The indicated sites are Oc: non-basal octagonal, Te: non-basal tetrahedral, NBt: non-basal trigonal, Hx: basal hexagonal and Tr: basal trigonal.

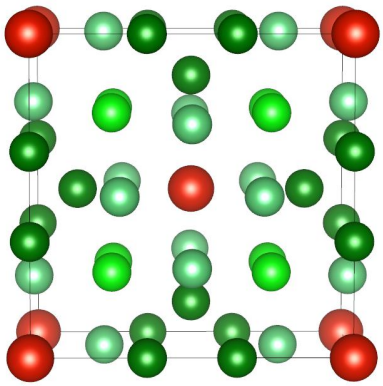


Figure 1.10: Unit cell of $Be_{12}V$ viewed from (0 0 1) direction, illustrating the typical unit cell of $Be_{12}M$ intermetallics. Different shades of green indicate symmetrically distinct Be sites while red indicates the V site.

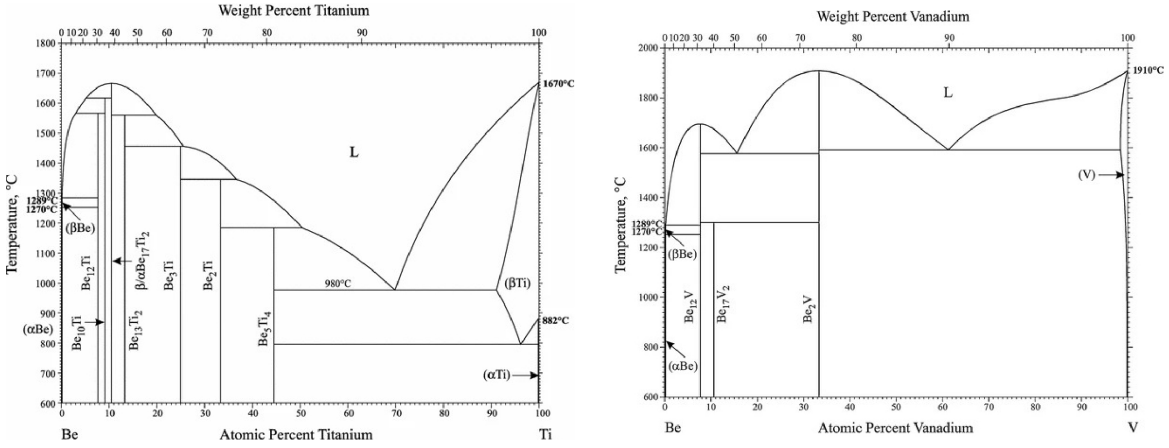


Figure 1.11: Phase diagrams of Be-Ti system reproduced from [117] and Be-V system reproduced from [118].

1.4 Radiation damage

Given that both fission and fusion reactors produce high energy particles such as neutrons (see Equations (1.1) and (1.2)), significant radiation damage of structural components via particle bombardment in nuclear reactors is to be expected. The mechanisms of radiation damage in various materials have therefore been studied both experimentally and computationally, in an effort to engineer materials more tolerant to radiation for use in reactors (i.e. to have longer in-reactor lifetimes).

1.4.1 Threshold displacement

When an atom is imparted sufficient energy from a neutron, it is displaced from its lattice site. Part of the kinetic energy transmitted to this atom can also be further imparted to other atoms, potentially causing more displacements material (this is known as a displacement cascade). The minimum energy required to displace an atom is known as threshold displacement energy. While most models simply use a single value of threshold displacement energy for each type of atom, it is actually a directionally dependent quantity as the energy required to displace an atom towards the nearest neighbour direction is expected to be different (lower in fact [119]) to that in a non-nearest neighbour direction. It has also been found that even for a given direction, the threshold displacement energy cannot be treated a single value due to the vibrationally distinct states of atoms in the same cell. That means for a significant range of energies, when imparted to a primary knock-on atom (PKA), only sometimes do they yield displacement [119]. This meant that the threshold displacement energy is actually probabilistic, as illustrated in Figure 1.12. Nevertheless, models incorporating threshold displacement energy as a singular value are still useful as a directionally and probability averaged approximation.

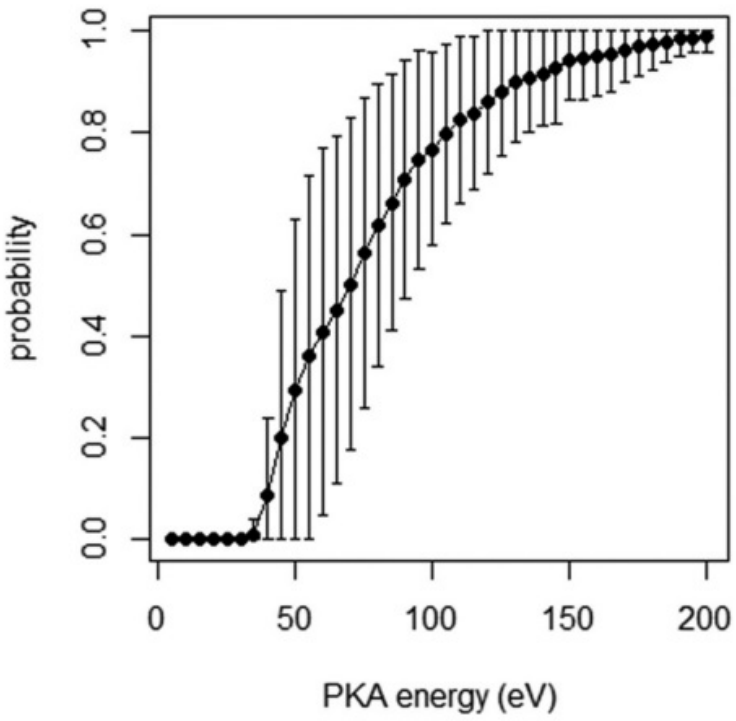


Figure 1.12: Directionally averaged displacement probability as a function of PKA energy in molecular dynamics simulations of HCP beryllium reproduced from [119]. Error bars indicate 1 standard deviation.

1.4.2 Damage generation

The current understanding of damage generation in metals consists of a consistent set of phases [120, 121], illustrated in Figure 1.13. First is a ballistic collision phase, where the PKA is imparted with energy and displaced, which then through ballistic collisions, displaces secondary atoms that may also lead to tertiary displaced atoms and so on [122]. The ballistic collision phase lasts on the order of 0.1 ps. This is followed by the thermal spike phase, where a disordered region forms along the collision cascade trajectory that persists for roughly 1-10 ps [120, 123]. Then comes the initial recovery phase where the thermal spike cools, recrystallising and thus recovering the majority of the damage generated in the thermal spike phase on a timescale of roughly 100 ps [122]. The resultant damage at the end of the intital recovery phase is considered to be the result of the damage cascade (or primary radiation damage), and further thermally activated recovery or formation of extended defects due to defect mobility is expected at longer timescales.

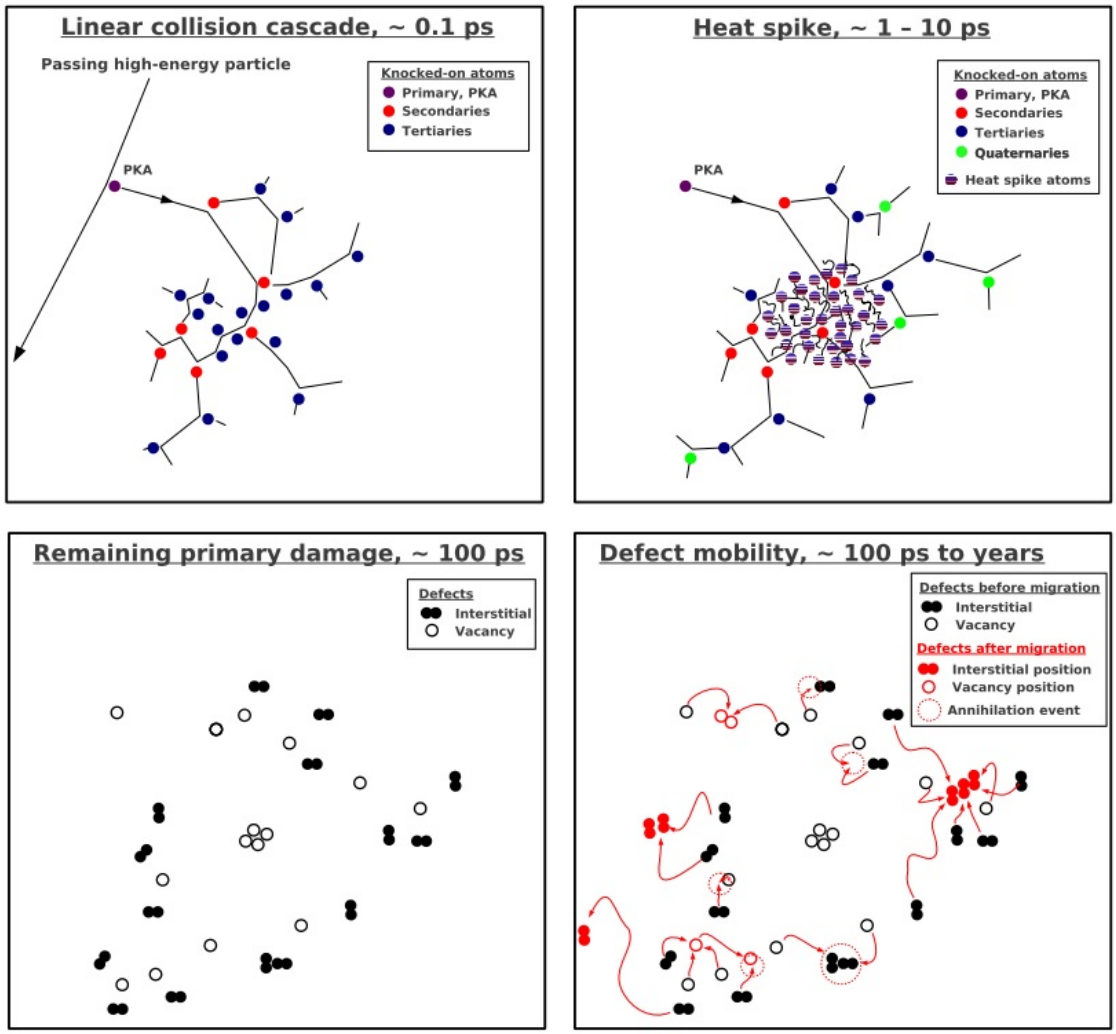


Figure 1.13: Distinct phases of radiation damage cascades identified in metals and their respective timescales. Figure reproduced from [121].

Damage production in semiconductors differs from that in metals in the lack of an initial recovery phase, leading to the persistence of defects formed in the ballistic collision and disordered regions in thermal spike phases that are stable over macroscopic timescales [124, 125]. The consequence is that the effect of radiation is more severe in semiconductors than metals.

Macroscopic effects

Defect generation from radiation damage cascades result initially in the formation of Frenkel pair defects. The formation of Frenkel pairs (which are displacements of atoms leading to a vacancy and an interstitial) in the first three phases of radiation damage is typically the first point of focus in analytical damage models and computational simulations. At macroscopic

timescales, the mobility of interstitials and vacancies can lead to recombination, thereby further recovering damage, but can also lead to segregation into extended defects that may impact the bulk properties of the material. Vacancies can coalesce to form voids in the material, leading to swelling [126]. Defect clusters in general can act as pining points to impede dislocation mobility, leading embrittlement from the loss of plasticity in the material [127].

Electronic effects

The above analysis mainly focuses on radiation damage as a result of ion-ion interaction. As Figure 1.14 shows however, even at low PKA energies, a significant portion of the PKA energy does get transferred to the electrons in the material. Therefore, the formation of electronic

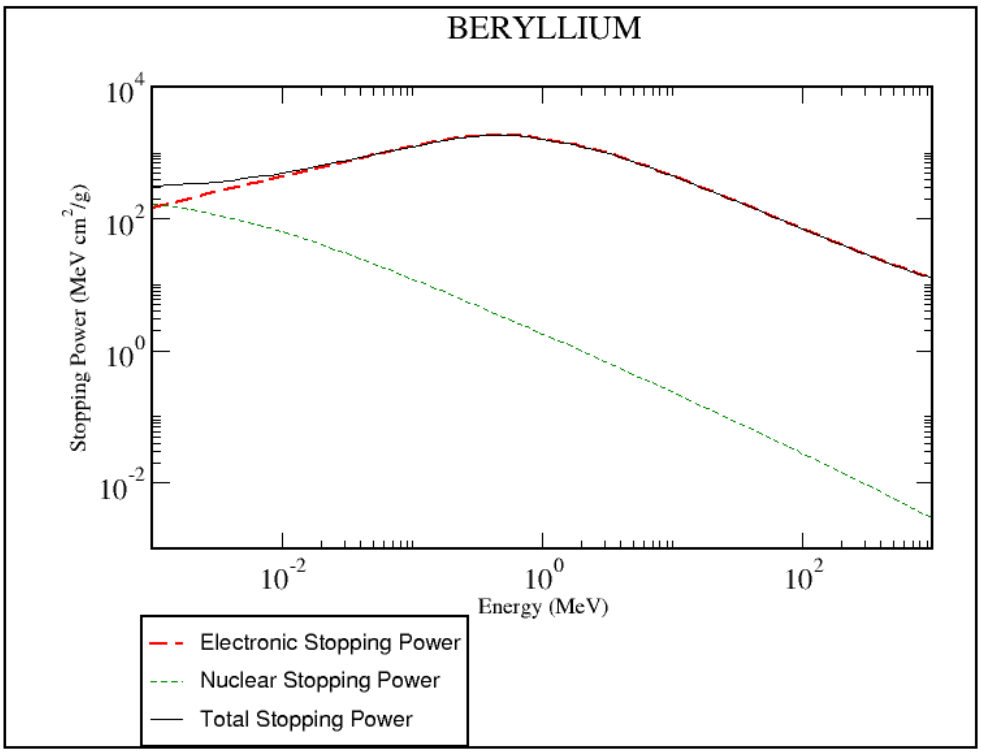


Figure 1.14: Nuclear and electronic stopping power for an α-particle into beryllium. Reproduced from [128].

defects is also an important aspect of radiation damage. At very high PKA energies (at least MeV range), electronic stopping is expected to dominate over nuclear stopping (see Figure 1.14) and therefore the picture of a displacement cascade will not be valid until sufficient slowing down of the PKA has occured. Such high energy PKA will instead form swift heavy ion tracks

that are long straight tracks of damage in the material [129]. At lower energy ranges where displacement cascades are exhibited, the electronic system is thought to store and transport energy (lost via electronic stopping) across the lattice via electron–phonon coupling [130, 131].

1.4.3 Analytical damage models

The simplest analytical model for radiation damage is the Kinchin-Pease (K-P) model [132]. This uses a single value for the threshold displacement energy E_{td}, which if imparted to a lattice atom by an incident radiation particle will displace this atom from its lattice site. This atom then becomes the PKA. Since the PKA is then only able to transfer half of its kinetic energy (which is the maximum in binary collisions) to the next atom, only $E_d/2$ is available for displacement beyond the PKA. The number of atomic displacements (or frenkel pairs) predicted by K-P is given analytically as:

$$N_{FP,KP}(E_d) = \begin{cases} 0 & E_d < E_{td} \\ 1 & E_{td} < E_d < 2E_{td} \\ \dfrac{E_d}{2E_{td}} & 2E_{td} < E_d \end{cases} \tag{1.7}$$

where the value for E_d here should not include losses to electronic stopping. It was later found in binary collision simulations that roughly 20% of vacated sites would be filled by a different displaced atom, which led to the modification to K-P known as the Norgett, Robinson, Torrens (NRT) model [133] with the prediction:

$$N_{FP,NRT}(E_d) = \begin{cases} 0 & E_d < E_{td} \\ 1 & E_{td} < E_d < \dfrac{2E_{td}}{0.8} \\ \dfrac{0.8E_d}{2E_{td}} & \dfrac{2E_{td}}{0.8} < E_d \end{cases} \tag{1.8}$$

There have been attempts since to improve on these simplistic models. For example, the

arc-dpa model [134] takes into account that displacements generated in the thermal spikes are able to readily recombine, and therefore an additional athermal recombination factor ξ_{arc} is added to the NRT model such that $N_{FP,arc}(E_d) = \frac{0.8E_d}{2E_{td}}\xi_{arc}(E_d)$ when $\frac{2E_{td}}{0.8} < E_d$. The recombination term is expressed as:

$$\xi_{arc}(E_d) = (1-\alpha)\Big(\frac{0.8}{2E_{td}}\Big)E_d^{\beta} + \alpha \tag{1.9}$$

where α and β are material constants.

1.4.4 Computational simulations of radiation damage

Given that processes such as radiation damage affect materials at the atomic scale, modelling of structural materials in reactors can start from as small as the quantum scale. However, simulations that include the physics of atoms and electrons at the quantum level are necessarily limited in length scale and time scale due to computational complexity. The results from quantum mechanical simulations could be used to guide larger scale simulations, with less precise physics, could in turn be again used to guide even larger scale simulations, until the scale of the actual components in reactors is reached [135]. Figure 1.15 shows the length and time scales associated with the different fields of simulation techniques.

At the smallest scale, quantum mechanical methods that are able to simulate the even the electronic structure of atoms include density functional theory. Quantum mechanical simulations are often used to calculate point defect energies and migration barriers, as well as fundamental lattice properties. These results can be used in the fitting of interatomic potentials, which dictate atomic interaction in molecular dynamics (MD) simulations. MD is the next step up from quantum mechanical methods that treat atoms as point objects while electronic structure is not simulated, but is able to include some electronic effects while remaining computationally tractable. MD simulations remain the main tool for investigating primary radiation damage [103, 137].

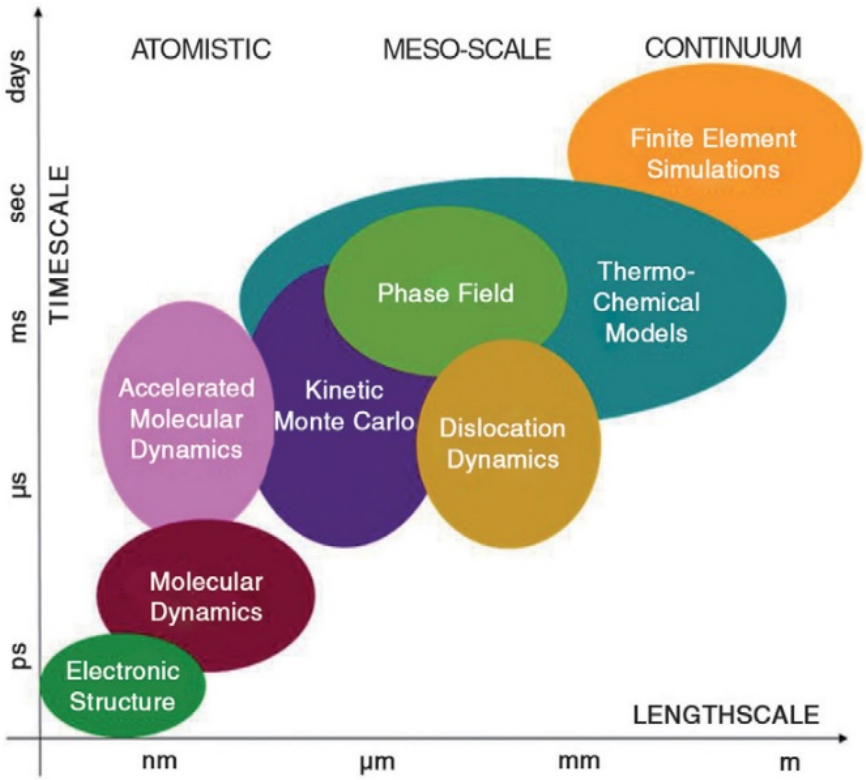


Figure 1.15: Length and time scales typically accessible, with today's computing power, to the common branches of simulation in materials. Figure reproduced from [136].

Beyond MD, accelerated molecular dynamics (AMD) utilises statistical mechanical concepts to accelerate the occurrence of events that are considered infrequent in the MD timescale such as point defect migration, at the expense of short time dynamics [138]. Kinetic monte carlo (KMC) methods also handle these infrequent (in MD timescale) events by utilising transition rates between states calculated from MD as input. KMC can be used to study radiation induced segregation and precipitation of extended defects [139]. Binary collision simulations such as that provided in the SRIM package [140] can also be considered monte carlo as randomness is incorporated into collision angles.

Methods at largest time and length scales include dislocation dynamics, which model the interaction between dislocations (which may be formed by radiation generated defects) via the resultant elastic strain energies [141]. Finite element methods (FEM) split the macroscopic bulk material into interacting cells called finite elements. This approach is generally used in engineering to model stress and deformation in structural mechanics. Data on how radiation

affects the elastic properties of materials (either from experiment or simulation) can be used as input in FEM simulations [142].

1.5 Aims and objectives

Having outlined structural materials of current industrial interest in fission and fusion reactors, behaviour that can impact the lifespan of these materials will be investigated using computer simulations. Both MD simulations using the LAMMPS [143] code and static simulations based on quantum mechanically based Density Functional Theory (DFT) [144] using the CASTEP code [145] will be used.

The first system to be studied is beryllium, which is a potential plamsa-facing material in fusion reactors where it will be subjected to high dosage of radiation damage. The aim is to begin to build a model of radiation damage processes in light metals such as beryllium and its derivatives, which will ultimately require simulations of various length and timescales. This work will begin with the most fundamental atomic scale simulations of radiation damage cascades in pure beryllium. While MD simulations of this type have already been done by Borodin and Vladimirov [103], the study employed an interatomic potential that exhibits negative thermal expansion [150]. Therefore for this thesis, a suitable interatomic potential is to be obtained for the MD simulations, for which the methods and results are presented in Section 3.1.2. The results of the MD simulations of the radiation damage cascades are presented in Chapter 4.

As discussed above, in fission reactors, ZrO_2 that forms on the surface of Zr-based cladding acts as in important barrier layer. The mechanism by which additions of alloying elements, namely, Fe, Cr, Ni, Cu and Sb in ZrO_2 affect cladding performance will be investigated via DFT calculations, to reflect the interest in further development Zr-based alloys that may, for example, provide greater safety margins for increased burnup in current reactors. The aim is to identify mechanisms by which current alloying elements benefit cladding lifetime and to be able to predict similar beneficial behaviour in candidate dopants via simulation. The defect

concentration diagrams generated in this study are reported in Chapter 5, along with other investigated mechanisms such as defect interaction and response to applied space charges. The extension addition the methodology to chemicals in the coolant water is also demonstrated with the consideration of Li from LiOH added into the coolant water of PWR reactors for which results are also reported in Chapter 5.

Finally, Chapter 6 will discuss the ongoing and future prospects of the research covered in this thesis, followed by a summary in Chapter 7.

Chapter 2

Theory

This chapter introduces the background theory for atomic scale modelling. For dynamics simulations, the molecular dynamics method based on classical mechanics is described. Whereas for static calculations, the quantum mechanical density functional theory is discussed.

2.1 Molecular dynamics

In classical molecular dynamics (MD), atomic nuclei are modelled as point objects that move under the influence of empirical interatomic potentials through classical equations of motion. Effects due to the quantum mechanical nature of objects such as charge transfer and energy level occupation at this scale are ignored.

The total energy (or Hamiltonian) of a classical system of atoms is given by

$$E = \sum_i \frac{1}{2} m_i \mathbf{v}_i^2 + \sum_{i>j} V_{ij}(\mathbf{r}_i) \tag{2.1}$$

where i is the index for the atoms, m_i are the atomic masses, $\mathbf{r}_i$ are the atomic positions, $\mathbf{v}_i = \dfrac{\mathrm{d}\mathbf{r}_i}{\mathrm{d}t}$ are the velocities and V_{ij} are the interatomic interaction terms between atoms indexed

i and j. The forces on the atoms are therefore:

$$\mathbf{F}_i = m_i \frac{\mathrm{d}\mathbf{v}_i}{\mathrm{d}t} = -\nabla_i E \tag{2.2}$$

where $\nabla_i = \mathbf{e}_x \frac{\partial}{\partial x_i} + \mathbf{e}_y \frac{\partial}{\partial y_i} + \mathbf{e}_z \frac{\partial}{\partial z_i}$, with $\mathbf{e}_x$, $\mathbf{e}_y$ and $\mathbf{e}_z$ being the unit vectors.

With the specification of an initial state (i.e. initial atom positions $\{\mathbf{r}_i(t_0)\}$ and velocities $\{\mathbf{v}_i(t_0)\}$), as well as the form of V_{ij}, the subsequent states for each atom can be obtained as a function of time with:

$$\mathbf{r}_i(t) = \int_{t_0}^{t} \mathbf{v}_i(t')\ \mathrm{d}t' \tag{2.3}$$

and

$$\mathbf{v}_i(t) = \frac{1}{m_i} \int_{t_0}^{t} \mathbf{F}_i(t')\ \mathrm{d}t' \tag{2.4}$$

Since E and therefore $\mathbf{F}_i$ is a function of $\mathbf{r}_i(t)$, the two equations are actually coupled. In any case, Equations (2.3) and (2.4) are to be solved using numerical integration methods.

Computational considerations

In the LAMMPS package [143] employed in this work, the Verlet integration method [147] is used, which stems from taking the Taylor expansion of $\mathbf{r}_i(t)$:

$$\mathbf{r}_i(t + \Delta t) = \mathbf{r}_i(t) + \mathbf{v}_i(t)\Delta t + \frac{1}{2}\frac{\mathbf{F}_i(t)}{m_i}\Delta t^2 + \ \cdots \tag{2.5}$$

Doing the same for $\mathbf{v}_i(t)$ yields:

$$\begin{aligned} \mathbf{v}_i(t + \Delta t) &= \mathbf{v}_i(t) + \frac{\mathbf{F}_i(t)}{m_i}\Delta t + \frac{1}{2}\frac{\mathrm{d}}{\mathrm{d}t}\frac{\mathbf{F}_i(t)}{m_i}\Delta t^2 + \ \cdots \\ &= \mathbf{v}_i(t) + \frac{1}{2m_i}\Big(\mathbf{F}_i(t + \Delta t) - \mathbf{F}_i(t)\Big)\Delta t + \ \cdots \end{aligned} \tag{2.6}$$

after employing the finite difference method:

$$\frac{\mathrm{d}}{\mathrm{d}t}\mathbf{F}_i(t) \approx \frac{\mathbf{F}_i(t + \Delta t) - \mathbf{F}_i(t)}{\Delta t} \tag{2.7}$$

while also noting that $\mathbf{F}_i(t + \Delta t)$ has been updated after solving Equation (2.5). The choice of timestep Δt is therefore crucial to ensure no important physical events such as atom collisions can happen within each timestep. Such requirements on Δt therefore limit the total possible simulation time in MD.

Another consideration is that currently available computer memory typically limits the practical simulation size to be at most a few million atoms. This means that lengthwise, atoms can only expect enough space to travel distances of at most hundreds of atom spacings, which can prove to be undesirable when simulating higher energy radiation damage events in a bulk material. Enforcing periodic boundary conditions is the most common approach, which provides more space and also ensures atoms on the edge of the simulation box have the correct bonding behaviour.

2.1.1 Macroscopic constraints

In most cases, it should not be expected that the system under study will be isolated from external factors. The external influences are typically accounted for by their effect on the macroscopic properties of the system being investigated. In MD this is achieved by applying constraints on the macroscopic properties, such as temperature and pressure, typically corresponding to a statistical ensemble in thermodynamics. This is achieved through modifications to the equations of motion (Equations (2.3) and (2.4)).

The simplest thermostat does not make any modifications, for which the system corresponds to the micro-canonical or NVE ensemble. The name NVE refers to the conserved properties: N for number of atoms, V for volume and E for energy. The NVE ensemble is used typically only when energy conservation is required. Other commonly used themostats include the NVT (canonical) ensemble and NPT (isothermal–isobaric) ensemble. P and T referring to pressure and temperature being controlled (not necessarily held constant) respectively.

There are several methods available for controlling temperature and pressure in MD, these are known as thermostats and barostats respectively. In this work, the Nosé-Hoover thermostat and barostat is utilised [148], which simulates a system connected to an external heat bath that contains an additional degree of freedom. This additional degree of freedom is applied to pressure to obtain a barostat. Position and momenta under the Nosé-Hoover thermostat adhere to the canonical distribution [149].

2.1.2 Interatomic potentials

The V_{ij} term described in Section 2.1 is the (classical) interatomic potential, which encodes the interaction between atoms. It will only be accurate so long as there are no changes in the interactions beyond that described by the physics of the functional. For example, the functions described below cannot account for charge transfer effects. This may mean that the potential is restricted to describe changes of interatomic distances associated with the inclusion of defects (relaxation) or due to mechanical deformation. Interatomic potentials are often parametrised using experimental data, and are considered only be able to perform well for the range of properties used in fitting the parameters (i.e. associated with the range of interatomic separations that these properties represent). Even more stark, a potential parameterised for Be-W interactions will not be suitable for describing Be-Be interactions. Typically each interaction pair (or triplet and above for multi-body potentials) is parameterised separately.

There are many types of interatomic potentials available that are optimised to capture various different physics. For example, bond-order potentials are able to model and count covalent bonding (localised electron density) between atoms while embedded atom methods (EAM) are suited to model metallic systems due to consideration of delocalised electron density.

2.2 Density functional theory

2.2.1 Schrödinger equation

In quantum mechanics, particle states are described by the wavefunction $\Psi(\mathbf{r}, t)$ rather than position $\mathbf{r}(t)$ and momentum $\mathbf{p}(t)$ as in classical mechanics. Another key feature of quantum mechanics is that when there is more than one particle involved, there will, in general, only be a multi-particle wavefunction $\Psi(\mathbf{r}_1, \mathbf{r}_2, \ldots, \mathbf{r}_N, t)$ rather than individual ones for each particle, though in certain cases (such as when all the particles are not interacting which other) the multi-particle wavefunction can be separated into individual components.

Non-relativistic quantum mechanics is primarily governed by the Schrödinger equation, which has to be solved to obtain the wavefunction. The most general form of the equation for a single particle is:

$$i\hbar\frac{\partial}{\partial t}\Psi(\mathbf{r}, t) = \hat{H}\Psi(\mathbf{r}, t) \tag{2.8}$$

where $\hat{H}$ is the Hamiltonian operator for the system and $\hbar$ is the reduced Planck constant. The most well known form that the Hamiltonian takes is for a single non-relativistic particle moving in a scalar field which gives the Schrödinger equation in the form:

$$i\hbar\frac{\partial}{\partial t}\Psi(\mathbf{r}, t) = \left[\frac{-\hbar^2}{2m}\nabla^2 + V(\mathbf{r}, t)\right]\Psi(\mathbf{r}, t) \tag{2.9}$$

The equation can be simplified when one is only interested in the stable (bound) configurations of the system, rather than the dynamics. This leads to the time independent Schrödinger equation described by:

$$E\Psi(\mathbf{r}) = \hat{H}\Psi(\mathbf{r}) \tag{2.10}$$

for a single particle, where E is the energy of the stationary state.

2.2.2 Born-Oppenheimer approximation

Unfortunately, even the time independent Schrödinger equation for the systems of hundreds atoms investigated in this work is extremely complicated. Therefore to further simplify things, the Born-Oppenheimer approximation [170] is almost always applied to allow electrons to be considered separately from the atomic nuclei. The justification for this is the observation that in the center-of-mass frame, the electrons collectively have equal and opposite momentum to the atomic nuclei, but the nuclei are roughly 10^4 times more massive. Therefore the electrons should have much higher velocities are thus are expected to be able to equilibrate to transient ground state configurations before any significant movement of the nuclei.

The result is that the Schrödinger equation only needs to be solved for the electrons, while the positions of the atomic nuclei become parameters in the potential term, where they interact with electrons via Coulomb forces. Thus the resulting time independent Schrödinger equation for a system of N electrons is:

$$E\Psi(\mathbf{r}_1, \mathbf{r}_2, \ldots, \mathbf{r}_N) = \left[-\sum_i \frac{\hbar^2}{2m_e}\nabla_i^2 + \sum_{i<j} \frac{1}{4\pi\epsilon_0|\mathbf{r}_j - \mathbf{r}_i|} - \sum_{i,\alpha} \frac{Z_\alpha}{4\pi\epsilon_0|\mathbf{R}_\alpha - \mathbf{r}_i|} \right] \Psi(\mathbf{r}_1, \mathbf{r}_2, \ldots, \mathbf{r}_N) \tag{2.11}$$

where $\mathbf{R}$ and Z indicate the positions and electronic charges of the atomic nuclei respectively, m_e is the electron mass and ϵ_0 is the permittivity of free space. Note that the index α does not run up to N as it accounts for the atomic nuclei.

2.2.3 Hohenberg-Kohn theorems

While Equation (2.11) is still too complex to solve in general, several methods are available from which approximate solutions can be obtained. Examples include Hartree-Fock, post-Hartree-Fock methods and DFT [144, 171]. DFT is based on the Hohenberg-Kohn theorems that the ground state properties can be fully determined by just an electron density that depends only on $\mathbf{r}$ instead of $\{\mathbf{r}_i\}$, thus greatly simplifying calculations. The Schrödinger Equation can then be reformulated as a functional, which has the electron density ρ as the basic variable instead

of the total wavefunction Ψ. The electron density for an N-electron system is defined from the total wavefunction as:

$$\rho(\mathbf{r}) = N \int \mathrm{d}^3 r_2 \cdots \int \mathrm{d}^3 r_N \; \Psi^*(\mathbf{r}, \mathbf{r}_2, \ldots, \mathbf{r}_N)\Psi(\mathbf{r}, \mathbf{r}_2, \ldots, \mathbf{r}_N) \tag{2.12}$$

The theorem states that for any two Hamiltonians $\hat{H}$ and $\hat{H}'$ that have distinct potential forms, that is:

$$\hat{H} \neq \hat{H}' + const \tag{2.13}$$

the ground state electronic wavefunctions Ψ_0 and Ψ_0' will necessarily be different as well as the ground state electron densities ρ_0 and ρ_0'. This means that any electron density ρ_0 will uniquely determine a Ψ_0 (and by extension a family of $\hat{H}$ differing by only a constant). In other words Ψ_0 is uniquely determined by a functional of ρ_0, or more explicitly:

$$\Psi_0 = \Phi[\rho_0] \tag{2.14}$$

It is best to clarify here that even though in the expression of equation (2.12), one can see that different Ψ may produce the same $\rho(\mathbf{r})$, the above result means that only one of these will be a ground state solution to some $\hat{H}$. Therefore in this way, the functional Φ can in principle be defined. It is not clear what form Φ takes but the Hohenberg-Kohn theorems have shown that it at least exists.

Given that the total energy of an N-electron system is given by:

$$\begin{aligned} E &= \int \mathrm{d}^3 r_1 \int \mathrm{d}^3 r_2 \cdots \int \mathrm{d}^3 r_N \; \Psi^*(\mathbf{r}_1, \mathbf{r}_2, \ldots, \mathbf{r}_N)\hat{H}\Psi(\mathbf{r}_1, \mathbf{r}_2, \ldots, \mathbf{r}_N) \\ &= \langle \Psi | \, \hat{H} \, | \Psi \rangle \end{aligned} \tag{2.15}$$

where the second term is expressed in bra-ket notation, a functional for the ground state energy can therefore be written in terms of ρ by utilising the functional Φ as:

$$E[\rho] = \left\langle \Phi[\rho] \,\middle|\, \left(\hat{T} + \hat{U} + \hat{V}\right) \,\middle|\, \Phi[\rho] \right\rangle = T[\rho] + U[\rho] + V[\rho] \tag{2.16}$$

where T is the kinetic term and U is the electron-electron interaction term associated with the 1st and 2nd term of the Hamiltonian in Equation (2.11). V is the potential term accounting for electron-nucleus interaction which can be written as:

$$V[\rho] = \int \sum_{\alpha} \frac{Z_\alpha \rho(\mathbf{r})}{4\pi\epsilon_0 |\mathbf{R}_\alpha - \mathbf{r}|} \, \mathrm{d}^3 r \tag{2.17}$$

As for T and U, their exact form is not known thus far. However, they are identical for all N-electron systems, thus are universal in that sense. Therefore, any method used to approximate and handle the two universal terms can be conveniently reused for every system.

Variational principle

The expression for the total energy, assuming knowledge of T and U can then be used to solve for the ground state electron density ρ_0. This follows from the variational principle which states that since no normalised wavefunction can have energy lower than the ground state, one can simply vary any trial wavefunction to minimise $E = \langle \Psi | \hat{H} | \Psi \rangle$ and that would give the best approximation of the ground state wavefunction Ψ_0 for the constraints of the trial wavefunction.

More rigorously, it means that since for any given Hamiltonian, the set of energy eigenfunctions $\{|E_n\rangle\}$ form an orthonormal basis set in the function space of Ψ. Therefore, any normalised wavefunction (or trial wavefunction for guessing the lowest energy state) can be uniquely expanded in terms of this basis set as:

$$|\Psi_{trial}\rangle = \sum_n C_n |E_n\rangle \qquad C_n \in \mathbb{C} \quad \text{and} \quad \sum_n |C_n|^2 = 1 \tag{2.18}$$

and thus:

$$E_{trial} = \langle \Psi_{trial} | \hat{H} | \Psi_{trial} \rangle = \sum_n |C_n|^2 E_n \geqslant \sum_n |C_n|^2 E_0 = E_0 \tag{2.19}$$

The Hohenberg-Kohn theorems then state that this extends naturally to when E is expressed as a functional of ρ instead of Ψ since $\rho[\Psi]$ is after all a functional of Ψ.

2.2.4 Kohn-Sham DFT

One possible method to carry out this minimisation is described by Kohn and Sham [146] which proceeds by constructing a fictitious system of non-interacting electron orbitals $\{\phi_i\}$, known as Kohn-Sham orbitals, that result in the exact actual electron density $\rho(\mathbf{r})$. The electron density is written in terms of these orbitals as:

$$\rho(\mathbf{r}) = \sum_i |\phi_i(\mathbf{r})|^2 \tag{2.20}$$

Note that unlike the case of the multi-particle wavefunction, this electron density can always be split in this way.

Now with the electron orbitals in consideration, it will be useful to separate terms relating to them out from the energy functional. The first is the kinetic term associated with the orbitals

$$T_s[\rho] = \sum_i \langle \phi_i | \hat{T} | \phi_i \rangle \tag{2.21}$$

that is separated from T and the second is the coloumb interaction term, J, between all the orbitals

$$J[\rho] = \frac{1}{2} \int \int \frac{\rho(\mathbf{r})\rho(\mathbf{r}')}{4\pi\epsilon_0 |\mathbf{r} - \mathbf{r}'|} \, \mathrm{d}^3 r \, \mathrm{d}^3 r' \tag{2.22}$$

that is separated from U. Note that T_s can be expressed as such since the Kohn-Sham orbitals are to be uniquely determined by ρ and therefore T_s is still a functional of ρ. The energy functional can thus be rewritten as:

$$E[\rho] = T_s[\rho] + V[\rho] + J[\rho] + E_{xc}[\rho] \tag{2.23}$$

Where the last term is called the exchange-correlation functional that is meant to contain the electron exchange and correlation effects that are not captured in the first three terms (Note: the physical basis of exchange and correlation are explained in Section 2.2.5 below). This

functional is defined as:

$$E_{xc}[\rho] = \Big(T[\rho] - T_s[\rho]\Big) + \Big(U[\rho] - J[\rho]\Big) \tag{2.24}$$

and one can see that with this, the Kohn-Sham energy functional is still exact.

The resultant functional in Equation (2.23) should be be minimised together with Lagrange multipliers for the constraint on $\rho(\mathbf{r})$ by setting:

$$\delta\bigg[E[\rho] - \lambda\Big(\int \rho(\mathbf{r})\ \mathrm{d}^3r - N\Big)\bigg] = 0 \tag{2.25}$$

Evaluating this against the variation of $\rho(\mathbf{r})$ (i.e. taking the functional derivative) will give:

$$\frac{\delta T_s[\rho]}{\delta\rho(\mathbf{r})} + \sum_\alpha \frac{Z_\alpha}{4\pi\epsilon_0|\mathbf{R}_\alpha - \mathbf{r}|} + \frac{1}{2}\int \frac{\rho(\mathbf{r}')}{4\pi\epsilon_0|\mathbf{r} - \mathbf{r}'|}\ \mathrm{d}^3r' + \frac{\delta E_{xc}[\rho]}{\delta\rho(\mathbf{r})} = \lambda \tag{2.26}$$

Making use of the orbital expansion again, the first term can be simplified by considering its variation on $\phi_i^*(\mathbf{r})$:

$$\frac{\delta T_s[\rho]}{\delta\rho(\mathbf{r})} = \frac{\delta T_s[\rho]}{\delta\phi_i^*(\mathbf{r})}\frac{\mathrm{d}\phi_i^*(\mathbf{r})}{\mathrm{d}\rho(\mathbf{r})} = \frac{\delta T_s[\rho]}{\delta\phi_i^*(\mathbf{r})}\frac{1}{\frac{\mathrm{d}\rho(\mathbf{r})}{\mathrm{d}\phi_i^*(\mathbf{r})}} = -\frac{\hbar^2}{2m}\Big(\nabla^2\phi_i(\mathbf{r})\Big)\frac{1}{\phi_i(\mathbf{r})} \tag{2.27}$$

The exchange-correlation term has no simplification unfortunately but by defining the exchange-correlation potential:

$$V_{xc}(\mathbf{r}) = \frac{\delta E_{xc}[\rho]}{\delta\rho(\mathbf{r})} \tag{2.28}$$

one can now obtain, by multiplying with $\phi_i(\mathbf{r})$, the following expression from equation (2.26):

$$\Big(-\frac{\hbar^2}{2m}\nabla^2 + V_{KS}(\mathbf{r})\Big)\phi_i(\mathbf{r}) = \xi_i\phi_i(\mathbf{r}) \tag{2.29}$$

where λ is now identified as the eigenvalues ξ_i and the effective Kohn-Sham potential is:

$$V_{KS}(\mathbf{r}) = \sum_\alpha \frac{Z_\alpha}{4\pi\epsilon_0|\mathbf{R}_\alpha - \mathbf{r}|} + \frac{1}{2}\int \sum_j \frac{\phi_j^*(\mathbf{r}')\phi_j(\mathbf{r}')}{4\pi\epsilon_0|\mathbf{r} - \mathbf{r}'|}\ \mathrm{d}^3r' + V_{xc}(\mathbf{r}) \tag{2.30}$$

It can now be seen that Equation (2.29), known as the Kohn-Sham equation, generates a fictitious system of non-interacting electrons that give the exact density of the actual interacting electrons. Up to this point, the method is still exact, which partly explains why it is still widely used today. Approximations only start to come into play when interpreting the form of $V_{xc}(\mathbf{r})$ and subsequently in solution methods. It is also important to point out that since the Kohn-Sham potential also includes $\phi_i(\mathbf{r})$, this can lead to self-interaction issues should this not be accounted for in the approximation of $V_{xc}(\mathbf{r})$ or otherwise.

Self-consistent field

The Kohn-Sham equations are a set of coupled equations for $\{\phi_i(\mathbf{r})\}$, which may be solved by an iterative process starting from trial solutions. This is achieved by modifying Equation (2.29) to

$$\Big(-\frac{\hbar^2}{2m}\nabla^2 + \tilde{V}_{KS}(\mathbf{r})\Big)\phi_i(\mathbf{r}) = \xi_i\phi_i(\mathbf{r}) \tag{2.31}$$

with $\tilde{V}_{KS}(\mathbf{r})$ being the resultant Kohn-Sham potential that incorporates $\{\tilde{\phi}_i(\mathbf{r})\}$, which are the trial solutions for $\{\phi_i(\mathbf{r})\}$. This allows for the $\{\phi_i(\mathbf{r})\}$ to be solved in their individual separate eigenvalue equations, which makes the problem computationally contractable. If all $\phi_i(\mathbf{r}) = \tilde{\phi}_i(\mathbf{r})$, then we have our final solution. If not, a new set of trial orbitals can be obtained from $\{\tilde{\phi}_i(\mathbf{r})\}$ and $\{\phi_i(\mathbf{r})\}$, usually as a linear combination, until the new $\{\tilde{\phi}_i(\mathbf{r})\}$ and $\{\phi_i(\mathbf{r})\}$ are sufficiently similar, or the resultant E from the $\{\phi_i(\mathbf{r})\}$ are sufficiently converged between iterations. In any case, the ground state electronic density is then obtained via Equation (2.20). Methods that work in this iterative manner are called Self-Consistent Field (SCF) methods.

Geometry optimisation

Just as in any other physical system, the response of the energy to small variations determines the static properties of the system. For example, the force on atom indexed α is given by:

$$\mathbf{F}_\alpha = -\nabla_\alpha E \tag{2.32}$$

while 2nd order derivatives with respect to lattice parameters will provide the elastic constants. Static properties such as the above can be used to guide the search for optimal atom configurations in geometry optimisation calculations, which is used extensively in this work.

2.2.5 Exchange-correlation functionals

The exchange-correlation functional is intended to capture the physics not included in the terms separated out in Equation (2.23) after applying the Kohn-Sham orbital expansion, which include electron exchange and electron correlation effects. Electron exchange comes from the quantum effects when positions (or quantum states in general) of identical particles are exchanged, described mathematically as:

$$\Psi(\mathbf{r}_1, \mathbf{r}_2) = \pm\Psi(\mathbf{r}_2, \mathbf{r}_1) \tag{2.33}$$

where (+) is for bosons and (-) is for fermions like electrons in this case. Electron correlation are the quantum mechanical interaction effects between the electrons, which are neglected when one tries to describe each electron orbital separately instead of using the multi-particle wavefunction. By taking physically sensible approximations to E_{xc}, one can hope to capture the missing effects at the desired level in the final solution. There have been at least 200 types of exchange-correlation functionals documented by Mardirossian and Head-Gordon [172]. The general categories that the functionals can fall under and described in order of complexity.

Local density approximation

The simplest approximation for the exchange-correlation functional is the local density approximation (LDA), which assumes that the contribution of E_{xc} from a point $\mathbf{r}_0$ in space is exactly the same as if all of space were filled a homogeneous electron gas (HEG) with the same density $\rho(\mathbf{r}_0)$. Putting together the contributions at each point gives:

$$E_{xc}^{LDA}[\rho] = \int \epsilon_{xc}\Big(\rho(\mathbf{r})\Big)\rho(\mathbf{r})\ \mathrm{d}^3r \tag{2.34}$$

Where $\epsilon_{xc}(\rho)$ is the per-particle exchange-correlation energy in a HEG of density ρ. This assumption makes it accurate for slowly varying densities, but unfortunately, the electron density in interesting systems will generally not be slow varying. In any case, the HEG exchange energy is known exactly [173], while the high and low density limits of the HEG correlation energy have also been computed [174, 175].

Generalised gradient approximation

The generalised gradient approximation (GGA) builds on LDA by requiring the exchange-correlation functional expressed in Equation (2.34) to also consider the gradient of the electron density at each point, meaning:

$$E_{xc}^{GGA}[\rho] = \int \epsilon_{xc}\Big(\rho(\mathbf{r}), \nabla\rho(\mathbf{r})\Big)\rho(\mathbf{r})\ \mathrm{d}^3r \tag{2.35}$$

Meta-GGA takes one step further and considers the dependence on $\nabla^2\rho(\mathbf{r})$ as well in the functional. In practice however, it is found that replacing $\nabla^2\rho(\mathbf{r})$ with the kinetic energy density $\tau_s(\mathbf{r})$ expressed as:

$$\tau_s(\mathbf{r}) = \sum_i |\nabla\phi_i(\mathbf{r})|^2 \tag{2.36}$$

is more computationally stable. Note that this kinetic energy term may be written as such since:

$$\int \phi^*(\mathbf{r})\nabla^2\phi(\mathbf{r})\ \mathrm{d}^3r = \underbrace{\int \nabla\cdot\Big(\phi^*(\mathbf{r})\nabla\phi(\mathbf{r})\Big)\ \mathrm{d}^3r}_{=0} - \int |\nabla\phi(\mathbf{r})|^2\ \mathrm{d}^3r \tag{2.37}$$

Hartree-Fock and hybrid functionals

While not the same as the Kohn-Sham equations, the derivation of the Hartree-Fock equations [171] is similar and therefore it is not surprising that physics from Hartree-Fock can be implemented in the Kohn-Sham equations by appropriate choice of E_{xc}. Instead of utilising the electron density, the Hartree-Fock method begins by making the assumption that the N-electron wavefunction is separable to into anti-symmetric orbitals using Slater determinants as

shown below:

$$\Psi(\mathbf{r}_1, \mathbf{r}_2, \ldots, \mathbf{r}_N) = \frac{1}{\sqrt{N!}} \begin{vmatrix} \phi_1(\mathbf{r}_1) & \phi_2(\mathbf{r}_1) & \ldots & \phi_N(\mathbf{r}_1) \\ \phi_1(\mathbf{r}_2) & \phi_2(\mathbf{r}_2) & \ldots & \phi_N(\mathbf{r}_2) \\ \vdots & \vdots & \ddots & \vdots \\ \phi_1(\mathbf{r}_N) & \phi_2(\mathbf{r}_N) & \ldots & \phi_N(\mathbf{r}_N) \end{vmatrix} \tag{2.38}$$

This can be substituted into $E = \langle \Psi | \hat{H} | \Psi \rangle$ resulting in a functional $E[\phi_1, \phi_2, \ldots, \phi_n]$, which has the form:

$$E[\phi_1, \phi_2, \ldots, \phi_n] = \sum_i \langle \phi_i | \hat{T} | \phi_i \rangle + \int \sum_\alpha \frac{Z_\alpha \rho(\mathbf{r})}{4\pi\epsilon_0 |\mathbf{R}_\alpha - \mathbf{r}|} \, \mathrm{d}^3 r$$

$$+ \frac{1}{2} \int \int \frac{\rho(\mathbf{r})\rho(\mathbf{r}')}{4\pi\epsilon_0 |\mathbf{r} - \mathbf{r}'|} \, \mathrm{d}^3 r \, \mathrm{d}^3 r' - \frac{1}{2} \sum_{i,j} \int \int \frac{\phi_j^*(\mathbf{r}')\phi_i(\mathbf{r}')\phi_i^*(\mathbf{r})\phi_j(\mathbf{r})}{4\pi\epsilon_0 |\mathbf{r}' - \mathbf{r}|} \, \mathrm{d}^3 r \, \mathrm{d}^3 r' \tag{2.39}$$

Despite being defined with different arguments, Equation (2.23) and Equation (2.39) have the same form with the exception of the last term. Therefore, the natural follow up is to match-up the terms and define:

$$E_{xc}^{HF}[\rho] = -\frac{1}{2} \sum_{i,j} \int \int \frac{\phi_j^*(\mathbf{r}')\phi_i(\mathbf{r}')\phi_i^*(\mathbf{r})\phi_j(\mathbf{r})}{4\pi\epsilon_0 |\mathbf{r}' - \mathbf{r}|} \, \mathrm{d}^3 r \, \mathrm{d}^3 r' \tag{2.40}$$

where the orbitals now refer to Kohn-Sham orbitals rather than Hartree-Fock orbitals.

Given that anti-symmetry was enforced into the wavefunction in Hartree-Fock [171], $E_{xc}^{HF}[\rho]$ fully captures the electron exchange effects and is also called the exact exchange functional. However, it is also considered to not contain any electron correlation given that Hartree-Fock also used individual orbitals in its approximation.

Hybrid functionals, as the name suggests, combine the exact exchange functional as well as one or more other Kohn-Sham exchange-correlation functionals into one, usually as a linear combination. These combinations will depend on the kinds of physics that are relevant to the

system in study and may include experimentally fitted parameters.

2.2.6 Periodic Systems

In the study of bulk systems, it is often necessary to reduce the problem to a finite one by taking advantage of their periodic arrangement, which can be achieved by taking a basis supercell (which is itself constructed from repreated copies of the unit cell), replicated periodically throughout all space. Systems with periodic boundary conditions as such can be described to have:

$$V(\mathbf{r}+\mathbf{L}) = V(\mathbf{r}) \tag{2.41}$$

where

$$\mathbf{L} = c_1\mathbf{a}_1 + c_2\mathbf{a}_2 + c_3\mathbf{a}_3, \qquad c_1, c_2, c_3 \in \mathbb{Z} \tag{2.42}$$

and $\mathbf{a}_i$ are the primitive vectors. The electron density in such an environment has to also be of the form:

$$\rho(\mathbf{r}+\mathbf{L}) = \rho(\mathbf{r}) \tag{2.43}$$

As a direct consequence, the associated wavefunction will have to obey:

$$\Psi(\mathbf{r}+\mathbf{L}) = e^{i\alpha}\Psi(\mathbf{r}) \tag{2.44}$$

for some $\alpha \in \mathbb{R}$. The Bloch theorem states that all single electron states will have wavefunctions of the form:

$$\phi_{\mathbf{k}}(\mathbf{r}) = e^{i\mathbf{k}\cdot\mathbf{r}}u_{\mathbf{k}}(\mathbf{r}) \tag{2.45}$$

where $u_{\mathbf{k}}(\mathbf{r})$ is a function with again the same periodicity and $\mathbf{k}$ is the associated wavevector. The Kohn-Sham equations can then be solved for each of the allowed $\mathbf{k}$ within the first Brillouin zone. Therefore the Kohn-Sham orbitals should now also be indexed with $\mathbf{k}$ as:

$$\phi_{j,\mathbf{k}}(\mathbf{r}) = e^{i\mathbf{k}\cdot\mathbf{r}}u_{j,\mathbf{k}}(\mathbf{r}) \tag{2.46}$$

and the total electron density would also have to be constructed from the contribution at each **k**-point as:

$$\rho(\mathbf{r}) = \sum_{i,\mathbf{k}} |\phi_{i,\mathbf{k}}(\mathbf{r})|^2 \tag{2.47}$$

Restrictions on the allowed **k** can arise from constraints on the single-electron wavefunction such as $\phi(\mathbf{r} + n\mathbf{a}_i) = \phi(\mathbf{r})$ for some predetermined n (i.e. the wavefunction itself is being required to repeat across a certain number of supercells). Taking $n \to \infty$ allows one to consider an infinite system, where all **k** within the first Brillouin zone will have to be considered. Instead of summing up the infinite **k**, the total electron density is taken as an average over all **k**, which converges to:

$$\rho(\mathbf{r}) = \frac{\Omega}{(2\pi)^3} \int_{\mathrm{BZ}} \sum_i |\phi_{i,\mathbf{k}}(\mathbf{r})|^2 \, \mathrm{d}^3k \tag{2.48}$$

where Ω is the volume of the supercell. With an infinite system care must also be taken regarding the $1/|\mathbf{r}' - \mathbf{r}|$ terms in V_{KS}, for which the sums are only conditionally convergent. Such summations are typically handled through the Ewald summation scheme [176].

Band structure

Applying the Bloch theorem in systems of infinitely repeating cells provides a set of Kohn-Sham orbital energies $\{\xi_{i,\mathbf{k}}\}$, for index i from 1 to N and all **k** in the first Brillouin zone. This provides an electronic band structure for the system, which is usually plotted on a **k**-point path along high symmetry points as shown in Figure 2.1. While useful, care should be taken when interpreting these band structure plots as the $\{\xi_{i,\mathbf{k}}\}$ are merely solutions of a fictitious system. In fact, the underestimation of band gaps in Kohn-Sham DFT is a commonly known issue [177].

2.2.7 Plane wave basis

To allow computational algorithms to handle Kohn-Sham equations, a set of basis functions will have to selected to represent $u_{\mathbf{k}}(\mathbf{r})$. This plane wave basis set allows $u_{\mathbf{k}}(\mathbf{r})$ to be expanded

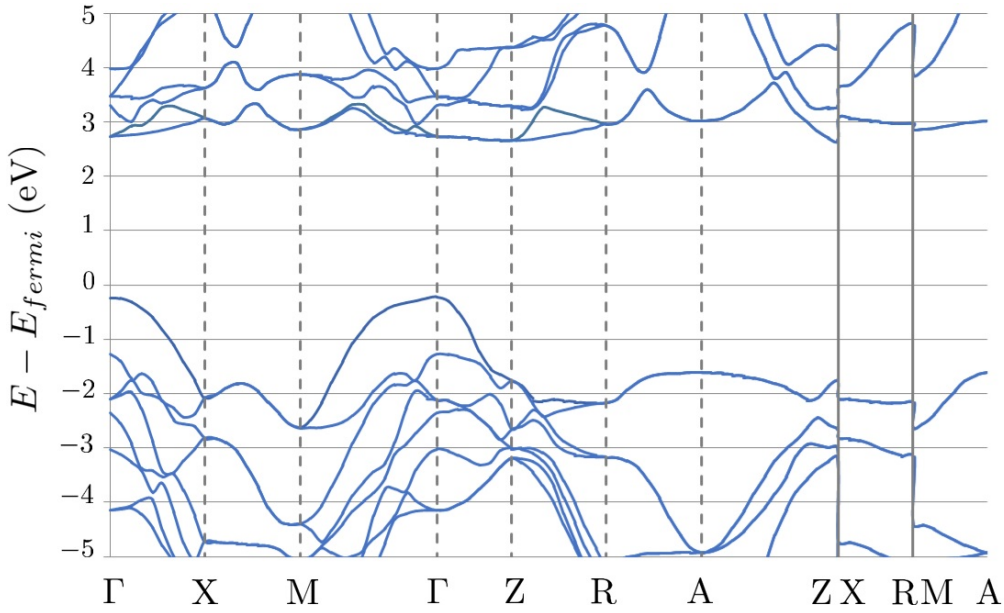


Figure 2.1: Band structure plot of tetragonal ZrO_2 used in this work along indicated high symmetry points in the Brillouin zone. Band energies are taken relative to the Fermi energy.

as:

$$u_{\mathbf{k}}(\mathbf{r}) = \sum_{\mathbf{g}} c_{\mathbf{k},\mathbf{g}} e^{i\mathbf{g}\cdot\mathbf{r}}, \qquad \sum_{\mathbf{g}} |c_{\mathbf{k},\mathbf{g}}|^2 = 1 \tag{2.49}$$

where $\mathbf{g}$ has the same constraints as $\mathbf{L}$. The summation can be truncated up to any specified $|\mathbf{g}|$ depending on the required accuracy of the calculation as components of high $|\mathbf{g}|$ generally have less contribution. In fact, each plane wave component has a kinetic energy of $\frac{\hbar^2}{2m}|\mathbf{k}+\mathbf{g}|^2$ and thus it is more common to impose the truncation criteria in terms of a maximum kinetic energy. The use of basis functions effectively reduces the Kohn-Sham equations into matrix operations that can be easily handled by computers.

2.2.8 Pseudopotentials

In order to improve the computational efficiency of DFT, it is useful to recognise that electrons closer to the inner core of the nuclei play little part in interatomic interactions. Furthermore, the inner core electrons tend to be highly localised and thus require more Fourier components to be accurately represented. The solution is therefore to split the electrons into core and valence electrons where the valence electrons are treated explicitly but the core electrons are replaced by an effective pseudopotential.

To obtain the pseudopotential for a chosen species of atom, the Kohn-Sham equation is first solved for an isolated atom that is (usually) its the ground state configuration, which gives the so called 'all-electron' eigenvalues $\{\xi^{AE}\}$ and wavefunctions $\{\phi^{AE}\}$. A suitable cut-off radius r_c is then chosen to enclose the core electrons, while also making sure core electrons chosen this way have minimal overlap with valence electrons. A pseudopotential V_{PS} is then fitted such that when replacing V_{KS} in the region $r < r_c$ (see Figure 2.2), it produces eigenvalues that match the valence all-electron energy levels, as well as satisfying other imposed constraints that depend on the type of pseudopotential desired. In practice, this is typically done by first fitting a suitable set of pseudowavefunctions ϕ^{PS} and then inverting the Kohn-Sham equation to obtain V_{PS}.

Norm-conserving Pseudopotentials

Norm-conserving pseudopotentials additionally require two conditions. The first being that the pseudowavefunctions reproduce the same valence and core charge densities as the all-electron wavefunction, ensuring that the total valence charge available in interactions is accurate. In other words,

$$\int_{r<r_c} \left|\phi_i^{AE}(\mathbf{r})\right|^2 \mathrm{d}^3r = \int_{r<r_c} \left|\phi_i^{PS}(\mathbf{r})\right|^2 \mathrm{d}^3r \tag{2.50}$$

The second condition is that ϕ^{AE} and ϕ^{PS} are identical outside $r > r_c$, which can be achieved by having ϕ^{AE} and ϕ^{PS} match up to the 2nd derivative at $r = r_c$.

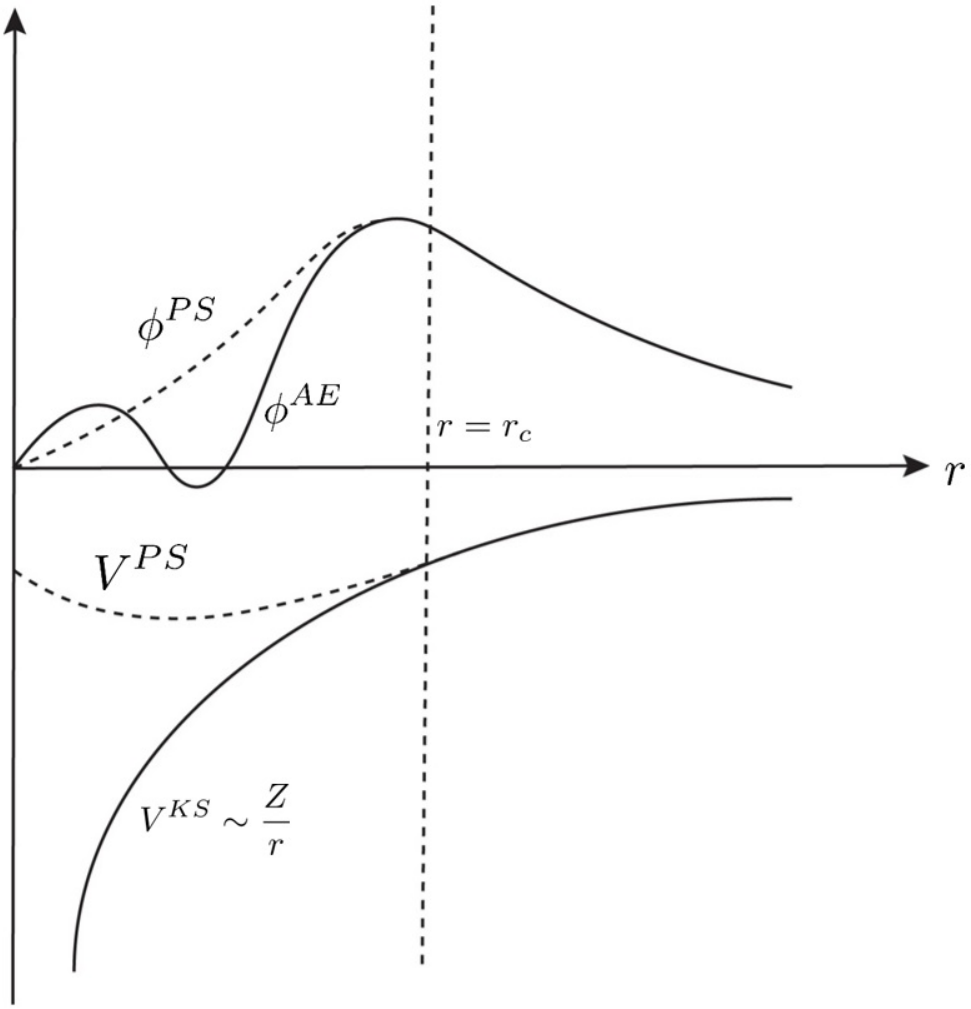


Figure 2.2: In the pesudopotential method, dashed lines representing the pseudopotential and the corresponding pseudowavefunction which replaces the all-electron wavefunction and Kohn-Sham potential at $r < r_c$. Adapted from [54].

Chapter 3

Methodology

This chapter introduces the methods for atomic-scale computational modelling utilised in this thesis. At this scale, both classical and quantum mechanical methods can be used depending on the simulation size and accuracy required. Classical molecular dynamics is applied for damage cascade simulations in the beryllium system, while a quantum mechanical technique based on density functional theory is used to calculate defect energies in the ZrO_2.

This work uses the Large-scale Atomic/Molecular Massively Parallel Simulator (LAMMPS) [143] package in all molecular dynamics simulations, while defects in ZrO_2 are modelled using the DFT software CASTEP [145] based on Kohn-Sham DFT [146].

Before discussing either simulation methods, this chapter first discusses the derivation of a suitable Be-Be interatomic potential to be used in the MD simulations.

3.1 Be-Be interatomic potentials

Currently available Be-Be potentials are mostly EAM and modified EAM potentials due to beryllium being a metal. Table 2.1 reports experimental values for lattice and elastic properties of beryllium and compared to values predicted using the various Be-Be potentials, as well as

Property	Experimental	DFT[g]	Bond-order[f]	EAM[g]	MEAM[h]	MEAM[i]	MEAM[j]
a (Å)	2.2856[a]	2.289	2.31	2.263	2.278	2.256	–
c/a	1.5677[a]	1.566	1.559	1.568	1.567	1.62	–
E_{coh} (eV/atom)	-3.32[b]	-3.32	-3.34	-3.31	-3.43	–	-3.43
B (GPa)	109.88[c], 116.8[d]	126.3	120.4	121	112	115	113
c_{11} (GPa)	293.6[d], 295.4[e]	302.7	250.4	291	3.62	259	331
c_{12} (GPa)	26.8[d], 25.9[e]	29.4	97.2	53	88	77	-11
c_{13} (GPa)	14.0[d], -1.0[e]	16	3.79	10	-22	9	18
c_{33} (GPa)	356.7[d], 356.1[e]	368	372.7	357	193	329	309
c_{44} (GPa)	166.2[d], 170.6[e]	166.9	85.9	124	156	65	19
Melting point (K)	1560[f]	–	1550	1350	–	1390	1550

[a]Ref: [110], [b]Ref: [152], [c]Ref: [153], [d]Ref: [154], [e]Ref: [155], [f]Ref: [150], [g]Ref: [156], [h]Ref: [157], [i]Ref: [158], [j]Ref: [159]

Table 3.1: Predicted properties of HCP beryllium for various Be-Be potentials with comparison to experiment and DFT values.

values derived from DFT. The bond-order Tersoff potential by Björkas *et al.* [150] seems most promising here as on top of having good agreement with experimental/DFT values and being able to accurately predict the melting temperature, it is also fitted against non-equilibrium structures in beryllium, thus it is more suitable for modelling dynamic events such as radiation damage cascades.

3.1.1 Tersoff potential

The Tersoff potential [151] for an atom indexed i under the influence of atom j takes the form:

$$V_{ij}(\mathbf{r}_i) = f_c(r_{ij})\Big(f_R(r_{ij}) + b_{ij} f_A(r_{ij})\Big) \tag{3.1}$$

where $r_{ij} = |\mathbf{r}_i - \mathbf{r}_j|$ and

$$f_c(r) = \begin{cases} 1 & r < R - D \\ \frac{1}{2} - \frac{1}{2}\sin\Big(\frac{\pi(r-R)}{2D}\Big) & |R - r| \leqslant D \\ 0 & r > R + D \end{cases} \tag{3.2}$$

is a cut-off function in the form of a sinusoidal spline implemented for practical computation. Here R is the midpoint distance at which this cut-off is implemented while D is the range around R in which this cut-off takes effect. The repulsive part of the potential $f_R(r)$ takes the form:

$$f_R(r) = \frac{D_0}{S-1}\exp\Big(-\beta\sqrt{2S}(r - r_0)\Big) \tag{3.3}$$

and the attractive part of the potential $f_A(r)$ is:

$$f_A(r) = \frac{SD_0}{S-1}\exp\Big(-\beta\sqrt{2/S}(r - r_0)\Big) \tag{3.4}$$

The multiplier to the attractive part of the potential is the bond-order term:

$$b_{ij} = \frac{1}{\sqrt{1 + \chi_{ij}}} \tag{3.5}$$

where

$$\chi_{ij} = \sum_{k \neq i,j} f_c(r_{ik}) g(\theta_{ijk}) \omega \exp(\alpha(r_{ij} - r_{ik})) \tag{3.6}$$

and

$$g(\theta) = \gamma\Big(1 + \frac{c^2}{d^2} - \frac{c^2}{d^2 + (\cos(\theta) - \cos(\theta_0))^2}\Big) \tag{3.7}$$

Here θ_{ijk} is the angle formed between $\mathbf{r}_j - \mathbf{r}_i$ and $\mathbf{r}_k - \mathbf{r}_i$. The remaining 10 terms S, D_0, r_0, α, β, γ, ω, c, d and θ_0 are fitting parameters.

ZBL screening function

In addition, the potential is modified in the usual manner with the Ziegler-Biersack-Littmark (ZBL) universal screening function [160] to account for nuclear repulsion, which is required when modelling high-energy collisions such as in radiation damage cascade events. Following the application of the ZBL screening function $V_{ZBL}(r)$, the total potential function between two atoms is given by:

$$V_{tot}(r_{ij}) = f_F(r_{ij}) V_{tersoff}(r_{ij}) + (1 - f_F(r_{ij})) V_{ZBL}(r_{ij}) \tag{3.8}$$

where $f_F(r)$ is a fermi-like splicing function with the form:

$$f_F(r) = \frac{1}{1 + e^{-a(r - r_c)}} \tag{3.9}$$

where $a = 7$ Å^{-1} and $r_c = 0.8$ Å are the adjustable parameters, values chosen by Björkas *et al.* [150], which allow for smooth joining of the functions as well as ensuring that the Tersoff potential remains unmodified at equilibrium and longer distances.

3.1.2 Potential fitting

While fitted with a methodology appropriate for the study of radiation damage, the Björkas *et al.* Be-Be potential does have a shortcoming. Figure 3.1 reports values for thermal properties,

in particular thermal expansion. Here the comparison between experiment and the model of Björkas *et al.* indicates the issue. Specifically for temperatures above 600 K the prediction is for negative expansion while experiment shows a positive value. This is a considerable problem when modelling a thermal related property (i.e. radiation damage). The aim here will be to rectify this issue and then refit a new potential.

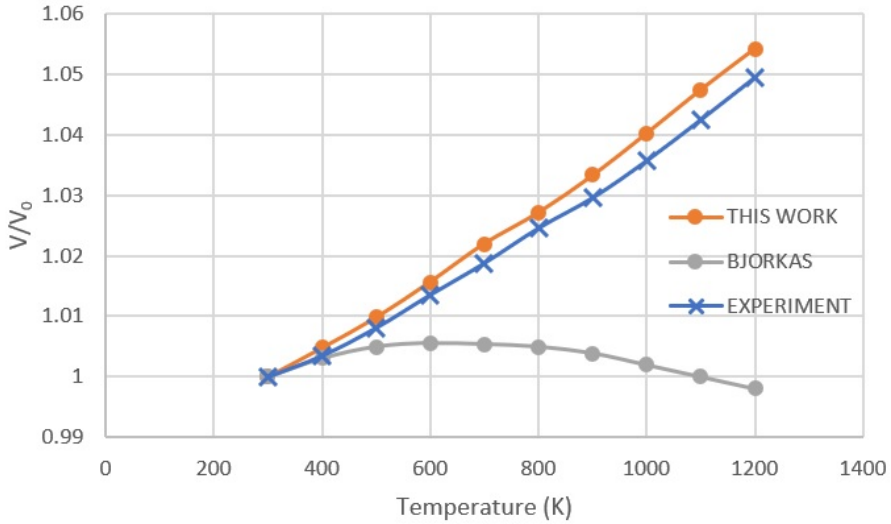


Figure 3.1: Comparison of experimental thermal expansion [161] with those predicted using the current modified and original Björkas *et al.* [150] potential.

The process of fitting a potential typically involves drawing up a table of the desired properties and their expected values, which can be either experimental or from higher fidelity simulations and models. These properties can be weighted in accordance to their importance to construct a merit function. This work uses a linear least-squares merit function, which is defined by

$$F(\mathbf{a}) = \sum_i w_i |q_i(\mathbf{a}) - q_i^*|^2 \tag{3.10}$$

where $\mathbf{a}$ is a vector containing the parameter values, $q_i(\mathbf{a})$ and q_i^* are the predicted and desired values respectively for the property indexed i and w_i is the associated weight. $F(\mathbf{a})$ is then minimised to obtain the parameter set. Table 3.2 shows a subset of the fitting parameters used in this work as an example.

In practice, simply applying a minimisation algorithm to the merit function does not lead

to an acceptable minima due to the complexity of the parameter landscape. It is therefore useful to understand the physics incorporated in the interatomic potentials in order to, through implementing constraints on the parameters, 'guide' the minimisation process. This concept is further explored below.

Table 3.2: Fitting table for HCP beryllium values.

Property	Target	Predicted value	Weightage	Merit value
a (Å)	2.2856	2.2848	1000	6.87×10^{-4}
c/a	1.5677	1.5677	3800	0
$2E_{coh}$ (eV/atom)	-6.64	-6.627	300	0.0532
B (GPa)	109.88	109.97	2	0.0159
$\mathrm{d}B/\mathrm{d}P$	3.584	5.427	0.01	0.0340
c_{11} (GPa)	293.6	287.4	0.5	19.46
c_{12} (GPa)	26.8	33.6	2.5	115.76
c_{13} (GPa)	14.0	2.68	5	640.71
c_{33} (GPa)	356.8	358.5	0.5	1.48
c_{44} (GPa)	166.2	98.2	0.5	2316

Thermal expansion

To understand why the potential of Björkas *et al.* exhibits a negative thermal expansion, it is first necessary to consider how thermal expansion emerges from the interatomic potential. This is illustrated in Figure 3.2 for the case of a pair of atoms: as it can be seen that when the inward slope of the potential is steeper than the outgoing slope, the average position, or atomic separation, would increase as the atoms get more energetic. This is exactly thermal expansion for a pair of atoms. For a solid, thermal expansion is derived from a sum of the interatomic potentials. Complexity arises because the sum involves different characteristic interatomic equilibrium separations due to anisotropy in the first shell atom-atom distances due to the sum being out to a number of shells of atoms. Nevertheless, for a metal, this lattice energy is dominated by the nearest neighbour distance so the idea illustrated in Figure 3.2 remains symptomatic.

It was found that the reason for the negative thermal expansion was due to the cut-off function

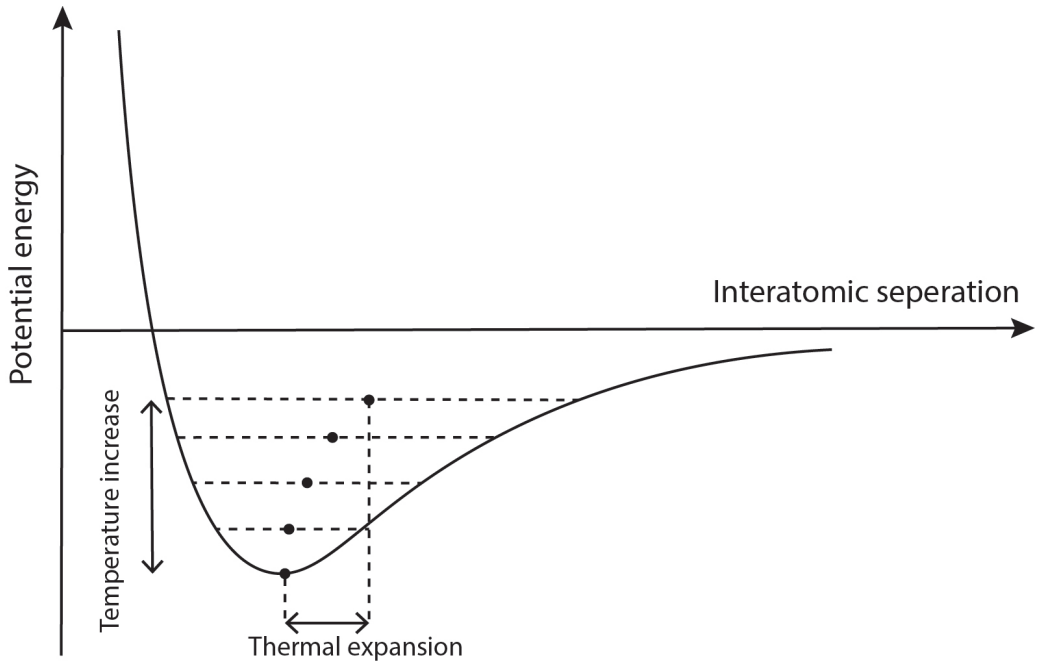


Figure 3.2: Illustration of how thermal expansion arises from the form of the interatomic potential. The dots show the average interatomic spacing at each temperature.

$f_c(r)$ being forced in between the first and second nearest neighbours in HCP-Beryllium. This resulted in an unrealistic attractive force when atom separations are within that range. This is illustrated in Figure 3.3 which shows that the out-going slope is at least as steep as the in-going slope. One can even see the point in which the cut-off function starts to dominate, explaining

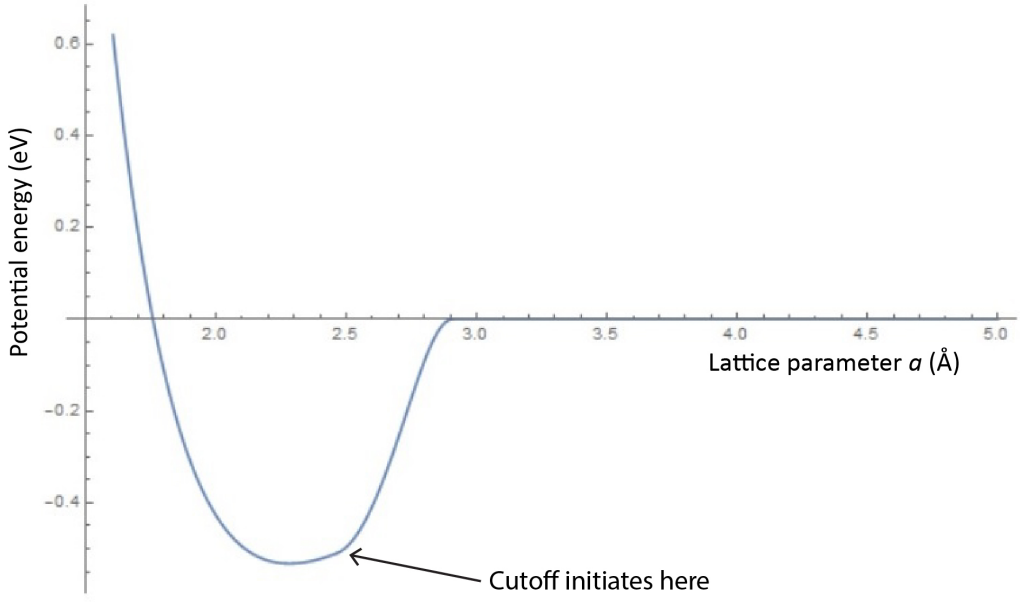


Figure 3.3: Plot of $V(r_{ij})$ against lattice parameter a in a HCP structure. The potential shows a small 'kink' where the cut-off function abruptly begins.

why the negative thermal expansion was in evidence above a specific temperature. Further,

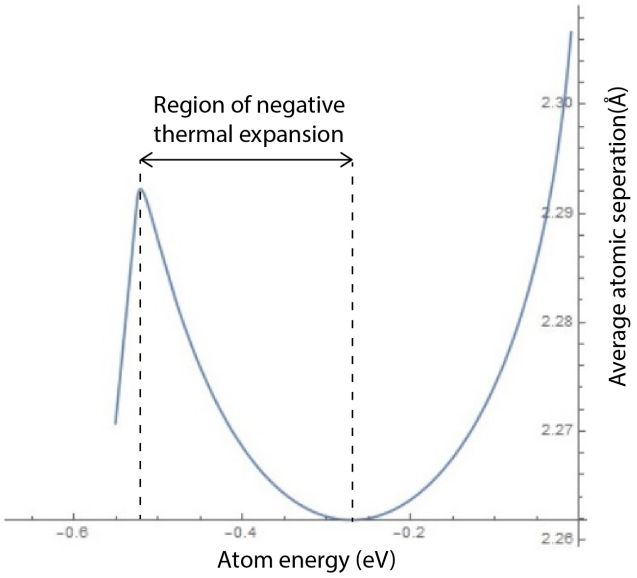


Figure 3.4: Plot of the average atomic separation in HCP beryllium against the atomic energy, which is directly related to temperature, for the potential from Björkas *et al.* [150]. The onset of negative thermal expansion is indicated.

Figure 3.4 shows that the average position does decrease after a certain energy. In contrast, we

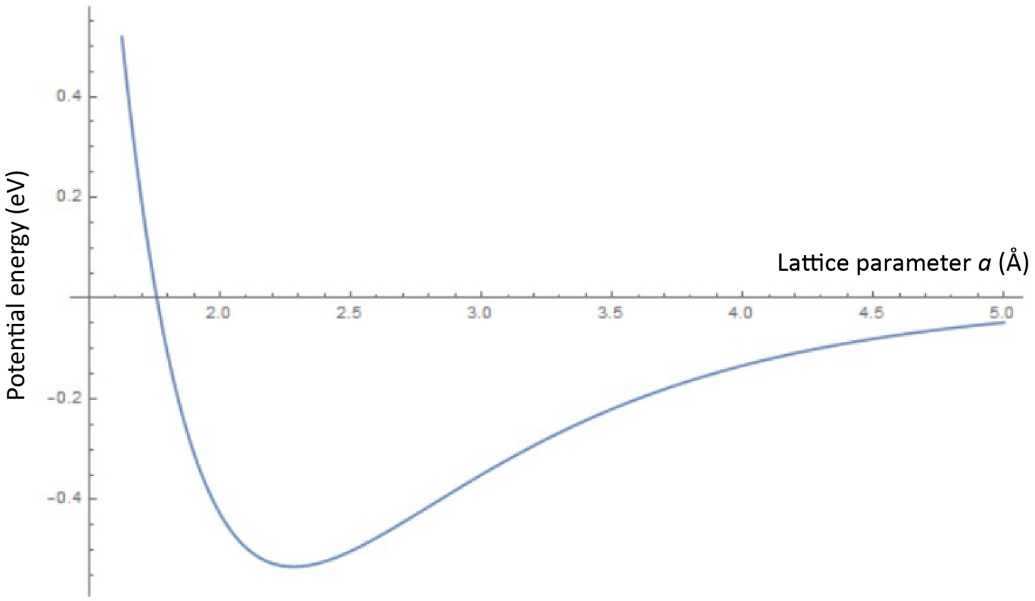


Figure 3.5: Plot of $V(r_{ij})$ against lattice parameter a in HCP beryllium using the same parameter set from Björkas *et al.* [150] with the exception that the cut-off function was modified by changing the parameters R from 2.685 Å to 6 Å and D from 0.223 Å to 1 Å.

plot in Figure 3.5 the same potential energy function with the cut-off applied from 5 Å to 7 Å instead of from 2.462 Å to 2.908 Å. In this case, the outgoing slope in the potential is more

gentle, thus we can be sure that this parameter set will produce positive thermal expansion (although this is no guarantee that other properties will remain acceptable).

The understanding delivered by this analysis leads to a simple solution to improve the potential: that is simply to apply the cut-off function further out and over a larger range to restore thermal expansion and then refit the parameter set using the same methods used by Björkas *et al.* [150].

This modification does mean that simulations are more computationally expensive, something that the original authors may have been trying to avoid. However, due to the type of simulations that will be performed using the potential (i.e. radiation damage involving an anisotropic temperature profile) it is important to reproduce the temperature dependence of the thermal expansion. By visually examining the form of the potential as the cut-off range changes, values of $R = 3.5$ Å and $D = 0.8$ Å were identified for the refitting process.

Static Properties

The most basic properties of a material are its static properties and therefore it is no surprise that some of them can be easily derived by again referring to energy vs lattice parameter plots. Figure 3.6 shows how properties like binding energy and bond length can be derived in this way.

An estimate of second-order properties like the bulk modulus of the simulation material may be obtained based from basic definitions with

$$\begin{aligned} B &= -V\frac{\mathrm{d}P}{\mathrm{d}V} \\ &= V\frac{\mathrm{d}^2E}{\mathrm{d}V^2} \\ &= V\frac{\mathrm{d}r}{\mathrm{d}V}\frac{\mathrm{d}}{\mathrm{d}r}\left(\frac{\mathrm{d}r}{\mathrm{d}V}\frac{\mathrm{d}E}{\mathrm{d}r}\right) \\ &= V\frac{\mathrm{d}r}{\mathrm{d}V}\frac{\mathrm{d}^2E}{\mathrm{d}r^2} \end{aligned} \tag{3.11}$$

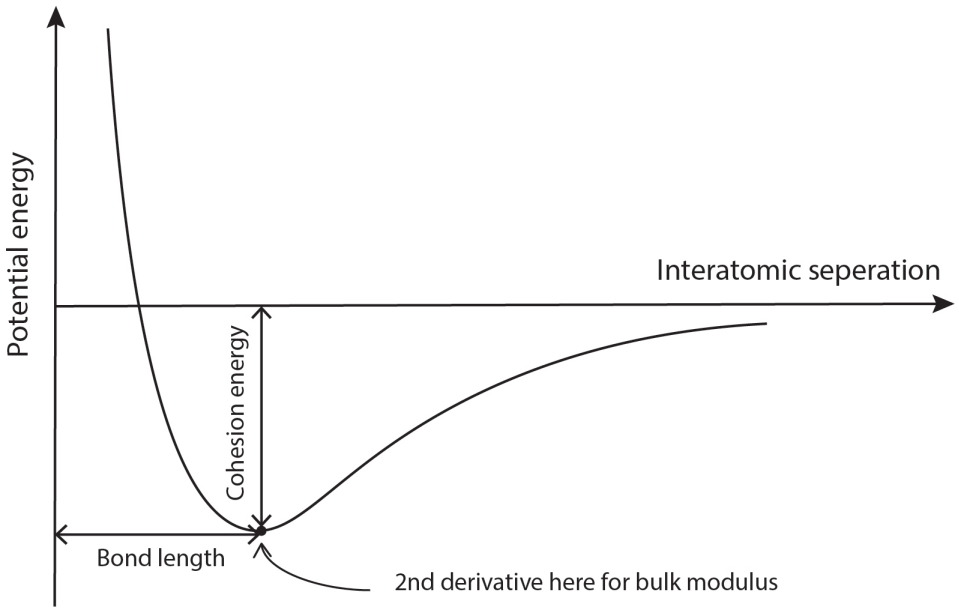


Figure 3.6: Correspondence of static material properties to interatomic potential.

recalling that $\dfrac{\mathrm{d}E}{\mathrm{d}r} = 0$ at equilibrium.

Melting point

As determining melting point in MD requires simulation of a solid-liquid interface (see Section 3.2), its inclusion in the merit function would be impractical. It is instead optimised by choosing from several converged parameter sets. Therefore, some understanding of melting point in relation to the interatomic potential would be helpful here.

Kumagai *et al.* developed a modified Tersoff potential that included a modification to the $g(\theta)$ term [162] where:

$$g_{mod}(\theta) = c_1 + \frac{c_2(h - \cos\theta)^2}{c_3 + (h - \cos\theta)^2}\Big(1 + c_4 \exp\big(-c_5(h - \cos\theta)^2\big)\Big) \tag{3.12}$$

The modified Tersoff potential was able to produce an almost linear dependence of the melting point on the parameter c_4 in silicon. The total of four additional parameters included in the modified Tersoff potential means that while more flexible, the resulting fitting process will be less efficient.

This work finds that it still possible to adjust melting point using the original Tersoff potential. The insight stems from three things: 1) the fact that Figures 3.3 and 3.5, which are essentially plotting the radial dependence in the Tersoff potential, shows no feature or threshold that can be linked to melting, 2) when considering the simplest atomic-scale picture of a solid vs liquid, the main difference is the lack of ordered structure rather than atomic separation (atoms sliding pass each other) and 3) the linear dependence of temperature is found in the angular component of the modified Tersoff potential.

The resulting hypothesis is that melting in the Tersoff potential occurs via overcoming a barrier in the θ direction and therefore can be controlled via a scaling factor in the b_{ij} term, which controls the angular dependence. The simplest scaling factor to manipulate is γ, for which we expect increasing γ to lead to decreasing b_{ij} and angular barrier height and therefore decreasing melting point. This relationship is shown for three different Be-Be Tersoff potentials in Figure 3.7 and it is further noted that the melting point dependence shown in the modified Tersoff potential for silicon [162] also appears to follow the same principle.

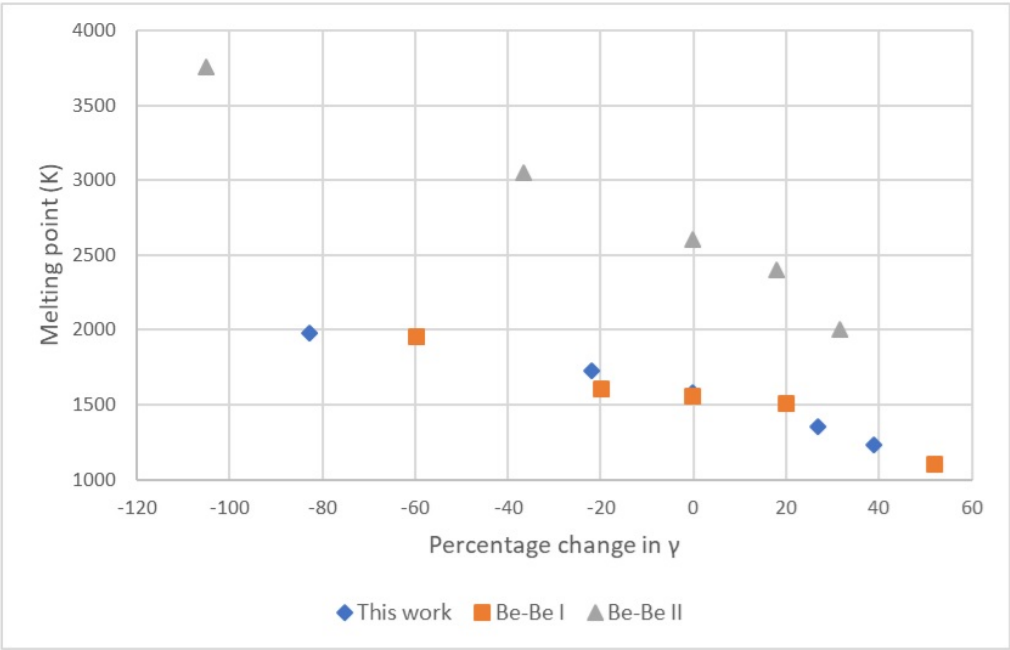


Figure 3.7: Inverse relationship of the γ parameter in Tersoff potentials with melting point, shown here for Be-Be I and Be-Be II from Björkas *et al* [150] as well as the potential fitted in this work.

3.1.3 New Be-Be potential

The new Be-Be potential is fitted using the same fitting table as Björkas *et al.* [150], with the additional requirement that $R = 3.5$ Å and $D = 0.8$ Å. The parameters in the ZBL screening function were kept as they are. The merit function is minimised using a downhill simplex algorithm developed by Nelder and Mead [163]. This approach was able to produce a Be-Be potential with the correct thermal expansion (see Figure 3.2).

Tables 3.3 and 3.4 show how predictions using the current potential (so far) compare to predictions using the original potential by Björkas *et al* [150]. The properties presented in both tables are used to fit the new parameter set, which is reported in Table 3.5. Table 3.4 also includes cohesive energies for beryllium in a set of different structures. It can be seen that HCP is the most energetically favourable (as it should be since it is the observed phase).

Table 3.3: Values for the properties of HCP beryllium that were used in the fitting process. Comparisons are made to experiment, DFT, the values predicted using the potential from Björkas *et al.* [150], and the new potential.

Structure	Experimental	DFT[g]	Björkas *et al.*	This work
HCP ($P6_3/mmc$)				
a (Å)	2.2856[a]	2.289	2.31	2.2848
c/a	1.5677[a]	1.566	1.559	1.5677
E_{coh} (eV/atom)	-3.32[b]	-3.32	-3.32	-3.31
B (GPa)	109.88[c], 116.8[d]	126.3	120.4	109.97
$\mathrm{d}B/\mathrm{d}P$	3.584[c], 4.6[e]	3.31	4.14	5.43
c_{11} (GPa)	293.6[d], 295.4[e]	302.7	250.4	287.4
c_{12} (GPa)	26.8[d], 25.9[e]	29.4	97.2	33.6
c_{13} (GPa)	14.0[d], -1.0[e]	16	3.79	2.7
c_{33} (GPa)	356.7[d], 356.1[e]	368	372.7	358.5
c_{44} (GPa)	166.2[d], 170.6[e]	166.9	85.9	98.1
Melting point (K)	1560[f]	–	1550	1575

[a]Ref: [110], [b]Ref: [152], [c]Ref: [153], [d]Ref: [154], [e]Ref: [155], [f]Ref: [150]

A hypothetical graphite structure of beryllium was also included in the fitting table by Björkas *et al* [150]. However, it was not possible to produce a stable graphene structure using the LAMMPS code, thus it is not included in the fitting table. Regardless, the properties obtained

Table 3.4: Values of the properties of theoretical beryllium structures that were used in the fitting process. Comparisons are made to experiment, DFT, the values predicted using the potential from Björkas *et al.* [150], and the new potential.

Structures	DFT	Björkas *et al.*	This work
Diamond ($Fd\bar{3}m$)			
a (Å)	4.94	4.93	4.67
E_{coh} (eV/atom)	-1.73	-1.71	-1.64
B (GPa)	45.1	30.3	30.3
dB/dP	3.68	3.94	3.96
Simple cubic ($Pm\bar{3}m$)			
a (Å)	2.20	2.18	2.08
E_{coh} (eV/atom)	-2.33	-2.20	-2.49
B (GPa)	75.7	58.9	105.5
dB/dP	3.24	4.03	4.90
Body-centered cubic ($Im\bar{3}m$)			
a (Å)	2.48	2.50	2.53
E_{coh} (eV/atom)	-3.22	-3.26	-3.08
B (GPa)	127.2	371.9	107.7
dB/dP	3.41	2.71	5.12
Face-centered cubic ($Fm\bar{3}m$)			
a (Å)	3.18	3.23	3.17
E_{coh} (eV/atom)	-3.24	-3.16	-3.13
B (GPa)	123.8	114.3	113.9
dB/dP	3.45	4.03	4.81

with the new parameter set are in good agreement with the DFT and experimental values. The new potential is also able to reproduce the melting point accurately. Finally, given that much of the resultant damage in the cascade simulations is expected to be in the form of Frenkel pairs, the predicted energies of vacancies and self-interstitials are verified in Table 3.6. The new potential is able to correctly predict the order of preference of each interstitial site as reported in the DFT work by Middleburgh and Grimes [101].

Table 3.5: Parameters for the Tersoff potential used in this work.

S	D_0 (eV)	r_0 (Å)	α	β (Å^{-1})	γ
8.0588	0.8661	2.2276	1.6001	1.1441	7.3088×10^{-7}
ω	c	d	θ_0 (rad)	R (Å)	D (Å)
1	30.4703	0.067188	0.60941	3.5	0.8

Table 3.6: Vacancy and intersititial defect energies predicted with the new Be-Be potential, compared with DFT values [101].

Defect type	DFT energy (eV)	Predicted energy (eV)
Vacancy	1.09	1.99
Non-basal octagonal interstitial	5.06	4.42
Non-basal tetrahedral interstitial	5.14	4.80
Non-basal trigonal interstitial	4.77	4.11
Basal hexagonal interstitial	5.67	4.81
Basal trigonal interstitial	4.01	4.03

3.2 MD simulations

3.2.1 Melting point calculations

Melting point calculations are performed in MD via a moving-interface method described by Govers *et al.* [164]. The method involves first constructing a supercell made by joining a liquid cell and a solid cell of equal size. In this work, a $5 \times 5 \times 50$ supercell is constructed from two $5 \times 5 \times 25$ supercells of a solid and a liquid phase. The simulation cell is then allowed to equilibrate for 100 ps (100000 timesteps of 1 fs) at an estimated melting temperature. Should the cell have more liquid then solid at the end of the simulation time, the estimated melting temperature is too high. Should there instead be more solid phase, the reverse is true. This is illustrated in Figure 3.8.

3.2.2 Radiation damage cascades

The cascades were modelled using a $100 \times 100 \times 64$ supercell, containing 1.28 million atoms, with periodic boundaries. Cascades are initiated by imparting a chosen atom, the primary knock-on

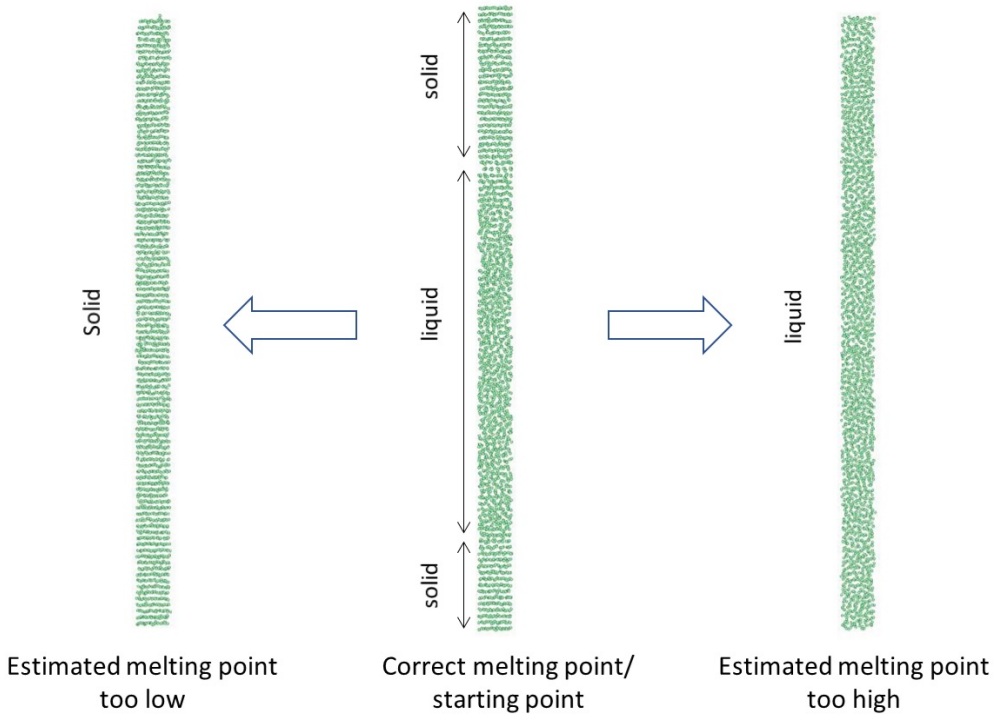


Figure 3.8: Possible results from the moving-interface method.

atom (PKA), with a given kinetic energy at $t = 0$ in a cell that has been equilibrated for 10000 steps of 2 fs timesteps at a chosen temperature. Variations were considered for temperature and PKA energy. For each temperature-PKA energy pair, 10 simulations were performed in 10 random directions (see Table 3.7) for the PKA, with the set of random directions being the same for all temperatures and PKA energy. The simulation was performed in accordance to the NVE ensemble. Electronic energy loss models were not considered in this work and thus the damage energy and PKA energy will be equivalent.

Table 3.7: List of directions in cartesian coordinates for displacement simulations.

Direction No.	x	y	z
1	4.915901	6.838752	9.035806
2	0.017895	0.258828	2.616523
3	1.173333	9.831851	7.581009
4	6.019825	8.049711	9.941972
5	0.070281	3.603135	3.166748
6	9.463249	9.830925	1.642074
7	9.061083	7.530391	2.942791
8	2.127385	0.645442	5.012050
9	5.788519	3.859021	4.302342
10	4.879197	2.243410	2.258219

Three different timesteps were used in the simulations to accomodate modelling the initial fast moving PKA accurately but with sufficient simulation time for cascade recovery. Even at 2.5 keV the PKA travels a distance less than that of the Bohr radius at each timestep, avoiding atoms tunneling through each other. In total, 20000 steps of 0.01 fs timesteps, followed by 10000 steps of 0.1 fs and finally 10000 steps of 1 fs timesteps were used. This provided a total simulation time of 11.2 ps. For the first 20000 timesteps, the NVE ensemble is used throughout the simulation cell. While for the remaining 20000 timesteps, a Nosé-Hoover thermostat [148] was applied to the cell excluding a 80 Å radius sphere from the initial position of the PKA.

3.2.3 Defect detection

Identification of defects in a disordered simulation cell can be rather complex depending on requirements. If one wishes to identify extended defects, post-processing of detected defects may be required as common methods that rely on comparison with a reference state only consider each displaced atom as an individual defect. Common methods include Lindemann spheres [165], which considers any atom not within a designated cut-off distance from a reference atom site to be displaced and the potential energy method [166] that considers any atom that has potential energy lower than its reference value by a designated amount to be displaced. Wigner-Seitz cell analysis is performed by considering the occupation within each Wigner-Seitz cell generated from a reference state, where any cell that contains anything other than one atom is considered a defect [167]. Wigner-Seitz cells are enclosed by perpendicular surfaces half the distance away from nearest neighbour atoms, shown here in Figure 3.9 for a 2D case.

In the context of the radiation damage simulations performed in this work, while the above methods alone may not be able to fully describe the damage a highly disordered cell such as in the peak of a damage cascade event, they are still sufficient in quantifying the disorder present in the simulation cell. Further, it has been shown that in regions of disorder, while different methods of damage detection like Wigner-Seitz cell analysis, Lindemann spheres [165], nearest-

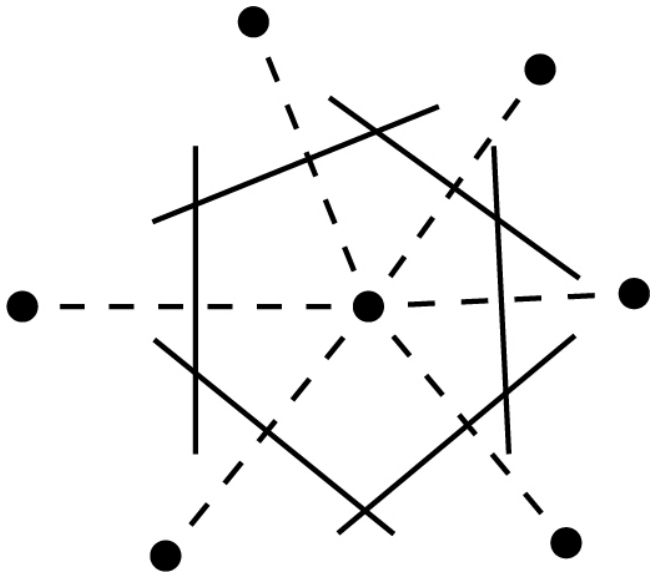


Figure 3.9: Construction of a Wigner-Seitz cell for the central atom in a group of seven atoms (black dots). The dotted lines are the path to the nearest neighbour atoms, for which the solid lines are the perpendicular bisectors that enclose the Wigner-Seitz cell.

neighbour spheres [168] and potential energy methods [166] all provide different values, they are still consistent with each other in the sense that they yield approximately the same ratios at every phase of a damage cascade simulation with respect to defects detected between the different schemes [137]. The Wigner-Seitz cell analysis is chosen for this work as it is the only method that does not require the input of an arbitrary cut-off parameter.

3.2.4 Threshold displacement

The minimum energy required to displace an atom from its lattice site, the threshold displacement energy (E_d), was also calculated using the modified interatomic potential, via a set of simulations with 5-200 eV PKA in a $10 \times 10 \times 6$ supercell at 300 K. PKA directions considered were in an upper hemisphere within 60° azimuthal angle of the $[10\bar{1}0]$ direction. Within this, a set of directions uniformly spaced 6° apart in the azimuthal ϕ and polar θ angles were used as the PKA directions (see Figure 3.10). The symmetry of the system allows the reduced section to be considered.

Care should be taken when sampling points on a sphere using uniformed separated points

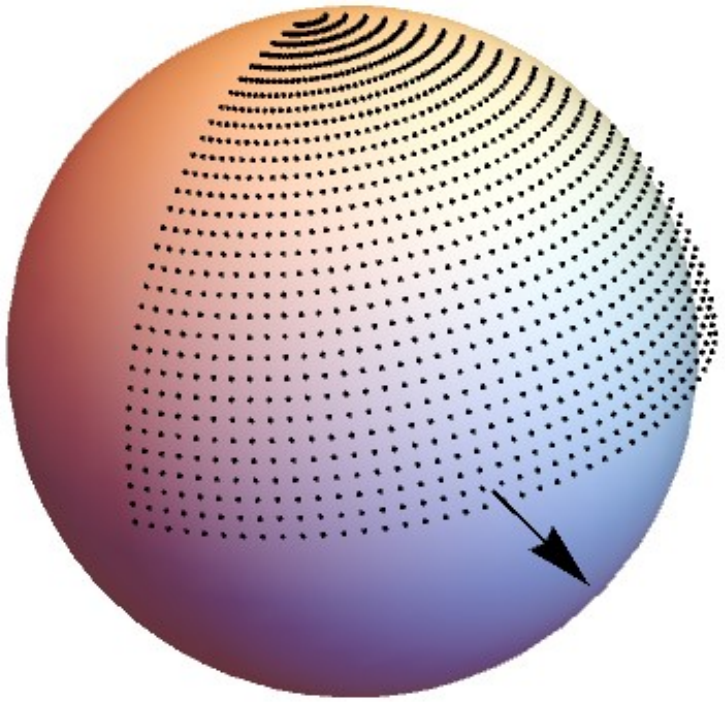


Figure 3.10: Directional points considered for threshold displacement, the arrow indicates the $[10\bar{1}0]$ direction.

in ϕ and θ. While there are no issues when considering angular variation of data, directional averages will require proper weighting of each point. This is clear when looking at the area element each point represents on a unit sphere

$$\mathrm{d}A = \sin\theta \ \mathrm{d}\theta\mathrm{d}\phi \tag{3.13}$$

and therefore each point has to be accordingly weighted proportional to $\sin\theta$.

For each direction and energy pair, 10 simulations were performed with a vibrationally different starting configuration by allowing the simulation to randomly run for up to 5000 steps of 1 fs before the chosen energy is imparted to the PKA. The simulation then ran for 11.2 ps using the same timesteps as the damage cascade simulations. The PKA is considered to be displaced at the end of the simulation time if it is at least half the nearest neighbour distance (rounded as 1.14 Å) from its original site. Thus, for each PKA energy there are a set of 2210 simulations, only some of which predict displacement. This yields a probability that displacement will occur

for a given PKA energy (i.e. directionally and vibrationally averaged). This approach has been used previously to predict threshold displacement in beryllium using a different Be-Be potential [114]. The probabilistic threshold displacement is defined to include replacement events, which has been shown to not be temperature sensitive, in contrast to the case where only defect production is considered as threshold displacement [169].

3.3 Defects in doped ZrO_2

Defects in ZrO_2 are modelled by performing geometry optimisation calculations in CASTEP [145] to find their formation energies, which are used to identify the favourable defects at different depths within the oxide. Tetragonal ($P4_2/nmc$) and monoclinic ($P2_1/c$) ZrO_2 are considered since both species can be found in the oxide layer. To be able to properly simulate the behaviour of the defects in bulk ZrO_2 with just a few hundred atoms in CASTEP, the simulations employ periodic boundary conditions. This approach could lead to defect image interaction, which is minimised by using a $2 \times 2 \times 2$ supercell (96 atoms) for monoclinic ZrO_2 while a $3 \times 3 \times 2$ supercell (108 atoms) is used for tetragonal ZrO_2 to minimise any directional effects. The cell sizes are sufficient to provide accurate results [54, 56].

Throughout the DFT calculations, the Perdew-Burke-Ernzerhof (PBE) [178] exchange-correlation functional was used. The PBE functional is a GGA functional that has been the the most commonly applied functional in the study of bulk materials [179, 180], and most importantly has also found success in modelling ZrO_2 [52–56, 181].

The norm-conserving pseudopotential used was generated from CASTEP version 6.0, the plane-wave basis cutoff energy was 550 eV while the Brillouin Zone sampling was done using the Monkhorst-Pack scheme [182] with a $2 \times 2 \times 2$ k-point grid. The self-consistent field calculation for solving the Kohn-Sham equations employed Pulay's density mixing algorithm [183], which gives good convergence speed, with a minimum energy convergence criteria of 10^{-6} eV. The geometry optimisation is considered to have converged when between iterations, the energy

difference is below 10^{-5} eV per ion, the maximum ion displacement is below 5×10^{-4} Å and the maximum force on each ion is not more than 0.01 eV/Å.

Intrinsic defects considered were zirconium (charge states 0 to 4+) and oxygen (charge states 0 to 2−) interstitials and corresponding vacancies. Possible interstitial sites in both phases of oxide were considered using the Wyckoff positions of the relevant space groups. In plane wave DFT simulations, charge can only be fixed for the overall supercell. For simulations containing a single defect, the defect charge is simply the charge of the supercell. When the supercell contains multiple defects, charge states of each defect will have to be inferred, employing Mulliken population analysis [184] when necessary.

Dopant containing defects are primarily based on substitutions on the zirconium site given that the dopants considered in this work are mostly transitional metals. Besides the single substitution, dopant clusters involving oxygen vacancies in the form $\{M_{Zr} : V_O^{\bullet\bullet}\}$ and $\{M_{Zr} : V_O^{\bullet\bullet} : M_{Zr}\}$ were also considered. Given that oxygen vacancies are an important component of oxygen transport in the oxide, its interaction with dopant species is a crucial point of study. For defects involving a single dopant bonded to an oxygen vacancy, 2nd nearest neighbour positions have also been considered as it has been shown in doped CeO_2 that nearest neighbours may not always be preferred in such situations [185].

3.3.1 Convergence testing

While there has been a good amount of work previously done on DFT simulation of defects in ZrO_2 for the purpose of constructing Brouwer diagrams, these examples tend to only incorporate single defects. Therefore, it needs to be ensured that energy calculations will properly converge for such trimers. The $\{Fe''_{Zr} : {}^4V_O^{\bullet\bullet} : Fe''_{Zr}\}''$ cluster for m-ZrO_2 and $\{Fe''_{Zr} : V_O^{\bullet\bullet} : Fe''_{Zr}\}''$ cluster for t-ZrO_2 are considered for the testing of convergence.

Results are reported in Figure 3.11, where the errors are taken relative to the strictest pa-

rameter considered. A $3 \times 3 \times 3$ Monkhorst-Pack k-point grid was also considered, for which

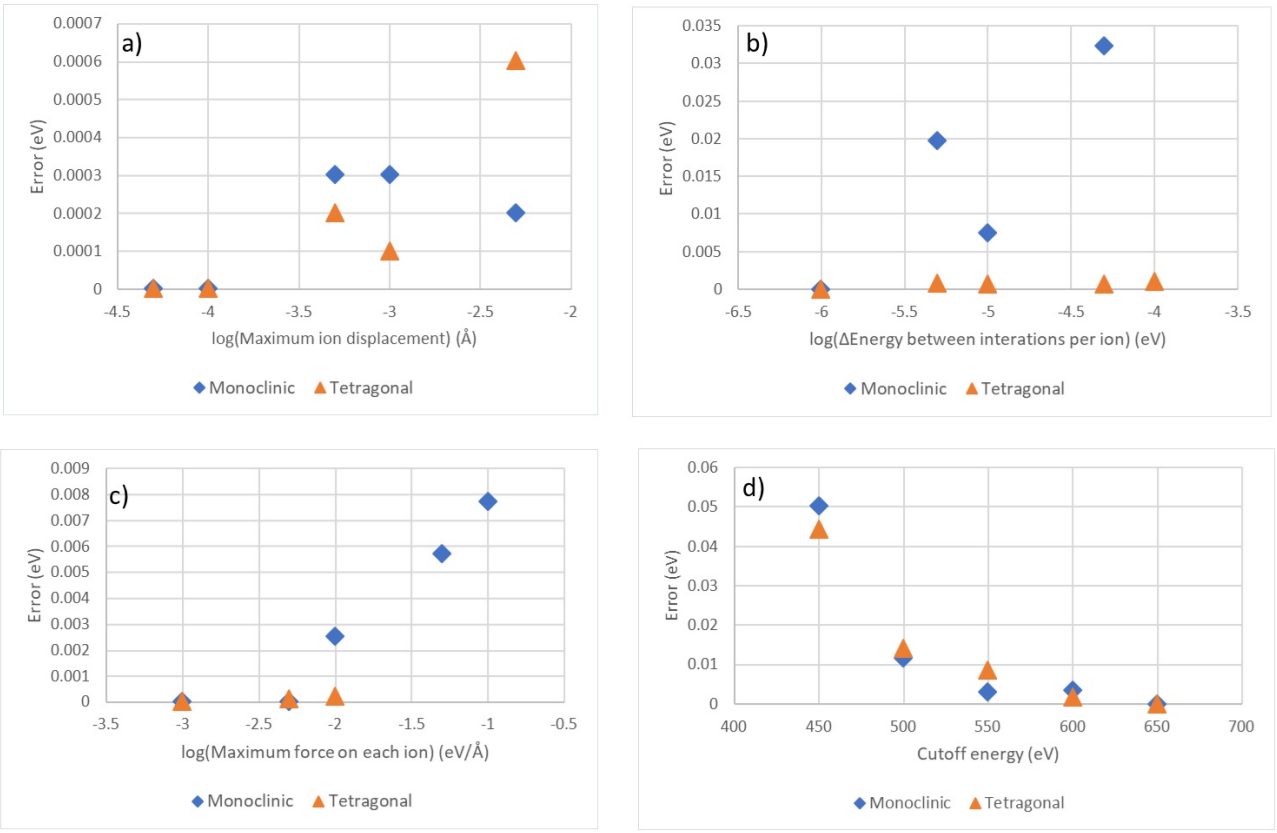


Figure 3.11: Convergence parameters plotted against error for: a) maximum ion displacement, b) energy change per ion, c) maximum force on each ion and d) plane wave cutoff energy. The errors are defined against the strictest value considered, shown here as points with zero error.

the errors relative to a $2 \times 2 \times 2$ grid are 0.0032 eV and 0.0005 eV respectively. Given that the average defect formation energies are of the order of 1 eV, the errors for the chosen convergence parameters are within acceptable limits. The convergence in m-ZrO_2 is noticably poorer however, especially for the maximum ion force. This can be attributed to the smaller supercell size chosen for m-ZrO_2.

3.3.2 Brouwer Diagrams

The defect energies obtained from the DFT calculations were then used to calculate formation energies of the defects with respect to the oxygen chemical potential based on an approach by

Zhang and Northup [58]. The concentration c_X of defect X is:

$$c_X \propto \exp\left(\frac{-\Delta E_X^f}{k_B T}\right) \tag{3.14}$$

where k_B is the Botlzmann constant and T is the temperature. For a defect X of charge q, the defect formation energy $E_{X^q}^f$ is given by:

$$E_{X^q}^f = E_{X_{\mathrm{Zr}}^q}^{\mathrm{DFT}} - E_{\mathrm{perfect}}^{\mathrm{DFT}} \pm \sum_i n_i \mu_i + q(E_{\mathrm{VBM}} + \mu_e) + E_{\mathrm{SM}} \tag{3.15}$$

where $E_{X^q}^{\mathrm{DFT}}$ is the DFT defect energy, $E_{\mathrm{perfect}}^{\mathrm{DFT}}$ is the DFT energy of the perfect cell, n_i is the number of atoms of species i removed or added, μ_i is the chemical potential of the atoms of species i, μ_e is the electron chemical potential, E_{VBM} is the valence band maximum energy and finally:

$$E_{\mathrm{SM}} = -\frac{q^2}{2} v_{\mathrm{SM}} \tag{3.16}$$

is the screened Madelung energy correction to account for defect image interactions [186]. v_{SM} is the screened Madeling potential constructed using the full dielectric tensor, which has been previously calculated for HfO_2 by Zhao and Vanderbilt [187]. Given the chemical and physical similarity between HfO_2 and ZrO_2, the same values are used in this work.

Electron and hole concentrations (c_e and c_h) are calculated as,

$$c_e = N_c \exp\left(\frac{-(E_g - \mu_e)}{k_B T}\right) \tag{3.17}$$

and

$$c_h = N_v \exp\left(\frac{-\mu_e}{k_B T}\right) \tag{3.18}$$

where N_c and N_v are the effective conduction and valence band density of states and E_g is the band gap of the perfect crystal. Boltzmann statistics are used here as ZrO_2 is insulating and thus the concentrations of the electrons and holes are expected to be low.

The chemical potentials μ_i are all functions of temperature and oxygen partial pressure and their values can be derived from the chemical potentials of solid ZrO_2 and Zr, which are obtained from DFT. The chemical potential for solid ZrO_2 can be expressed as:

$$\mu_{ZrO_{2(s)}} = \mu_{Zr}(T, P_{O_2}) + \mu_{O_2}(T, P_{O_2}) \tag{3.19}$$

Ideally $\mu_{O_2}(T, P_{O_2})$ can be calculated from DFT values as well, but it is known that DFT is not able to describe the O_2 molecule adequately. Fortunately, Finnis *et al.* [188] proposed a method to obtain $\mu_{O_2}(T, P_{O_2})$ using the experimental formation energy of ZrO_2 in standard temperature and pressure:

$$\mu_{O_2}(T, P_{O_2}) = \mu_{O_2}(T^\circ, P^\circ_{O_2}) + \Delta\mu(T) + \frac{1}{2}k_B \log\left(\frac{P_{O_2}}{P^\circ_{O_2}}\right) \tag{3.20}$$

where k_B is the Boltzmann constant, $T^\circ = 298$K, $P^\circ_{O_2} = 1$ atm is the standard temperature and pressure and:

$$\Delta\mu(T) = -\frac{1}{2}(S^\circ_{O_2} - C^\circ_p)(T - T^\circ) + C^\circ_p T \log\left(\frac{T}{T^\circ}\right) \tag{3.21}$$

comes from an ideal gas for rigid dumbbells. $C^\circ_p = 7k_B$ and $S^\circ_{O_2} = 0.0021$ eV/K are the heat capacity at constant pressure and molecular entropy of oxygen gas at standard temperature and pressure [189].

The chemical potential of the dopant μ_{dopant} is not expected to be the same value in its corresponding bulk oxide or metal. Therefore μ_{dopant} is determined to be the value that results in a predetermined total dopant concentration. This method allows dopant concentrations to be adjusted in the Brouwer diagrams. Finally, the electron chemical potential μ_e, can be obtained by imposing an overall net space charge q_{sc} on the system. This gives the relation:

$$\sum_i q_i c_i - N_c \exp\left(\frac{-(E_g - \mu_e)}{k_B T}\right) + N_v \exp\left(\frac{-\mu_e}{k_B T}\right) = q_{sc} \tag{3.22}$$

where c_i is the concentration of each of the ionic defects and N_c and N_v are the effective density of states for the valence band and the conduction band respectively. Using the Boltzmann statistics for the density of states here is reasonable as ZrO_2 is insulating [54], thus the concentration of electrons and holes are expected to be low.

Brouwer diagrams are typically constructed by imposing overall charge neutrality given that they predict equilibrium defect concentrations: this work will therefore also use $q_{sc} = 0$ by default. The difference in diffusivities of electrons and $V_O^{\bullet\bullet}$ results in a positive space charge in the middle of the oxide, for which that Couet *et al.* predict to have a concentration of around 10^{-3} e to 10^{-2} e per ZrO_2 [7]. To simulate the oxide in such conditions, a negative q_{sc} is used to allow the defects to compensate for the positive space charge.

These formation energies can then be directly related to defect concentrations through the Boltzmann distribution. This then allows us to generate Brouwer diagrams through a script developed by Murphy *et al.* [190] which implements the procedure mentioned above.

The Brouwer diagrams illustrate the concentrations of the various types defects at different oxygen partial pressure P_{O_2}, which correspond to various depths within the ZrO_2 layer, with $P_{O_2} = 1$ atm corresponding to the oxide surface. The Brouwer diagram for monoclinic ZrO_2 considering only intrinsic defects is shown as an example in Figure 3.12. Note that other than the oxide surface, no exact P_{O_2} to oxide depth correlation is known.

3.3.3 Defect properties

Binding energy

Once defects favourable in ZrO_2 have been identified, sevaral useful properties can be calculated. The first is binding energies for cluster defects, which are obtained by taking the difference between the formation energy of a cluster and the sum of the formation energies of the individual components of the cluster. For example, the binding energy of a cluster formed by defects X

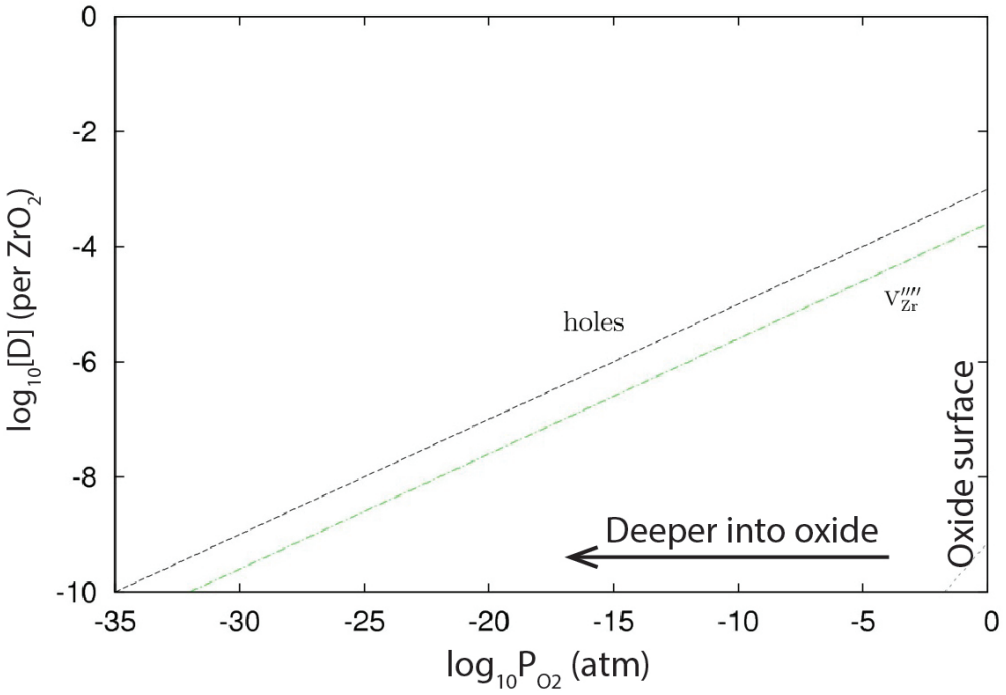


Figure 3.12: Brouwer diagram for intrinsic m-ZrO_2 (based on preliminary results) where the correspondence to oxide depth is indicated.

and Y is given by

$$E^B_{\{X:Y\}} = E^f_X + E^f_Y - E^f_{\{X:Y\}} \tag{3.23}$$

where $E^f_{\{X:Y\}}$ is the formation energy of the cluster and E^f_X and E^f_Y are the formation energies of defects X and Y respectively. Thus, positive binding energies indicate favourable clustering. Positive binding energy is a necessary though not sufficient condition if the clusters are to be apparent in the Brouwer diagrams.

Relaxation volume

Relaxation volumes allow us to consider the effects of stress on the oxide that were not included in the DFT model. It is an estimate of the change in volume of the supercell as a result of introducing a defect. The relaxation volume ΔV is calculated from:

$$\Delta V = -\frac{V}{3B}\,\mathrm{Tr}(\boldsymbol{\sigma}_{res}) \tag{3.24}$$

where V is the volume of the perfect supercell, B is the bulk modulus and $\boldsymbol{\sigma}_{res}$ is the residue stress tensor for the defect of interest. It is possible that in the real system, defects with more negative relaxation volumes could be more favourable than the Brouwer diagrams suggest due to the compressive stresses present.

It is important to note here that the relaxation volumes obtained in this method (using constant volume calculations) may not necessarily produce reliable results for charged defects. Bruneval *et al.* have linked this to the different conventions imposed on the electrostatic potential [191], thus different DFT programs can give rather different values of ΔV. For reference, CASTEP uses a zero-average convention, ensuring that the average electrostatic potential over the cell is always zero. For relevant defects, another set of relaxation volumes have been obtained using constant pressure calculations, which has been shown to agree for CASTEP and the VASP program and therefore not convention dependent [192].

It is also useful to calculate the clustering volume from the relaxation volumes to investigate the net volume change when the defects cluster. For defects X and Y, the clustering volume $\Delta V^c_{\{X:Y\}}$ is obtained from:

$$\Delta V^c_{\{X:Y\}} = \Delta V_{\{X:Y\}} - \Delta V_X - \Delta V_Y \tag{3.25}$$

Should defects show negative clustering volume then clustering will be favourable under compressive stress will contribute to the stability of these defects.

Mulliken bond population

Mulliken population analysis [184, 193, 194] was used to determine bond population between selected ion species. The analysis projects the Kohn-Sham eigenstates onto local atomic orbitals to determine the population in each orbital. Throughout this work, the atomic orbitals used as basis for the projection are the pseudo-atomic orbitals obtained from the calculation of the pseudo-potentials. However, this projection may be imperfect as the pseudo-atomic orbitals

may not necessarily form a spanning set in the function space spanned by the Kohn-Sham eigenstates. The quality of the projection can be quantified by the spilling parameter $\mathcal{S}$ defined by:

$$\mathcal{S} = \frac{1}{N} \sum_{\mathbf{k}} \sum_{i} w_{\mathbf{k}} \left\langle \phi^{KS}_{i,\mathbf{k}} \right| (1 - \hat{\mathbf{P}}_{\mathbf{k}}) \left| \phi^{KS}_{i,\mathbf{k}} \right\rangle \tag{3.26}$$

where $w_{\mathbf{k}}$ are the weights at each $\mathbf{k}$-point, N is the number of electronic bands and $\hat{\mathbf{P}}_{\mathbf{k}}$ is the projection operator given by:

$$\hat{\mathbf{P}}_{\mathbf{k}} = \sum_{i} \left| \phi^{PS}_{i,\mathbf{k}} \right\rangle \left\langle \phi^{PS}_{i,\mathbf{k}} \right| \tag{3.27}$$

A perfect projection will have $\mathcal{S} = 0$. For the structures investigated in this study, the spilling parameter for this projection was no more than 0.21%.

Chapter 4

Radiation damage in beryllium

This chapter presents the results of MD simulation of radiation damage in beryllium. Damage cascade simulations were performed at five different PKA energies from 0.5 keV to 2.5 keV at 300 K temperature as well as five different temperatures from 300 K to 1300 K at 1 keV PKA energy. The simulations used the new Be-Be potential described in Section 3.1.3 via the methodology described in Section 3.2. The PKA energy and temperature dependence of damage cascade characteristics will be discussed and compared with simulation work published by other authors. A more direct comparison with the original Björkas potential [150] is also made at 800 K to illustrate the implications of negative thermal expansion in the context of primary radiation damage.

The probabilistic threshold displacement energies (replacement events considered as a displacement) are also studied via the methodology described in Section 3.2.4. The results are then tied in with the damage cascade findings to propose a modification to the K-P damage prediction model.

The majority of the work presented in this chapter has been published in *Philosophical Magazine* [195].

4.1 Damage cascade simulations

Figure 4.1 shows examples of the general progress of damage cascades. The damage is produced primarily adjacent to the cascade backbone (identified here by the grey lines), as the PKA and other secondary knock-on atoms, decelerate though the material. This damage generation is the first (ballistic collision) phase of the radiation damage process as mentioned in Section 1.4.2. It is not necessarily that the PKA travels through the material and generates the majority of the damage, as it may impart much of its energy to another atom which then produces the damage cascade: this is shown in the first example in Figure 4.1. The damage cascades can also exhibit quite different lengths (this can be seen by comparing the third example to the other two in Figure 4.1). The branch-like structure of the damage process illustrated in Figure 4.1 is in contrast to that observed in heavier elements, where the majority of the damage is not generated along the cascade atom trajectory but forms a cascade core and shell [137, 196]. As such it is not possible to identify regions with predominantly vacancy or interstitial excess.

Figure 4.2 further supports the picture of a significant variance in damage trajectories, where there is a very large standard deviation for PKA displacement. This is also true for other PKA energies and temperatures. Figure 4.3 shows that the PKA undergoes smooth deceleration in the material before the maximum displacement is reached at around 0.1 ps. It is clear that the PKA travels further with increasing PKA energy. While the same may also appear to be true for increasing temperature, the relationship is not so clear with the average maximum PKA displacement being higher for 600 K than it is for 800 K in this work. The large variance in PKA displacement means conclusive statement cannot be made in this case.

Figures 4.4 and 4.5 shows that peak damage is reached at around 0.1 ps, which coincides closely with the time taken for the PKA to stop. Following the damage production (or ballistic) phase, a recovery phase progresses for ~ 0.9 ps, after which most of the initial displacement damage has been eliminated. Thus after ~ 1 ps, the simulation cells are left with residual damage primarily in the form of Frenkel pairs that survive the initial recovery process. Almost all of these

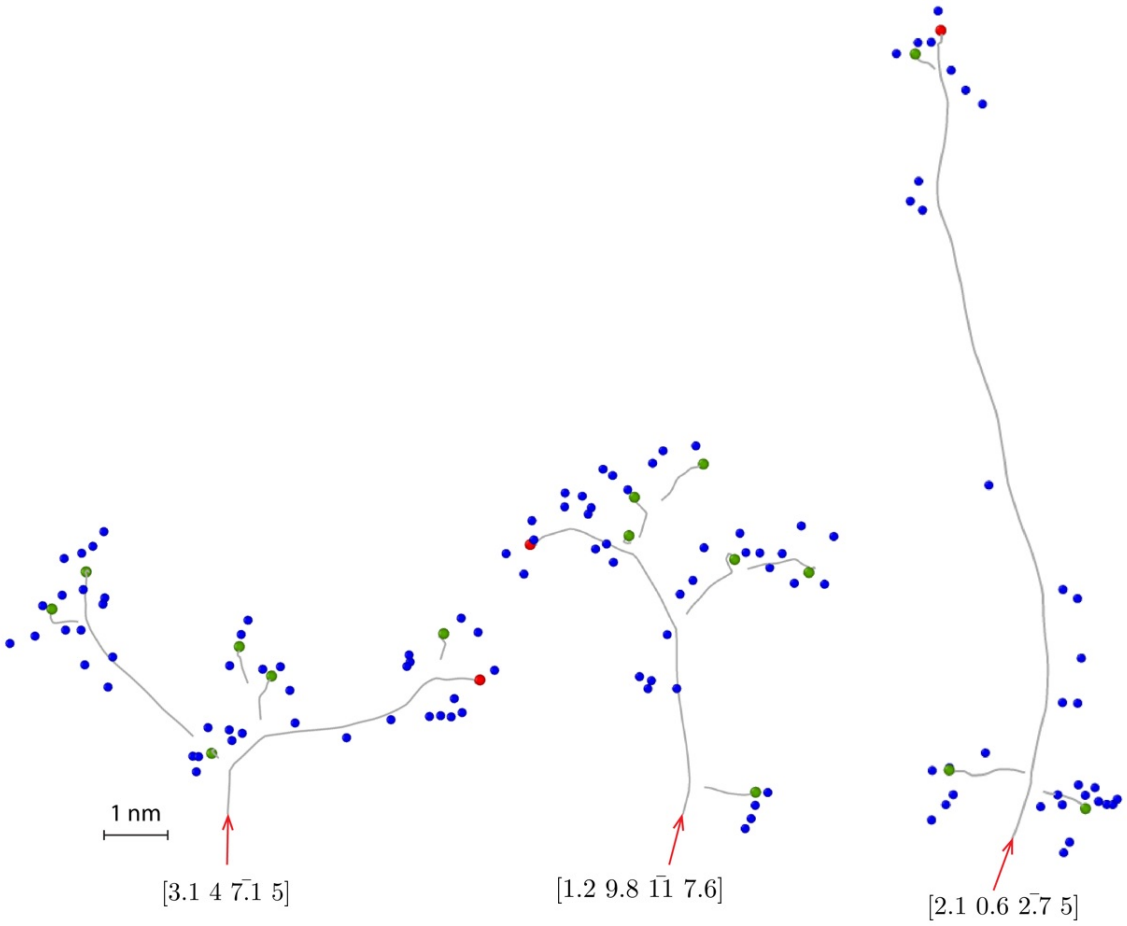


Figure 4.1: Examples of cascade trajectories from simulations at 300 K with 2 keV PKA energy after 0.12 ps. Atoms with displacements >2.4 Å are shown as blue circles, with the PKA in red. The atoms displaced >6 Å have trajectories indicated as grey lines and are highlighted green. The initial PKA direction is indicated by a red arrow and Miller index.

remain for the rest of the simulation time (i.e. out to 11.2 ps). This result is considered to be the primary radiation damage mentioned in Section 1.4.2. Note that the result for $T = 1300$ K was not presented in Figure 4.5 as the Wigner-Seitz cell method of defect identification was not reliable at such high temperatures. Comparing Figure 4.2 and Figure 4.4 for the case of 1 keV PKA and 300 K temperature as an example, the damage produced does not show as much variance despite the large variance in PKA distance. This is also true in general, as seen in Figure 4.6 and further supports the idea that it is not necessarily the PKA that directly generates the majority of the damage in the material.

Figures 4.5 and 4.6 shows that both peak damage and residual damage increase with increasing PKA energy. Conversely, while increasing temperature does show higher peak damage (despite

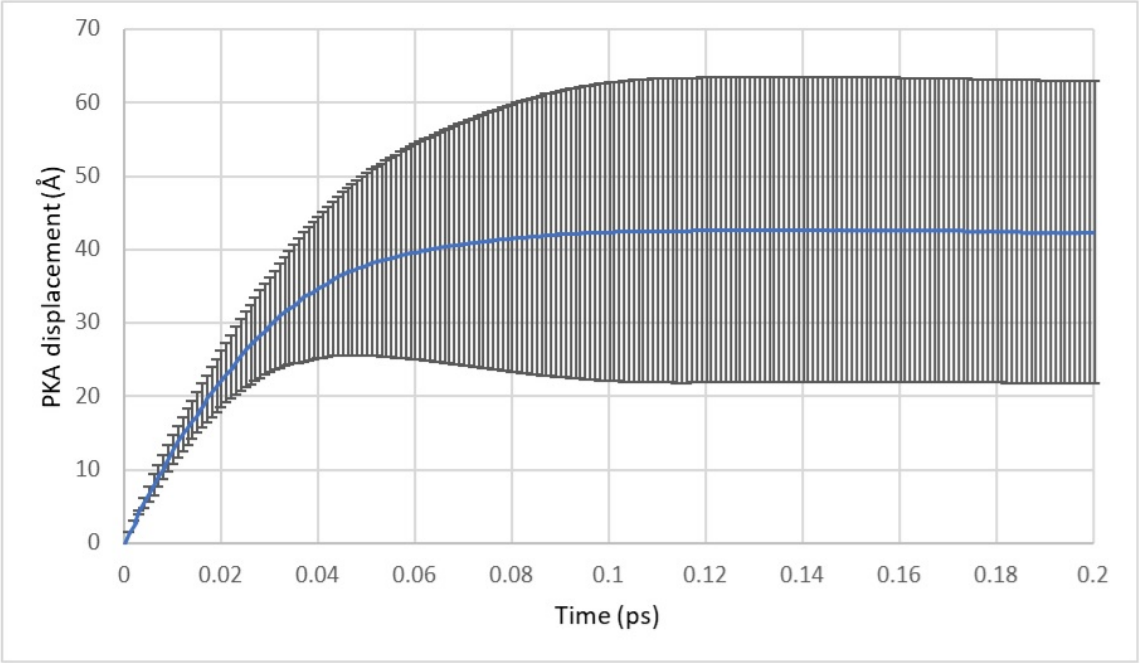


Figure 4.2: PKA displacement as a function of time first 0.2 ps, averaged over the 10 simulations carried out at 1 keV PKA energy and 300 K temperature. Error bars indicated one standard deviation.

lack of linear trend) it does not significantly increase the residual damage out to 1.2 ps. While higher temperatures mean many more atoms are displaced during the damage generation process, the degree of recovery is also greater so that higher temperatures do not lead to more residual damage.

The trends in key parameters from Figures 4.2 and 4.4 are reported in Figure 4.6, which includes the standard errors and standard deviations. For all temperatures and PKA energies, the standard error for average peak damage obtained is less than 7% while for the residual damage is less than 1 Frenkel pair. Due to the large variance, there is up to 16% standard error for maximum PKA displacement. A linear least squares fit shows a clear relationship of PKA energy with PKA displacement, peak and residual damage, whereas a linear dependence of these three parameters with simulation temperature cannot be established.

The cluster sizes of the residual defects are reported in Tables 4.1 and 4.2, where it can be seen that majority are single defects. The defect clusters are defined here as consecutive Wigner-Seitz cells (i.e. adjacent to each other) containing interstitials or vacancies. While

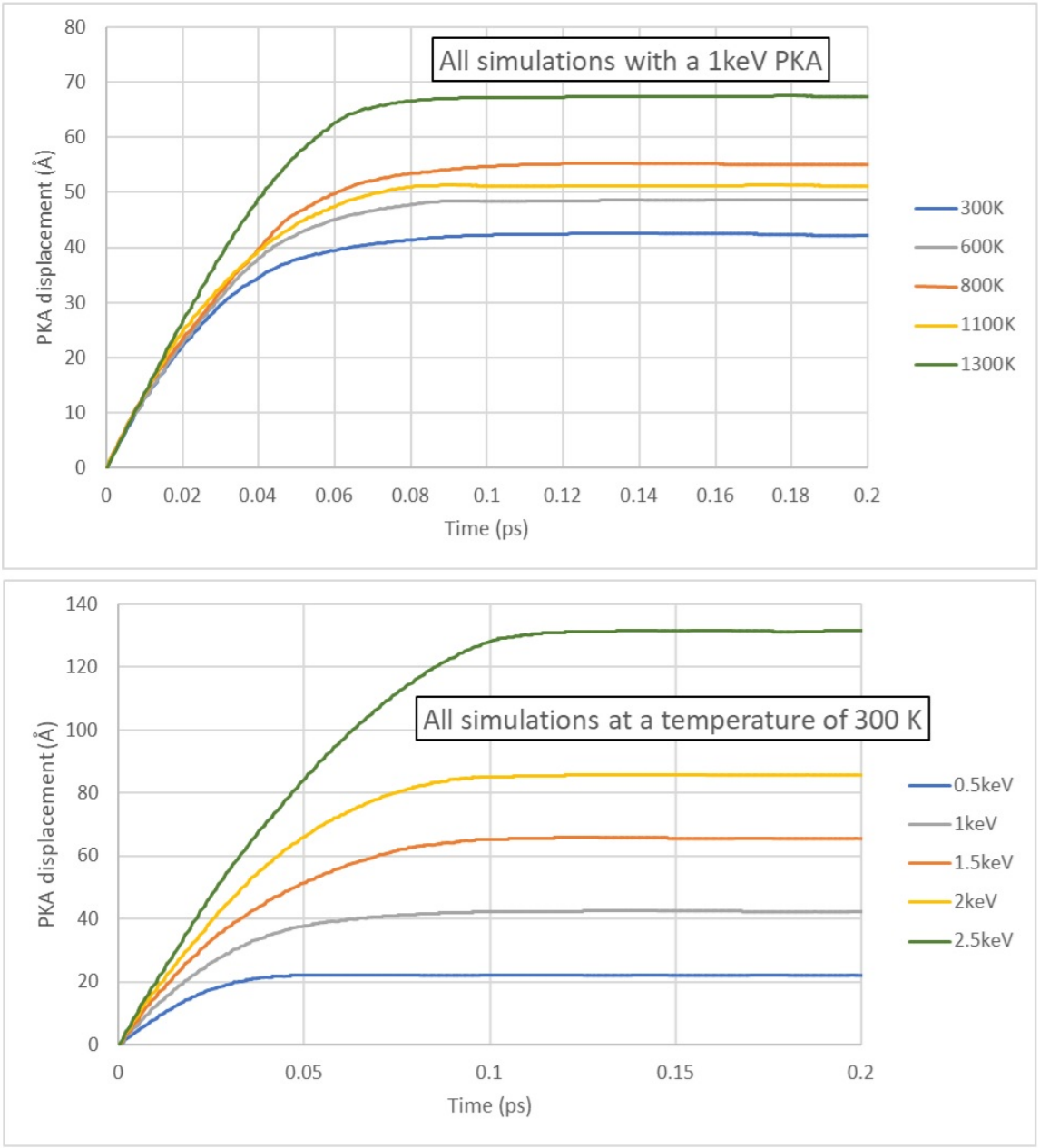


Figure 4.3: PKA displacement as a function of time first 1.2 ps, averaged over the 10 simulations carried out at a given PKA energy and temperature.

no temperature or E_{PKA} dependent trends are observed in terms of defect cluster size, vacancy clusters appear to be slightly more favourable in comparison to interstitial clusters.

In previous MD simulation work by Borodin and Vladimirov [103], E_{PKA} dependence was investigated, the overall spatial cascade structure reported is similar, though peak damage was reached only after 0.5-0.8 ps. Given that the main difference this work and the previous is the interatomic potential (previous work used the original Björkas potential [150]), it is postulated

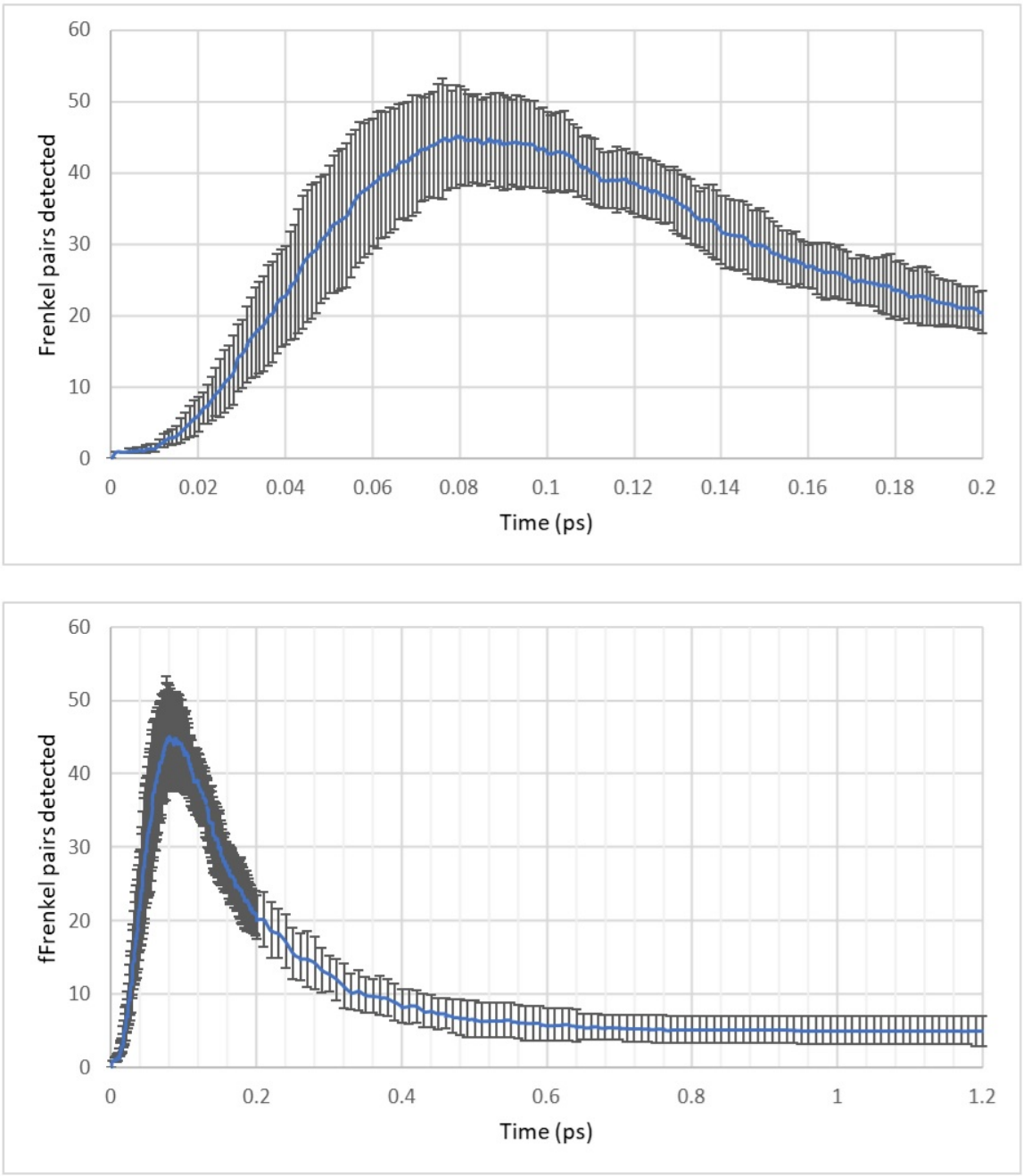


Figure 4.4: Frenkel pairs detected as a function of time first 0.2 ps and 1.2 ps, averaged over the 10 simulations carried out at 1 keV PKA energy and 300 K temperature. Error bars indicate one standard deviation.

that the underestimation of second nearest neighbour interaction due to shorter cutoff distance can result in weaker stopping power. The number of Frenkel pairs predicted after 3 ps of simulation time was around 3-4 times higher, this could be a consequence of the negative thermal expansion predicted in the potential used where the locally energetic regions around the cascade backbone undergo contraction, creating a local region of negative pressure. Defect cluster sizes

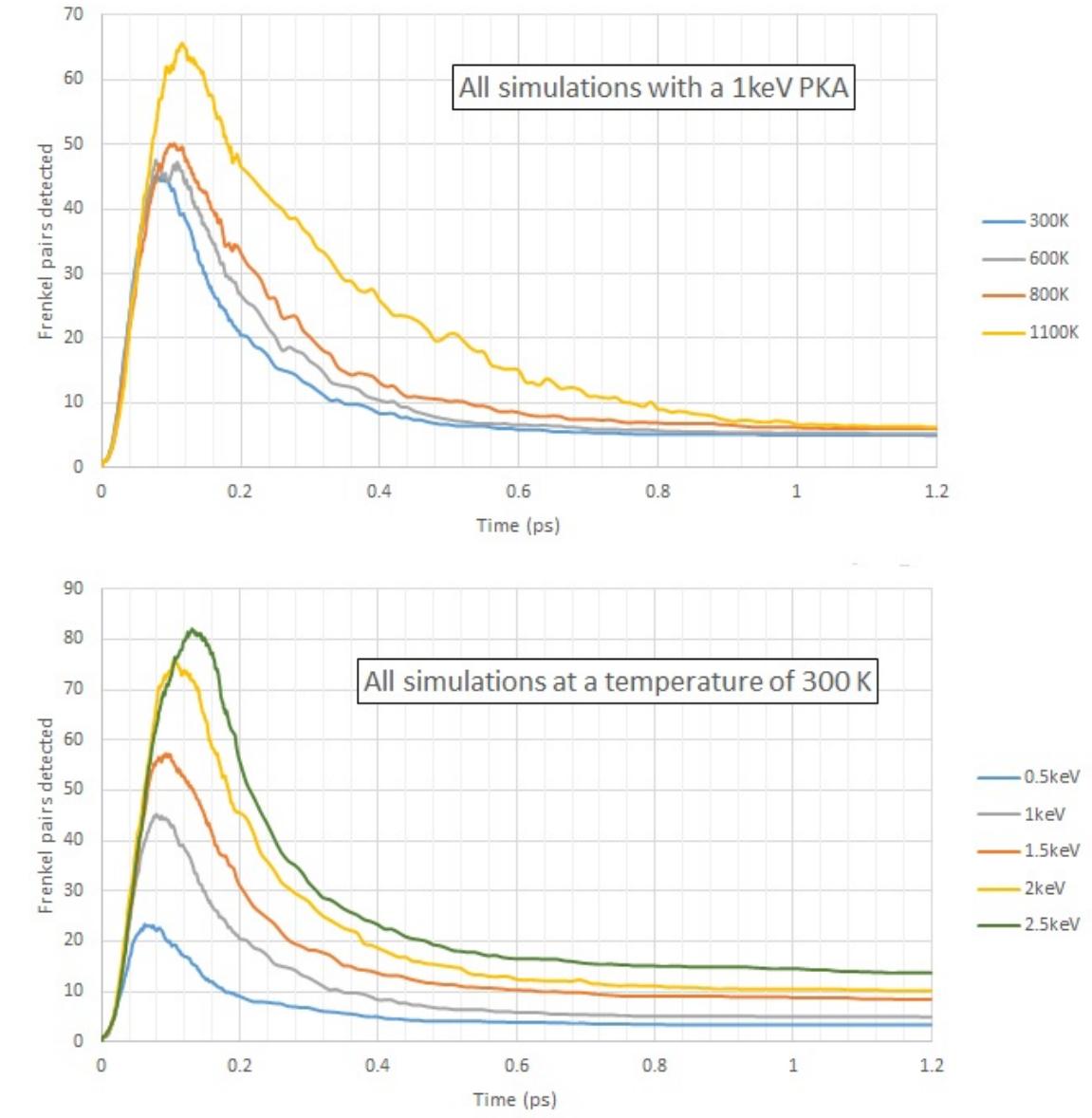


Figure 4.5: The damage identified as the simulations progress over the first 1.2 ps, averaged over the 10 simulations carried out at a given PKA energy and temperature.

reported were similar, as well as the preference of vacancy to interstitial clusters [103].

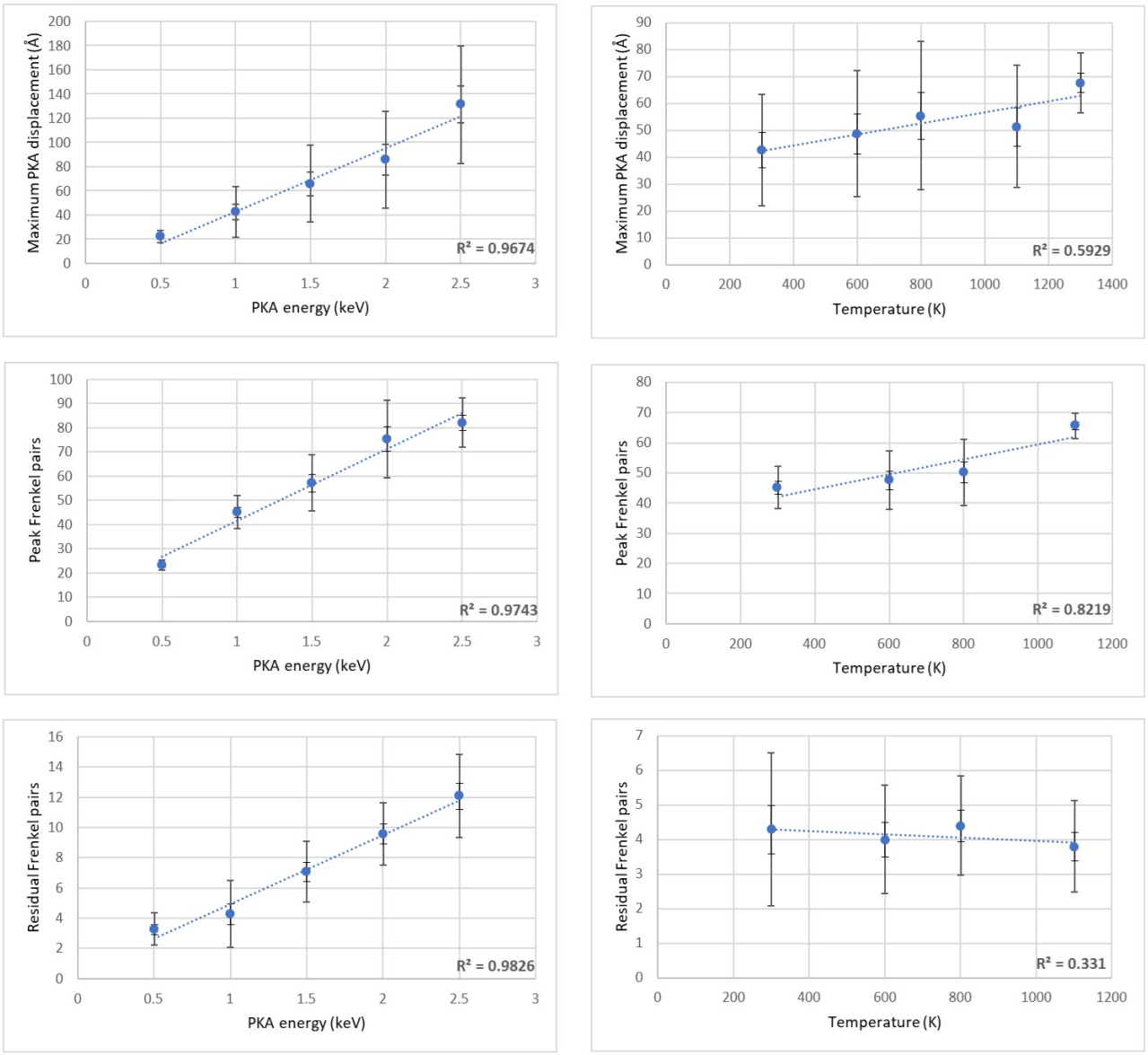


Figure 4.6: Some key parameters of the damage cascade (namely maximum PKA displacement, peak damage and residual damage) as a function of PKA energy and temperature. Values are averaged over 10 simulations. The inner markings on the error bars indicate the standard error while the outer markings indicate one standard deviation. The R^2 value for a linear least squares fit (not weighted to errors) is also indicated.

The equilibrium concentration of Frenkel pairs at $T = 1100$ K, given by $e^{-\Delta H_f/2k_BT}$, where k_B is Boltzmann's constant, is one in 5.86×10^{13} atoms. This value will be even lower for lower temperatures. The equilibrium value is predicted by calculating the dilute limit Frenkel formation energy ΔH_f using the potential developed in this study. The value 6.01 eV for Frenkel pairs involving an interstitial in the basal trigonal site was calculated in Section 3.1.3. The post-damage residual Frenkel defect concentration is much higher than the predicted equilibrium concentration, even at the highest simulation temperature. Even when considering that each

Table 4.1: Proportion of defects in respective cluster sizes identified for varying PKA energy at 300 K. nV and nI indicate clusters of n vacancies and n interstitials respectively.

E_{PKA} (keV)	V	I	2V	2I	3V	3I	4V
0.5	0.33	0.32	0.12	0.18	0.05	0	0
1.0	0.36	0.41	0.05	0.09	0.04	0	0.05
1.5	0.39	0.44	0.09	0.06	0.02	0	0
2.0	0.35	0.37	0.11	0.13	0.03	0	0.01
2.5	0.36	0.41	0.09	0.09	0.03	0	0.02

Table 4.2: Proportion of defects in respective cluster sizes identified for varying simulation temperature with 1 keV PKA energy. nV and nI indicate clusters of n vacancies and n interstitials respectively.

Temperature (K)	V	I	2V	2I	3V	3I	4V
300	0.36	0.41	0.05	0.09	0.04	0	0.05
600	0.38	0.47	0.08	0.03	0.04	0	0
800	0.39	0.36	0.04	0.11	0.03	0.03	0.04
1100	0.37	0.42	0.05	0.08	0.08	0	0

simulation cell only contains a single event, the concentration of residual defects in the cell volume for a 2 keV PKA at 1100 K is approximately one Frenkel pair in 10^5 atoms. Thus, further thermally activated recovery will happen at timescales much longer than the current simulations, though it will be complicated by further radiation damage processes which may promote cluster formation.

4.1.1 Threshold displacement

Section 3.2.4 described the computational approach to calculating the directionally averaged probability of displacement as a function of PKA energy. This yields a cut-off value for E_d, at and below which, the probability of displacement is zero, (i.e. $E_d^P = E_d^{0.0}$). Higher energies have higher probability for displacement (e.g. $E_d^P = E_d^{0.5}$ is the PKA energy at which the probability of displacement is 50%). Threshold displacement in the $0-0.2$ keV energy range was simulated and the directionally dependent threshold displacement energies are presented in Figure 4.7. The directional dependence agrees well with previous work by Jackson *et al.* [114] that used an EAM potential, though the $E_d^{0.0}$ and $E_d^{0.5}$ values predicted here are significantly lower. The E_d

values are lower around the nearest neighbour directions as expected. Threshold displacement in beryllium has also been studied with the original Björkas potential [150] which also showed similar directional dependence [197]. The same work predicted significantly lower directionally averaged E_d values in MD simulations and also predicted DFT simulations that suggested the E_d values to be higher [197]. The E_d values predicted in this work lie between the two previous MD predictions [114, 197], more in line with what was suggested in DFT results [197].

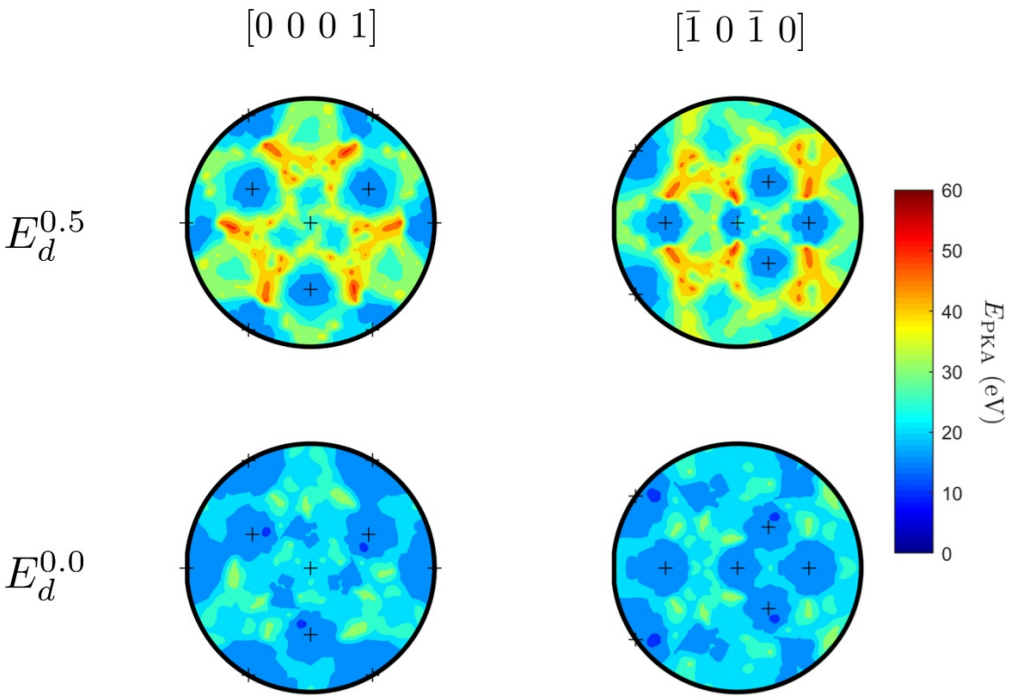


Figure 4.7: $E_d^{0.0}$ and $E_d^{0.5}$ as a function of PKA direction at 300 K plot using stereographic projection on the [0 0 0 1] and [$\bar{1}$ 0 $\bar{1}$ 0] direction. The '+' symbols indicate nearest neighbour positions.

Figure 4.8 reports the directionally averaged final displacements as a function of energy, with critical energies indicated. Jackson *et al.* [114] proposed two separate models for predicting average PKA displacements at energies just above $E_d^{0.0}$. The models are based on Newtonian mechanics with either a momentum dependent or a kinetic energy dependent drag coefficient. The respective equations of motion (for PKA displacement x, valid only for $E_{PKA} > E_d^{0.0}$) are written as:

$$m\frac{\mathrm{d}^2x}{\mathrm{d}t^2} + \alpha m\frac{\mathrm{d}x}{\mathrm{d}t} = 0 \tag{4.1}$$

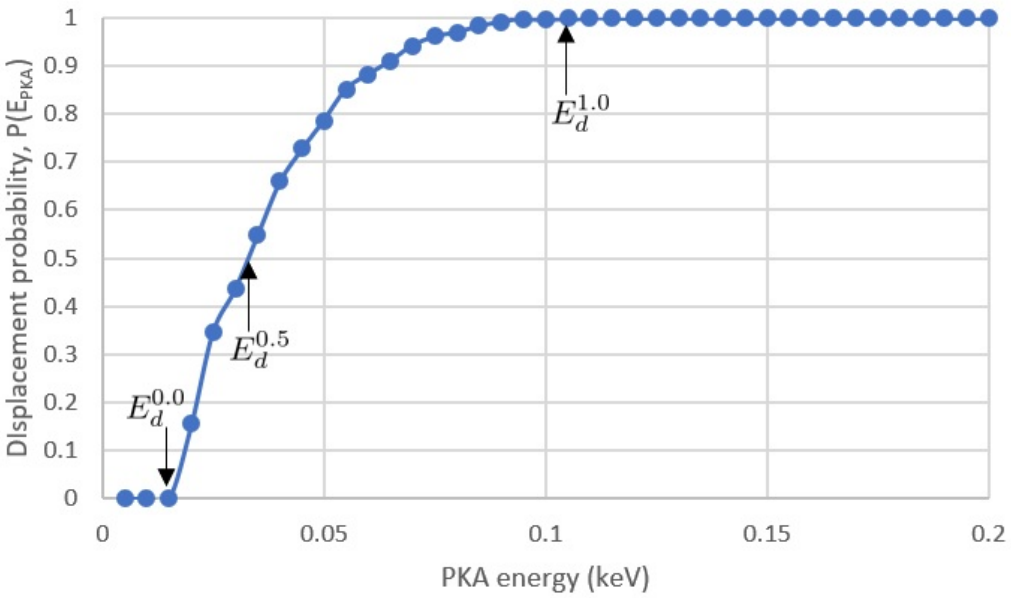


Figure 4.8: The probability for displacement $P(E_{PKA})$ as a function of PKA energy at 300 K. Points marked E_d^P are the minimum energies at which the directionally averaged probability of displacement is P, except for $E_d^{0.0}$, which is the maximum energy with no probability of displacement.

and

$$m\frac{\mathrm{d}^2x}{\mathrm{d}t^2} + \beta\frac{m}{2}\left(\frac{\mathrm{d}x}{\mathrm{d}t}\right)^2 = 0 \tag{4.2}$$

respectively, where m is the mass of the PKA while α and β are drag coefficients. Imposing the initial boundary conditions (at $t = 0$) $\left.\frac{\mathrm{d}x}{\mathrm{d}t}\right|_{t=0} = \sqrt{\frac{2E_{PKA}}{m}}$ and $x(0) = x_0$, the solutions are:

$$x(t) = \frac{1}{\alpha}\sqrt{\frac{2E_{PKA}}{m}}(1 - e^{-\alpha t}) + x_0 \tag{4.3}$$

and

$$x(t) = \frac{2}{\beta}\ln\left(\frac{t+\gamma}{\gamma}\right) + x_0, \qquad \text{where} \quad \gamma = \frac{2}{\beta}\sqrt{\frac{m}{2E_{PKA}}} \tag{4.4}$$

respectively. x_0 is associated with the non-zero displacement resulting from thermal vibrations at the lattice site. The final displacements of the PKA can be obtained in the limit $t \to \infty$, for which only Equation (4.3) has a finite solution:

$$\lim_{t\to\infty} x(t) = \frac{1}{\alpha}\sqrt{\frac{2E_{PKA}}{m}} + x_0 \tag{4.5}$$

This solution can be related to the stopping power $S(E)$, for $E_{PKA} > E_d^{0.0}$ via:

$$\frac{1}{\alpha}\sqrt{\frac{2E_{PKA}}{m}} + x_0 = \int_0^{E_{PKA}} \frac{1}{S(E)}\,\mathrm{d}E \tag{4.6}$$

In Figure 4.9 the simulation results are fitted (in the least squares sense) to Equation (4.5) to obtain $\alpha = 0.073$ fs^{-1} and $x_0 = -1.97$ Å. The negative value for x_0 is unexpected and in fact, requiring x_0 to be positive will not result in a good fit. A possible interpretation is that significant energy is lost from the initial displacement from the lattice site, but beyond that, the model appears to be a good fit for PKA displacement. This idea can be further investigated

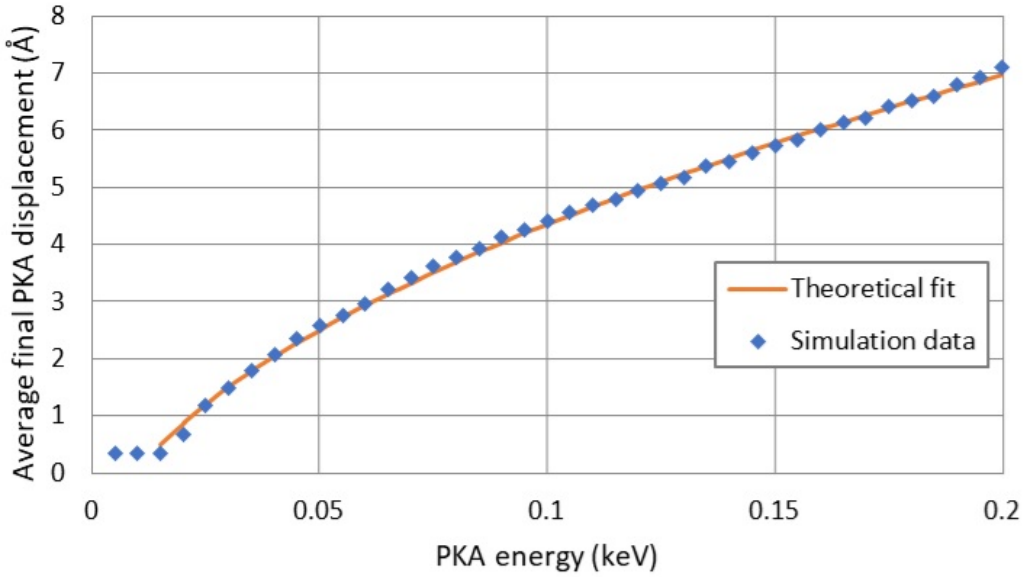


Figure 4.9: The probability for displacement $P(E_{PKA})$ as a function of PKA energy at 300 K, with a theoretical fit using Equation (4.3) with values $\alpha = 0.073$ fs^{-1} and $x_0 = -1.97$ Å.

by replacing E_{PKA} with $E_{PKA} - E_d$ in Equation (4.5) to obtain a new fitting equation:

$$\lim_{t\to\infty} x(t) = \frac{1}{\alpha}\sqrt{\frac{2(E_{PKA} - E_d)}{m}} + x_0 \tag{4.7}$$

where E_d here is meant to quantify the energy loss from initial displacement from lattice site. Even with the maximum possible value of $E_d = E_d^{0.0}$ (higher E_d values will start resulting in complex values in the $E_{PKA} > E_d^{0.0}$ range for which the fitting equation is mean to be valid for) the optimised fitting parameters are $\alpha = 0.086$ fs^{-1} and $x_0 = -0.49$ Å. The fitted x_0 value is still negative here, suggesting that on average, it requires more than $E_{PKA} = E_d^{0.0}$ (of additional

energy, on top of the thermal energy of the PKA) to displace the PKA from its lattice site. This is consistent with how the $E_d^{0.0}$ value is derived. This also further illustrates that E_d is not meant to be a singular value. Modelling equations such as Equations (4.1) and (4.2) should therefore be able to incorporate the probabilistic definition of E_d in order to accurately predict results in the $E_d^{0.0} < E_{PKA} < E_d^{1.0}$.

4.2 Temperature dependence of residual defects

This section analyses the prediction that there is no temperature dependence of the residual defects reported in Section 4.1, which can be understood by analysing the peak damage and recovery phases of the cascade process. Figure 4.10 shows a 5-atom thick slice of an example

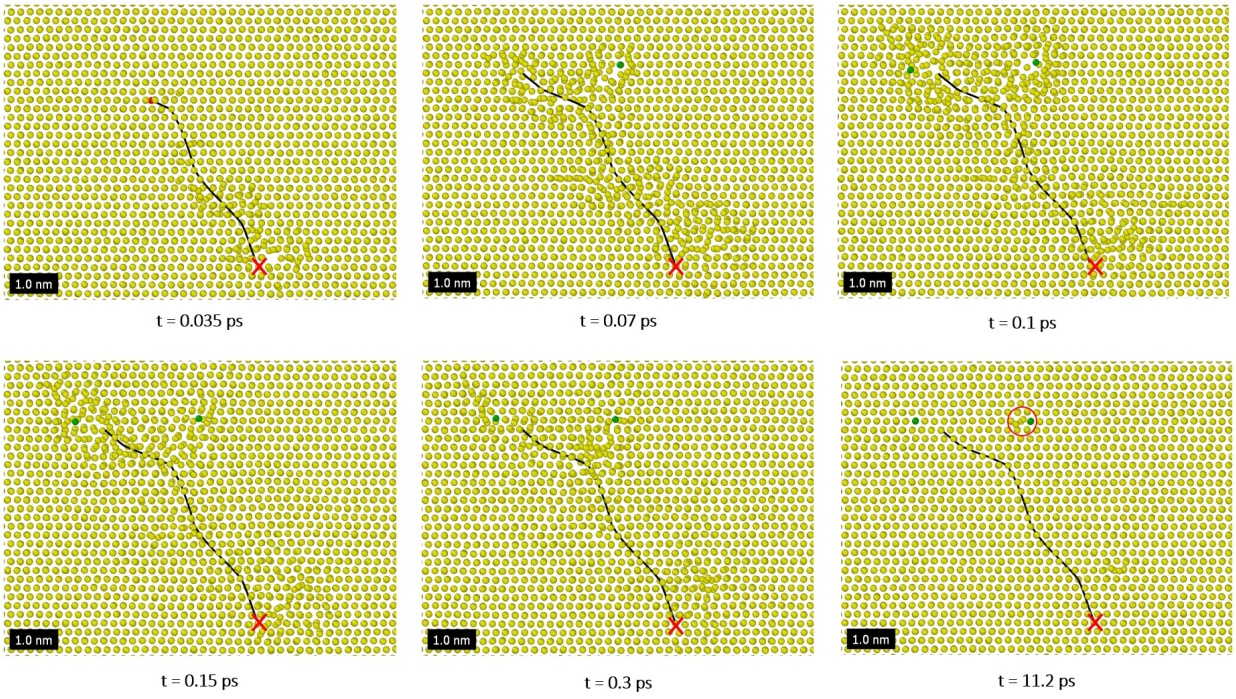


Figure 4.10: Timelapse series showing the progression of a 1.5 keV PKA fired in the *c*-direction in a 5-atom thick slice of the simulation box in the (1 0 0) orientation at 300 K. The PKA is coloured red while secondary atoms displaced > 6 Å are indicated in green. The red cross marks a reference position where the PKA first entered the slice, with the black line indicating its trajectory. The red circle in the final snapshot highlights a residual defect associated with a secondary atom displaced > 6 Å.

simulation region at different times as the damage cascade progresses. It can be seen that during the damage production phase (which occurs roughly within the first picosecond), the PKA

produces a highly disordered region along its path, which contributes to the initial damage recorded in Figure 4.5. This dynamic region only exists for a short time while it equilibrates with the lattice. Thus, as time progresses, the disordered region is largely restored to the perfect lattice. It should be remembered that locally, in the region immediately around the PKA trajectory, there are roughly as many displaced atoms as there are vacancies to fill, and that the species that should fill these vacancies and the interstitial atoms are identical in a pure material.

It is observed in Figure 4.5 that the time taken for recovery increases with temperature, this is consistent with both there being a larger disordered region generated at a higher temperature and a slightly longer time to reach peak damage. Figure 4.10 also shows the damage production significantly lagging behind the PKA, which is related to the evolution of the branch-like cascade structure predicted for this material.

It is postulated that what remains as residual defects after the recovery process are a result of a few atoms being imparted with enough energy to escape the local disordered region. This is supported by Figure 4.11c, which shows that increasing temperature does not give rise to significantly more highly displaced atoms (here defined as atoms displaced > 6 Å throughout the simulation). These atoms are the ones that are more likely to be able to escape the local disordered region during the damage production process. Moreover, the higher peak damage at higher temperature (Figures 4.5 and 4.11a) can be attributed to a larger disordered region, which recovers readily. A larger disordered region may also mean that secondary atoms have to be displaced further to escape the region. The prediction in Figure 4.11e that the number of atoms displaced > 6 Å as a percentage of the total displaced (i.e. from Figures 4.11a and 4.11c), decreases with increasing temperature, is consistent with this view.

The weak dependence of residual defects on temperature has also been observed in MD simulations of α-Fe [198] and Ni_3Al [199] despite these materials being known to not have the same branch-like cascade structure. In fact, a very similar mechanism has been proposed for materials that exhibit a single centralised cascade core. Referring to Figure 4.12, Nordlund *et*

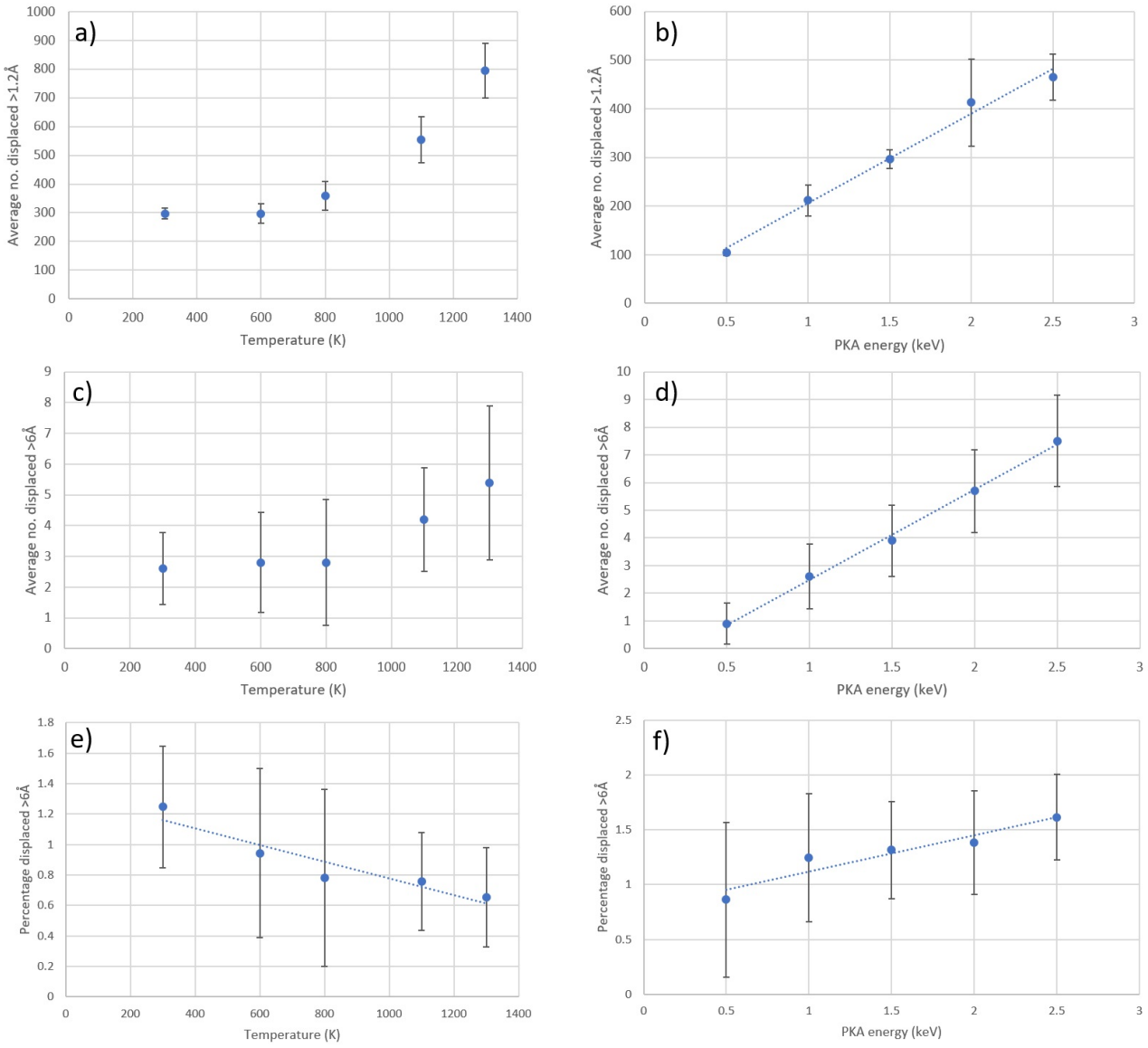


Figure 4.11: a) - d), Graphs detailing the number of atoms (not including the PKA) that have ever been displaced (taken as > 1.2 Å) and atoms that have ever been highly displaced (defined here as > 6 Å) throughout the 11.2 ps simulation time. The error bars indicate one standard deviation, calculated by averaging the 10 simulation conducted for each PKA energy at the specified temperature. e) and f), the percentage of atoms that ever displaced > 6 Å.

al. [134] suggested the picture of a hot cascade core of radius R, with a peripheral region of thickness L. Only defects in this peripheral region survive the initial recovery phase. The fact that R increases with temperature means that there is a smaller proportion of defects in the peripheral region, which is essentially what is observed in Figure 4.11e. It is therefore very likely that the same mechanisms are in play: with increasing temperature, increasing number of highly displaced atoms as well as a larger disordered region, secondary atoms will have to escape further to form residual damage, resulting in the weak temperature dependence of resid-

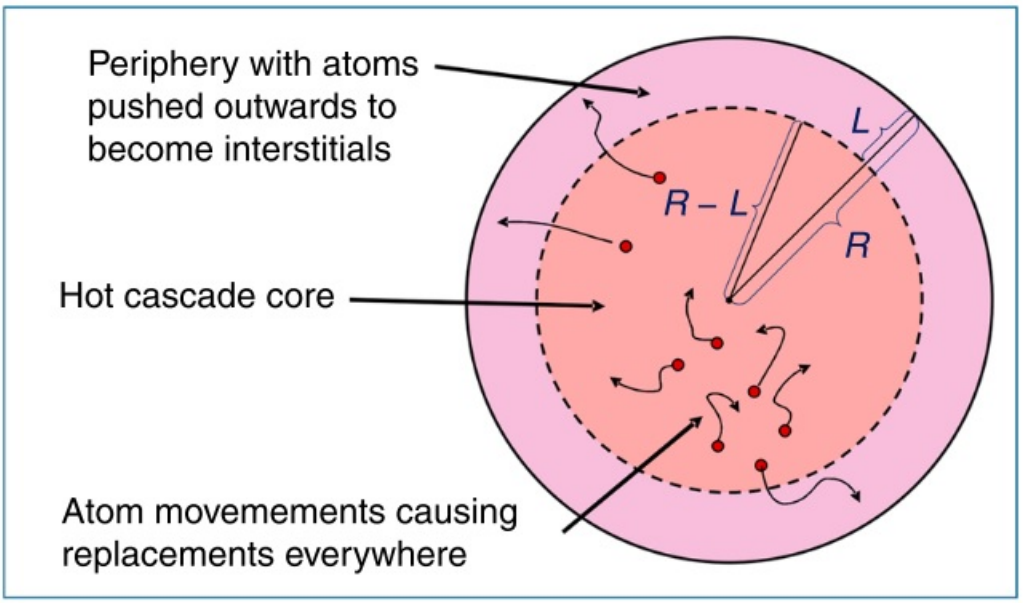


Figure 4.12: Mechanism for defects surviving the thermal spike recovery phase. Reproduced from [134]. In this diagram the PKA moves directly into (or out of) the plane. A hot cascade region with radius R is produced along the PKA trajectory which recrystallises after the thermal spike phase. Atoms that are pushed beyond the cascade core avoid the recrystallisation process and result in the formation of interstitials.

ual defect numbers. Further, the core and peripheral regions described in Figure 4.12 need not be of a spherical shape, but can also follow the backbone of a branch-like damage cascade trajectory.

Turning now to displacement as a function of PKA energy at a target temperature of 300 K, with the increase of PKA energy, the proportion of highly displaced atoms increases (see Figure 4.11f). This is driven by the increase in the number of residual defects observed in Figure 4.5 and shown in Figure 4.11d. The results suggest that for pure beryllium, subject to radiation damage, a high operating temperature may be advantageous because, while damage cascade processes will not generate more residual defects, the long time scale ($\gg 10^{-12}$ s) thermally activated recovery of these defects will be more efficient. Of course, higher temperatures also offer the possibility for defects to coalesce into voids and interstitial loops, which are deleterious to materials performance [200, 201]. The balance between the two opposing effects can be investigated via longer timescale simulations such as Accelerated MD and Kinetic Monte Carlo with the knowledge that defect generation in primary radiation damage is not dependent on

temperature, as demonstrated in this work.

4.3 Further comparison with original potential

Borodin and Vladimirov's work [103] using the original Björkas potential [150] was performed at 300 K and included a friction term to account for electronic stopping. This section will compare results derived using the new potential (developed for this thesis) to results derived using the original potential [150], with both sets of results at 800 K. The results for the original potential presented in this section are generated with the same methodology described in Section 3.2 (the simulations averaged over the same 10 PKA directions). 800 K is in the negative thermal expansion range of the original potential and thus can provide useful insights into the implications of using a potential with this erroneous property. Breeder blankets in some reactor designs, as mentioned in Section 1.1.2, can also be expected to reach such temperatures [97,202].

Figures 4.13 and 4.14 shows that with the original potential, the PKA takes a much longer time reach maximum displacement (roughly 0.3 ps versus 0.1 ps from the new potential), as well as travelling twice as far (113 Å versus 56 Å). The higher PKA displacement is likely due to the lack of second neighbour interaction in the original potential (as explained in Section 4.1). The original potential exhibits a larger percentage PKA displacement variance as compared to the new potential (68% vs 50%) as shown in Figure 4.14. In fact, the percentage PKA displacement variance for all temperatures and PKA displacements considered for the new potential in this thesis do not exceed 50%.

Interestingly, the damage production curves reported in Figures 4.13 and 4.15 does not reflect the difference in peak PKA displacement timing. The number of Frenkel pairs detected peaks much earlier with a rather flat peak, at around 0.1 to 0.16 ps simulation time. This is far shorter than the peak damage time of around 0.5-0.8 ps reported by Borodin and Vladimirov at 300 K [103], which is surprising given the additional friction term they used. The flat peaks in Figures 4.13 and 4.15 appear to be due to the disordered (thermal spike) regions produced

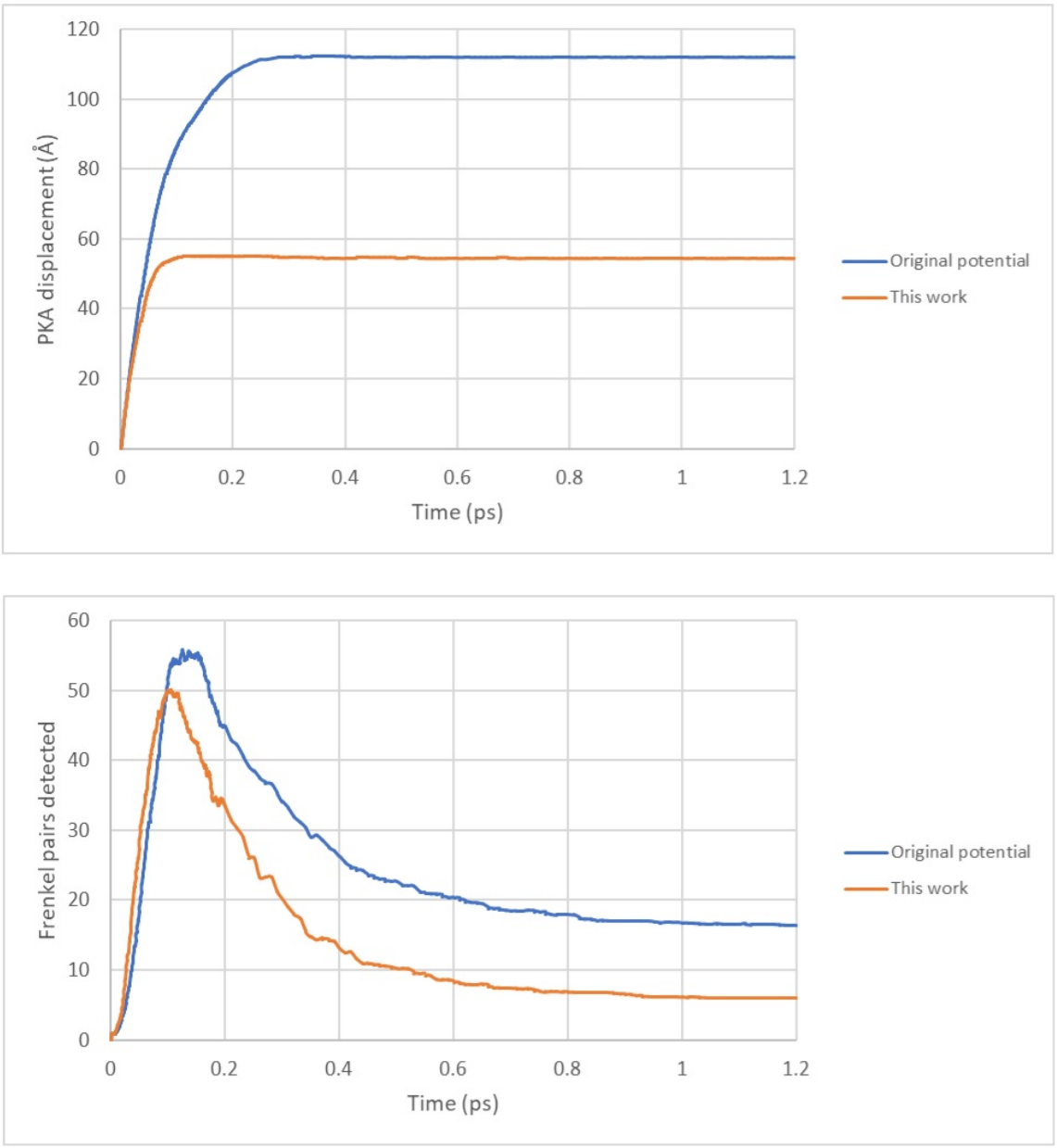


Figure 4.13: Comparison of PKA displacement and Frenkel pairs detected over the first 1.2 ps of simulation time (averaged over 10 simulations) between the original Björkas potential [150] and this work at 1 keV PKA energy and 800 K temperature.

at the earlier sections of the damage cascade recovering before the end of the ballistic phase. In fact, the disordered regions produced in both potentials show significant recovery after about 1 ps (see Figure 4.10).

While the peak damage produced with the original potential is not much higher than with the new potential, the standard deviation is twice as high. Further, defect recovery is not as efficient, with an average of 14.2 residual defects in contrast to only 4.4 at the end of simulation

time with the new potential. This mirrors the prediction by Borodin and Vladimirov at 300 K and is a possible consequence of the negative thermal expansion in the original potential (as explained in Section 4.1).

Finally, the comparison of cluster sizes of residual defects are reported in Table 4.3. While majority of the residual defects in the original potential are still single defects, there is a significant preference for the formation of vacancy clusters to interstitial clusters. In contrast, the new potential does not show any preference for either cluster type. Even when considering results in Tables 4.1 and 4.2, the preference for vacancy clusters does not compare to the original potential.

Table 4.3: Proportion of residual defects in respective cluster sizes identified at 800 K temperature 1 keV PKA energy for the original Björkas potential [150] and the new potential. nV and nI indicate clusters of n vacancies and n interstitials respectively.

	V	I	2V	2I	3V	3I	4V
This work	0.39	0.36	0.04	0.11	0.03	0.03	0.04
Björkas *et al.*	0.25	0.45	0.18	0.05	0.07	0	0

4.4 Revisiting the Kinchin-Pease model

The prediction that residual damage is largely independent of temperature (explained in Section 4.2) supports the use of simple radiation damage models such as Kinchin-Pease (K-P) [132] and Norgett-Robinson-Torrens (NRT) [133]. Such models predict that for PKA energies above twice the threshold displacement energy E_d, the PKA energy and damage produced follow a linear relationship, under the assumption of temperature independence. Thus, for K-P, given a PKA energy of E_{PKA}, for $E_{PKA} > 2E_d$, the number of Frenkel pairs produced, N_{FP} is

$$N_{FP} = \frac{E_{PKA}}{2E_d} \tag{4.8}$$

The number of Frenkel pairs may be fractional and should be regarded as an average value across multiple events. The current MD damage simulations follow this relationship (see Figures 4.11b and 4.11f). Translating these values to a K-P model, as presented in Figure 4.16, our simulations provide upper (peak maximum damage) and lower (residual damage) lines. Predictions made using the K-P model, however, require a value for E_d. The results presented in Section 4.1.1 allow E_d to be extended to the probabilistic value E_d^P. From Figure 4.8 the values $E_d^{0.0} = 15$ eV and $E_d^{1.0} = 105$ eV are obtained.

In Figure 4.16 there are three K-P lines predicted using equation 4.8. The top line corresponds to $E_d^{0.0}$ while the bottom line $E_d^{1.0}$. The middle is for an E_d value of 25 eV, which is the default value used in the Monte-Carlo binary collision code SRIM [140]. Both the SRIM default value and $E_d^{0.0}$ predictions yield damage predictions significantly higher than the residual damage line. This has been noted in previous work [203]. However, the peak damage line is close to the $E_d^{0.0}$ line.

Considering now the K-P prediction line corresponding to $E_d^{1.0}$, this passes through the residual defect values predicted by the MD damage cascade simulations. While more studies are required on a variety of systems, it may be that $E_d^{1.0}$ via the K-P prediction yield a useful approximation of the residual defects from an MD damage cascade.

For $E_d < E_{PKA} < 2E_d$, the K-P model states that a single Frenkel pair will be created and if $E_{PKA} < E_d$, none are formed; this is illustrated in Figure 4.17. Given the results in Figure 4.8 it is possible to replace the K-P model with one that takes into account the probability of displacement $P(E_{PKA})$. The attempt at modelling final PKA displacement in Section 4.1.1 also highlighted the importance of taking into account the probabilistic nature of E_d. In this new proposed model, the expected number of Frenkel pairs produced is $\frac{E_{PKA}}{2E_d^{1.0}}$ given that the PKA is displaced. Expressed mathematically, for any E_{PKA}:

$$N_{FP} = \frac{P(E_{PKA})E_{PKA}}{2E_d^{1.0}} \tag{4.9}$$

Note that $P(E_{PKA}) = 1$ when $E_{PKA} \geqslant E_d^{1.0}$, which ensures that when $E_{PKA} > 2E_d^{1.0}$, the original K-P linear relationship between E_{PKA} and N_{FP} is resumed. Using $P(E_{PKA})$, the original piecewise K-P model is joined into a single smooth function.

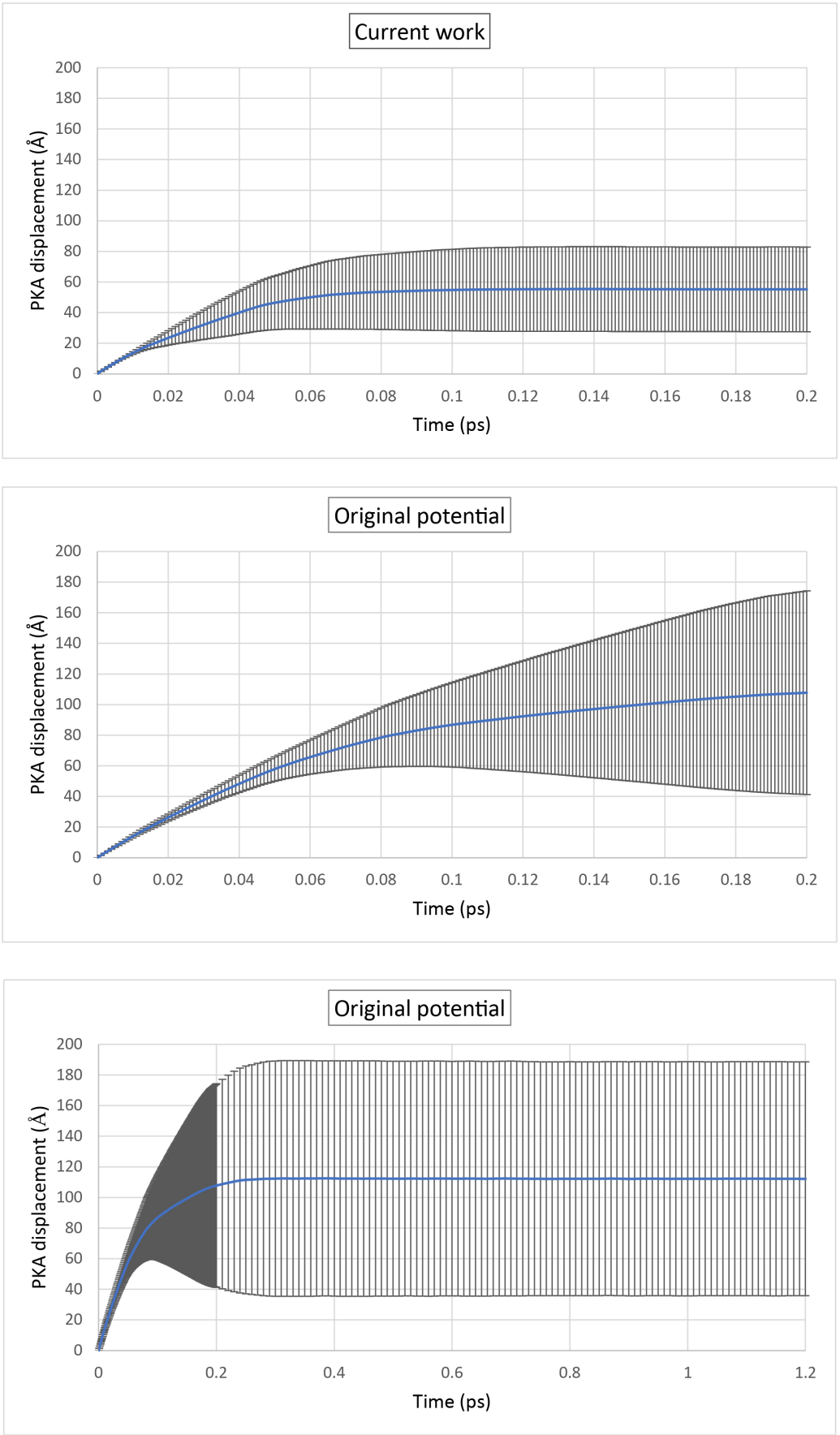


Figure 4.14: Comparison of PKA displacement over the first 0.2 ps and 1.2 ps of simulation time (averaged over 10 simulations) between the original Björkas potential [150] and this work at 1 keV PKA energy and 800 K temperature. Error bars indicate one standard deviation.

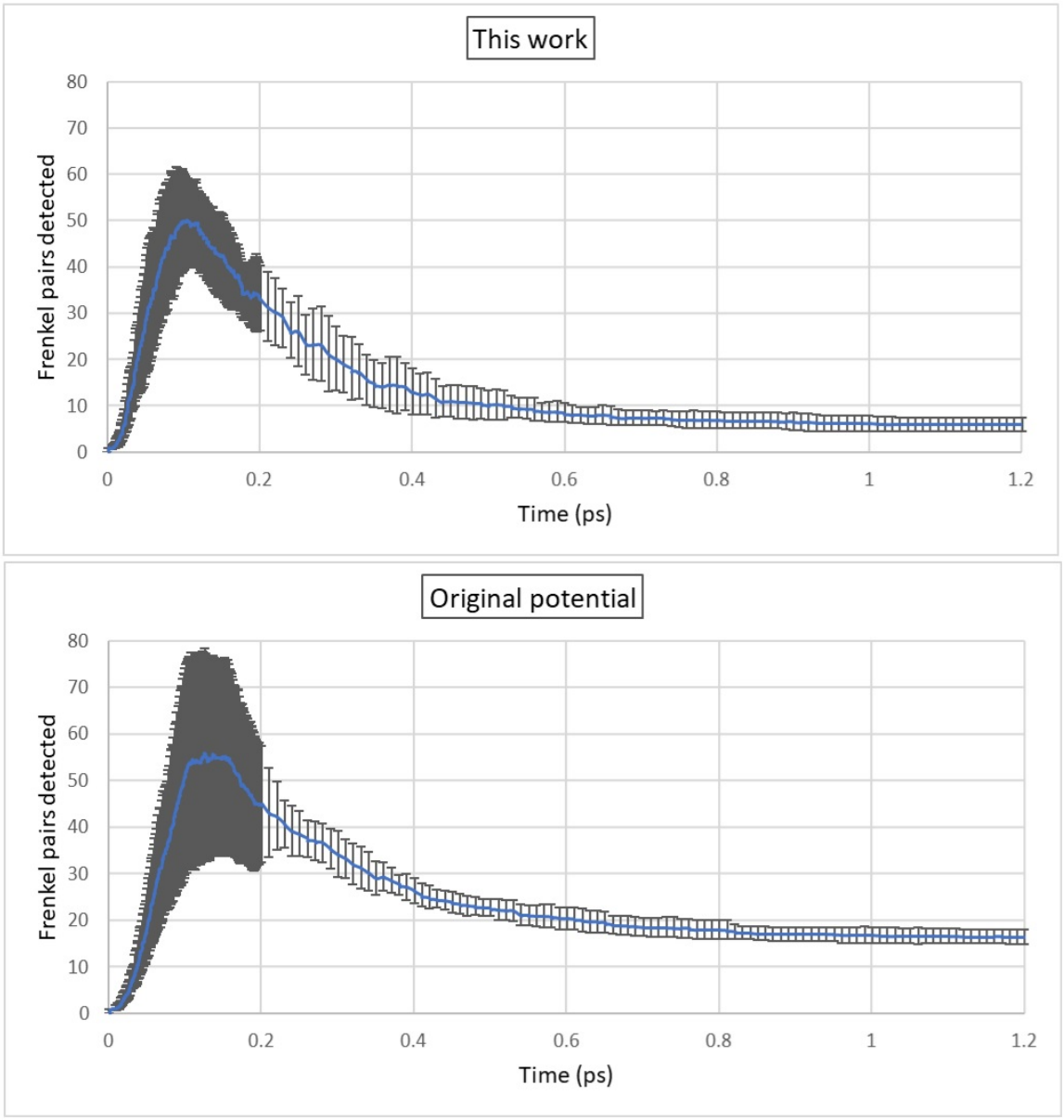


Figure 4.15: Comparison of Frenkel pairs detected over the first 1.2 ps of simulation time (averaged over 10 simulations) between the original Björkas potential [150] and this work at 1 keV PKA energy and 800 K temperature. Error bars indicate one standard deviation.

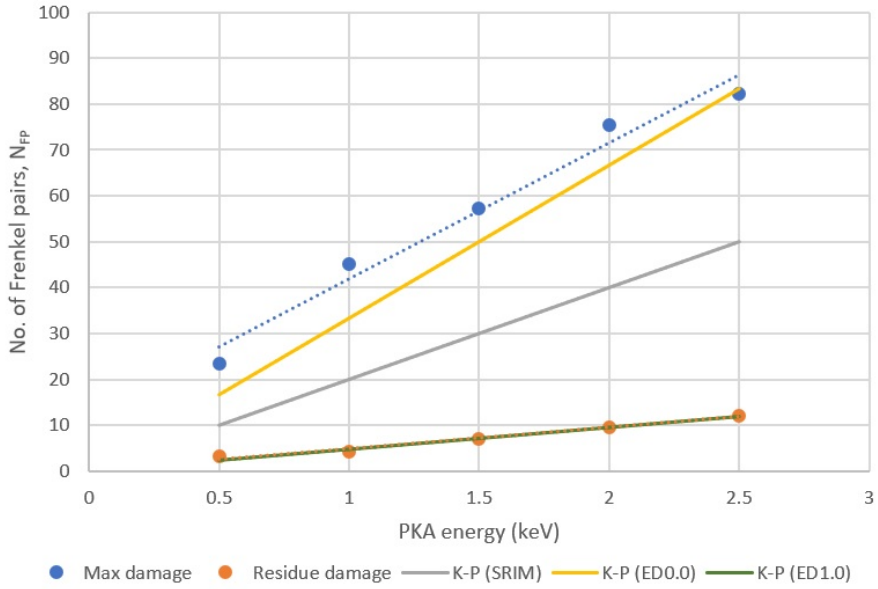


Figure 4.16: MD predicted maximum and residual damage as a function of PKA energy at 300 K. Also shown are predictions using the K-P model assuming a threshold displacement energy of 25 eV [140] as well as 15 eV and 105 eV corresponding to $E_d^{0.0}$ and $E_d^{1.0}$ values calculated using the current potential model.

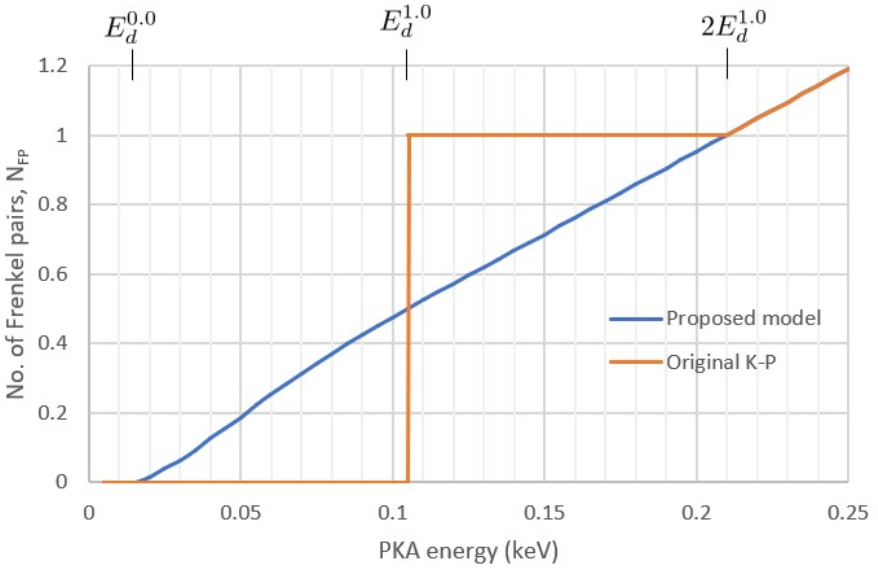


Figure 4.17: Predicted Frenkel pairs, N_{FP}, as a function of E_{PKA} based on equation 4.9 in comparison with the original K-P model using $E_d = E_d^{1.0}$.

4.5 Summary

MD simulations of damage cascades were performed for pure beryllium using a Tersoff interatomic potential that has been improved from the original potential by Björkas *et al.* [150]. The key improvement is that this potential model reproduces the experimental thermal expansion behaviour over a range of temperatures appropriate for studying damage evaluation. This was also achieved without compromising on the potential's ability to predict static properties as well as the melting point in beryllium (see Tables 3.3 and 3.4).

In the simulated cascades, the damage produced is centered along the PKA trajectory, which produces a highly disordered region along its path. In all cases the disordered regions recovered readily, but left a small percentage of damage that persisted beyond the end of the simulations. This was linked to highly displaced atoms that were able to escape the recovering disordered regions. Increasing simulation temperature increased the volume of the disordered region, leading to higher peak damage, but insignificant change in the residual damage after the recovery phase. That is, higher temperature did not facilitate the occurrence of more secondary atoms sufficiently displaced from the cascade backbone. Conversely, higher PKA energy did lead to a larger proportion of highly displaced atoms, and thereby increased the residual damage. Thus, for this pure material at temperatures well below any phase transition, over timescales smaller than that for thermal recombination of defects, the number of Frenkel pairs produced in a damage cascade event is proportional to the PKA energy but is independent of the simulation temperature.

The lack of dependence of Frenkel pairs produced on simulation temperature means, for this light metal system, simple approaches such as the K-P model are useful in predicting the total number of defects generated per PKA energy; that is, so long as it is possible to generate reliable values for parameters such as the threshold displacement energy, E_d. On this point, the probability for displacement by a PKA was calculated as a function of PKA energy, $P(E_{PKA})$, using MD and the same potential model as for cascade simulations. There was excellent cor-

respondence between the K-P prediction using the calculated $E_d^{1.0}$ value and the number of residual defects remaining after the initial recovery phase. Based on this, a modification to the K-P model, equation 4.9, was proposed that utilises the directionally averaged threshold displacement probabilities and $E_d^{1.0}$.

The results represent the model for primary radiation damage at the atomic scale predicted by the interatomic potential developed in this work. The distribution and clustering of defects generated as primary radiation damage predicted in this work can be used, in conjunction with the proposed new K-P model, as starting points for larger time and length scale simulations (described in Section 1.4.4) in order to continue building the overall picture of the radiation damage process. One such possible application was raised in Section 4.2 where results presented here can be used in Accelerated MD or Kinetic Monte Carlo to predict an optimum operating temperature in terms of radiation tolerance of beryllium based on the trade-off between thermally-activated defect recovery and coalition.

Chapter 5

Prediction of defect concentrations in ZrO_2

In this chapter, defect concentrations in both monoclinic ($P2_1/c$) and tetragonal ($P4_2/nmc$) ZrO_2 are presented, as a function of oxygen partial pressure P_{O_2}, in the form of Brouwer diagrams. As mentioned in Chapter 2, both intrinsic and dopant containing defects are considered. The Brouwer diagram for undoped ZrO_2 will be presented first, followed by Brouwer diagrams for a range of current and potential alloying elements in Zr-based cladding. These are Fe, Ni, Cr, Cu and Sb. The results will be presented in the order in which the alloying elements were investigated, starting from those already in use in current Zr-based fuel cladding. Sn and Nb, which are also current alloying additions, have already been investigated by Bell in previous work [54]. This leaves current additions Fe, Ni and Cr, which will be presented in that order. Following the understanding derived from current alloying elements, the same methodology will be applied to investigate candidate alloying additions to Zr-based cladding, namely Cu and Sb. Finally the effect of Li is also investigated. Rather than a dopant, Li comes into contact with fuel cladding from LiOH in the coolant water (see Section 1.2.1).

Defect concentrations predicted in the Brouwer diagrams will be discussed primarily in relation to the corrosion rate and hydrogen pickup of Zr-based cladding. The properties of predicted

defects, such as binding energy and relaxation volume, are also analysed.

The majority of the results presented for Fe, Ni and Cr have been published in two separate papers in the *Journal of Nuclear Materials* [204, 205]. The results presented for Cu and Sb is under consideration by *Journal of Applied Physics*.

5.1 Undoped ZrO_2

The brouwer diagrams for purely intrinsic defects (i.e. no dopants) are constructed first. It is important to be able to reproduce results from previous work using similar methodology [52, 54–57]. This follows the methodology described in Section 3.3.2 with input parameters reported in Table 5.1. The v_{SM} values are obtained from HfO_2 calculations by Zhao and Vanderbilt [187], while the rest of the parameters are obtained from DFT calculations of ZrO_2 supercells.

Table 5.1: All input parameters for Brouwer diagrams except for the DFT defect energies.

Brouwer diagram input parameters	
Parameter	Value
Dopant reference (FeO)	-1201.00 eV
Zr reference (Zr metal)	-1476.55 eV
Band gap (t-ZrO_2)	3.95 eV
N_v (t-ZrO_2)	108
N_c (t-ZrO_2)	21.5
E_{VBM} (t-ZrO_2)	10.7 eV
v_{SM} (t-ZrO_2)	0.11835 eV/e^2
Band gap (m-ZrO_2)	3.40 eV
N_v (m-ZrO_2)	96
N_c (m-ZrO_2)	38.5
E_{VBM} (m-ZrO_2)	10.13 eV
v_{SM} (m-ZrO_2)	0.26626 eV/e^2

5.1.1 Monoclinic ZrO_2

The intrinsic defects predicted for monoclinic ZrO_2 are presented in Figure 5.1. The picture is

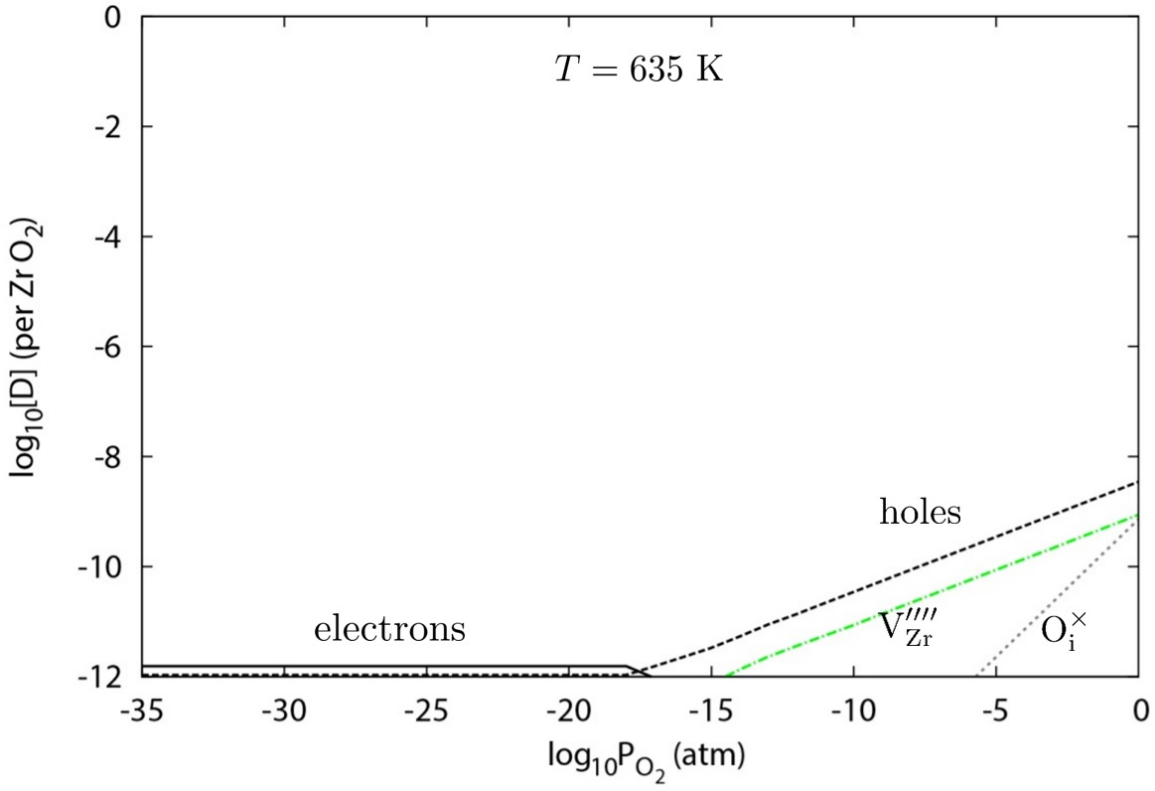


Figure 5.1: Brouwer diagram showing the predicted defect concentration as a function of oxygen partial pressure in monoclinic ZrO_2 at 635 K.

simple: at P_{O_2} above 10^{-15} atm the fully charged zirconium vacancy concentration increases with increasing P_{O_2}. These vacancies are charge compensated by electron holes in the oxide. This is consistent with the picture of ZrO_2 being a p-type semiconductor. Below 10^{-15} atm P_{O_2}, electrons and holes balance each other as the zirconium vacancy concentration has fallen below the intrinsic electron/hole concentration. At high P_{O_2}, the neutral oxygen interstitial is also predicted in small concentrations. The results presented in Figure 5.1 are also consistent with previous work [54, 55].

5.1.2 Tetragonal ZrO_2

It is important to note that for tetragonal ZrO_2 the temperature used for the Brouwer diagram is 1500 K, rather than the cladding operating temperature of about 635 K. Below this temper-

ature the tetragonal phase is not stable without stress or doping. This approach has also been taken in previous work and has produced results consistent with experiment [52, 54–57] and the work in this thesis will therefore follow suit. It has been argued that the effect of raising temperature is analogous to applying stress into the defect system [54]. The Brouwer diagram for tetragonal ZrO_2 is presented in Figure 5.2. There is a larger variety of defects predicted in

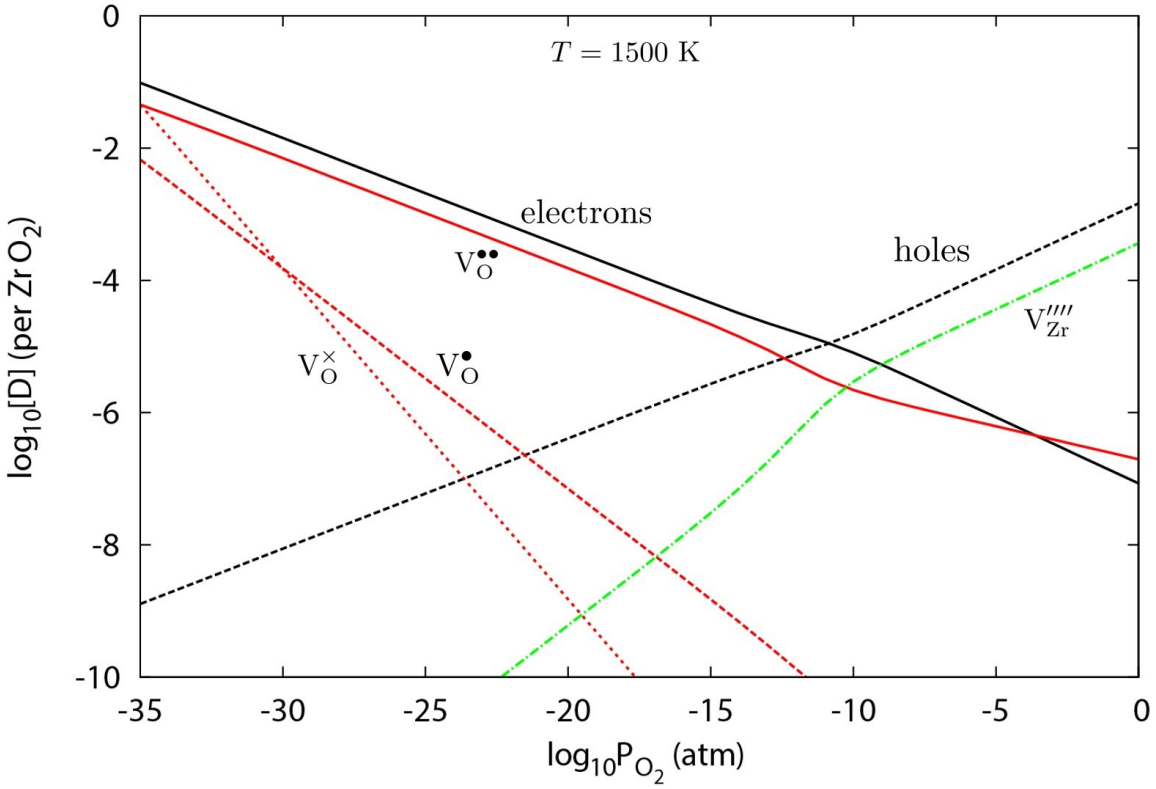


Figure 5.2: Brouwer diagram showing the predicted defect concentration as a function of oxygen partial pressure in tetragonal ZrO_2 at 1500 K. Defects with concentrations below 10^{-6} at all P_{O_2} are not shown.

much higher concentrations in comparison to monoclinic ZrO_2. This can be attributed to the significant increase in system temperature. The electron hole and zirconium vacancy pairing is also seen here, though with much higher concentrations. Unique to tetragonal ZrO_2 are oxygen vacancies predicted in significant concentrations, which increase in concentration as P_{O_2} drops. Oxygen vacancies are predicted with 0, 1+ and 2+ charges, with the doubly charge oxygen vacancies being the most populous. These oxygen vacancies are charge balanced by electrons and when in comparison to the monoclinic ZrO_2 (Figure 5.1) appear to also suppress $[V_{Zr}^{''''}]$ below 10^{-10} atm P_{O_2}.

For reference, the Brouwer diagram for tetragonal ZrO_2 at 635 K is shown in Figure 5.3. The concentration of intrinsic defects predicted are significantly lower, similar to Figure 5.1

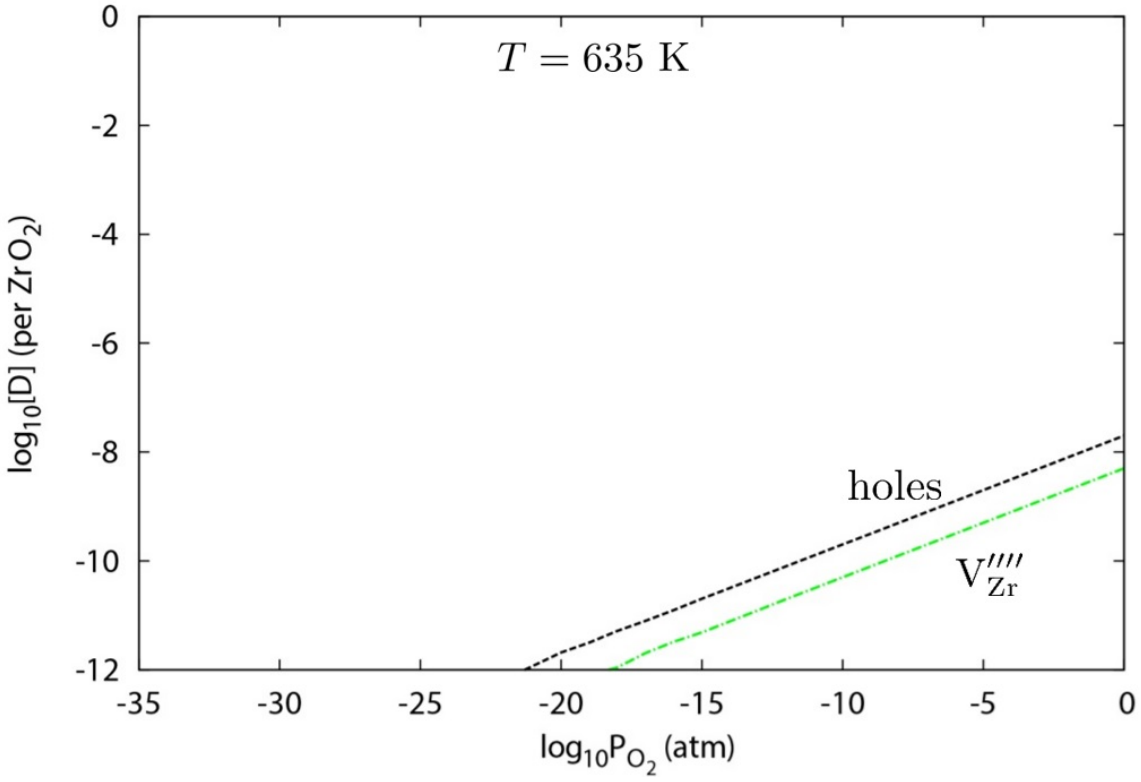


Figure 5.3: Brouwer diagram showing the predicted defect concentration as a function of oxygen partial pressure in tetragonal ZrO_2 at 635 K.

for monoclinic ZrO_2, with none predicted to be of concentrations higher than 10^{-12} units per ZrO_2 below 10^{-21} atm P_{O_2}. The significantly lower concentrations of intrinsic defects can make the interactions with dopants (especially when included at higher concentrations) difficult to investigate.

5.2 Iron

5.2.1 Brouwer diagrams

Common alloys like ZIRLO can have about 0.003 at% to 0.018 at% [73] Fe while the HiFi alloy can have up to 0.65 at.% [206]. With this in mind, Brouwer diagrams are generated for 0.001 at.%, 0.01 at.% and 0.1 at.% concentration of iron within the oxide. Charge states of 2^+ and

3^+ were considered for iron as these are the states that have been reported in ZrO_2 [70, 71]. Figure 5.4 shows the defect concentrations in iron-doped monoclinic ZrO_2 at 635 K, which is a typical temperature for autoclave experiments on zirconium cladding. The Brouwer diagram shown is for 0.01 at.% of iron in the cladding, which corresponds to 0.0001 units of iron per ZrO_2. Other concentrations demonstrate the same trends.

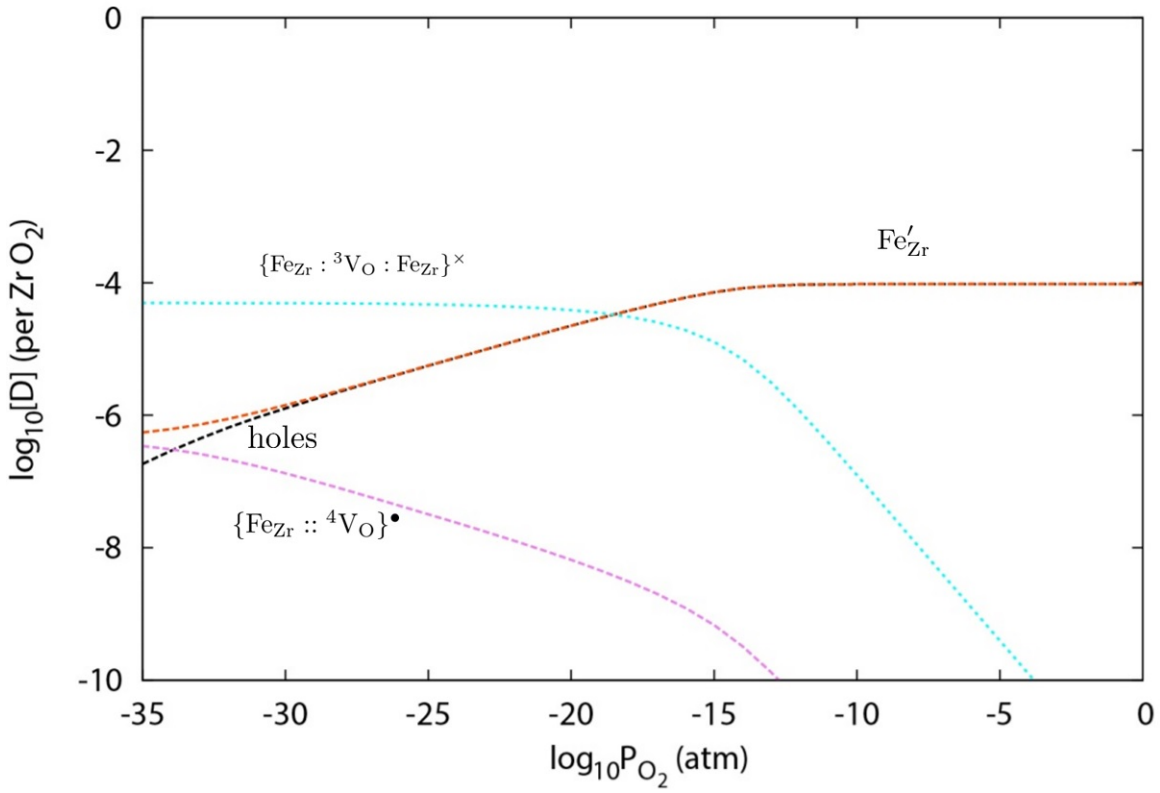


Figure 5.4: Brouwer diagrams showing defect concentrations in monoclinic ZrO_2 at 635 K as a function of oxygen partial pressure with 0.0001 units of iron per ZrO_2. ^3V_O and ^3V_O refer to vacancies in the 3-coordinated and 4-coordinated oxygen sites respectively. The double colon indicates the oxygen vacancy at a 2nd nearest neighbour site with respect to the iron atom Defects with concentrations below 10^{-7} at all P_{O_2} are not shown.

It can be seen that for oxygen partial pressures above 10^{-18} atm in iron-doped monoclinic ZrO_2, the preferred defect is Fe'_{Zr}; that is Fe^{3+} on a zirconium site charge compensated by holes. Compared to the undoped ZrO_2, there is a significant increase in the concentration of holes at lower oxygen partial pressures, which indicates that, in monoclinic ZrO_2, iron is acting as a p-type dopant. Possible consequences of this may be understood by looking at the behaviour of holes in monoclinic ZrO_2. The mobility of holes in monoclinic ZrO_2 is two orders

of magnitude lower than that of electrons [207] and thus electronic conduction is expected to still be the dominant charge carrier. This is important as should holes be migrating instead, they would be unable to recombine and stop the influx of H^+ ions, leading to greater HPUF. Furthermore, it has been shown that the mobility of holes is much lower at surfaces than in the bulk, causing them to readily segregate to surfaces [208]. This would imply that the increase in hole concentration could lead to an increase in positive charge accumulation on surfaces such as grain boundaries, which may impede the ingress of H^+ into the oxide and thus lowering HPUF. At P_{O_2} lower than 10^{-18} atm, the $\{Fe'_{Zr} : {}^3V^{\bullet\bullet}_O : Fe'_{Zr}\}^\times$ cluster is dominant. This suggests that in this phase, under low P_{O_2} conditions, iron atoms cluster with oxygen vacancies, and that the presence of substitutional iron locks the oxygen vacancies. These oxygen vacancies however, are not expected to signficantly contribute to the transport of oxygen through the oxide due to the high cluster binding energy of 1.62 eV exhibited by the $\{Fe'_{Zr} : {}^3V^{\bullet\bullet}_O : Fe'_{Zr}\}^\times$ cluster. Note that unpaired oxygen vacancies are predicted to form in both undoped and iron-doped monoclinic ZrO_2 but have concentrations that are too low be significant.

While for tetragonal ZrO_2, Brouwer diagrams (Figure 5.5) were generated at 1500 K since it is the temperature where this phase becomes stable, while a Brouwer diagram was also generated at 900 K for comparison.

Comparing first the undoped (Figure 5.5a) and the iron-doped (Figure 5.5b) diagrams at 1500 K, doubly charged oxygen vacancies charge compensated by electrons are the dominant defect at low P_{O_2} with very similar concentrations in both cases. Equivalently at high P_{O_2}, holes compensating for fully charged zirconium vacancies dominate in doped and undoped materials. It is only at intermediate P_{O_2} that there is a difference with the $\{Fe'_{Zr} : V^{\bullet\bullet}_O : Fe'_{Zr}\}'$ cluster dominating in the doped case.

Figure 5.5b is consistent with the dominant iron defect, across all P_{O_2}, consisting of two substituted iron ions adjacent to an oxygen vacancy (i.e. a trimer). At higher P_{O_2}, both iron species prefer to be in the 3+ state, gradually shifting to a preference for 2+ as the environment be-

comes more reducing. A single Fe^{3+} ion paired to an oxygen vacancy (i.e. a dimer) trails by an order of magnitude in concentration across all P_{O_2} while an isolated Fe^{3+} is of minor significance even at the highest P_{O_2}. At this concentration of iron (10^{-4} iron per ZrO_2), the concentration of the (most favourable) trimer is roughly constant across the range of P_{O_2} studied.

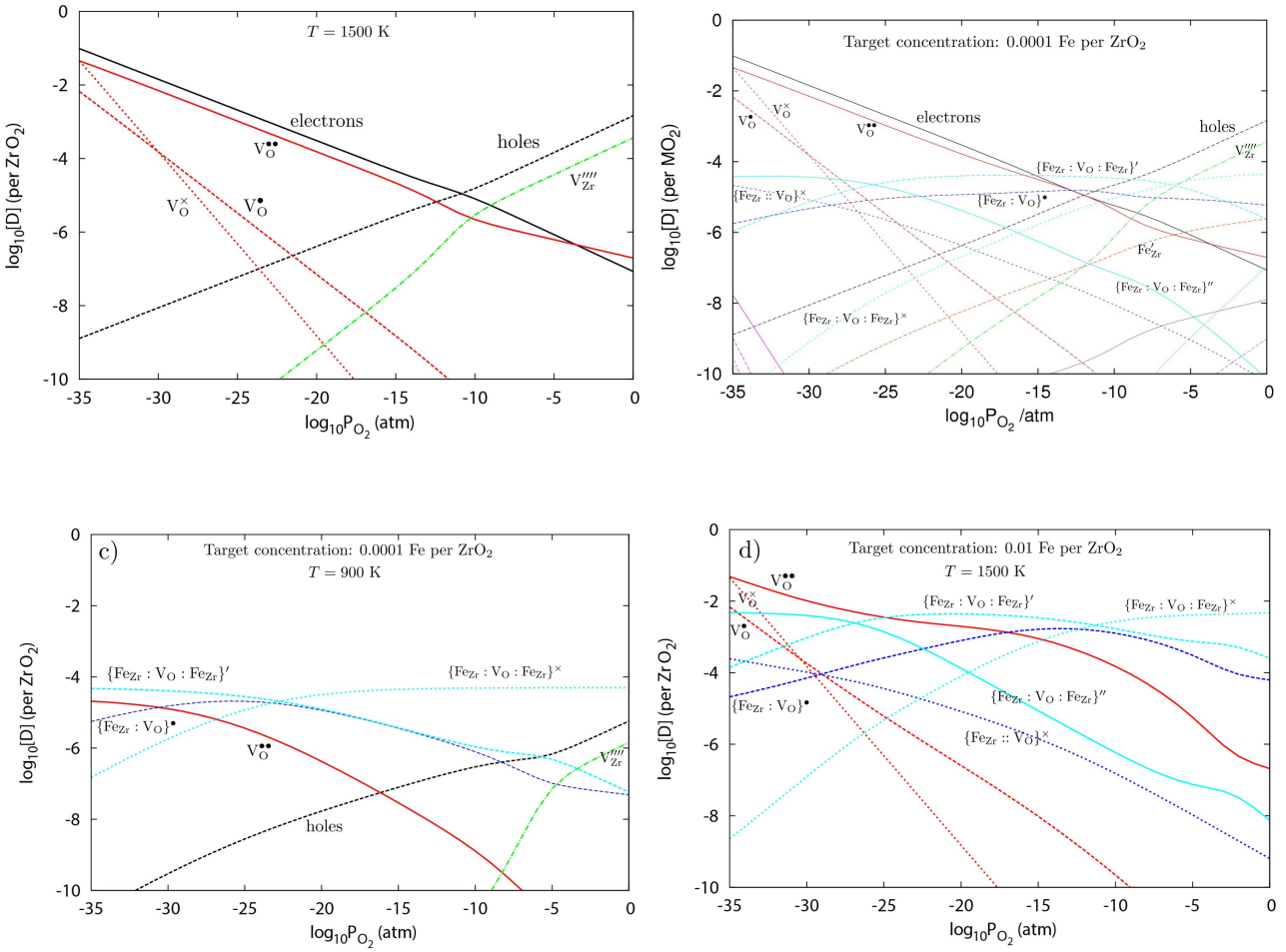


Figure 5.5: Brouwer diagrams showing defect concentrations in tetragonal ZrO_2 as a function of oxygen partial pressure for a) ZrO_2 with no iron at 1500 K, b) 0.0001 units of iron per ZrO_2 at 1500 K, c) 0.0001 units of iron per ZrO_2 at 900 K and d) 0.01 units of iron per ZrO_2 at 1500 K showing only the oxygen vacancies and paired iron defects. The double colon indicates the oxygen vacancy at a 2nd nearest neighbour site with respect to the iron atom. In all diagrams, defects with concentrations below 10^{-6} at all P_{O_2} are not shown.

Figure 5.5b predicts that most oxygen vacancies will remain unpaired at very low P_{O_2}, suggesting oxygen ion migration would not be affected by the presence of iron. This may not, however, necessarily hold true in a thermally grown oxide on zirconium cladding, as oxygen vacancies are only significant in Brouwer diagrams above 1000 K, which is significantly above

the cladding operating temperature, or where locally, the iron concentration is much higher. To help illustrate these points, two further Brouwer diagrams were generated; Figure 5.5c where the temperature is reduced and Figure 5.5d where the concentration of iron is increased. Figure 5.5c shows the predicted defect concentrations for the iron doped tetragonal ZrO_2 at 900 K and it can be seen that across all P_{O_2}, oxygen vacancies now show a preference to be bound to iron atoms. The Brouwer diagrams also predict that this pairing of iron atoms with oxygen vacancies becomes more significant at low P_{O_2} if the concentration of iron is sufficiently high. This is also evident when comparing Figures 5.5b and 5.5d, where at low P_{O_2}, with higher concentration of iron, the concentration of paired iron defects becomes more significant in comparison to the dominant oxygen vacancies.

The strong preference of iron ions to cluster with oxygen vacancies predicted in this study suggests that iron could be binding the oxygen vacancies at key specific locations such as grain boundaries and the oxide-metal interface. This could be especially important in regions where iron content is higher. Thus, if the migration of O^{2-} ions through the oxide is primarily via an oxygen vacancy hopping mechanism, then migration could be significantly slowed when the iron content in the oxide is higher locally, which could lead to a reduced corrosion rate. This is supported by the Coupled Current Charge Compensation (C4) model for oxidation developed by Couet *et al.* [7]. Fromhold's oxidation theory [209], that the C4 model is based on, suggests that there is no net charge transport across the oxide at all times. This implies that diffusion of charged species across the oxide layer is coupled. Couet *et al.* suggest that the $V_O^{\bullet\bullet}$ and electrons are the main charge carriers diffusing through the oxide [7]. Therefore, in most cases, only either the diffusivity of $V_O^{\bullet\bullet}$ or electrons will be rate limiting with regards the resultant oxidation rate. By comparing electron untrapping energies in literature presented by Couet *et al.* and the C4 model [7], it is the diffusivity of $V_O^{\bullet\bullet}$ which is rate limiting, which is expected to outweigh any electronic effects. Further, it has been shown that oxygen vacancies are favourable for the stabilisation of the tetragonal ZrO_2 phase [210], thus it is reasonable to expect the proportion of tetragonal to monoclinic ZrO_2 to be higher in samples containing greater amounts of Fe.

The results are in good agreement with previous work reporting DFT simulations of strongly iron-doped (> 1 at.%) oxides in both monoclinic and tetragonal ZrO_2, as well as experimental characterisation of iron-doped ZrO_2 thin films [71]. The study suggested that iron predominantly favours the 3+ state and charge compensates $V_O^{\bullet\bullet}$ at a ratio of two iron atoms to one oxygen vacancy.

5.2.2 Binding Energies and Relaxation Volumes

Defect cluster binding energies and relaxation volumes are reported in Tables 5.3 and 5.4. The clusters generally show positive (favourable) binding energies, which are reflected in the Brouwer diagrams, where clustered defects are favourable (in general) over isolated defects (in general the propensity for cluster formation is a function of dopant ion concentration due to the configurational entropy penalty upon cluster formation).

As mentioned in Section 3.3.3, there is a possibility that relaxation volumes as obtained from constant volume calculations may be unreliable for charged defects. Therefore, for some of the relevant charged defects, constant pressure calculations were performed (which required the additional convergence criteria of a maximum stress of 0.05 GPa on the cell). The relaxation volume here is then obtained by simply taking the volume difference between the perfect and defective supercell. Section 5.2.2 reports the comparison between the relaxations volumes obtained using constant volume calculations (from which the energies where used to construct the Brouwer diagrams) and the constant pressure calculations. The difference is small enough to have no significant impact on the subsequent analysis. Therefore relaxation volumes will continue to be discussed with the constant volume values.

The reported binding energies are large in comparison to thermal energies (i.e. kT), suggesting that once a substitutional iron atom is bound to an oxygen vacancy, it is not likely to become unbound. Therefore the presence of iron could effectively immobilise the oxygen

Table 5.2: Comparison between relaxation volumes obtained using constant volume calculations versus constant pressure calculations for relevant charged defects.

	Relaxation volume (Å^3)	
Defect	Const volume	Const pressure
Tetragonal		
$\{Fe'_{Zr} : V^{\bullet\bullet}_O : Fe''_{Zr}\}'$	25.7	70.6
$\{Fe''_{Zr} : V^{\bullet\bullet}_O : Fe''_{Zr}\}''$	42.9	86.4
$\{Fe'_{Zr} : V^{\bullet\bullet}_O\}^{\bullet}$	-17.5	-29.1
Fe'_{Zr}	13.8	16.9
Fe''_{Zr}	31.3	38.9
$V^{\bullet\bullet}_O$	-37.1	-40.1
Monoclinic		
$\{Fe'_{Zr} : {}^3V^{\bullet\bullet}_O : Fe''_{Zr}\}'$	6.42	7.53
$\{Fe''_{Zr} : {}^3V^{\bullet\bullet}_O : Fe''_{Zr}\}''$	19.7	21.7
$\{Fe'_{Zr} : {}^4V^{\bullet\bullet}_O : Fe''_{Zr}\}'$	-0.55	8.90
$\{Fe''_{Zr} : {}^4V^{\bullet\bullet}_O : Fe''_{Zr}\}''$	16.5	16.1
$\{Fe'_{Zr} : {}^3V^{\bullet\bullet}_O\}^{\bullet}$	-17.1	-17.9
$\{Fe'_{Zr} : {}^4V^{\bullet\bullet}_O\}^{\bullet}$	-13.4	-18.5
$\{Fe'_{Zr} :: {}^4V^{\bullet\bullet}_O\}^{\bullet}$	-16.0	-16.5
Fe'_{Zr}	9.98	7.01
Fe''_{Zr}	21.6	23.2
${}^3V^{\bullet\bullet}_O$	-26.2	-27.7
${}^4V^{\bullet\bullet}_O$	-22.5	-26.9

vacancies, which further supports the case for iron slowing the movement of O^{2-} through the oxide.

The relaxation volume values help explain why clustering is energetically favourable (though coulomb attraction of charge defects is still the dominant factor). Relaxation volumes of (single) substitutional iron are large and positive. These may be compensated by oxygen vacancies, which have negative relaxation volumes if they cluster together (i.e. the total stresses can be reduced). Iron in the 3+ state also shows a smaller relaxation volume compared to the 2+ state, contributing to the stability of the 3+ oxidation state.

The relaxation volumes also allow us to consider the possible effects that stress in the oxide may have on defect stability, which were not accounted for in the DFT model. It seems likely

that in the real oxides, defects with modestly negative relaxation volumes would be slightly more favourable than the Brouwer diagrams suggest if large compressive stresses are present, as are indeed observed (up to 3 GPa) [20, 211].

Table 5.3 reports that the defect cluster most in evidence in the Brouwer diagram (Figure 5.4), that is $\{Fe'_{Zr} : {}^{3}V_{O}^{\bullet\bullet} : Fe'_{Zr}\}^{\times}$, has a negative relaxation volume and there is a small reduction in total defect volume when the three defects cluster to form this trimer defect. Thus, the conclusion from the Brouwer diagram that this is the important cluster should hold true in the real (compressed) oxide layer. Indeed the cluster should be evident to slightly higher P_{O_2} values through the small binding energy (compared to other clusters) and the small volume change means that it is not going to be significant compared to isolated Fe'_{Zr} (as in the Brouwer diagram) at higher P_{O_2}.

Table 5.4 reports larger positive binding energies for tetragonal ZrO_2 in comparison to the monoclinic phase, which drives the cluster formation observed in the Brouwer diagrams (Figure 5.5). Considering then the change in defect volume upon clustering, the three trimer defects give rise to volume increases comparable to isolated defects. Despite this, the trimer defects are still expected to be dominant (as in the Brouwer diagrams) as defect charges are the main driving force for the clustering. Thus, it is then expected that the formation of these trimers will lead to an increase in the stresses within the oxide, which may in turn result in an earlier onset of cracking in the protective oxide layer.

Table 5.3: Binding energies, relaxation volumes and clustering volumes of defects in monoclinic ZrO_2 at 635 K. Binding energies for clustered defects are calculated from the $V_O^{\bullet\bullet}$ ground state. ^3V_O and ^4V_O refer to vacancies in the 3-coordinated and 4-coordinated oxygen sites respectively.

Defect	Binding energy (eV)	Relaxation Volume (Å^3)	Volume change upon clustering (Å^3)
$\{Fe'_{Zr} : {}^3V_O^{\bullet\bullet} : Fe'_{Zr}\}^{\times}$	1.62	-7.52	-1.33
$\{Fe'_{Zr} : {}^3V_O^{\bullet\bullet} : Fe''_{Zr}\}'$	3.78	6.42	0.98
$\{Fe''_{Zr} : {}^3V_O^{\bullet\bullet} : Fe''_{Zr}\}''$	5.07	19.68	2.61
$\{Fe'_{Zr} : {}^4V_O^{\bullet\bullet} : Fe'_{Zr}\}^{\times}$	-1.85	-14.97	-12.4
$\{Fe'_{Zr} : {}^4V_O^{\bullet\bullet} : Fe''_{Zr}\}'$	0.57	-0.55	-9.61
$\{Fe''_{Zr} : {}^4V_O^{\bullet\bullet} : Fe''_{Zr}\}''$	3.34	16.49	-4.20
$\{Fe'_{Zr} : {}^3V_O^{\bullet\bullet}\}^{\bullet}$	0.59	-17.11	-0.94
$\{Fe''_{Zr} : {}^3V_O^{\bullet\bullet}\}^{\times}$	2.40	-3.90	0.64
$\{Fe'_{Zr} : {}^4V_O^{\bullet\bullet}\}^{\bullet}$	0.67	-13.35	-0.85
$\{Fe'_{Zr} :: {}^4V_O^{\bullet\bullet}\}^{\bullet}$	1.40	-16.00	-3.45
$\{Fe''_{Zr} : {}^4V_O^{\bullet\bullet}\}^{\times}$	0.93	-4.98	-4.06
Fe'_{Zr}	-	9.98	-
Fe''_{Zr}	-	21.61	-
$^3V_O^{\bullet\bullet}$	-	-26.15	-
$^4V_O^{\bullet\bullet}$	-	-22.53	-

Table 5.4: Binding energies, relaxation volumes and clustering volumes of defects in tetragonal ZrO_2 at 1500 K. Binding energies for clustered defects are calculated assuming the oxygen vacancies have a 2^+ charge.

Defect	Binding energy (eV)	Relaxation Volume (Å^3)	Volume change upon clustering (Å^3)
$\{Fe'_{Zr} : V_O^{\bullet\bullet} : Fe'_{Zr}\}^{\times}$	4.05	-3.05	6.51
$\{Fe'_{Zr} : V_O^{\bullet\bullet} : Fe''_{Zr}\}'$	5.42	25.7	17.7
$\{Fe''_{Zr} : V_O^{\bullet\bullet} : Fe''_{Zr}\}''$	5.83	42.9	17.34
$\{Fe'_{Zr} : V_O^{\bullet\bullet}\}^{\bullet}$	2.11	-17.47	5.85
$\{Fe''_{Zr} : V_O^{\bullet\bullet}\}^{\times}$	1.30	-8.82	-3.06
$\{Fe''_{Zr} :: V_O^{\bullet\bullet}\}^{\times}$	2.38	-2.87	2.89
Fe'_{Zr}	-	13.76	-
Fe''_{Zr}	-	31.32	-
$V_O^{\bullet\bullet}$	-	-37.08	-
$V_O^{\bullet}$	-	-19.04	-
$V_O^{\times}$	-	-2.16	-

5.3 Nickel

Ni can exist in oxidations states from Ni^0 to Ni^{4+}. The Brouwer diagram is generated with concentration of 10^{-4} units of Ni per ZrO_2, which roughly corresponds to the amount of Ni found

in regions outside areas of elevated concentration in Zircaloy-2 and Zircaloy-4 cladding [85]. As Figure 5.6 shows, $\{Ni_{Zr} : V_O\}$ type dimer clusters are predicted to be the important defect species. $\{Ni_{Zr} : V_O : Ni_{Zr}\}$ type clusters containing Ni^{2+} and Ni^{3+} was predicted to have concentrations less than 10^{-6} at all P_{O_2} considered.

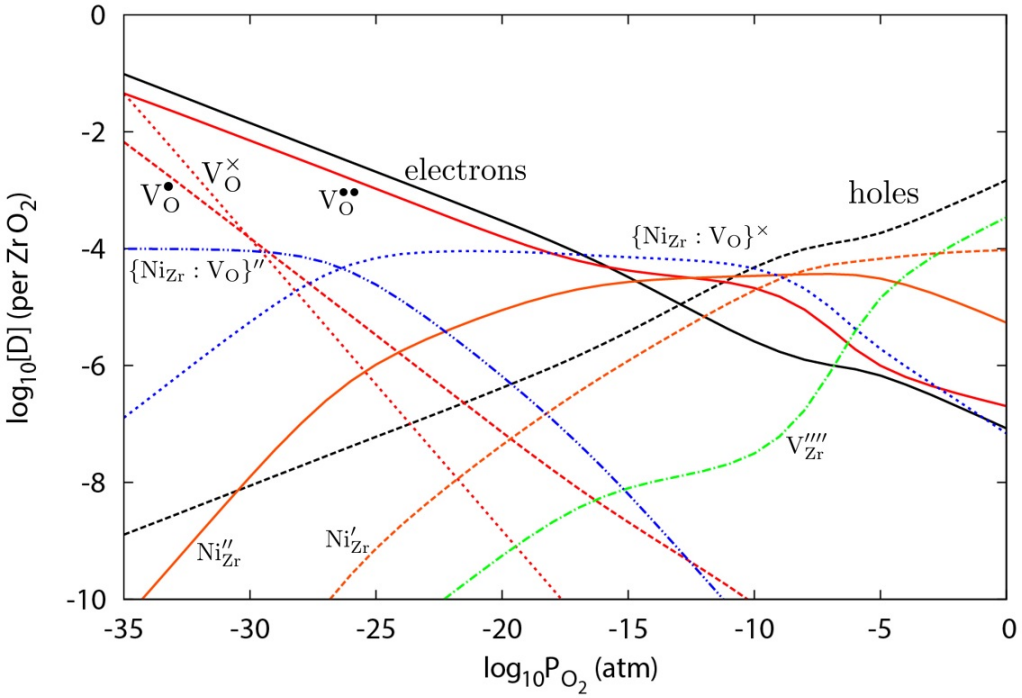


Figure 5.6: Brouwer diagram showing the predicted defect concentration as a function of oxygen partial pressure in tetragonal ZrO_2 at 1500 K at a total Ni dopant concentration of 10^{-4} atoms per formula unit ZrO_2. Defects with concentrations below 10^{-6} at all P_{O_2} are not shown.

Figure 5.6 shows at high P_{O_2}, Ni^{3+} is dominant while Ni^{2+} is also seen at the significant concentration of about ~10^{-5} units per ZrO_2. At lower P_{O_2}, clustering with oxygen becomes favourable, with $\{Ni''_{Zr} : V^{\bullet\bullet}_O\}^\times$ being the preferred Ni defect species below 10^{-9} atm and $\{Ni''''_{Zr} : V^{\bullet\bullet}_O\}''$ below 10^{-27} atm. While $\{Ni'''_{Zr} : V^{\bullet\bullet}_O\}'$ was included in the simulations it is predicted at a concentration of less than 10^{-6} at all P_{O_2}. The binding energy for the $\{Ni''''_{Zr} : V^{\bullet\bullet}_O\}''$ and $\{Ni''_{Zr} : V^{\bullet\bullet}_O\}^\times$ clusters are 5.30 eV and 2.86 eV respectively. These binding energies are sufficiently high to suggest that an oxygen vacancy is unlikely to break free once bound to a Ni ion, suggesting that Ni may also enhance corrosion resistance by the same oxygen vacancy locking mechanism suggested for Fe.

$\{Ni''''_{Zr} : V^{\bullet\bullet}_{O}\}''$ is unique since all other dopants considered in this study (i.e. Fe and Cr), or elsewhere [52,54,55,57], exhibit dopant charge states of 2+, 3+, 4+ or even 5+, while Ni in this cluster is in a metallic 0 charge state. This seems unusual, as it suggests that despite the single substitutional ion exhibiting a 2+ or a 3+ charge state, it is energetically favourable for Ni in the cluster to retain all of its electrons. Yet this was reported by Shivprasad *et al.* [50] following experimental work on samples of Zircaloy-2 with higher HPUF.

Now turning to monoclinic ZrO_2, the Brouwer diagram is presented in Figure 5.7. At above

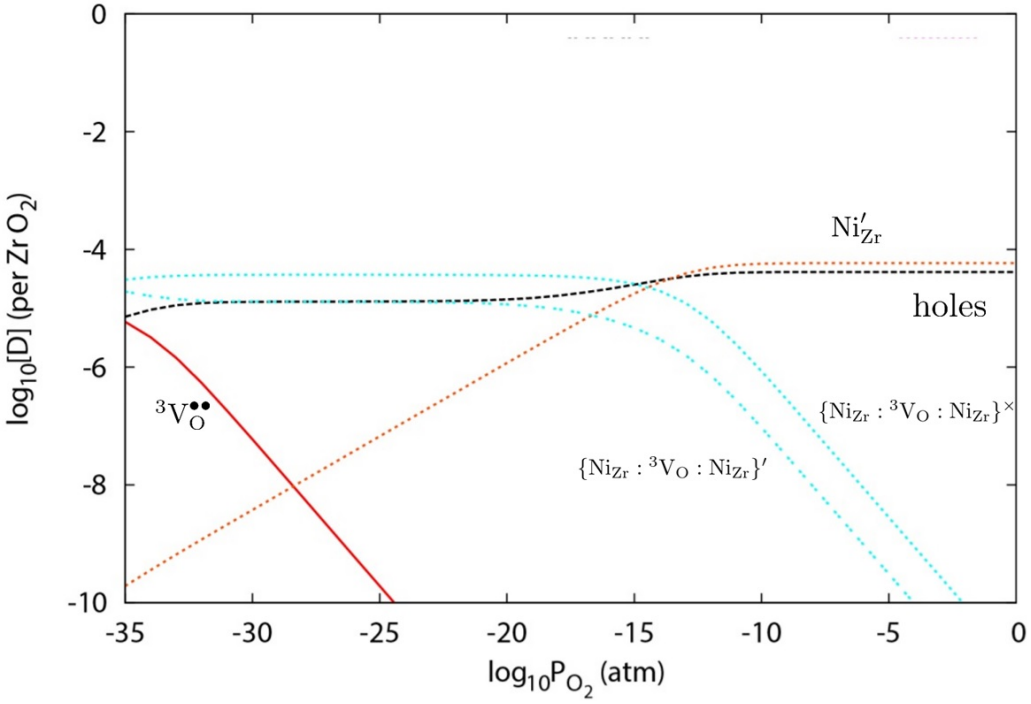


Figure 5.7: Brouwer diagram showing the predicted defect concentration as a function of oxygen partial pressure in monoclinic ZrO_2 at 635 K at a total Ni dopant concentration of 10^{-4} atoms per formula unit ZrO_2. Defects with concentrations below 10^{-7} at all P_{O_2} are not shown. ^3V_O refers to vacancies at the 3-coordinated oxygen site (as opposed to the 4-coordinated site) in m-ZrO_2.

10^{-14} atm P_{O_2}, the single Ni^{3+} substituted on the Zr site is the primary Ni defect. At lower P_{O_2}, the $\{Ni'_{Zr} : {}^3V^{\bullet\bullet}_{O} : Ni'_{Zr}\}^{\times}$ cluster is dominant, followed closely by $\{Ni''_{Zr} : {}^3V^{\bullet\bullet}_{O} : Ni'_{Zr}\}'$. At all P_{O_2}, the negatively charged Ni defects are charge compensated by electron holes. The significant increase in hole concentration compared to Figure 5.1 points to the role of Ni as a p-type dopant.

The oxygen vacancies stabilised in the $\{Ni'_{Zr} : {}^{3}V^{\bullet\bullet}_{O} : Ni'_{Zr}\}^{\times}$ and $\{Ni''_{Zr} : {}^{3}V^{\bullet\bullet}_{O} : Ni'_{Zr}\}'$ clusters are not expected to be mobile and contribute to oxygen conductivity. This comes from the respective binding energies of 2.38 eV and 3.71 eV for the clusters. A sharp increase in single oxygen vacancies at the 3-coordinated oxygen site (not seen in the intrinsic case) is observed in Figure 5.7 at very low P_{O_2}, corresponding to the inner layer of the oxide where the monoclinic phase is not expected to be prevalent. The concentration of free oxygen vacancies is also far less than that predicted for tetragonal ZrO_2. The spike in ${}^{3}V^{\bullet\bullet}_{O}$ can be attributed to oxygen vacancies being preferred over electron holes as charge compensation at very low P_{O_2}.

THe presence of metallic Ni in ZrO_2 been seen recently in experiment and correlated with increase HPUF [50]. While the results for monoclinic ZrO_2 do not indicate the presence of Ni in the metallic state, the prediction of metallic Ni^0 in $\{Ni''''_{Zr} : V^{\bullet\bullet}_{O}\}''$ clusters in tetragonal ZrO_2 may be a significant discriminator. Further investigation on the interactions of Ni^0 with hydrogen will be presented in Section 5.5.

5.4 Chromium

Cr is known to exhibit a wide range of oxidation states; as such single Cr defects with charges from Cr^{2-} to Cr^{6+} were considered in this study. Unlike the Fe case, only dimer defects were considered for cluster defects due to the large number of possible charge states. However, considering just the $\{Cr_{Zr} : V_O\}$ type defects will give a good picture of how Cr interacts with oxygen vacancies. It has been shown that in cubic ZrO_2, the binding energies of $\{M_{Zr} : V_O\}$ and $\{M_{Zr} : V_O : M_{Zr}\}$ clusters show similar trends [212]. Further, given the potential significance of Ni^0 in tetragonal ZrO_2, and also given that tetragonal ZrO_2 is observed more in the inner protective oxide of the cladding, this study on Cr will only consider the tetragonal phase.

As shown in Figure 5.8, above 10^{-20} P_{O_2}, Cr mainly resides at Zr sites in the 4+ charge state, forming neutrally charged defects. This is understandable in light of how readily Cr can access different charge states with relatively little energy penalty. Thus, since the lattice environment

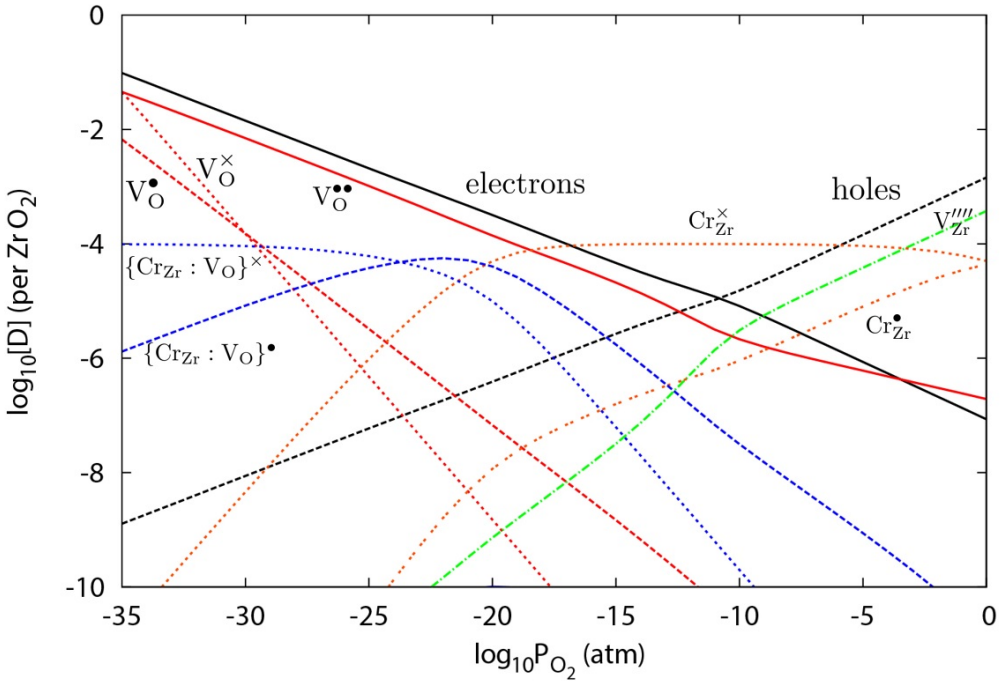


Figure 5.8: Brouwer diagram showing the predicted defect concentration as a function of oxygen partial pressure in tetragonal ZrO_2 at 1500 K at a total Cr defect concentration of 10^{-4} atoms per formula unit ZrO_2. Defects with concentrations below 10^{-6} at all P_{O_2} are not shown.

would promote a charge neutral defect, Cr^{4+} is the most thermodynamically favourable. At high P_{O_2}, Cr^{3+} is also predicted in significant concentrations; it is also to be expected since it is the most stable charge state for Cr in an oxide lattice (e.g. Cr_2O_3).

Below 10^{-20} P_{O_2}, Cr binds to oxygen vacancies. In the small region from 10^{-23} to 10^{-20} P_{O_2} Cr assumes a 3+ charge state and below that, Cr takes on the 2+ charge state to form the charge neutral defect cluster $\{Cr''_{Zr} : V^{\bullet\bullet}_O\}^\times$. The binding energy for the $\{Cr''_{Zr} : V^{\bullet\bullet}_O\}^\times$ defect is 3.37 eV and 2.26 eV for $\{Cr'_{Zr} : V^{\bullet\bullet}_O\}^\bullet$. These binding energies are sufficiently high to suggest that an oxygen vacancy is unlikely to break free once bound to a Cr ion. Similar to Fe, areas of elevated concentration of Cr have also been observed [74]. The preference for Cr to bind with oxygen vacancies at low P_{O_2} (i.e. where the protective oxide forms) suggests that Cr may also enhance corrosion resistance by the same mechanism suggested for Fe.

5.5 Fe, Cr and Ni interaction with hydrogen

To understand the underlying mechanisms responsible for the increased HPUF due to Ni (be it due to the existence of Ni^0 or not) single H or H^+ ions are placed at either interstitial or oxygen vacancy sites adjacent to a dopant species. These sites are associated with those dimer and trimer defect clusters, predicted in Figures 5.5, 5.6 and 5.8, to be present at low P_{O_2} in concentrations of $> 10^{-6}$ defects per ZrO_2 (the domiant defects for each dopant are summarised in Figure 5.9). No significant difference in behaviour was predicted in how H or H^+ behave

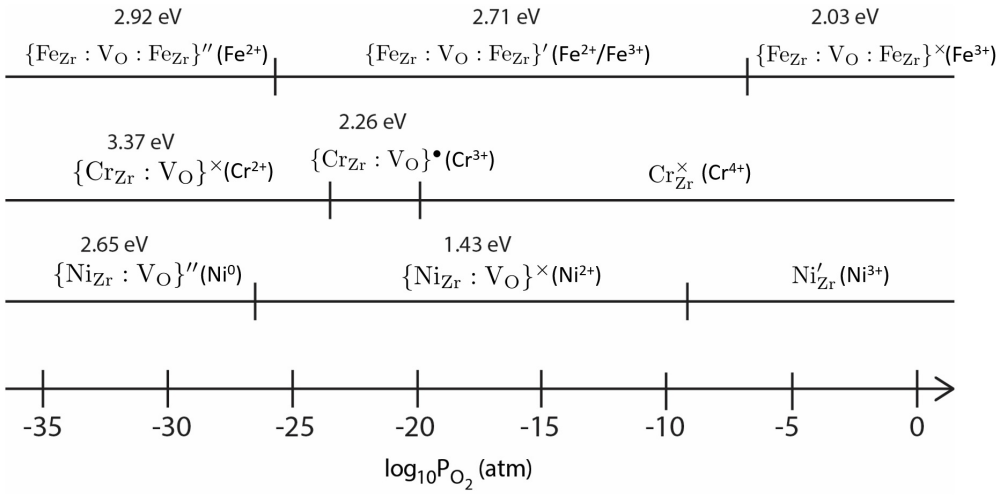


Figure 5.9: The dominant dopant containing defect for each of Fe, Cr and Ni, are identified as a function of P_{O_2}. Numbers beside the indicated defects are the binding energies per bond of each cluster. The charge state of the dopant cations are indicated in parenthesis.

when placed in the defects associated with different dopant species. When placed in the oxygen vacancy position, H and H^+ both favour bonding to the dopant atom, with a bond population of around $0.5e$. For the control case of an isolated vacancy, the H and H^+ bond to two neighbouring Zr atoms (rather than one dopant) but still exhibit a total bond population of around $0.5e$. When placed in interstitial sites, H and H^+ favour bonding to the neighbouring oxygen ion to form a hydroxyl group.

Next, configurations were considered that resulted from placing two H^+ ions into the oxygen vacancy sites of the defect clusters reported in Table 5.5, which includes the $V_O^{\bullet\bullet}$ defect as a control case. Importantly, the two H^+ species were initially separated by ~1.27 Å, much

greater than the bond separation of H_2 or H_2^+ molecules. For most clusters predicted in the Brouwer diagrams, the two H^+ ions simply combine into an H_2^+ molecule (see Figure 5.11 and Table 5.5 for the bond populations and the H-H bond lengths). The only exception to molecular formation occurred with the $\{Ni_{Zr}'''' : V_O^{\bullet\bullet}\}''$ cluster. Unlike for all other clusters in the Brouwer diagrams, with this cluster the geometry optimisation results in one H^+ binding to the dopant ion and the other binding to a neighbouring oxygen. During the DFT geometry optimisation calculation, the H^+ ions in both the oxygen vacancy and interstitial sites initially start to come together to a distance of 0.86 Å (as compared to the DFT H_2 bond length of 0.75 Å) before splitting apart, with one H^+ binding to the dopant ion and the other binding to a neighbouring oxygen. This process is illustrated in figure 5.10 for the H^+ ions in the oxygen vacancy site of the $\{Ni_{Zr}'''' : V_O^{\bullet\bullet}\}''$ defect. The resulting H-H bond population is zero and the final H-H distance

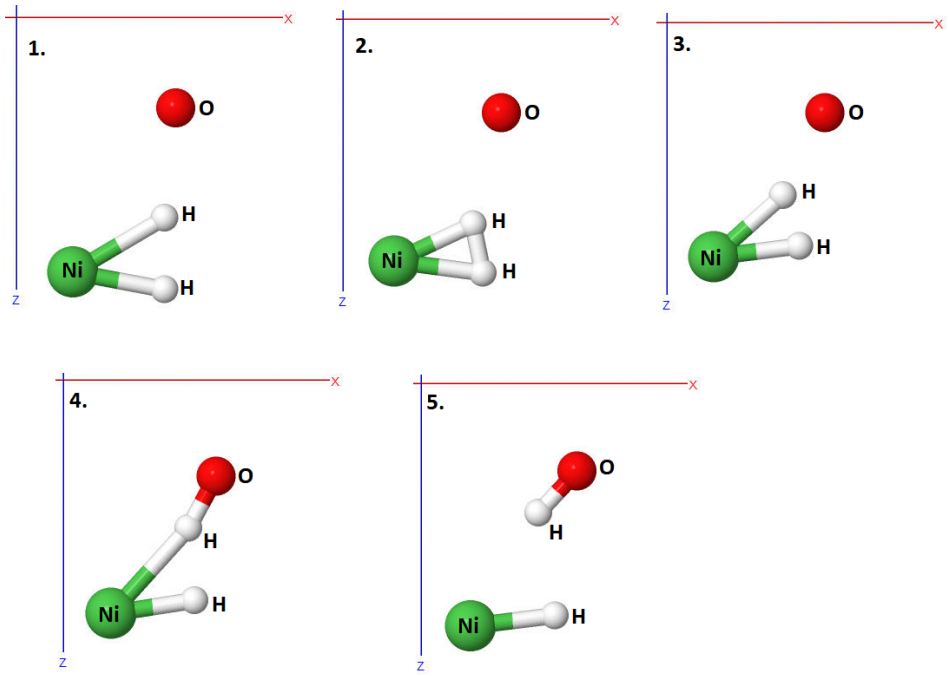


Figure 5.10: Diagram illustrating ion positions during the geometry optimisation calculation of two H^+ ions in the oxygen vacancy site of a $\{Ni_{Zr}'''' : V_O^{\bullet\bullet}\}''$ defect. The two H^+ explore the energy space that would consider H_2 formation before finding the lowest energy configuration split apart.

is 2.23 Å (see Table 5.5): the H^+ ions are not bonded to each other. Thus, this defect cluster, thermodynamically favoured at low P_{O_2}, does not facilitate the formation of the H_2^+ molecule. It is also interesting to note that the other Ni cluster examined, $\{Ni_{Zr}'' : V_O^{\bullet\bullet}\}^\times$, gives rise to

a slightly weaker H-H bond compared to the other two $\{M''_{Zr} : V^{\bullet\bullet}_{O}\}^{\times}$ clusters, according to the population analysis in Table 5.5 and Figure 5.11. This suggests that Ni behaves slightly differently as a dopant in ZrO_2.

Table 5.5: Mulliken bond populations and bond length (or atomic separation) between the two H^+ ions associated with oxygen vacancy-dopant cluster defects. Defects marked with a $(*)$ are not present in the Brouwer diagram figures.

Defect	H-H bond population	H-H distance (Å)
$\{Fe''_{Zr} : V^{\bullet\bullet}_{O} : Fe''_{Zr}\}''$	1.20	0.78
$\{Fe''_{Zr} : V^{\bullet\bullet}_{O} : Fe'_{Zr}\}'$	1.23	0.77
$\{Fe'_{Zr} : V^{\bullet\bullet}_{O} : Fe'_{Zr}\}^{\times}$	1.25	0.77
$\{Fe''''_{Zr} : V^{\bullet\bullet}_{O}\}''$ $(*)$	0.67	0.94
$\{Fe''_{Zr} :: V^{\bullet\bullet}_{O}\}^{\times}$	1.33	0.77
$\{Fe'_{Zr} : V^{\bullet\bullet}_{O}\}^{\bullet}$	1.18	0.79
$\{Cr''''_{Zr} : V^{\bullet\bullet}_{O}\}''$ $(*)$	0.26	1.26
$\{Cr''_{Zr} : V^{\bullet\bullet}_{O}\}^{\times}$	1.25	0.78
$\{Cr'_{Zr} : V^{\bullet\bullet}_{O}\}^{\bullet}$	1.29	0.76
$\{Ni''''_{Zr} : V^{\bullet\bullet}_{O}\}''$	0	2.23
$\{Ni'''_{Zr} : V^{\bullet\bullet}_{O}\}'$ $(*)$	0	1.82
$\{Ni''_{Zr} : V^{\bullet\bullet}_{O}\}^{\times}$	1.09	0.81
$V^{\bullet\bullet}_{O}$	1.31	0.77

A further calculation for two H^+ ions in $\{Ni''''_{Zr} : V^{\bullet\bullet}_{O}\}''$ was performed, this time with the H^+ ions starting at 0.79 Å apart, which is the approximate final H-H distance in most other clusters where the H^+ ions formed a molecule. This calculation also resulted in the same final dissociated configuration as predicted in the first calculation, that is, there is no bonding between the H^+ ions. This demonstrates the propensity of the $\{Ni''''_{Zr} : V^{\bullet\bullet}_{O}\}''$ cluster to dissociate H_2^+ in these simulations.

The predicted concentrations of $\{Ni'''_{Zr} : V^{\bullet\bullet}_{O}\}'$, $\{Cr''''_{Zr} : V^{\bullet\bullet}_{O}\}''$ and $\{Fe''''_{Zr} : V^{\bullet\bullet}_{O}\}''$ clusters are very much smaller than $\{Ni''''_{Zr} : V^{\bullet\bullet}_{O}\}''$. Consequently, these clusters can have little, if any, influence on HPUF. Nevertheless, the Fe and Cr clusters exhibit metal atoms in the zero charge state, while Ni^+ may have a low enough oxidation state to exhibit properties similar to Ni^0. It is therefore useful to investigate their interaction with H_2^+. Thus, two H^+ ions were placed into the oxygen vacancy site of the $\{Ni'''_{Zr} : V^{\bullet\bullet}_{O}\}'$, $\{Cr''''_{Zr} : V^{\bullet\bullet}_{O}\}''$ and $\{Fe''''_{Zr} : V^{\bullet\bullet}_{O}\}''$ clusters. Figure 5.11

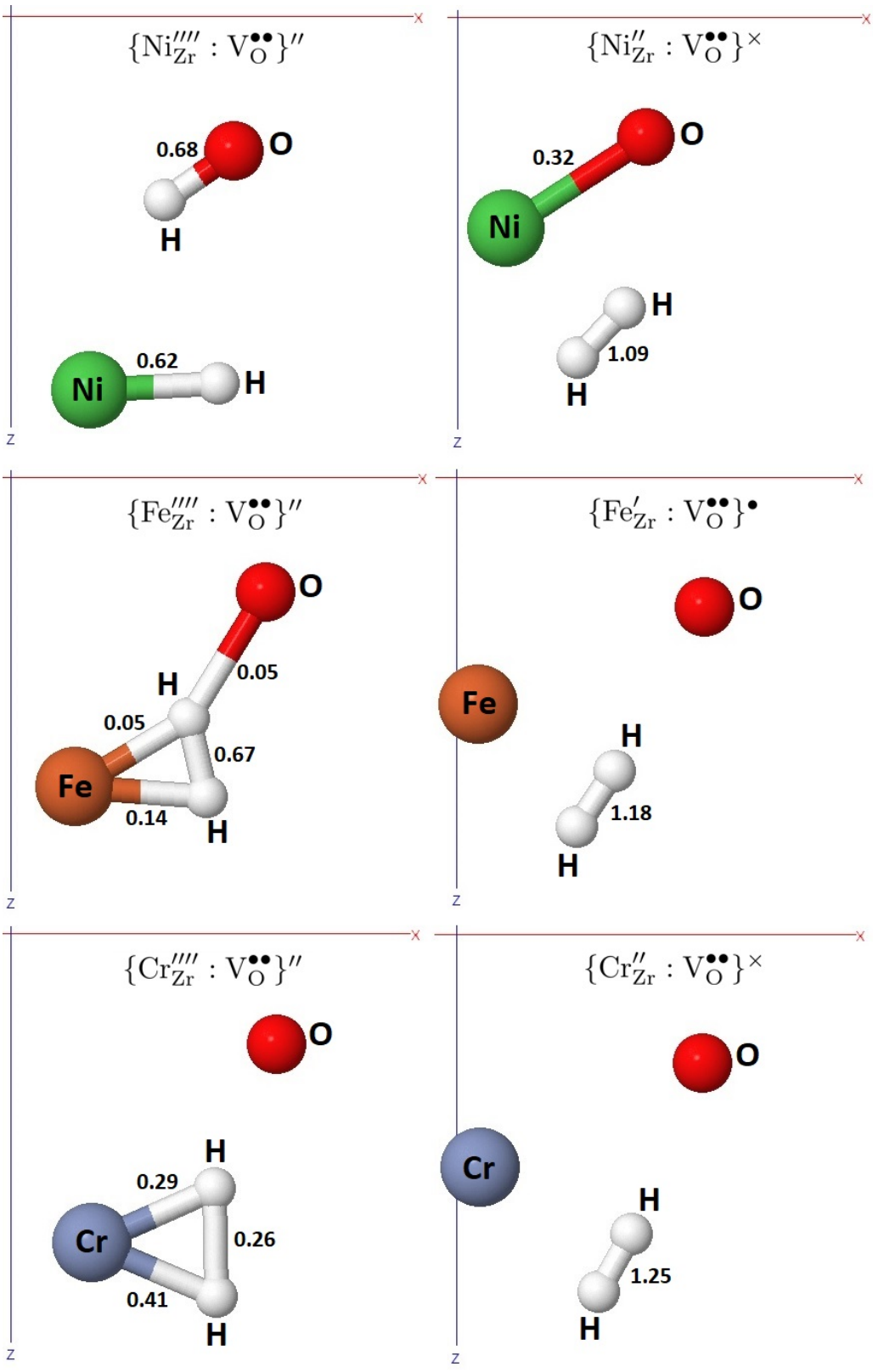


Figure 5.11: Predicted bonding interactions resulting from placing two H^+ ions into the oxygen vacancy site of the $\{M^Z_{Zr} : V^{\bullet\bullet}_O\}$ cluster with M = Ni, Cr or Fe. The numbers indicate the Mulliken bond populations.

illustrates that both the Cr^0 and Fe^0 containing clusters, do not lead to the dissociation of H_2^+. However, the resulting H_2^+ molecules exhibit lower H-H bond populations and longer bond lengths (see Table 5.5) than all other Cr and Fe containing defects that are predicted to be sufficient in concentration to be present in the Brouwer diagrams. Conversely, the $\{Ni_{Zr}''' : V_O^{\bullet\bullet}\}'$ cluster will promote H_2^+ dissociation in the same manner as $\{Ni_{Zr}'''' : V_O^{\bullet\bullet}\}''$. This supports the hypothesis that the propensity of the dopant Ni ion to take on a sufficiently low charge state, which in the case of ZrO_2 formed on Zircaloy-2 cladding is the predominantly neutral charge state, is crucial.

The interaction of the $\{Ni_{Zr}'''' : V_O^{\bullet\bullet}\}''$ cluster with H^+ ions might explain why Ni has been observed as detrimental to the HPUF of Zr based cladding by offering a mechanism in which Ni^0 is involved in a catalytic process. Given that Ni has been observed recently by XANES analysis to have a zero oxidation state close to the oxide metal interface [50], these results perhaps provide a mechanism for increased HPUF. Since one of the hydrogen atoms is bonded to the Ni and the other bonded to an oxygen, this offers the possibility that single H or H^+ species subsequently de-bond (either thermally or through some other mechanism) and continue their migration into the Zr metal. Finally, note the work by Lindgren and Panas [213]. They found, by investigating hydrogen reaction pathways in ZrO_2, a significantly lower chemical drive for H^+ ions confined in grain boundaries to recombine and be released as H_2, in the presence of a Ni dopant, as opposed to other transition metal dopant ions in the 2+ and 3+ charge states.

5.6 Copper and Antimony

In this section, defect concentrations are predicted for candidate dopants Cu and Sb. The focus will be on tetragonal ZrO_2 as this is the phase in which the proposed mechanism for increased HPUF by Ni addition was identified. Further, tetragonal ZrO_2 is observed in higher proportions the inner protective oxide of the cladding.

5.6.1 Brouwer diagrams

Predicted dopant concentrations are presented in Figures 5.12 and 5.13 for Sb at 10^{-4} and 10^{-3} units per ZrO_2 respectively and Figures 5.14 and 5.15 for Cu at 10^{-4} and 10^{-3} units per ZrO_2. The Brouwer diagram methodology assumes the dopant is distributed evenly in the oxide. This may well not be the case and further, the amount of Cu and Sb in the oxide will not be identical, which is why concentration dependence was considered.

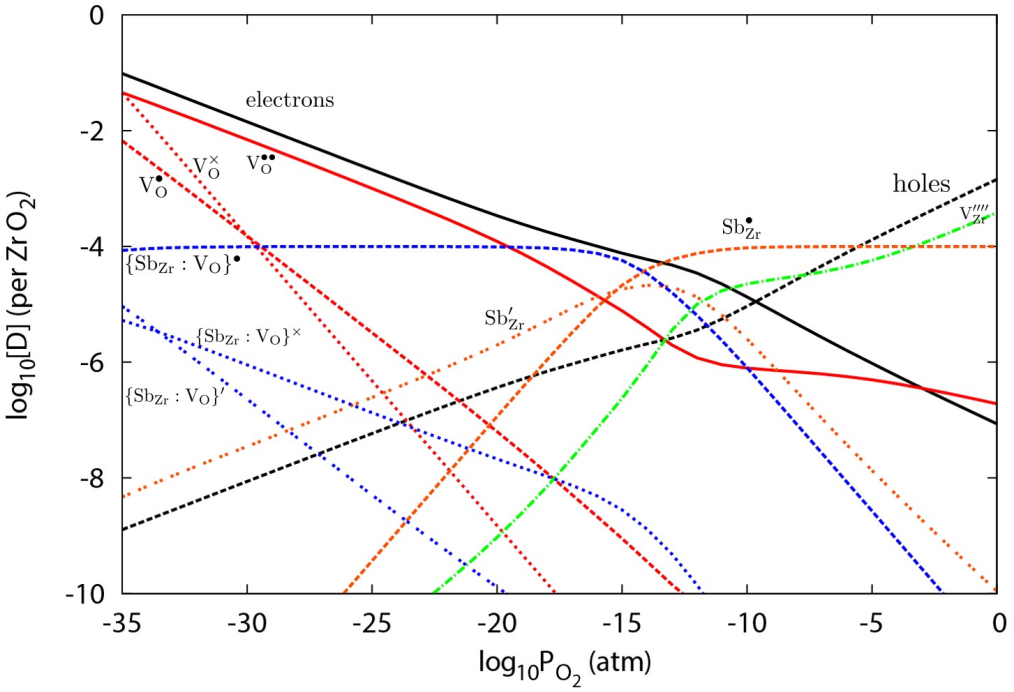


Figure 5.12: Brouwer diagram showing the predicted defect concentrations as a function of oxygen partial pressure in tetragonal ZrO_2 at 1500 K at a total Sb defect concentration of 10^{-4} atoms per formula unit ZrO_2. Substitutional dopants, dimer and trimer clusters are in orange, dark blue and light blue lines respectively. Defects with concentrations below 10^{-6} at all P_{O_2} are not shown.

Figures 5.12 and 5.13 show the predicted favourable charge states for Sb are 3+ and 5+, as in previous work [54]. Above approximately 10^{-14} P_{O_2}, Sb mainly occupies Zr sites in the 5+ charge state. At lower P_{O_2}, Sb assumes the 3+ state as well as binding with an oxygen vacancy to form $\{Sb'_{Zr} : V^{\bullet\bullet}_O\}^{\bullet}$. This transition point is the same for Sb concentrations 10^{-3} and 10^{-4} units per ZrO_2, though with increasing Sb content, Sb'_{Zr} becomes dominant around this transition point rather than the cluster.

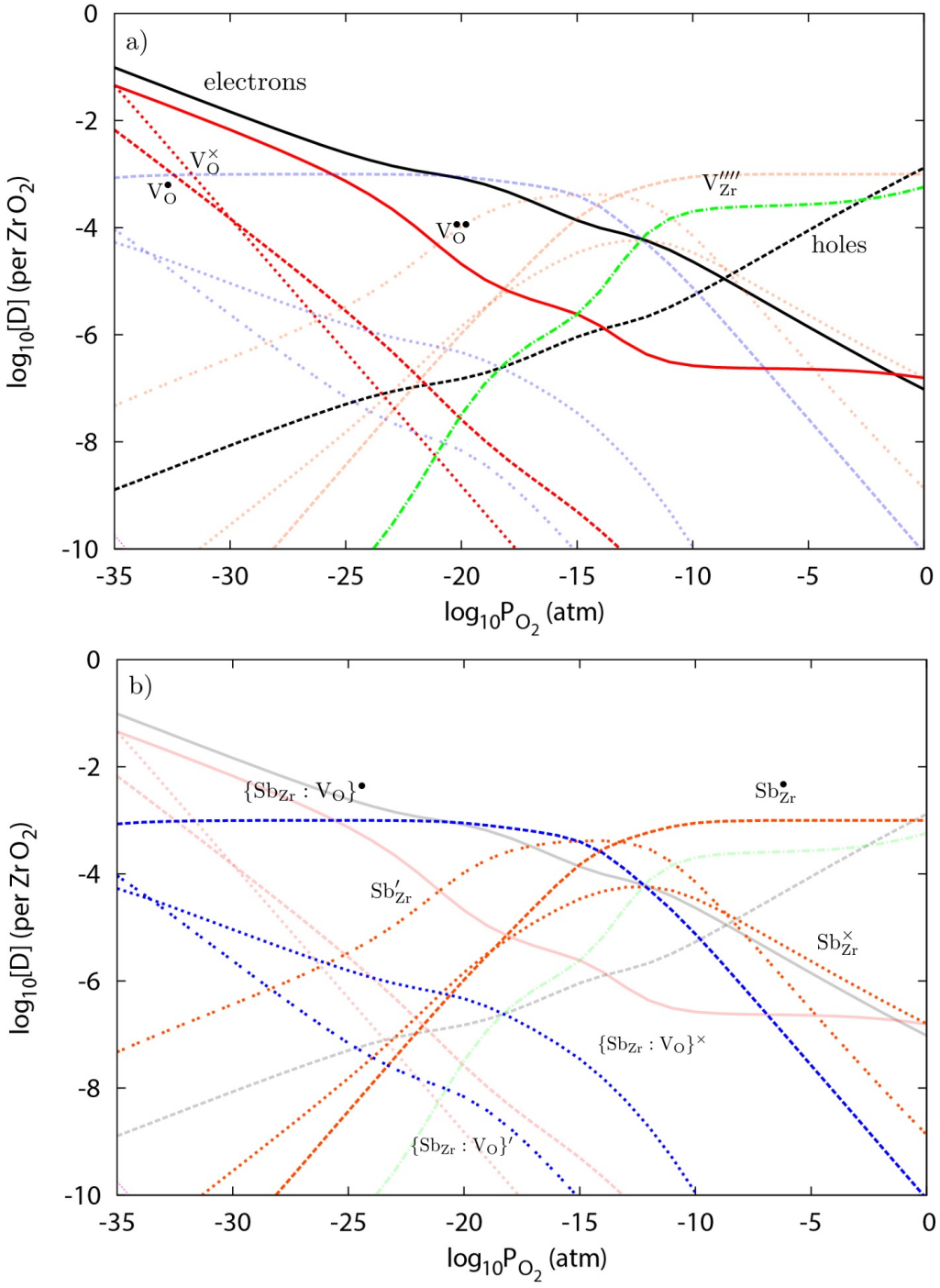


Figure 5.13: Brouwer diagram showing defect concentrations as a function of oxygen partial pressure in tetragonal ZrO_2 at 1500 K, at a total Sb defect concentration of 10^{-3} atoms per formula unit ZrO_2. a) highlights the intrinsic defects while b) highlights the dopant containing defects. Substitutional dopants, dimer and trimer clusters are shown as orange, dark blue and light blue lines respectively. Defects with concentrations below 10^{-5} at all P_{O_2} are not shown.

Figures 5.14 and 5.15 indicate for Cu, the preference is for 1+, 2+ and 3+ charge states. When introduced at 10^{-4} units per ZrO_2, the Cu'_{Zr} defect is dominant at P_{O_2} higher than

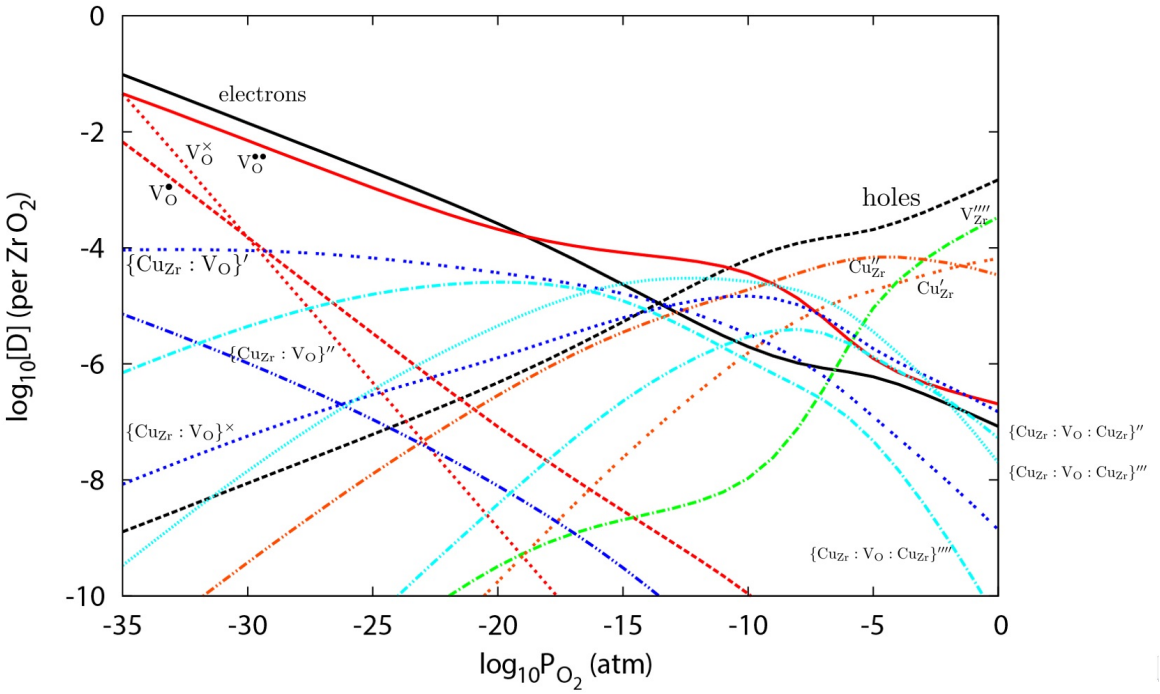


Figure 5.14: Brouwer diagram showing defect concentrations as a function of oxygen partial pressure in tetragonal ZrO_2 at 1500 K, at a total Cu defect concentration of 10^{-4} atoms per formula unit ZrO_2. Substitutional dopants, dimer and trimer clusters are shown as orange, dark blue and light blue lines respectively. Defects with concentrations below 10^{-6} at all P_{O_2} are not shown.

10^{-2}, and the Cu_{Zr}'' defect at P_{O_2} between 10^{-2} and 10^{-9}. From 10^{-16} to 10^{-9} P_{O_2}, the trimer $\{Cu_{Zr} : V_O : Cu_{Zr}\}'''$ is dominant and at P_{O_2} below that $\{Cu_{Zr}''' : V_O^{\bullet\bullet}\}'$ is the most populous Cu containing defect. At a concentration of 10^{-3} units per ZrO_2, Cu_{Zr}' is most prevalent above 10^{-5} P_{O_2} and below that, a mixture of dimer and trimer states containing Cu^{1+} and Cu^{2+} make the situation complex. Clearly the dominant defect species and charge state are more dopant concentration dependent in the case of Cu than for Sb. The predicted dominant dopant containing defect for both dopant species at 10^{-4} units per ZrO_2 concentration across P_{O_2} values is summarised in Figure 5.16.

The binding energies reported in Figure 5.16 are significant enough that it is not expected that these clusters dissociate thermally even at temperatures well beyond normal reactor operation. It is therefore likely that Cu and Sb impact oxygen transport by impeding the vacancy hopping mechanism and in this manner (alone), reduce the cladding corrosion rate. This effect was also identified for Fe, Cr and Ni in earlier sections. On the other hand for Cu, Figures 5.14

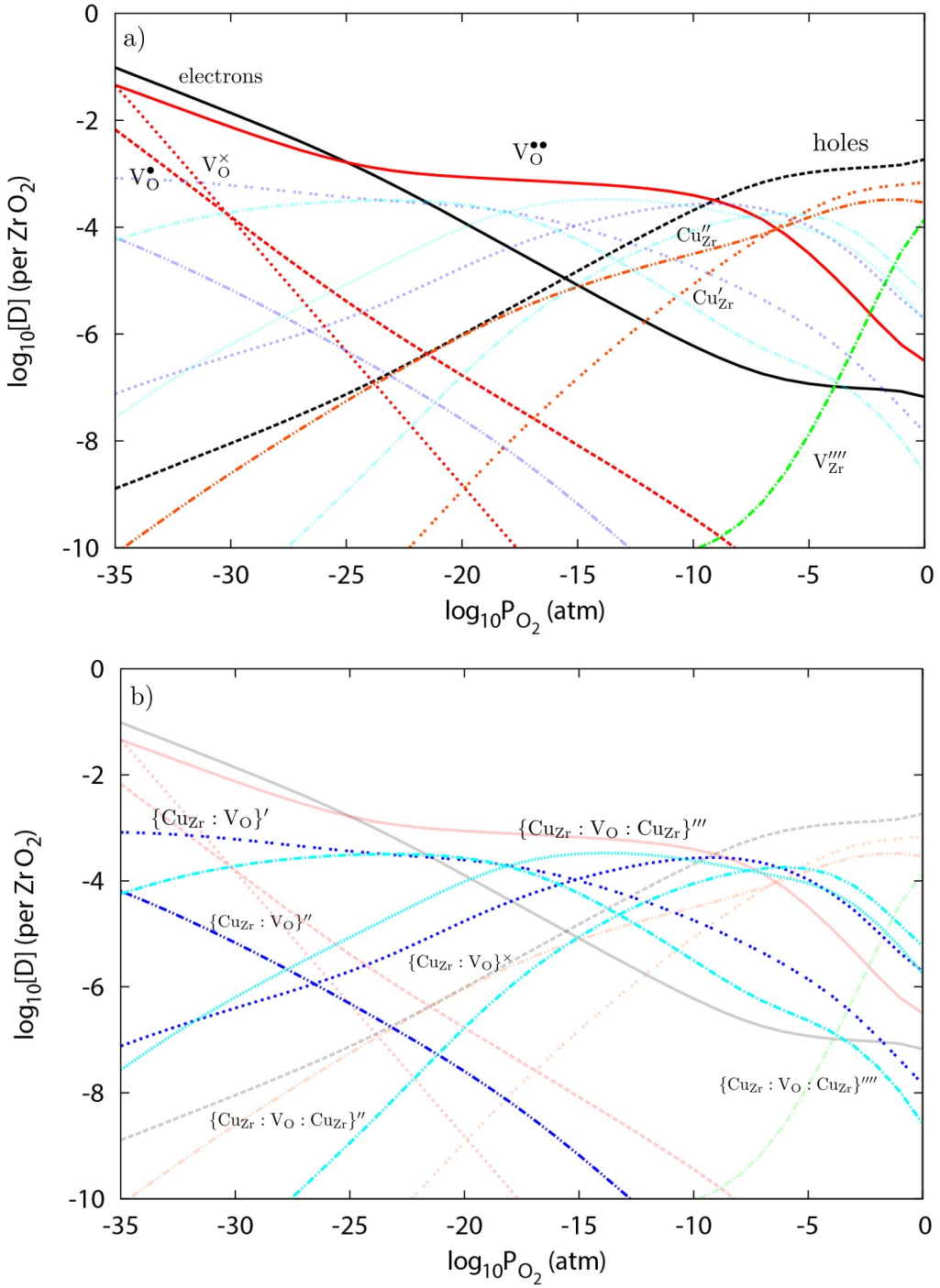


Figure 5.15: Brouwer diagram showing defect concentrations as a function of oxygen partial pressure in tetragonal ZrO_2 at 1500 K, at a total Cu defect concentration of 10^{-3} atoms per formula unit ZrO_2. a) highlights the intrinsic and dopant substitution defects while b) highlights the cluster defects. Substitutional dopants, dimer and trimer clusters are shown as orange, dark blue and light blue lines respectively. Defects with concentrations below 10^{-5} at all P_{O_2} are not shown.

and 5.15 indicate an elevated concentration of single $V_O^{\bullet\bullet}$ compared to a Cu free material. This will elevate the oxygen conductivity and will therefore increase the corrosion rate. Figure 5.17

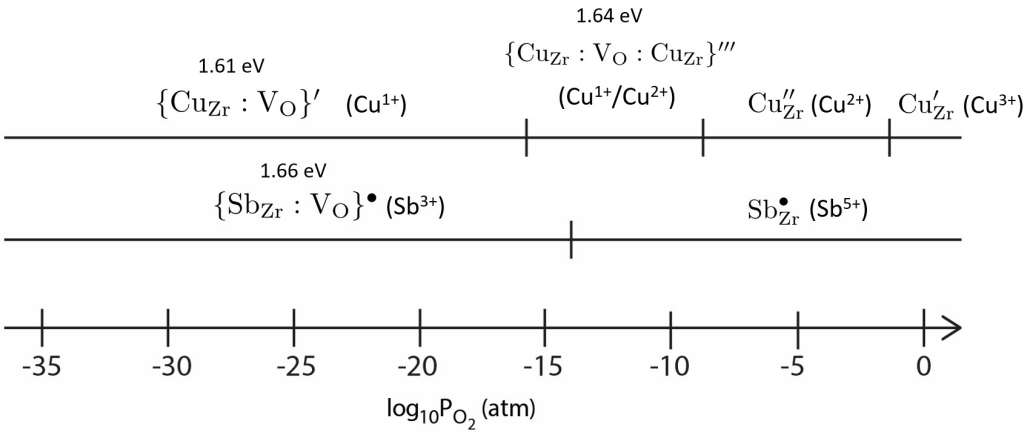


Figure 5.16: The dominant dopant containing defect for Cu and Sb, at a concentration of 10^{-4} units per ZrO_2, as a function of P_{O_2}. Energies beside the indicated defects are the binding energies per bond of each cluster. The charge state of the dopant cations are indicated in parenthesis.

shows that the concentration of free $V_O^{\bullet\bullet}$ increases with increasing Cu concentration. Further, with increasing Cu concentration, the onset of an elevation in the $V_O^{\bullet\bullet}$ concentration (i.e. beyond that expected in a Cu free material) begins at a lower P_{O_2} and also covers a wider P_{O_2} range. The increased number of Cu adjacent sites to which $V_O^{\bullet\bullet}$ can be bound is in opposition to the elevation of free $V_O^{\bullet\bullet}$ at higher Cu content. Therefore, the benefit to corrosion resistance from the clustering mechanism should be balanced against the increase in carriers ($V_O^{\bullet\bullet}$). This may be the reason why, in experimental work, a Cu concentration was identified at around 0.1 wt.% in the alloy, beyond which further additions of Cu were detrimental to corrosion [86]. Of course, 0.1 wt.% in the alloy does not mean this is the amount dissolved in the metal, which will be less but it would nonetheless increase the amount of Cu available to be dissolved into the matrix.

In contrast to Cu, increasing Sb content causes a decrease in the $V_O^{\bullet\bullet}$ concentration (see Figure 5.17). This implies that an increased Sb concentration should slow the corrosion rate. This may be attributed to the dominant Sb defects having net positive charge in contrast with dominant Cu defects having net negative charge. Furthermore, with Sb the electron concentration increased as charge compensation for the positively charged Sb defects. This could lead to reduced hydrogen pickup in the metal, as the reduction of H^+ back to harmless H_2 should be more efficient.

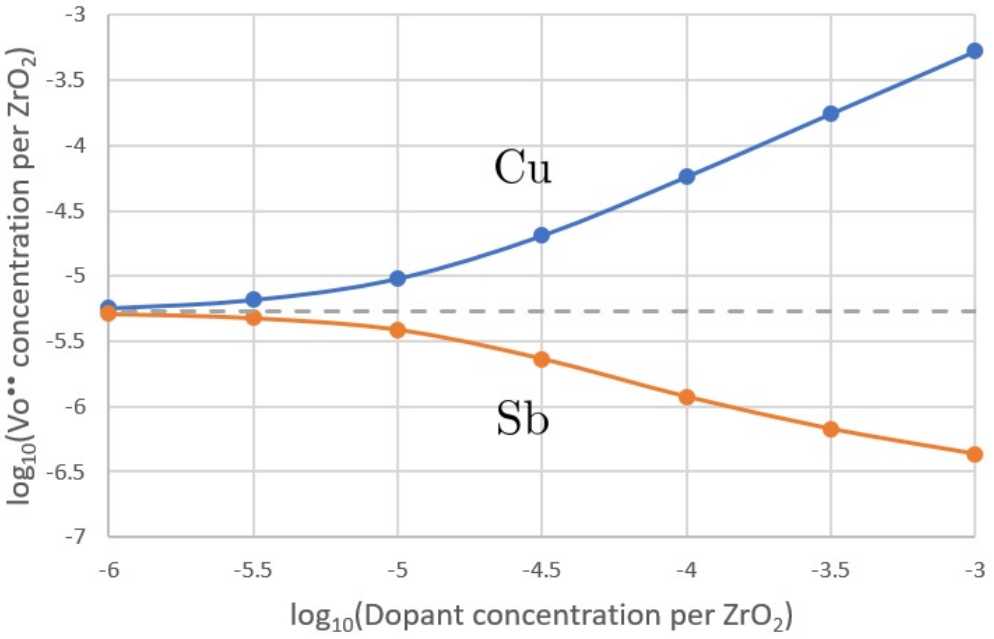


Figure 5.17: Change in free $V_O^{\bullet\bullet}$ concentration as a function of dopant concentration at $P_{O_2} = 10^{-12}$ atm and 1500 K temperature. The grey dashed line indicates the case of undoped ZrO_2.

Finally, the defect relaxation and clustering volumes for relevant defects are reported in Table 5.6. As with the case of Fe, the large positive relaxation volumes of single substitutional Cu and Sb, in contrast to the negative relaxation volume of $V_O^{\bullet\bullet}$, is a key driver in the favourable formation energies of the cluster defects. Comparing Cu and Sb, the volume changes upon clustering in Cu are significantly larger those associated with Sb. Further, Cu forms trimers that exhibit even larger clustering volumes while Sb does not. It is then expected with the addition of Cu, the formation of trimers defects, as well as all other Cu-containing defects having large positive relaxation volumes, will lead to an increase in compressive stresses within the oxide. This may, in turn, result in an earlier onset of cracking in the protective oxide layer. Sb however, supports a mix of defects with both positive and negative relaxation volumes, thus the impact on oxide stability is expected to be minimal.

Table 5.6: Relaxation volumes and clustering volumes of selected Cu and Sb defects in tetragonal ZrO_2.

Defect	Relaxation Volume (Å^3)	Volume change upon clustering (Å^3)
$\{Cu''_{Zr} : V^{\bullet\bullet}_{O}\ Cu''_{Zr}\}''$	52.91	24.21
$\{Cu'''_{Zr} : V^{\bullet\bullet}_{O}\ Cu''_{Zr}\}'''$	64.63	17.82
$\{Cu'''_{Zr} : V^{\bullet\bullet}_{O}\ Cu'''_{Zr}\}''''$	79.00	14.08
$\{Cu''_{Zr} : V^{\bullet\bullet}_{O}\}^{\times}$	3.96	8.15
$\{Cu'''_{Zr} : V^{\bullet\bullet}_{O}\}'$	17.90	3.98
$\{Cu''''_{Zr} : V^{\bullet\bullet}_{O}\}''$	36.09	4.72
Cu'_{Zr}	19.07	-
Cu''_{Zr}	32.89	-
Cu'''_{Zr}	51.00	-
Cu''''_{Zr}	68.45	-
$\{Sb'_{Zr} : V^{\bullet\bullet}_{O}\}^{\bullet}$	-10.14	2.91
$\{Sb''_{Zr} : V^{\bullet\bullet}_{O}\}^{\times}$	4.78	0.15
$\{Sb'''_{Zr} : V^{\bullet\bullet}_{O}\}'$	24.19	1.87
$Sb^{\bullet}_{Zr}$	-15.92	-
$Sb^{\times}_{Zr}$	3.75	-
Sb'_{Zr}	24.03	-
Sb''_{Zr}	41.71	-
Sb'''_{Zr}	59.40	-
$V^{\bullet\bullet}_{O}$	-37.08	-

5.6.2 Cu and Sb interaction with hydrogen

The prediction that the $\{Cu'''_{Zr} : V^{\bullet\bullet}_{O}\}'$ cluster is present at a significant concentration is potentially important, as it contains the Cu^{1+} ion. This has the same electronic structure as metallic Ni^0. Section 5.5 reports that Ni^0 may make a key contribution towards the negative impact of Ni in increasing the hydrogen pickup in Zr based cladding. The potential influence of $\{Cu'''_{Zr} : V^{\bullet\bullet}_{O}\}'$ is therefore investigated though the same approach. Thus, calculations were conducted to determine if it is more energetically favourable for two H^+ to form H_2^+ compared to being separated as in the configuration favoured adjacent to the $\{Ni''''_{Zr} : V^{\bullet\bullet}_{O}\}''$ cluster (see Figure 5.18). This includes the energy where only an isolated $V^{\bullet\bullet}_{O}$ is involved (i.e. without the intervention of a dopant metal species). The difference in DFT energies for the two configurations are reported in Table 5.7. Significantly, the $\{Cu'''_{Zr} : V^{\bullet\bullet}_{O}\}'$ cluster does not stand out in this aspect. Further, the energy difference in the presence of Cu is the same as for the free $V^{\bullet\bullet}_{O}$ (i.e. in the absence of Cu). Conversely, in the case of Ni, as reported in Section 5.5, the H_2^+

molecule is not stable; it is only stable in the dissociated configuration.

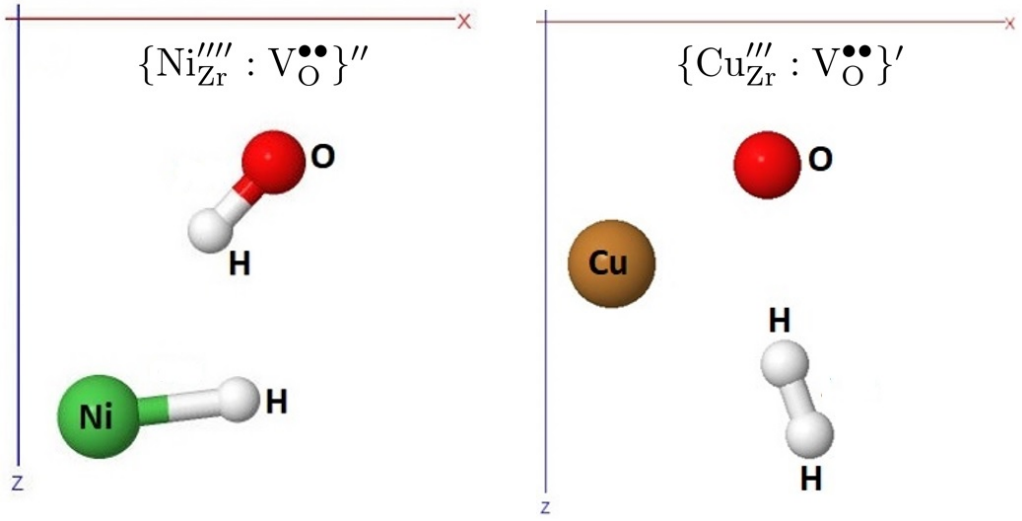


Figure 5.18: Final atomic configurations resulting from placing two H^+ ions into the oxygen vacancy site of $\{Ni''''_{Zr} : V^{\bullet\bullet}_{O}\}''$ and $\{Cu'''_{Zr} : V^{\bullet\bullet}_{O}\}'$ clusters.

To investigate further, DFT calculations were performed as according to Section 5.5. In the case of the Ni^0 containing $\{Ni''''_{Zr} : V^{\bullet\bullet}_{O}\}''$ cluster, the H^+ ions remain split, binding to the substitutional Ni ion and an adjacent oxygen ion respectively. This behaviour was not observed for Cu^{1+} (nor other Cu charge states). Thus, the results imply that the additional positive charge on the Cu^{1+} ion, as compared to Ni^0, is sufficient to negate the detrimental hydrogen pickup behaviour seen in Ni.

The same analysis was performed on the defect configurations dominant at the lowest P_{O_2} for Sb (i.e. $\{Sb'_{Zr} : V^{\bullet\bullet}_{O}\}^{\bullet}$). The two H^+ ions combined to form a H_2^+ molecule. This suggests the Sb containing cluster will not increase hydrogen pickup in the same fashion as postulated for Ni.

Table 5.7: Energy difference between split H^+ and molecular H_2^+ configurations when two H^+ ions are placed into the oxygen vacancy sites of the specified defects. A positive value indicates the H_2^+ configuration is lower in energy but an energy barrier between the configurations exists. (* For $\{Ni_{Zr}'''' : V_O^{\bullet\bullet}\}''$ no barrier exists with the split configuration exhibiting the minimum energy.)

Defect	Energy difference (eV)
$\{Cu_{Zr}''' : V_O^{\bullet\bullet}\}'$	-0.32
$\{Cu_{Zr}'' : V_O^{\bullet\bullet}\}^\times$	-0.49
$\{Cr_{Zr}'' : V_O^{\bullet\bullet}\}^\times$	0.05
$\{Sb_{Zr}''' : V_O^{\bullet\bullet}\}'$	0.18
$\{Fe_{Zr}' : V_O^{\bullet\bullet}\}^\bullet$	-0.27
$\{Ni_{Zr}'''' : V_O^{\bullet\bullet}\}''$	—*
$V_O^{\bullet\bullet}$	-0.31

5.6.3 Space charge considerations

The difference in diffusivities of electrons and $V_O^{\bullet\bullet}$ results in a positive space charge away from the metal/oxide interface and the oxide surface [7]. Note that Couet *et al.* predict the amount of space charge present in the oxide from around 10^{-4} e^- at the both the metal/oxide interface and oxide surface to 10^{-2} e^- per ZrO_2 in the middle of the oxide [7]. The response of the dopants to charge compensate is simulated by imposing a negative q_{sc} on the defect system (see Section 3.3.2 for further details).

With regard to Sb, previous simulation work (that assumed the presence of only isolated Sb defects) predicted that the charge state of Sb would change smoothly from 3+ to 5+ to compensate for any local space charge due to the relatively small energy difference between the charge states [54]. The analysis from Bell *et al.* [54] is verified by applying a space charge q_{sc} to the Sb and Cu systems, here with the added consideration of cluster defects.

The results for Sb, with clusters now included, are presented in Figure 5.19 for the usual range of P_{O_2}. This shows that the charge state of Sb, still smoothly compensates for positive space charge via the transition between 3+ and 5+ charge states. Space charge effects were also considered for Cu, which show, especially when considering the preferred Cu charge state, smooth compensation even when space charge is applied beyond 10^{-3} e^- per ZrO_2 (see Figure 5.20).

The transition at P_{O_2} around $10^{-3.6}$ atm is, however, rather steep. Figure 5.20a shows that there is a transition in the dominant defect from a single Cu^{1+} to a $\{Cu_{Zr} : V_O : Cu_{Zr}\}''''$ cluster followed by a further transition to a $\{Cu_{Zr} : V_O\}'$ cluster at even lower P_{O_2}. Crucially, Figure 5.20b shows that none of these affect the Cu charge state, which stays at +1.

Within the relevant space charge range, both Cu and Sb retain their energetic preference for clustering and thus the associated benefit to corrosion resistance is still expected. Outside of the crossover points, the dominant defects significantly outnumber other dopant containing defects and thus no significant response to the applied space charge is expected. The inability to build up charge in the oxide is associated with higher hydrogen pickup and tendency towards undesirable parabolic corrosion kinetics in Zr-Nb alloys [7, 8, 54]. For the dopants investigated in this work, charge compensation mechanisms occur above P_{O_2} of 10^{-16} atm for Cu (see Figure 5.20) and around 10^{-14} to 10^{-9} atm for Sb (see Figure 5.19) and thus are not expected to impact the inner protective oxide. In contrast, similar analysis for Nb has reported a transition from 3+ to 5+ charge state at a P_{O_2} of around 10^{-29} atm [54].

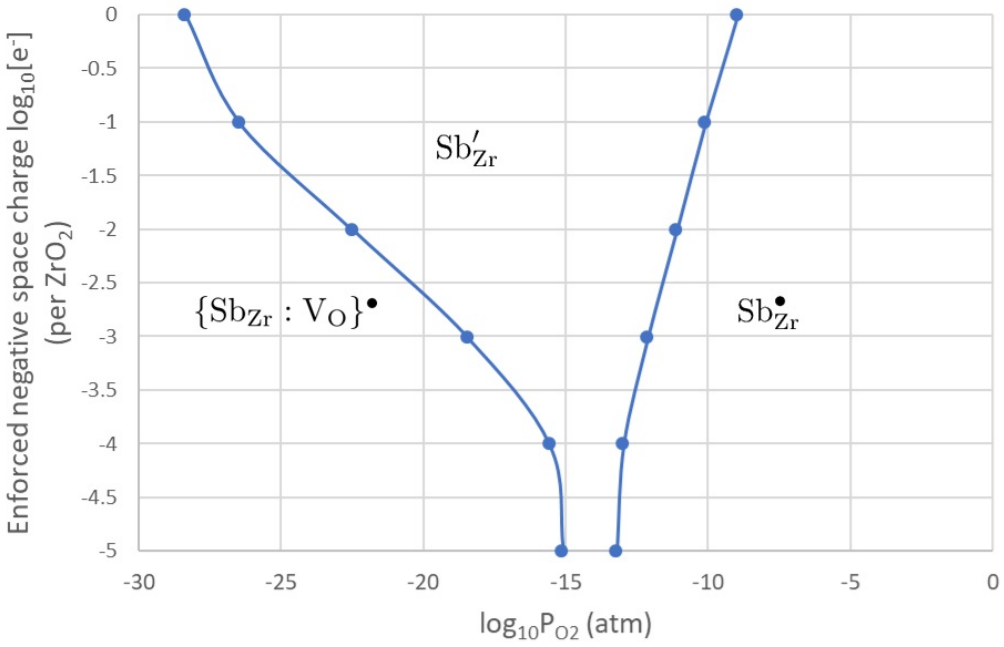


Figure 5.19: Boundaries signifying changes to the dominant Sb defect (when included at 10^{-3} units per ZrO_2) as a function of applied space charge and P_{O_2}.

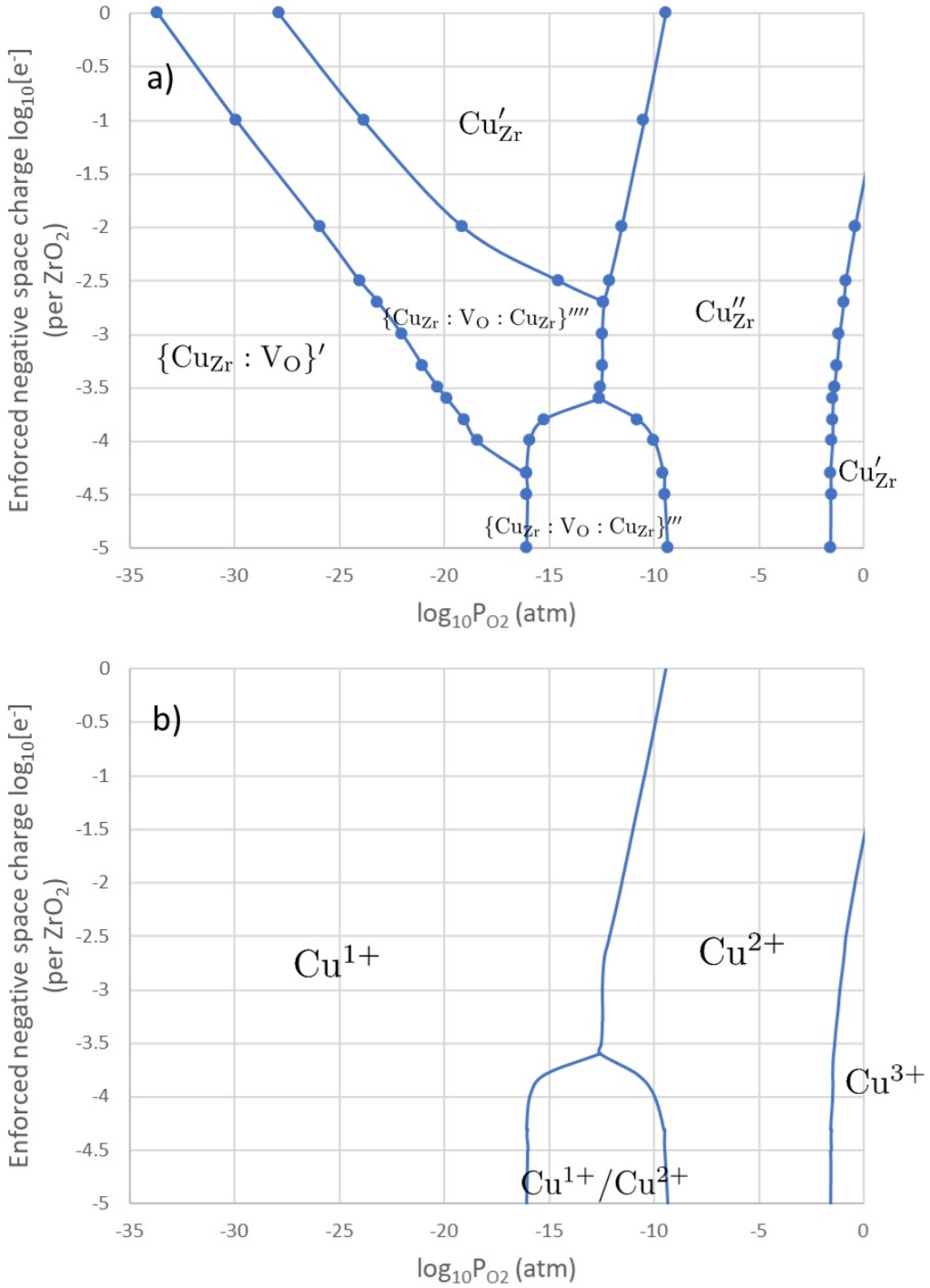


Figure 5.20: Boundaries signifying changes to: a) the dominant Cu defect and b) the dominant Cu charge state (when included at 10^{-4} units per ZrO_2) as a function of applied space charge and P_{O_2}.

5.7 Lithium

Figures 5.21 and 5.22 shows the predicted defect concentrations for in tetragonal ZrO_2 when Li is incorporated at 10^{-4} units per ZrO_2 at 1500 K. Li favours the 1+ oxidation state at all

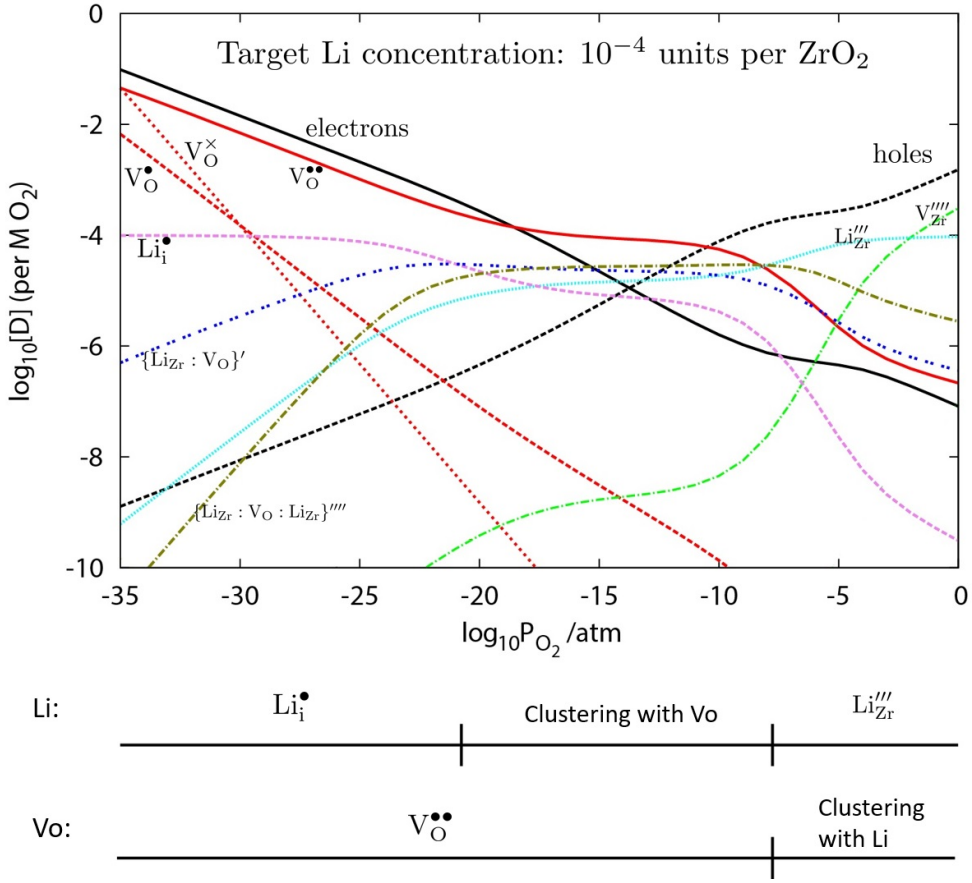


Figure 5.21: Brouwer diagram showing the predicted defect concentration as a function of oxygen partial pressure in tetragonal ZrO_2 at 1500 K at a total Li defect concentration of 10^{-4} atoms per formula unit ZrO_2. Transition points for the prefered sites for Li and oxygen vacancies are also shown. Defects with concentrations below 10^{-6} at all P_{O_2} are not shown.

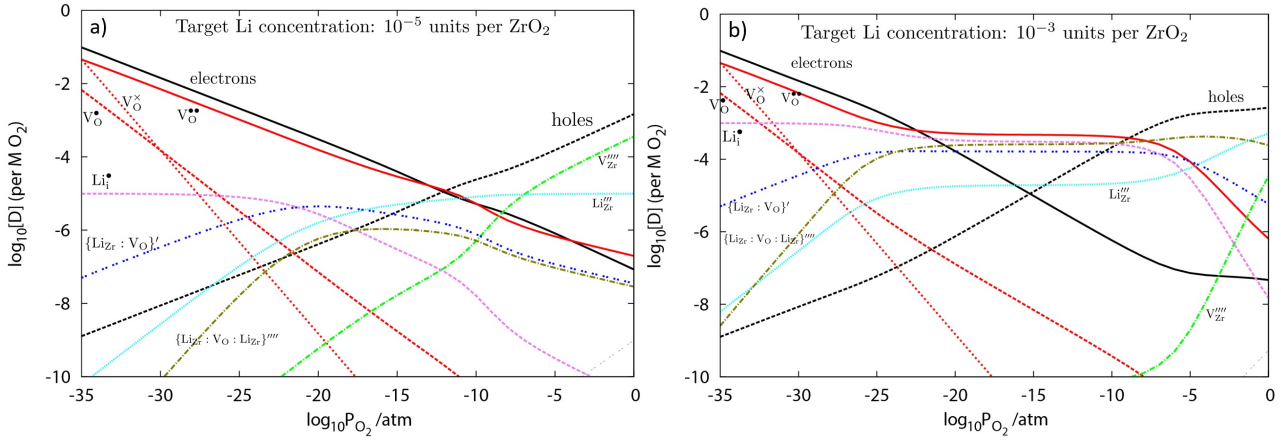


Figure 5.22: Brouwer diagrams showing defect concentrations in tetragonal ZrO_2 at 1500 K as a function of oxygen partial pressure at Li concentration of a) 10^{-5} atoms per formula unit ZrO_2 and b) 10^{-3} atoms per formula unit ZrO_2. Defects with concentrations below 10^{-6} at all P_{O_2} are not shown.

P_{O_2}. At low P_{O_2}, Li occurs preferentially as a single substitution Li'''_{Zr}. As P_{O_2} decreases below 10^{-8} atm, Li begins to prefer clustering in a mixture of $\{Li_{Zr} : V_O\}'$ and $\{Li_{Zr} : V_O : Li_{Zr}\}''''$, with binding energies of 2.52 eV and 2.72 eV respectively. This is due to the higher concentration of $V_O^{\bullet\bullet}$ available. As P_{O_2} decreases below 10^{-21} atm, Li is pushed to interstitial sites as the concentration of V_{Zr} becomes too low for the substitutional defect to be favourable. Figure 5.23 shows these transition points as a function of Li concentration. Similar analysis was performed

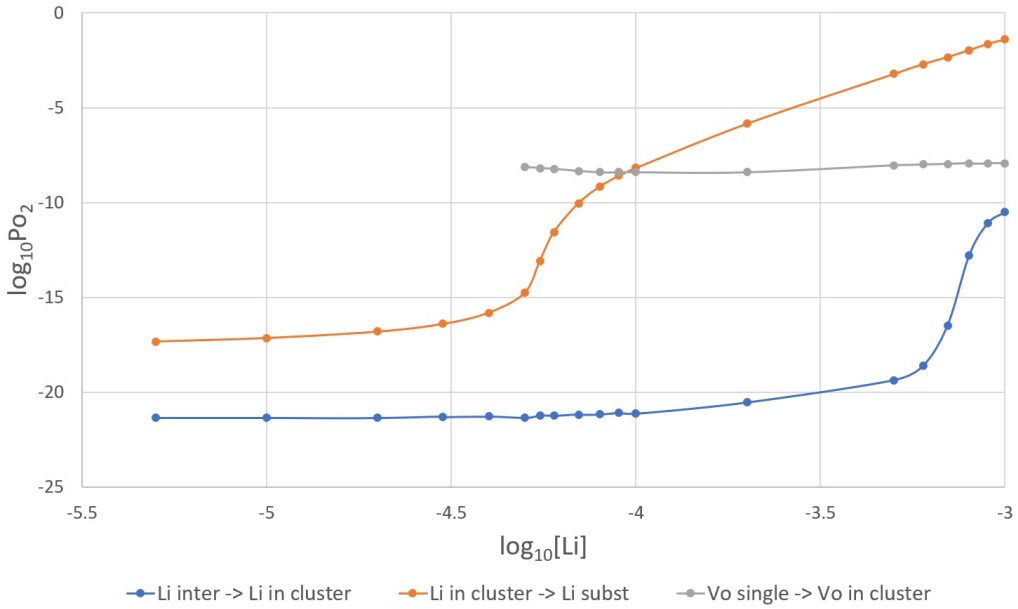


Figure 5.23: Plot showing transition points for Li favouring $Li_i^{\bullet}$, to clustering with $V_O^{\bullet\bullet}$, and then to Li'''_{Zr} as a function of Li concentration. Also shown are the transition points for single $V_O^{\bullet\bullet}$ being favoured to clustering with Li being favoured as a function of Li concentration. Below a Li concentration of 3×10^{-5}, $V_O^{\bullet\bullet}$ is the dominant oxygen vacancy defect at all P_{O_2}.

for V_O, where at Li concentrations below 3×10^{-5} units per ZrO_2, $V_O^{\bullet\bullet}$ is prefered at all P_{O_2}. Above 3×10^{-5} Li per ZrO_2, $V_O^{\bullet\bullet}$ always clusters with Li at above around 10^{-8} P_{O_2}.

Elevated free $V_O^{\bullet\bullet}$ concentrations at an increasingly wider P_{O_2} range are also predicted with increasing Li concentration (compare plots in Figures 5.21 and 5.22). The elevated $V_O^{\bullet\bullet}$ concentration would boost oxygen diffusivity, thereby contributing to an increased corrosion rate. This mechanism for accelerated corrosion contrasts with results presented by Yang *et al.*, which predict an increased O_i'' concentration as the consequence of the presence of Li [18]. It is interesting to note that Yang *et al.* predict oxygen vacancies to have concentrations below $10^{-}20$ units per ZrO_2 even at P_{O_2} as low as 10^{-30} atm in tetragonal and monoclinic ZrO_2 for both the

doped and undoped cases [18]. Given that the inner protective layer of the oxide is expected to be oxygen deficient (approaching where sub-stoichiometric oxide is formed, see Section 1.2.4), the Brouwer diagrams presented by Yang *et al.* may not be representative of the oxide in such regions. In fact, in a separate publication, simulation work by the same authors have predicted oxygen transport at low P_{O_2} to be vacancy dominated [9]. Nevertheless, the results presented here supplements the analysis by Yang *et al.* by providing insight on the behaviour of Li in oxygen deficient regions fo the oxide.

The Brouwer diagrams for monoclinic ZrO_2 are shown in Figure 5.24. At low P_{O_2}, Li exhibits

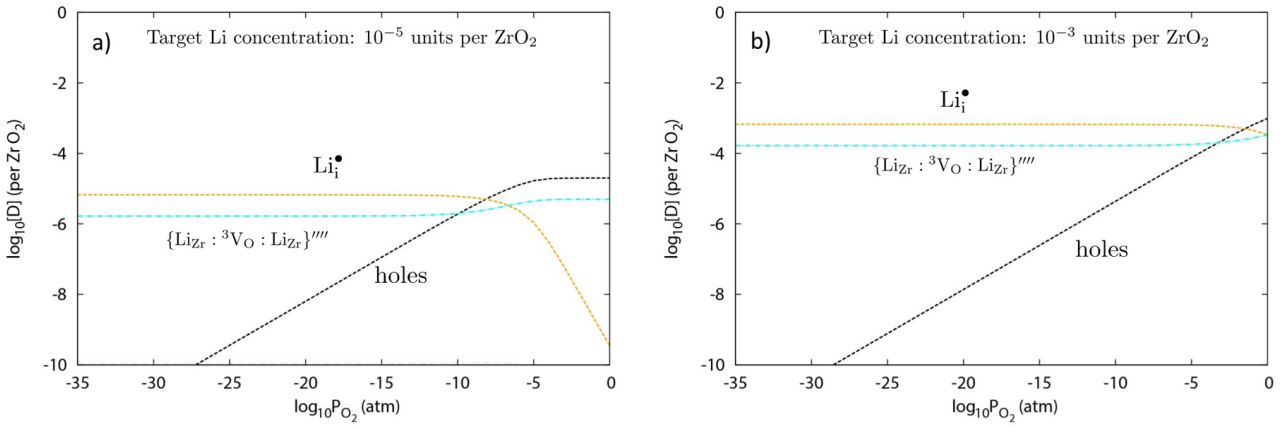


Figure 5.24: Brouwer diagram showing the predicted defect concentration as a function of oxygen partial pressure in monoclinic ZrO_2 at 635 K at a total Li defect concentration of a) 10^{-5} atoms per formula unit ZrO_2 and b) 10^{-3} atoms per formula unit ZrO_2. Defects with concentrations below 10^{-7} at all P_{O_2} are not shown. ${}^3V_O$ refers to vacancies at the 3-coordinated oxygen site (as opposed to the 4-coordinated site) in m-ZrO_2.

a preference to occupy an interstitial site with a 1+ charge state at low P_{O_2}, with formation of the $\{Li_{Zr} : {}^3V_O : Li_{Zr}\}''''$ cluster also predicted as a charge compensation mechanism. With increasing P_{O_2}, the preference for electron holes instead of $Li_i^{\bullet}$ as charge compensation for the $\{Li_{Zr} : {}^3V_O : Li_{Zr}\}''''$ cluster grows, until a threshold is reached where the $Li_i^{\bullet}$ concentration drops sharply, leaving the $\{Li_{Zr} : {}^3V_O : Li_{Zr}\}''''$ cluster as the predominant Li defect. This threshold occurs at around 10^{-7} atm P_{O_2} when Li is included at a concentration of 10^{-5} units per ZrO_2 and increases with Li concentration, until at a Li concentration of 10^{-3} units per ZrO_2, above which the switch ceases to occur.

Tables 5.8 and 5.9 report the defect relaxation and clustering volumes for relevant defects. In both phases of oxide, substitutional and clustered Li defects have large positive relaxation volumes while the Li interstitial has a negative relaxation volume. Both types of defects are predicted in significant concentrations in both phases of oxide, therefore, a strong impact on internal stresses and oxide stability is not expected.

Table 5.8: Relaxation volumes and clustering volumes of selected Li defects in tetragonal ZrO_2.

Defect	Relaxation Volume (Å^3)	Volume change upon clustering (Å^3)
$\{Li_{Zr}''' : V_O^{\bullet\bullet}\ Li_{Zr}'''\}''''$	69.44	10.26
$\{Li_{Zr}''' : V_O^{\bullet\bullet}\}'$	15.13	4.08
$\{Li_{Zr}'''' : V_O^{\bullet\bullet}\}''$	32.86	4.45
Li_{Zr}'''	48.13	-
Li_{Zr}''''	65.49	-
$Li_i^{\bullet}$	-9.45	-
$V_O^{\bullet\bullet}$	-37.08	-

Table 5.9: Relaxation volumes and clustering volumes of selected Li defects in monoclinic ZrO_2.

Defect	Relaxation Volume (Å^3)	Volume change upon clustering (Å^3)
$\{Li_{Zr}''' : {}^3V_O^{\bullet\bullet}\ Li_{Zr}'''\}''''$	47.89	-5.44
Li_{Zr}'''	39.74	-
Li_{Zr}''''	53.02	-
$Li_i^{\bullet}$	-11.05	-
${}^3V_O^{\bullet\bullet}$	-26.15	-

5.8 Summary

Defect processes were investigated in monoclinic and tetragonal ZrO_2 doped with current alloying elements (Fe, Cr and Ni) in Zr-based cladding, as well as candidate alloying elements (Cu and Sb) and Li which comes into contact with ZrO_2 in the coolant water. Using DFT based simulations (see Section 3.3.2), defect formation energies were calculated. These were used to predict the concentrations of the different configurations in which the dopant species are accommodated, along with charge compensating oxygen vacancies.

All dopant elements (current and proposed) were predicted to bind strongly to oxygen vacancies at low P_{O_2}. This impedes oxygen vacancy mobility in the oxide, which is proposed as the mechanism by which the dopant elements hinder oxygen transport and thereby lower corrosion rate.

When two H^+ ions were placed in the oxygen vacancy site of a $\{Ni''''_{Zr} : V^{\bullet\bullet}_{O}\}''$ cluster, one of the H^+ ions bonded to the Ni^0 while the other bonded to a neighbouring oxygen. Interaction with $2H^+$ was also considered for all other clusters (for current and proposed dopant elements) that are predicted in significant enough concentration to be in the Brouwer diagrams. None were able to produce the same effect as Ni^0 but instead the H^+ ions came together to form a H_2^+ molecule. The unique interaction of Ni^0 with hydrogen differentiates Ni from the other alloying elements, and offers a possible mechanism for the increase in HPUF of Zr-based fuel cladding observed experimentally. This also means that the proposed alloying elements investigated here (Cu and Sb) are not expected to be harmful to the HPUF in the same manner as Ni, which could have been a cause for concern.

In a comparison of the proposed alloying elements Cu and Sb, Cu promotes the formation of free oxygen vacancies (increases the oxygen vacancy concentration), which may increase the oxygen conductivity of the oxide and thus act to increase the corrosion rate. This may reflect experimental data where the corrosion rate increases when Cu is added beyond a certain critical concentration [86]. In contrast, Sb lowers the free oxygen vacancy concentration while also increasing the electron concentration, which explains the reduced corrosion and hydrogen pickup observed experimentally [54, 88]. Sb also facilitates the build up of space charges near the metal-oxide interface, thus avoiding the undesirable parabolic corrosion kinetics seen in Zr-Nb alloys. Further, considerations of defect volumes suggest the addition of Cu will contribute to compressive stresses in tetragonal ZrO_2 that lead to early oxide breakaway. Conversely, Sb additions are expected to have minimal impact on the oxide stress. Sb therefore shows good promise as a candidate alloying element in Zr based cladding.

The methodology employed here can also be extended to study the effect of chemicals that are present in the coolant water on the cladding oxide by treating them as dopant elements in the oxide. This is demonstrated here with inclusion of Li into ZrO_2, which is predicted to elevate free $V_O^{\bullet\bullet}$ concentration in tetragonal ZrO_2. This is a proposed mechanism by which Li accelerates oxidation of Zr-based cladding.

With regard to the objectives laid out in Section 1.5, two main mechanisms that can significantly impact cladding lifetime identified here are: dopant binding with oxygen vacancy and suppression of free oxygen vacancy concentration, which is predicted to lead to lower corrosion rates, as well as dopant interaction with H^+ ions described in Section 5.5 which is shown to be a key predictive factor for deleterious hydrogen pickup. By investigating prospective dopants for Zr-based cladding in the context of these mechanisms, Sb is identified to be a promising candidate that can be further studied in experiments. Finally, while not demonstrated in this work, the mechanisms identified here may also provide an initial methodology the similarly identify suitable dopant elements for other oxide forming cladding materials (that are also exposed to coolant water in operation) such as FeCrAl.

Chapter 6

Future Work

6.1 Electronic effects in MD damage cascade simulations

Electronic effects were not considered in MD radiation damage cascade simulations presented in Chapter 4 due to computational constraints. Other authors have attempted to address electronic effects by introducing a friction term to account for electronic stopping [103]. The PKA energy lost in this manner is permanently lost from the system, where in fact the energy is transferred to the electronic system, possibly forming electronic defects such as excitations in bound electron states which possibly transfer energy back into the lattice at a later time.

To further expand upon the MD simulation work, an appropriate model for the electronic system is required. A possible choice may be the two-temperature model (TTM) developed by Duffy and Rutherford [130]. In TTM, the electronic system is modelled as a separate subsystem parametrised by its temperature T_e at each point. Under the influence of the electronic subsystem, the equation of motion for the ionic system is:

$$m_i \frac{\mathrm{d}\mathbf{v}_i}{\mathrm{d}t} = \mathbf{F}_i(t) - \gamma \mathbf{v}_i + \tilde{\mathbf{F}}_i(t) \tag{6.1}$$

where $\mathbf{F}_i(t)$ is the force on atom i as defined in Equation (2.2). γ is a friction term that is a sum of contributions from electronic stopping γ_s and electron-ion interaction γ_p (i.e. $\gamma = \gamma_s + \gamma_p$). $\tilde{\mathbf{F}}_i(t)$ is a stochastic force with random magnitude and direction that satisfies:

$$\left|\tilde{\mathbf{F}}_i(t)\right|^2 = 2k_B T_e \gamma_p \tag{6.2}$$

$\tilde{\mathbf{F}}_i(t)$ simulates the energy gain from electron-ion collisions, thereby being the mechanism by which energy is transferred from the electronic subsystem back to the lattice.

The temperature of the electron subsystem, which determines the average magnitude of $\tilde{\mathbf{F}}_i(t)$, is governed by:

$$C_e \frac{\partial T_e}{\partial t} = \kappa_e \nabla^2 T_e + g_s T - g_p (T_e - T) \tag{6.3}$$

which is essentially a heat equation with an additional source/sink term each for electronic stopping and electron-ion interactions. C_e and κ_e are the specific heat capacity and thermal conductivity of the electronic system, g_s and g_p are the coupling constants for electronic stopping and the electron-ion interaction that can be calculated from energy balancing.

In simulations, Equation (6.3) is implemented as a finite difference equation on a set of constant temperature cells. The number of temperature cells required can be determined by sensitivity analysis.

With the inclusion of electronic effects, the impact on threshold displacement energies and radiation damage cascades in Be (and other materials) can be investigated. It would be of particular interest to determine if the modified K-P model proposed in Equation (4.9) would still hold with the new $E_d^{1.0}$ value.

6.2 Brouwer diagrams with multiple dopant elements

Brouwer diagrams presented in Chapter 5 only consider one dopant element at a time. However, the methodology described in Section 3.3.2 does not preclude the inclusion of additional dopants in the same Brouwer diagram. Defect concentrations can be calculated so long as the respective dopant chemical potentials can be derived. Given a set of dopants ($d1$, $d2$, ...), the respective dopant chemical potentials (μ_{d1}, μ_{d2}, ...) can be obtained by defining the desired dopant concentrations ($\tilde{c}_{d1}$, $\tilde{c}_{d2}$, ...). In the case of a single dopant as in this work, μ_{d1} is adjusted such that c_{d1}, the sum of dopant containing defect concentrations is equal to $\tilde{c}_{d1}$. For multiple dopants this process is the same, requiring a system of equations of the form:

$$c_{di}(\mu_{d1}, \mu_{d2}, ...) = \tilde{c}_{di} \tag{6.4}$$

to be solved, where $i = 1, 2, 3, ...$

Brouwer diagrams with multiple dopants will be of great interest in future research because dopants do not exist in isolation and their interactions may modify how they impact on cladding behaviour.. For example, the presence of Ni^0 has been identified as a key part of the mechanism by which Ni increases HPUF. It may be possible that a second (or maybe more) potential dopant can be identified which when included in the same Brouwer diagram, is predicted to either suppresses the Ni^0 concentration or incorporates Ni^0 in a multi-dopant cluster that does not exhibit the same hydrogen interaction as the $\{Ni''''_{Zr} : V^{\bullet\bullet}_{O}\}''$ cluster.

6.3 MD radiation damage simulations in ZrO_2

The defect concentrations predicted in Chapter 5 are based on equilibrium calculations. During reactor operation, it is expected that radiation effects will have a significant impact on the stability of defects (intrinsic and dopant-containing), as well as the distribution of the dopant elements. This can be investigated via MD damage cascade simulations in monoclinic and

tetragonal ZrO_2. Defects can be introduced into the simulation cells at concentrations predicted in the Brouwer diagrams.

It is clear from Chapter 5 that dopant elements have a considerable effect on defect concentrations, including of those defects that influence transport properties (e.g. oxygen vacancies in ZrO_2). It is therefore likely that dopants will have a significant effect on how a materials responds to radiation damage. Thus, it is important to predict key measurables (e.g. residual defect concentrations and threshold displacement energies) as a function of defect concentration. This would also enable future work to connect the framework developed in this thesis on Be damage to the work on defect concentrations in ZrO_2.

Turning to the methodology of the proposed MD simulations, having a minimum of three elements in the simulation usually means that a set of interatomic potentials are required to describe all permutations of atomic element interactions in the system. It may be possible to use suitable existing potentials for the ZrO_2 system, which leaves the dopant containing potentials sets that will have to be fitted. In any case, the set of interatomic potentials is at the minimum expected to be able to reproduce bulk ZrO_2 properties (such as lattice parameter and elastic constants), as well as all relevant defect energies.

Chapter 7

Summary

The simulation work carried out for this thesis focuses on two separate material systems. In the beryllium metal system, MD radiation damage cascade simulations were performed to understand the processes of primary radiation damage in the material. This is the first step to building a comprehensive model, from atomic to macroscopic scales, for beryllium and its derivatives as a plasma facing material (as well as in other structural components) in fusion reactors. It is also noted that the previous attempt at MD cascade simulations in beryllium [103] employed a potential with negative thermal expansion [150], which this work aims to remedy.

The second material system is ZrO_2, which forms on the surface of Zr-based fuel cladding during reactor operation and effectively acts as a barrier layer between the cladding metal and the coolant water. With the current interest in uprating existing PWR and BWR reactors, the development Zr-based cladding with longer lifetimes by looking at alloying additions is a topic of ongoing research. This thesis aims to, via DFT simulations of dopant behaviour in ZrO_2, identify atomic scale behaviour that alloying elements affect cladding lifetime in terms of corrosion rate and hydrogen pickup. Dopant elements already included in existing cladding materials, such as Fe in Zircaloy-2 and ZIRLO, will be studied first as the consequences of their addition are known experimentally. The findings can then be applied to predict the behaviour of prospective alloying additions and identify suitable candidates for experimental focus. Finally,

the extension of this methodology to study the effect of coolant water chemistry on Zr-based cladding is demonstrated with Li from LiOH as a dopant element.

Results from MD simulations of radiation damage cascades in pure beryllium are presented in Chapter 4, while predicted defect concentrations based on DFT in doped ZrO_2 are presented in Chapter 5.

MD simulations in beryllium utilised an improved form of a Tersoff potential developed by Björkas *et al.* [150]. The original Björkas potential predicted a negative thermal expansion at above 600 K [150], which is undesirable considering the nature of the simulation, in the sense that the simulation cell (locally or even the whole cell) will be brought to temperatures in the negative thermal expansion range. The cause of this negative thermal expansion was discovered and a new potential was fitted based on the methodology by Björkas *et al.* [150] with the correct thermal expansion properties.

Radiation damage cascades in beryllium are predicted to exhibit a branch-like trajectory with defects populating the backbone of the cascade. The number of residual defects surviving the recovery of the thermal spike phase was found to have no significant correlation to simulation temperature. This is attributed to the mechanism by which residual defects survive, which is proposed to result from highly displaced atoms that escape the disordered region generated around the cascade backbone in the thermal spike phase. While more atom displacements may be generated with increasing temperature, the atoms have to escape a larger disorder region to form residual defects. Thus the net effect is that the formation of residual defects is at most weakly dependent on temperature. This mechanism has also been proposed in materials that do not exhibit branch-like damage trajectories [134].

The weak dependence of residual defects on temperature supports the use of simple damage models such as K-P [132]. Through fitting the predicted residual defects to the K-P model, it is found that the optimal E_d value corresponded to $E_d^{1.0}$, the minimum E_{PKA} value at which the

probability of PKA displacement is predicted to be 1 in threshold displacement simulations. This led to the proposal of a modification to the K-P model that utilises the directionally averaged threshold displacement probability. It is proposed for similar MD simulations to be carried out with the addition of a model for electronic effects such as the TTM [130] in future work, to determine if he modified K-P model proposed in Equation (4.9) would hold with the new $E_d^{1.0}$ value.

Defect concentrations calculated for alloying elements currently used in Zr based cladding (Fe, Ni and Cr) show a strong preference for these dopants to form clusters with oxygen vacancies in tetragonal ZrO_2. These clusters have significant binding energies and cluster formation is proposed to be the mechanism by which the addition of these alloying elements reduce corrosion rate in the cladding: by strongly locking in oxygen vacancies, thereby suppressing oxygen transport through the oxide. The prediction of the Ni^0-containing $\{Ni_{Zr}'''' : V_O^{\bullet\bullet}\}''$ cluster at low P_{O_2} is significant. The presence of Ni^0 has been correlated to an increase in hydrogen pickup in a recent experimental study of Zircaloy-2 samples [50]. Through further DFT calculations, it was found that $\{Ni_{Zr}'''' : V_O^{\bullet\bullet}\}''$ is the only predicted defect cluster (amongst the Brouwer diagrams for Fe, Ni and Cr) that prevents the formation of the H_2^+ molecule when two H^+ ions are placed in the oxygen vacancy site. $\{Ni_{Zr}'''' : V_O^{\bullet\bullet}\}''$ formation is thus proposed to be the mechanism by which Ni increases HPUF in Zr-based cladding. The construction of Brouwer diagrams with multiple dopants is suggested in further work to search for a candidate dopant that is able to suppress $\{Ni_{Zr}'''' : V_O^{\bullet\bullet}\}''$ formation.

The above methodology provides a way to predict potential harmful effects to the cladding HPUF (in the same manner as Ni) in candidate alloying elements to help guide experimental work. In this work it is found that neither candidate alloying elements Cu and Sb are expected to have a harmful impact on the HPUF. Regardless, the same oxygen vacancy locking mechanism is also observed for the two candidate dopants, in line with the reduced corrosion rate seen in experiments [54, 86]. Further comparison showed that Cu promotes formation of free oxygen vacancies, increasing oxygen conductivity while Sb does the opposite. For Cu, this

mechanism may eventually negate any possible benefit from its binding to oxygen vacancies. This is reflected in experiment where beyond a critical Cu concentration, further increase in concentration is harmful to corrosion rate [86]. By applying an enforced charge into the defect system, it is found that both Cu and Sb facilitate the build up of space charges near the metal-oxide interface, avoiding undesirable parabolic corrosion kinetics [7]. Overall, the modelling results suggest Sb will exhibit some advantage over Cu as a candidate alloying element for Zr-based cladding with longer in-reactor lifetimes, or increased safety margins for uprated reactors. Further prospective alloying additions can also be investigated in the metholodogy laid out in this thesis to identify and narrow down candidates for further experimental validation.

Finally, in part to demonstrate the extension of the methodology for studying dopants in ZrO_2 to the effect from coolant chemistry, the effect of Li (from LiOH in the coolant water) as a dopant incorporated into the ZrO_2 layer was also considered. Li addition was found elevate the free $V_O^{\bullet\bullet}$ concentration in tetragonal ZrO_2, which may be a mechanism by which Li accelerates the corrosion rate in Zr-based cladding.

Bibliography

[1] *Nuclear Power Reactors in the World*. Number 2 in Reference Data Series. International Atomic Energy Agency, Vienna, 2016.

[2] *Key World Energy Statistics 2016*. International Energy Agency, 2016.

[3] V. Koritarov, J. Kuiper, K. Hlava, et al. Energy Zones Study: A Comprehensive Web-Based Mapping Tool to Identify and Analyze Clean Energy Zones in the Eastern Interconnection. Technical Report May 2014, National Renewable Energy Laboratory (NREL), Golden, CO (United States), sep 2013.

[4] M. Hageman. *Experimental investigation of the thermal performance of gas-cooled divertor plate concepts*. PhD thesis, Georgia Institute of Technology, 2016.

[5] F. Ashby. Materials for nuclear power systems. 2010.

[6] A. Nikulina. Metal Materials for the Elements Zirconium-Niobium Alloys for Core Elements of Pressurized Water Reactors. *Metal Science and Heat Treatment*, 45(No. 8):7–13, 2003.

[7] A. Couet, A. T. Motta, and A. Ambard. The coupled current charge compensation model for zirconium alloy fuel cladding oxidation: I. Parabolic oxidation of zirconium alloys. *Corrosion Science*, 100:73–84, 2015.

[8] A. T. Motta, A. Couet, and R. J. Comstock. Corrosion of Zirconium Alloys Used for Nuclear Fuel Cladding. *Annual Review of Materials Research*, 45(1):311–343, 2015.

[9] J. Yang, M. Youssef, and B. Yildiz. Oxygen self-diffusion mechanisms in monoclinic Zr O2 revealed and quantified by density functional theory, random walk analysis, and kinetic Monte Carlo calculations. *Physical Review B*, 97(2):1–7, 2018.

[10] H. J. Beie, A. Mitwalsky, F. Garzarolli, H. Ruhmann, and H. J. Sell. Examinations of the corrosion mechanism of zirconium alloys. *Astm-Stp*, 1245:615–643, 1994.

[11] C. Lemaignan and A. T. Motta. Zirconium Alloys in Nuclear Applications. *Materials Science and Technology: a Comprehensive Treatment. Vol. 10b: Nuclear Material*, pages 1–51, 1994.

[12] G. Sabol, R. Comstock, R. Weiner, P. Larouere, and R. Stanutz. In-Reactor Corrosion Performance of ZIRLO™ and Zircaloy-4. In *Zirconium in the Nuclear Industry: Tenth International Symposium*, pages 724–744. ASTM International, 100 Barr Harbor Drive, PO Box C700, West Conshohocken, PA 19428-2959, 1994.

[13] A. T. Motta, M. J. Gomes da Silva, A. Yilmazbayhan, et al. Microstructural Characterization of Oxides Formed on Model Zr Alloys Using Synchrotron Radiation. *Journal of ASTM International*, 5(3):1–20, 2008.

[14] A. Couet, A. T. Motta, and R. J. Comstock. Hydrogen pickup measurements in zirconium alloys: Relation to oxidation kinetics. *Journal of Nuclear Materials*, 451(1-3):1–13, 2014.

[15] Y. H. Jeong, H. G. Kim, Y. H. Jung, and H. Ruhmann. Effect of LiOH, NaOH and KOH on corrosion and oxide microstructure of Zr-based alloys. Technical report, International Atomic Energy Agency (IAEA), 1999. IAEA-TECDOC–1128.

[16] M. Oskarsson, E. Ahlberg, and K. Pettersson. Phase transformation of stabilised zirconia in water and 1.0 M LiOH. *Journal of Nuclear Materials*, 295(1):126–130, 2001.

[17] T. Kido, S. Wada, T. Takahashi, et al. Behavior of lithium and boron in irradiated and unirradiated oxides formed on Zircaloy-4 claddings. *ASTM Special Technical Publication*, (1354):773–792, 2000.

[18] J. Yang, M. Youssef, and B. Yildiz. Electro-chemo-mechanical effects of lithium incorporation in zirconium oxide. *Physical Review Materials*, 2(7):1–8, 2018.

[19] B. Cox. Some thoughts on the mechanisms of in-reactor corrosion of zirconium alloys. *Journal of Nuclear Materials*, 336(2-3):331–368, 2005.

[20] E. Polatidis, P. Frankel, J. Wei, et al. Residual stresses and tetragonal phase fraction characterisation of corrosion tested Zircaloy-4 using energy dispersive synchrotron X-ray diffraction. *Journal of Nuclear Materials*, 432(1-3):102–112, 2013.

[21] A. Yilmazbayhan, A. T. Motta, R. J. Comstock, et al. Structure of zirconium alloy oxides formed in pure water studied with synchrotron radiation and optical microscopy: Relation to corrosion rate. *Journal of Nuclear Materials*, 324(1):6–22, 2004.

[22] C. Simpson and C. Ells. Delayed Hydrogen Embrittlement In Zr-2.5 wt % Nb. *Journal of Nuclear Materials*, 52:289–295, 1974.

[23] IAEA - International Atomic Energy Agency. Delayed hydride cracking in zirconium alloys in pressure tube nuclear reactors IAEA-TECDOC-1410, 2004.

[24] P. Raynaud and A. Bielen. Cladding hydrogen based regulations in the United States. *2011 Water Reactor Fuel Performance Meeting*, 2011.

[25] X. Wang, M. J. Zheng, I. Szlufarska, and D. Morgan. Continuum model for hydrogen pickup in zirconium alloys of LWR fuel cladding. *Journal of Applied Physics*, 121(13), 2017.

[26] N. Ramasubramanian, V. Perovic, and M. Leger. Hydrogen transport in the oxide and hydrogen pickup by the metal during out- and in-reactor corrosion of Zr-2.5Nb pressure tube material. *ASTM Special Technical Publication*, pages 853–876, 2000.

[27] T. Smith. Kinetics and mechanism of hydrogen permeation of oxide films on zirconium. *Journal of Nuclear Materials*, 18(3):323–336, 1966.

[28] B. Cox. A mechanism for the hydrogen uptake process in zirconium alloys. *Journal of Nuclear Materials*, 264(3):283–294, 1999.

[29] Y. Hatano, M. Sugisaki, K. Kitano, and M. Hayashi. Role of Intermetallic Precipitates in Hydrogen Transport through Oxide Films on Zircaloy. In *Zirconium in the Nuclear Industry: Twelfth International Symposium*, pages 901–917. ASTM International, 100 Barr Harbor Drive, PO Box C700, West Conshohocken, PA 19428-2959, 2000.

[30] N. Ramasubramanian. Localised electron transport in corroding zirconium alloys. *Journal of Nuclear Materials*, 55(2):134–154, 1975.

[31] J. D. McCullough and K. N. Trueblood. The crystal structure of baddeleyite (monoclinic ZrO2). *Acta Crystallographica*, 12(7):507–511, jul 1959.

[32] P. Bouvier, E. Djurado, G. Lucazeau, and T. Le Bihan. High-pressure structural evolution of undoped tetragonal nanocrystalline zirconia. *Physical Review B - Condensed Matter and Materials Physics*, 62(13):8731–8737, 2000.

[33] N. Selmi and A. Sari. Study of Oxidation Kinetics in Air of Zircaloy-4 by in Situ X-Ray Diffraction. *Advances in Materials Physics and Chemistry*, 03(02):168–173, 2013.

[34] B. De Gabory, A. T. Motta, and K. Wang. Transmission electron microscopy characterization of Zircaloy-4 and ZIRLO oxide layers. *Journal of Nuclear Materials*, 456:272–280, 2015.

[35] H. Gadiyar and J. Balachandra. Stress measurements and structural studies during oxidation of zirconium base alloys. *Transactions of the Indian Institute of Metals*, 28(5):391–397, 1975.

[36] H. Anada and K. Takeda. Microstructure of Oxides on Zircaloy-4, 1.0Nb Zircaloy-4, and Zircaloy-2 Formed in 10.3-MPa Steam at 673 K. In *Zirconium in the Nuclear Industry: Eleventh International Symposium*, pages 35–35–20. ASTM International, 100 Barr Harbor Drive, PO Box C700, West Conshohocken, PA 19428-2959, 2009.

[37] A. Yilmazbayhan, E. Breval, A. T. Motta, and R. J. Comstock. Transmission electron microscopy examination of oxide layers formed on Zr alloys. *Journal of Nuclear Materials*, 349(3):265–281, 2006.

[38] D. Hudson, N. Ni, S. Lozano-Perez, et al. The atomic scale structure and chemistry of the zircaloy-4 metal-oxide interface. *14th International Conference on Environmental Degradation of Materials in Nuclear Power Systems Water Reactors 2009*, 2:1407–1418, 2009.

[39] F. Garzarolli and H. Seidel. Oxide growth mechanism on zirconium alloys. *Zirconium in the Nuclear Industry: Ninth International Symposium*, pages 395–415, 1991.

[40] T. Müller, G. Kästle, H.-G. Boyen, et al. Structural phase transitions in ZrO2 films induced by ion bombardment—Argon irradiation versus implantation. *Journal of Applied Physics*, 93(9):5251–5254, may 2003.

[41] N. Bérerd, A. Chevarier, N. Moncoffre, et al. Zirconium oxidation under high-energy heavy-ion irradiation. *Journal of Applied Physics*, 97(8):083528, apr 2005.

[42] B. Cox. A porosimeter for determining the sizes of flaws in zirconia or other insulating films "In Situ". *Journal of Nuclear Materials*, 27(1):1–11, 1968.

[43] B. Cox and Y. Yamaguchi. The development of porosity in thick zirconia films. *Journal of Nuclear Materials*, 210(3):303–317, 1994.

[44] N. Ni, S. Lozano-Perez, M. L. Jenkins, et al. Porosity in oxides on zirconium fuel cladding alloys, and its importance in controlling oxidation rates. *Scripta Materialia*, 62(8):564–567, 2010.

[45] D. Féron. Overview of nuclear materials and nuclear corrosion science and engineering. In *Nuclear Corrosion Science and Engineering*, pages 31–56. Elsevier, 2012.

[46] H. Takiishi, J. H. Duvaizen, I. M. Sato, et al. Recycling of zircaloy machining chips by VAR remelting and powder metallurgy techniques. *Materials Science Forum*, 727-728(August):356–361, 2012.

[47] R. B. Rebak. The long-term environmental degradation of zirconium alloys in contact with spent nuclear fuel - A review. *American Society of Mechanical Engineers, Pressure Vessels and Piping Division (Publication) PVP*, 7(January 2008):209–214, 2008.

[48] A. Couet, A. T. Motta, B. De Gabory, and Z. Cai. Microbeam X-ray Absorption Near-Edge Spectroscopy study of the oxidation of Fe and Nb in zirconium alloy oxide layers. *Journal of Nuclear Materials*, 452(1-3):614–627, 2014.

[49] K. Sakamoto, K. Une, M. Aomi, and K. Hashizume. Depth profile of chemical states of alloying elements in oxide layer of Zr-based alloys. *Progress in Nuclear Energy*, 57:101–105, 2012.

[50] A. P. Shivprasad, A. T. Motta, A. Kucuk, S. Yagnik, and Z. Cai. Microbeam X-Ray Absorption Near-Edge Spectroscopy of Alloying Elements in the Oxide Layers of Irradiated Zircaloy-2. In *Zirconium in the Nuclear Industry: 18th International Symposium*, pages 524–554. ASTM International, 100 Barr Harbor Drive, PO Box C700, West Conshohocken, PA 19428-2959, jan 2018.

[51] G. Kuri, H. Ramanantoanina, J. Bertsch, M. Martin, and I. Panas. Chemical state and atomic scale environment of nickel in the corrosion layer of irradiated Zircaloy-2 at a burn-up around 45 MWd/kg. *Corrosion Science*, 143:200–211, oct 2018.

[52] B. D. C. Bell, S. T. Murphy, P. A. Burr, R. W. Grimes, and M. R. Wenman. Accommodation of tin in tetragonal ZrO2. *Journal of Applied Physics*, 117(8):1–18, 2015.

[53] B. Bell, S. Murphy, P. Burr, et al. The influence of alloying elements on the corrosion of Zr alloys. *Corrosion Science*, 105:36–43, apr 2016.

[54] B. Bell. *The Influence of Alloying Elements on the Corrosion of Zr-based Nuclear Fuel Cladding Using Density Functional Theory*. PhD thesis, Imperial College London, 2016.

[55] B. Bell, S. Murphy, R. Grimes, and M. Wenman. The effect of Nb on the corrosion and hydrogen pick-up of Zr alloys. *Acta Materialia*, 132:425–431, 2017.

[56] M. Youssef and B. Yildiz. Intrinsic point-defect equilibria in tetragonal ZrO_2: Density functional theory analysis with finite-temperature effects. *Physical Review B*, 86(14):144109, oct 2012.

[57] U. Otgonbaatar, W. Ma, M. Youssef, and B. Yildiz. Effect of Niobium on the Defect Chemistry and Oxidation Kinetics of Tetragonal ZrO_2. *The Journal of Physical Chemistry C*, 118(35):20122–20131, 2014.

[58] S. Zhang and J. Northrup. Chemical potential dependence of defect formation energies in GaAs: Application to Ga self-diffusion. *Physical Review Letters*, 67(17):2339–2342, oct 1991.

[59] R. Krishnan and M. K. Asundi. Zirconium alloys in nuclear technology, 1981.

[60] S. Kass. The Development of the Zircaloys. In *Corrosion of Zirconium Alloys*, pages 3–27. ASTM International, 100 Barr Harbor Drive, PO Box C700, West Conshohocken, PA 19428-2959, 1964.

[61] A. Garde, S. Pati, M. Krammen, G. Smith, and R. Endter. Corrosion Behavior of Zircaloy-4 Cladding with Varying Tin Content in High-Temperature Pressurized Water Reactors. *Zirconium in the Nuclear Industry: Tenth International Symposium*, pages 760–760–19, 1994.

[62] K. Takeda and H. Anada. Mechanism of corrosion rate degradation due to tin. *ASTM Special Technical Publication*, (1354):592–608, 2000.

[63] J. Schefold, D. Lincot, A. Ambard, and O. Kerrec. The Cyclic Nature of Corrosion of Zr and Zr-Sn in High-Temperature Water (633 K). *Journal of The Electrochemical Society*, 150(10):B451, 2003.

[64] J. Wei, P. Frankel, E. Polatidis, et al. The effect of Sn on autoclave corrosion performance and corrosion mechanisms in Zr-Sn-Nb alloys. *Acta Materialia*, 61(11):4200–4214, 2013.

[65] D. Charquet. Improvement of the uniform corrosion resistance of Zircaloy-4 in the absence of irradiation. *Journal of Nuclear Materials*, 160(2-3):186–195, 1988.

[66] H. Lee and W. Cai. Ewald summation for Coulomb interactions in a periodic supercell. *Lecture Notes, Stanford University*, 3(1):1–12, 2009.

[67] D. Pecheur, V. Filippov, A. Bateev, and J. Ivanov. Mössbauer Investigations of the Chemical States of Tin and Iron Atoms in Zirconium Alloy Oxide Film. *Zirconium in the Nuclear Industry: Thirteenth International Symposium*, pages 135–135–19, 2002.

[68] H. Hulme, F. Baxter, R. P. Babu, et al. An X-ray absorption near-edge structure (XANES) study of the Sn L3 edge in zirconium alloy oxide films formed during autoclave corrosion. *Corrosion Science*, 105:202–208, 2016.

[69] G. Sundell, M. Thuvander, and H. O. Andrén. Tin clustering and precipitation in the oxide during autoclave corrosion of Zircaloy-2. *Journal of Nuclear Materials*, 456:409–414, 2015.

[70] B. A. van Hassel and A. J. Burggraaf. Oxidation state of Fe and Ti ions implanted in yttria-stabilized zirconia studied by XPS. *Applied Physics A Solids and Surfaces*, 52(6):410–417, 1991.

[71] D. Sangalli, A. Lamperti, E. Cianci, et al. Role of oxygen vacancies on the structure and density of states of iron-doped zirconia. *Physical Review B*, 87(8):085206, feb 2013.

[72] B. M. Ensor, A. T. Motta, R. A. M. Bajaj, J. R. Seidensticker, and Z. Cai. Xanes analysis of iron in Zircaloy-4 oxides formed at different temperatures studied with microbeam synchrotron radiation. 2015.

[73] D. Hudson, G. D. W. Smith, and B. Gault. Optimisation of mass ranging for atom probe microanalysis and application to the corrosion processes in Zr alloys. *Ultramicroscopy*, 111(6):480–486, 2011.

[74] G. Sundell, M. Thuvander, P. Tejland, et al. Redistribution of alloying elements in Zircaloy-2 after in-reactor exposure. *Journal of Nuclear Materials*, 454(1-3):178–185, 2014.

[75] J. Hu, L. Yang, G. Cao, et al. On the oxidation behavior of $(Zr,Nb)_2Fe$ under simulated nuclear reactor conditions. *Corrosion Science*, 112:718–723, 2016.

[76] K. Kakiuchi, K. Ohira, N. Itagaki, et al. Irradiated Behavior at High Burnup for HiFi Alloy. *Journal of Nuclear Science and Technology*, 43(9):1031–1036, 2006.

[77] C. Anghel, G. Hultquist, and M. Limbäck. Influence of Pt, Fe/Ni/Cr-containing intermetallics and deuterium on the oxidation of Zr-based materials. *Journal of Nuclear Materials*, 340(2-3):271–283, 2005.

[78] K. Kakiuchi, N. Itagaki, T. Furuya, et al. Role of Iron for Hydrogen Absorption Mechanism in Zirconium Alloys. *Journal of ASTM International*, 1(10):1–16, 2004.

[79] Y. Hatano, R. Hitaka, M. Sugisaki, and M. Hayashi. Influence of size distribution of $Zr(Fe,Cr)_2$ precipitates on hydrogen transport through oxide film of Zircaloy-4. *Journal of Nuclear Materials*, 248:311–314, 1997.

[80] G. Cao, L. Yang, G. Yuan, et al. Chemical diversity of iron species and structure evolution during the oxidation of C14 Laves phase $Zr(Fe,Nb)_2$ in subcritical environment. *Corrosion Science*, 162(September 2019):108218, 2020.

[81] D. Peng, X. Bai, R. Yu, et al. Role of chromium ion implantation on the corrosion behavior of zircaloy-4 in 0.5M H_2SO_4. *Electrochimica Acta*, 49(9-10):1403–1408, apr 2004.

[82] W. Yeniscavich, R. Wolfe, and R. Lieberman. Hydrogen absorption by nickel enriched zircaloy-2. *Journal of Nuclear Materials*, 1(3):271–280, oct 1959.

[83] S. Kass. Hydrogen Pickup in Various Zirconium Alloys during Corrosion Exposure in High-Temperature Water and Steam. *Journal of The Electrochemical Society*, 107(7):594–597, 1960.

[84] W. Berry, D. Vaughan, and E. White. Hydrogen Pickup During Corrosion of Zirconium Alloys. Technical report, Divison of Technical Information Extension, U.S. Atomic Energy Commission, sep 1959.

[85] G. Sundell, M. Thuvander, and H. O. Andrén. Enrichment of Fe and Ni at metal and oxide grain boundaries in corroded Zircaloy-2. *Corrosion Science*, 65:10–12, 2012.

[86] H. S. Hong, J. S. Moon, S. J. Kim, and K. S. Lee. Investigation on the oxidation characteristics of copper-added modified Zircaloy-4 alloys in pressurized water at 360°C. *Journal of Nuclear Materials*, 297(2):113–119, 2001.

[87] H. S. Hong, H. S. Kim, S. J. Kim, and K. S. Lee. Effects of copper addition on the tensile properties and microstructures of modified Zircaloy-4. *Journal of Nuclear Materials*, 280(2):230–234, 2000.

[88] W. E. Berry, D. A. Vaughan, and E. L. White. Hydrogen Pickup During Aqueous Corrosion Of Zirconium Alloys. *Corrosion*, 17(3):109–117, mar 1961.

[89] H. Okamoto. The Sb-Zr (antimony-zirconium) system. *Journal of Phase Equilibria*, 14(2):228–231, apr 1993.

[90] G. Sundell, M. Thuvander, and H.-O. Andrén. Tin clustering and precipitation in the oxide during autoclave corrosion of Zircaloy-2. *Journal of Nuclear Materials*, 456:409–414, jan 2015.

[91] Y. Hatano and M. Sugisaki. Oxidation Behavior of Iron and Nickel in Zr_2(Fe, Ni) Precipitates in Zircaloy-2. *Journal of Nuclear Science and Technology*, 33(11):829–833, 1996.

[92] T. A. Tomberlin. Beryllium - a Unique Material in Nuclear Applications. *36th International SAMPE Technical Conference*, pages 2–12, 2004.

[93] P. S. Bejarano and R. G. Cocco. Beryllium Reflectors for Research Reactors . Review and Preliminary Finite Element Analysis. *4th International Symposium on Material Testing Reactors*, (December 2011), 2011.

[94] G. Federici. Plasma wall interactions in ITER. *Physica Scripta T*, T124:1–8, 2006.

[95] M. Rubel. Fusion Neutrons: Tritium Breeding and Impact on Wall Materials and Components of Diagnostic Systems. *Journal of Fusion Energy*, 38(3-4):315–329, 2019.

[96] H. Bolt, V. Barabash, G. Federici, et al. Plasma facing and high heat flux materials - Needs for ITER and beyond. *Journal of Nuclear Materials*, 307-311(1 SUPPL.):43–52, 2002.

[97] S. M. González De Vicente, E. R. Hodgson, and T. Shikama. Functional materials for tokamak in-vessel systems - Status and developments. *Nuclear Fusion*, 57(9), 2017.

[98] A. Burkholz. Irradiation Damage in Beryllium. *European Atomic Energy Community (EURATOM) Report*, 1966.

[99] V. P. Chakin, A. O. Posevin, and R. N. Latypov. Radiation damage in beryllium at 70–440° C and neutron fluence (0.3–18)· 10 22 cmˆ-2 (En > 0.1 MeV). *Atomic Energy*, 101(4):743–749, 2006.

[100] D. Gelles and H. Heinisch. Neutron damage in beryllium. *Journal of Nuclear Materials*, 191:194–198, 1992.

[101] S. C. Middleburgh and R. W. Grimes. Defects and transport processes in beryllium. *Acta Materialia*, 59(18):7095–7103, 2011.

[102] R. Watson and J. Whitley. Thermal fatigue tests of a prototype beryllium limiter for jet. *Nuclear Engineering and Design. Fusion*, 4(1):49–60, jan 1986.

[103] V. Borodin and P. Vladimirov. Damage production in atomic displacement cascades in beryllium. *Nuclear Materials and Energy*, 0(Md):1–5, 2016.

[104] P. Zhang, J. Zhao, and B. Wen. Retention and diffusion of H, He, O, C impurities in Be. *Journal of Nuclear Materials*, 423(1-3):164–169, 2012.

[105] P. Kurinskiy, A. Moeslang, V. Chakin, et al. Characteristics of microstructure, swelling and mechanical behaviour of titanium beryllide samples after high-dose neutron irradiation at 740 and 873 K. *Fusion Engineering and Design*, 88(9-10):2198–2201, 2013.

[106] M. L. Jackson. Atomistic Simulations of Materials for Nuclear Fusion. (January), 2018.

[107] H. Kawamura, H. Takahashi, N. Yoshida, et al. Application of beryllium intermetallic compounds to neutron multiplier of fusion blanket. *Fusion Engineering and Design*, 61-62:391–397, 2002.

[108] P. Vladimirov, D. Bachurin, V. Borodin, et al. Current status of beryllium materials for fusion blanket applications. *Fusion Science and Technology*, 66(1):28–37, 2014.

[109] H. Yamada, Y. Nagao, H. Kawamura, et al. Preliminary neutronic estimation for demo blanket with beryllide. *Fusion Engineering and Design*, 69(1-4 SPEC):269–273, 2003.

[110] B. Finlayson. *Ullmann's Encyclopedia of Industrial Chemistry*. Number December 2006. 2006.

[111] Y. W. Yang and P. Coppens. The electron density and bonding in beryllium metal as studied by Fourier methods. *Acta Crystallographica Section A*, 34(1):61–65, 1978.

[112] M. C. Heaven, V. E. Bondybey, J. M. Merritt, and A. L. Kaledin. The unique bonding characteristics of beryllium and the group IIA metals. *Chemical Physics Letters*, 506(1-3):1–14, 2011.

[113] F. W. von Batchelder and R. F. Raeuchle. The structure of a new series of M Be 12 compounds . *Acta Crystallographica*, 10(10):648–649, 1957.

[114] M. L. Jackson, P. A. Burr, and R. W. Grimes. Resolving the structure of TiBe 12. *Acta Crystallographica Section B Structural Science, Crystal Engineering and Materials*, 72(2):277–280, 2016.

[115] TiBe12 (Be12Ti) Crystal Structure: Datasheet from "PAULING FILE Multinaries Edition – 2012" in SpringerMaterials (https://materials.springer.com/isp/crystallographic/docs/sd_0451342).

[116] Be12V Crystal Structure: Datasheet from "PAULING FILE Multinaries Edition – 2012" in SpringerMaterials (https://materials.springer.com/isp/crystallographic/docs/sd_0528339).

[117] H. Okamoto. Be-Ti (Beryllium-Titanium). *Journal of Phase Equilibria and Diffusion*, 29(2):202–202, 2008.

[118] H. Okamoto. Be-V (Beryllium-Vanadium). *Journal of Phase Equilibria and Diffusion*, 33(4):341–341, aug 2012.

[119] M. L. Jackson, P. C. M. Fossati, and R. W. Grimes. Simulations of threshold displacement in beryllium. *Journal of Applied Physics*, 120(4), 2016.

[120] T. D. De La Rubia, R. S. Averback, R. Benedek, and W. E. King. Role of thermal spikes in energetic displacement cascades. *Physical Review Letters*, 59(17):1930–1933, 1987.

[121] K. Nordlund and F. Djurabekova. Multiscale modelling of irradiation in nanostructures. *Journal of Computational Electronics*, 13(1):122–141, 2014.

[122] K. Nordlund, S. J. Zinkle, A. E. Sand, et al. Primary radiation damage: A review of current understanding and models. *Journal of Nuclear Materials*, 512:450–479, 2018.

[123] J. A. Brinkman. On the Nature of Radiation Damage in Metals. *Journal of Applied Physics*, 25(8):961–970, aug 1954.

[124] T. Diaz De La Rubia and G. H. Gilmer. Structural transformations and defect production in ion implanted silicon: A molecular dynamics simulation study. *Physical Review Letters*, 74(13):2507–2510, 1995.

[125] I. Jenčič and I. M. Robertson. Low-energy electron beam induced regrowth of isolated amorphous zones in Si and Ge. *Journal of Materials Research*, 11(9):2152–2157, 1996.

[126] F. Garner, S. Porollo, Y. Konobeev, and O. Maksimkin. Void Swelling of Austenitic Steels Irradiated with Neutrons at Low Temperatures and Very Low Dpa Rates. 2005.

[127] K. Farrell, S. Mahmood, R. Stoller, and L. Mansur. An evaluation of low temperature radiation embrittlement mechanisms in ferritic alloys. *Journal of Nuclear Materials*, 210(3):268–281, jun 1994.

[128] M. Berger, J. Coursey, M. Zucker, and J. Chang. Stopping-Power & Range Tables for Electrons, Protons, and Helium Ions, 2017.

[129] D. Kanjilal. Swift heavy ion-induced modification and track formation in materials. *Current Science*, 80(12):1560–1566, 2001.

[130] D. Duffy and A. Rutherford. Including the effects of electronic stopping and electron–ion interactions in radiation damage simulations. *Journal of Physics: Condensed Matter*, 19(1):16207, 2007.

[131] A. Rutherford and D. Duffy. The effect of electron-ion interactions on radiation damage simulations. *Journal of Physics: Condensed Matter*, 19(49):1–9, 2007.

[132] G. H. Kinchin and R. S. Pease. The Displacement of Atoms in Solids by Radiation. *Reports on Progress in Physics*, 18(1):301, jan 1955.

[133] M. J. Norgett, M. T. Robinson, and I. M. Torrens. A proposed method of calculating displacement dose rates. *Nuclear Engineering and Design*, 33(1):50–54, 1975.

[134] K. Nordlund, S. J. Zinkle, A. E. Sand, et al. Improving atomic displacement and replacement calculations with physically realistic damage models. *Nature Communications*, 9(1):1084, dec 2018.

[135] K. Nordlund. Historical review of computer simulation of radiation effects in materials. *Journal of Nuclear Materials*, 520:273–295, 2019.

[136] M. Stan. Discovery and design of nuclear fuels. *Materials Today*, 12(11):20–28, 2009.

[137] K. Nordlund, M. Ghaly, R. S. Averback, et al. Defect production in collision cascades in elemental semiconductors and fcc metals. *Physical Review B*, 57(13):7556–7570, 1998.

[138] B. P. Uberuaga and A. F. Voter. Accelerated Molecular Dynamics Methods. In K. E. Sickafus, E. A. Kotomin, and B. P. Uberuaga, editors, *Radiation Effects in Solids*, pages 25–43, Dordrecht, 2007. Springer Netherlands.

[139] F. Soisson. Kinetic Monte Carlo simulations of radiation induced segregation and precipitation. *Journal of Nuclear Materials*, 349(3):235–250, 2006.

[140] J. F. Ziegler, M. D. Ziegler, and J. P. Biersack. SRIM - The stopping and range of ions in matter (2010). *Nuclear Instruments and Methods in Physics Research, Section B: Beam Interactions with Materials and Atoms*, 268(11-12):1818–1823, 2010.

[141] R. J. Amodeo and N. M. Ghoniem. Dislocation dynamics. I. A proposed methodology for deformation micromechanics. *Physical Review B*, 41(10):6958–6967, apr 1990.

[142] S. L. Dudarev, D. R. Mason, E. Tarleton, P. W. Ma, and A. E. Sand. A multi-scale model for stresses, strains and swelling of reactor components under irradiation. *Nuclear Fusion*, 58(12), 2018.

[143] S. Plimpton. Fast Parallel Algorithms for Short – Range Molecular Dynamics. *Journal of Computational Physics*, 117(June 1994):1–19, 1995.

[144] P. Hohenberg and W. Kohn. Inhomogeneous Electron Gas. *Physical Review*, 136(3B):B864–B871, nov 1964.

[145] S. J. Clark, M. D. Segall, C. J. Pickard, et al. First principles methods using CASTEP. *Zeitschrift für Kristallographie*, 220(5-6-2005):567–570, 2005.

[146] W. Kohn and L. J. Sham. Self-consistent equations including exchange and correlation effects. *Physical Review*, 140(4A), 1965.

[147] L. Verlet. Computer "Experiments" on Classical Fluids. I. Thermodynamical Properties of Lennard-Jones Molecules. *Physical Review*, 159(1):98–103, jul 1967.

[148] W. G. Hoover. Canonical dynamics: Equilibrium phase-space distributions. *Physical Review A*, 31(3):1695–1697, mar 1985.

[149] G. J. Martyna, M. L. Klein, and M. Tuckerman. Nosé-Hoover chains: The canonical ensemble via continuous dynamics. *The Journal of Chemical Physics*, 97(4):2635–2643, 1992.

[150] C. Björkas, N. Juslin, H. Timko, et al. Interatomic potentials for the Be-C-H system. *Journal of physics. Condensed matter : an Institute of Physics journal*, 21(44):445002, 2009.

[151] J. Tersoff. New empirical approach for the structure and energy of covalent systems. *Physical Review B*, 37(12):6991–7000, 1988.

[152] C. Kittel. *Introduction to solid state physics*. John Wiley & Sons Inc., 8th edition, 2004.

[153] W. Evans, M. Lipp, H. Cynn, et al. X-ray diffraction and Raman studies of beryllium: Static and elastic properties at high pressures. *Physical Review B*, 72(9):094113–1–6, 2005.

[154] A. Migliori, H. Ledbetter, D. J. Thoma, and T. W. Darling. Beryllium's monocrystal and polycrystal elastic constants. *Journal of Applied Physics*, 95(5):2436–2440, 2004.

[155] D. J. Silversmith and B. Averbach. Pressure Dependence of the Elastic Constants of Beryllium and Beryllium Copper Alloys. *Physical Review B*, 1(2):567–571, 1970.

[156] A. Agrawal, R. Mishra, L. Ward, K. M. Flores, and W. Windl. An embedded atom method potential of beryllium. *Modelling and Simulation in Materials Science and Engineering*, 21(8):085001, dec 2013.

[157] M. I. Baskes and R. A. Johnson. Modified embedded atom potentials for HCP metals. *Modelling and Simulation in Materials Science and Engineering*, 2(1):147–163, 1994.

[158] A. P. Thompson, J. M. D. Lane, M. P. Desjarlais, et al. Molecular Dynamics Simulation of Dynamic Response of Beryllium. In *AIP Conference Proceedings*, volume 1426, pages 833–836, 2009.

[159] V. V. Dremov, A. V. Karavaev, F. A. Sapozhnikov, M. A. Vorobyova, and L. Soulard. Molecular dynamics simulation of thermodynamic and mechanical properties of Be (part II). *AIP Conference Proceedings*, 1195(Part Ii):837–840, 2009.

[160] J. F. Ziegler and J. P. Biersack. The Stopping and Range of Ions in Matter. In D. A. Bromley, editor, *Treatise on Heavy-Ion Science: Volume 6: Astrophysics, Chemistry, and Condensed Matter*, pages 93–129. Springer US, Boston, MA, 1985.

[161] P. Gordon. A high temperature precision x-ray camera: Some measurements of the thermal coefficients of expansion of beryllium. *Journal of Applied Physics*, 20(10):908–917, 1949.

[162] T. Kumagai, S. Izumi, S. Hara, and S. Sakai. Development of bond-order potentials that can reproduce the elastic constants and melting point of silicon for classical molecular dynamics simulation. *Computational Materials Science*, 39(2):457–464, 2007.

[163] J. A. Nelder and R. Mead. A Simplex Method for Function Minimization. *The Computer Journal*, 7(4):308–313, jan 1965.

[164] K. Govers, S. Lemehov, M. Hou, and M. Verwerft. Comparison of interatomic potentials for UO2. Part II: Molecular dynamics simulations. *Journal of Nuclear Materials*, 376(1):66–77, 2008.

[165] H. Hensel and H. M. Urbassek. Implantation and damage under low-energy Si self-bombardment. *Physical Review B - Condensed Matter and Materials Physics*, 57(8):4756–4763, 1998.

[166] M. Ghaly and R. S. Averback. Effect of viscous flow on ion damage near solid surfaces. *Physical Review Letters*, 72(3):364–367, jan 1994.

[167] J. B. Gibson, A. N. Goland, M. Milgram, and G. H. Vineyard. Dynamics of radiation damage. *Physical Review*, 120(4):1229–1253, 1960.

[168] M. Caturla, T. Díaz de la Rubia, L. Marqués, and G. Gilmer. Ion-beam processing of silicon at keV energies: A molecular-dynamics study. *Physical Review B - Condensed Matter and Materials Physics*, 54(23):16683–16695, 1996.

[169] M. Robinson, N. A. Marks, and G. R. Lumpkin. Sensitivity of the threshold displacement energy to temperature and time. *Physical Review B*, 86(13):134105, oct 2012.

[170] M. Born and R. Oppenheimer. Zur Quantentheorie der Molekeln. *Annalen der Physik*, 389(20):457–484, 1927.

[171] D. R. Hartree and W. Hartree. Self-consistent field, with exchange, for beryllium. *Proceedings of the Royal Society of London. Series A - Mathematical and Physical Sciences*, 150(869):9–33, may 1935.

[172] N. Mardirossian and M. Head-Gordon. Thirty years of density functional theory in computational chemistry: An overview and extensive assessment of 200 density functionals. *Molecular Physics*, 115(19):2315–2372, 2017.

[173] P. A. Dirac. Note on Exchange Phenomena in the Thomas Atom. *Mathematical Proceedings of the Cambridge Philosophical Society*, 26(3):376–385, 1930.

[174] M. Gell-Mann and K. A. Brueckner. Correlation Energy of an Electron Gas at High Density. *Physical Review*, 106(2):364–368, apr 1957.

[175] J. P. Perdew and Y. Wang. Accurate and simple analytic representation of the electron-gas correlation energy. *Physical Review B*, 45(23):13244–13249, jun 1992.

[176] P. P. Ewald. Die Berechnung optischer und elektrostatischer Gitterpotentiale. *Annalen der Physik*, 369(3):253–287, 1921.

[177] D. Bagayoko. Understanding density functional theory (DFT) and completing it in practice. *AIP Advances*, 4(12), 2014.

[178] J. P. Perdew, K. Burke, and M. Ernzerhof. Generalized Gradient Approximation Made Simple. *Physical Review Letters*, 77(18):3865–3868, 1996.

[179] P. A. Burr. *Ab-initio modelling of Zr and Be alloys for nuclear applications*. PhD thesis.

[180] K. Burke. Perspective on density functional theory. *Journal of Chemical Physics*, 136(15), 2012.

[181] M. Youssef and B. Yildiz. Hydrogen defects in tetragonal ZrO_2 studied using density functional theory. *Phys. Chem. Chem. Phys.*, 16(4):1354–1365, 2014.

[182] H. J. Monkhorst and J. D. Pack. Special points for Brillouin-zone integrations. *Physical Review B*, 13(12):5188–5192, jun 1976.

[183] P. Pulay. Convergence acceleration of iterative sequences. the case of scf iteration. *Chemical Physics Letters*, 73(2):393–398, 1980.

[184] R. S. Mulliken. Electronic Population Analysis on LCAO–MO Molecular Wave Functions. I. *The Journal of Chemical Physics*, 23(10):1833–1840, oct 1955.

[185] L. Minervini, M. O. Zacate, and R. W. Grimes. Defect cluster formation in M_2O_3-doped CeO_2. *Solid State Ionics*, 116(3):339–349, 1999.

[186] S. T. Murphy and N. D. M. Hine. Anisotropic charge screening and supercell size convergence of defect formation energies. *Physical Review B - Condensed Matter and Materials Physics*, 87(9):1–18, mar 2013.

[187] X. Zhao and D. Vanderbilt. First-principles study of structural, vibrational, and lattice dielectric properties of hafnium oxide. *Physical Review B - Condensed Matter and Materials Physics*, 65(23):1–4, 2002.

[188] M. Finnis, A. Lozovoi, and A. Alavi. The Oxidation of NiAl: What Can We Learn from Ab Initio Calculations? *Annual Review of Materials Research*, 35(1):167–207, aug 2005.

[189] E. Weast, R.C. *CRC Handbook of Chemistry, and Physics*. CRC Press, 97th edition, 1989.

[190] S. T. Murphy and N. D. M. Hine. Point defects and non-stoichiometry in Li_2TiO_3. *Chemistry of Materials*, 26(4):1629–1638, 2014.

[191] F. Bruneval, C. Varvenne, J. P. Crocombette, and E. Clouet. Pressure, relaxation volume, and elastic interactions in charged simulation cells. *Physical Review B - Condensed Matter and Materials Physics*, 91(2):1–8, 2015.

[192] A. Goyal, K. Mathew, R. G. Hennig, et al. The conundrum of relaxation volumes in first-principles calculations of charge defects. pages 1–16, 2017.

[193] M. D. Segall, C. J. Pickard, R. Shah, and M. C. Payne. Population analysis in plane wave electronic structure calculations. *Molecular Physics*, 89(2):571–577, oct 1996.

[194] M. D. Segall, R. Shah, C. J. Pickard, and M. C. Payne. Population analysis of plane-wave electronic structure calculations of bulk materials. *Physical Review B*, 54(23):16317–16320, 1996.

[195] Y. R. Than and R. W. Grimes. Predicting Radiation Damage in Beryllium. *Philosophical Magazine*, 2020.

[196] V. A. Borodin. Molecular dynamics simulation of annealing of post-ballistic cascade remnants in silicon. *Nuclear Instruments and Methods in Physics Research, Section B: Beam Interactions with Materials and Atoms*, 282:33–37, 2012.

[197] P. V. Vladimirov and V. A. Borodin. First-principles and classical molecular dynamics study of threshold displacement energy in beryllium. *Nuclear Instruments and Methods in Physics Research, Section B: Beam Interactions with Materials and Atoms*, 393:195–199, 2017.

[198] F. Gao, D. J. Bacon, P. E. Flewitt, and T. A. Lewis. A molecular dynamics study of temperature effects on defect production by displacement cascades in α-iron. *Journal of Nuclear Materials*, 249(1):77–86, 1997.

[199] D. J. Bacon, F. Gao, and Y. N. Osetsky. Primary damage state in fcc, bcc and hcp metals as seen in molecular dynamics simulations. *Journal of Nuclear Materials*, 276(1):1–12, 2000.

[200] T. R. Allen. High Dose Radiation Effects in Steels. In *Radiation Effects in Solids*, pages 99–121. Springer Netherlands, Dordrecht.

[201] G. S. Was. *Fundamentals of Radiation Materials Science*. Springer Berlin Heidelberg, Berlin, Heidelberg, 2007.

[202] Y. Wu. Design analysis of the China dual-functional lithium lead (DFLL) test blanket module in ITER. *Fusion Engineering and Design*, 82(15-24):1893–1903, 2007.

[203] R. Averback and T. de la Rubia. Displacement damage in irradiated metals and semiconductors. *Solid State Physics: Advances in Research and Applications*, 51(C):281–402, December 1997.

[204] Y. R. Than, M. R. Wenman, B. D. Bell, et al. Modelling and experimental analysis of the effect of solute iron in thermally grown Zircaloy-4 oxides. *Journal of Nuclear Materials*, 2018.

[205] Y. R. Than, R. W. Grimes, B. D. Bell, and M. R. Wenman. Understanding the role of Fe, Cr and Ni in Zircaloy-2 with special focus on the role of Ni on hydrogen pickup. *Journal of Nuclear Materials*, 530:151956, 2020.

[206] K. Kakiuchi, K. Ohira, N. Itagaki, et al. Irradiated Behavior at High Burnup for HiFi Alloy. *Journal of Nuclear Science and Technology*, 43(9):1031–1036, 2006.

[207] W. Weppner. Voltage relaxation measurements of the electron and hole mobilities in yttria-doped zirconia. *Electrochimica Acta*, 22(7):721–727, jul 1977.

[208] M. J. Wolf, K. P. McKenna, and A. L. Shluger. Hole Trapping at Surfaces of m-ZrO_2 and m-HfO_2 Nanocrystals. *The Journal of Physical Chemistry C*, 116(49):25888–25897, 2012.

[209] A. T. Fromhold. *Theory of Metal Oxidation: Space charge*. Defects in crystalline solids. North Holland Publishing Company, 1976.

[210] G. Cao, Y. Yun, H. Xu, et al. A mechanism assessment for the anti-corrosion of zirconia coating under the condition of subcritical water corrosion. *Corrosion Science*, 152(March):54–59, 2019.

[211] C. Roy and B. Burgess. A study of the stresses generated in zirconia films during the oxidation of zirconium alloys. *Oxidation of Metals*, 2(3):235–261, 1970.

[212] M. O. Zacate, L. Minervini, D. J. Bradfield, R. W. Grimes, and K. E. Sickafus. Defect cluster formation in M_2O_3-doped cubic ZrO_2. *Solid State Ionics*, 128(1-4):243–254, 2000.

[213] M. Lindgren and I. Panas. Confinement dependence of electro-catalysts for hydrogen evolution from water splitting. *Beilstein Journal of Nanotechnology*, 5:195–201, 2014.